THE EFFICACY OF UTILIZING SOLIDWORKS

FINITE ELEMENT ANALYSIS FOR DESIGN OF

COMPOSITE I-BEAM WING SPARS IN UAVS

By

MICHAEL DAVID SALLAZ

Bachelor of Science in Aerospace Engineering

Bachelor of Science in Mechanical Engineering

Oklahoma State University

Stillwater, OK

2021

Submitted to the Faculty of the
Graduate College of the
Oklahoma State University
in partial fulfillment of
the requirements for
the Degree of
MASTER OF SCIENCE
May, 2023

THE EFFICACY OF UTILIZING SOLIDWORKS

FINITE ELEMENT ANALYSIS FOR DESIGN OF

COMPOSITE I-BEAM WING SPARS IN UAVS

Thesis Approved:

Dr. Andrew Arena

Thesis Adviser

Dr. Joseph Conner

Dr. Ryan Paul

ACKNOWLEDGEMENTS

Thank you to my committee members for your support throughout all phases of my research, especially at the beginning. Your guidance, insight, and feedback greatly assisted in ensuring that my research was well planned, executed, and explored. A special thank you to Dr. Conner for equipping me with the appropriate strain gage instrumentation to properly acquire experimental stresses. Thank you for putting up with the many questions I had for you about strain gages as well! Without this equipment and your assistance, I have no doubt this aspect of my research would have been severely lacking due to my initial naivety on the subject.

To my friends and family, thank you for your unwavering support in my pursuit of a Master's Degree. Juggling academic, thesis, GRA, and social responsibilities over the last two years was by no means easy and there were many times I felt overwhelmed by it all. It was in times like these that your support was most effective, providing me with the necessary motivation to continue on. Due in large part to your support, I have achieved far more than I could have ever hoped for, and I hope you understand how important you all were in ensuring that I reached this milestone in my life. I am truly grateful.

To my colleagues in Dr. Arena's Lab at OSU, thank you for being there through it all. The camaraderie (and on occasion, the suffering) we shared during my time there made my post-graduate experience that much better. In fact, the work we did and the friendships I formed with you all will no doubt be a source of nostalgia whenever I think back to this period of my life. In addition, thank you for being there when I needed someone to bounce research ideas off of. Your suggestions and assistance were incredibly beneficial, even if you did not realize it. I wish you all the best!

Name: MICHAEL DAVID SALLAZ

Date of Degree: MAY, 2023

Title of Study: THE EFFICACY OF UTILIZING SOLIDWORKS FINITE ELEMENT ANALYSIS FOR DESIGN OF COMPOSITE I-BEAM WING SPARS IN UAVS

Major Field: MECHANICAL AND AEROSPACE ENGINEERING

Abstract: Labs in which unmanned composite aircraft are produced by Oklahoma State University currently lack the capability to adequately analyze wing structural designs computationally. This is especially true regarding the design of the main composite wing spar. Within these labs, utilization of SolidWorks for modeling and CFD analysis of designs to be built is commonplace. It would be advantageous to capitalize on this familiarity with SolidWorks to extend pre-prototype analysis capabilities by utilizing the SolidWorks FEA package to analyze wing spars designed for both graduate level and undergraduate capstone projects. Proof of good correlation between experimental 3-Point Bending testing and FEA results for these composite spars would allow for further pre-prototype structural refinement, thus reducing the man hours and material costs associated with the prototyping phase. To this end, this research endeavor seeks to determine the feasibility of various Finite Element Modeling techniques through direct comparison of FEA results with both experimentation and existing Beam Theory methods. Initial baseline testing of isotropic aluminum beams established the proper procedures for boundary and loading condition application as well as for model meshing. Results from these baseline tests further established that SolidWorks FEA is capable of predicting deflection, bending stress, and shear stress to within ~16%, ~8%, and ~13% on average, respectively. Main testing of the composite I-beams revealed that both fully orthotropic FEA models and existing Beam Theory models struggled to correctly predict experimental deflection of the I-beams, with percent errors of ~81% and ~89%, respectively. In addition, the orthotropic models also struggled to replicate measured strains. Due to stress concentrations present in these FEA solutions at the locations of the supports and the applied load, errors here exceeded 130%. Similar orthotropic model performance was confirmed in other FEA programs such as Ansys. Ultimately, utilization of a modeling method by which the composite and orthotropic nature of the I-beams are reduced to an equivalent isotropic representation produced the best beam deflection solution at an average error of ~8% with experimentation. Prediction of bending and shear stresses with this idealizing method were consistent with the performance of existing Beam Theory analysis tools.

TABLE OF CONTENTS

LIST OF TABLES

LIST OF FIGURES

Figure   Page

Figure   Page

CHAPTER I

INTRODUCTION

At Oklahoma State University, development and testing of a wide variety of Unmanned

Aerial Systems (UAS) constitute a major portion of the research focus for multiple Aerospace

Engineering professors as well as undergraduate and graduate level students. In particular, the

research lab operated by Dr. Arena specializes in design, fabrication, integration, and flight

testing of composite UAVs which are intended for a whole host of missions. In addition, this lab

also provides undergraduate seniors in Aerospace Engineering a unique opportunity to participate

in a hands-on design contract competition for their final semester capstone project. As part of this

capstone, two teams are provided with a statement of work detailing the design requirements for

that year. They are then given only a few months to develop a feasible design as well as produce

working prototypes for competition with other entries at the annual Speedfest event. Just as is the

case for these seniors, many contracts taken on by the graduate students have stringent timetables

and budgets with which to produce and deliver a functioning airframe. In either case, working

efficiently and effectively is a necessity.

To this end, considerable effort has been made towards shortening the pre-prototyping phase

for these aircraft. This effort has yielded positive results for many of the initial design analysis

requirements associated with development of a UAS platform. As an example, the areas of

vehicle propulsion and aircraft aerodynamics have at their disposal a combination of quite

effective analysis tools that greatly expedite pre-prototype iteration of proposed designs. In the case of the latter, aerodynamics and stability and control analysis tools developed by Dr. Arena greatly assist in rapid development of a working design. Moreover, finalized designs can be further refined through the use of Computational Fluid Dynamics (CFD) simulations conducted through SolidWorks, which has been found by the lab to produce reliable results when set up properly.

The one area that is lacking in such an abundance of pre-prototyping analysis tools is the design of the airframe structure. Until recently, most structural engineering for airframes produced by this lab consisted of sizing the structure based on intuition and, if time allowed, manufacturing a test bed with which to validate said intuition. Especially in the case of Speedfest, there is often not enough time for the structures sub-teams to simultaneously manufacture aircraft molds, airframes, and test articles. Therefore, these structural designs are typically first put to the test during maiden flights. This is also the case at times for designs produced at the graduate level. If and when the aircraft fails structurally, the typical procedure is to just add more reinforcement so as to prevent the observed failure mode from reoccurring. Where this design loop is most prevalent is in the proper sizing of the main wing spars, which are often times the main load-bearing component of the entire airframe.

Within the last few years, effort has been made to better develop structural analysis capability as it relates to these wing spars, which are typically composite I-beams consisting of unidirectional carbon fiber spar caps and balsa wood shear webs. Much graduate level research has been invested in exploring the properties of these materials as well as expanding static testing capabilities of the lab specifically for testing wing structure. Despite this, there currently exists only one spar design analysis tool to assist in initially sizing this component to withstand expected flight loads. While this tool has greatly aided in reducing the amount of time spent on wing structural iteration and validation, the solutions resulting from it are still considered, at best, reasonable approximations. As such, the "guess-and-check" approach still prevails.

2

The research presented in this thesis aims to further expand the pre-prototype structural analysis capabilities of Dr. Arena's research lab through the utilization of Finite Element Modeling and Analysis (FEM/FEA). Specifically, it would be advantageous to capitalize on the lab's familiarity with SolidWorks, which contains an FEA package, to both design and analyze these orthotropic composite I-beam wing spars. With this in mind, this research endeavor will seek to validate the solving and modeling capabilities of this SolidWorks Simulation FEA package. This will be accomplished through direct comparison of FEA results with the results of experimentation as well as with the results from the existing spar analysis tool. Ultimately, proof of good correlation will allow for the expansion of wing structural analysis capabilities through the addition of SolidWorks FEA into the lab's analysis tool repertoire.

A. Research Goals and Objectives

The overarching goal of this thesis is to characterize the modeling and solving capabilities of the SolidWorks FEA package, especially as this relates to its ability to handle both the orthotropic and composite nature of these I-beam wing spars. In pursuit of this goal, the following list of objectives has been formulated:

1) Conduct an extensive review of existing literature pertaining to the following:
    a. Fundamentals of Finite Element Analysis
    b. Orthotropic Mechanical Properties of Carbon Fiber and Balsa Wood
    c. Existing work regarding modeling of orthotropic/composite components
    d. Practical methods of acquiring experimental data for comparison and validation

2) Develop proper experimental testing capabilities so that important parameters, such as beam deflection, bending stress, and shear stress, can be obtained from the physical beams.

3) Simulate a simplistic bending load, such as a point load, on a beam (or beams) of simpler construction and material composition in order to establish a baseline for the capabilities of the SolidWorks FEA package.

a. Compare these FEA results to experimentation as well as to models developed from theory.

b. Utilize this baseline test case to establish proper procedure for the application of boundary conditions, loading conditions, model meshing, and other modeling constraints and parameters as needed.

4) Manufacture wing spars for experimental testing, ensuring that the materials and construction techniques utilized for these spars on the UAVs are replicated as accurately as possible.

5) Explore methods of modeling the orthotropic and composite nature of these I-beam spars to determine the best FEA modeling approach.

6) For the models developed as a result of Objective 5, simulate a simplistic load, such as a point load, and compare the results with experimentation as well as with the existing spar analysis tool.

7) Based on the findings in Objective 6, determine the overall feasibility of utilizing the SolidWorks FEA package to model the behavior of these composite I-beams effectively and reliably under load.

CHAPTER II

REVIEW OF LITERATURE

A. Fundamentals of Finite Element Analysis (FEA)

Finite Element Analysis has become an essential and effective analytical technique across most engineering disciplines. Aerospace and other structurally oriented industries utilize this approach to model complex components and understand how they respond to expected applied loads without first having to physically create and test said components. Because the purpose of this research is to apply these Finite Element Methods to a more irregular beam composition, it is necessary to gain a basic understanding of the inner workings of FEA. As such, the remainder of this section provides insight into aspects of FEA, such as general calculation steps and derivations, as well as several types of mesh element geometries and their advantages/disadvantages.

The simple answer to how Finite Element Analysis works is that it is an analytical method that "takes a complex region defining a continuum [and discretizes it] into simple geometric shapes" [1]. These simpler shapes, called elements, are easier to mathematically model the effects of an applied load than would be the case for the initial complex region that these shapes comprise. The standard element shapes that are typically utilized for this discretization are composed of either triangles or rectangles (known as shells for 2D analyses) and tetrahedrons (known as solids for 3D analyses). For simplicity, only the 2D shell geometries will be discussed in detail in the remainder of this section.

2D FEA Using TRI Shell Elements

In two dimensions, the overarching idealization of plane stress or plane strain must be applied due to the elements not having a defined thickness. Instead, the thickness of the modeled component at each element is factored into the calculations as a constant across that element, as will be seen later in this section. For triangular elements, the most basic iteration is known as a six degree-of-freedom (D.O.F.) constant strain triangle (CST). This name is earned due to the key assumption that all strains in these elements are considered constant across each element [1], [2]. This type of element can be observed in Figure 1 below. In this figure, the element is defined by three nodes with corresponding (x, y) coordinate pairs. At each of these nodes, there are two
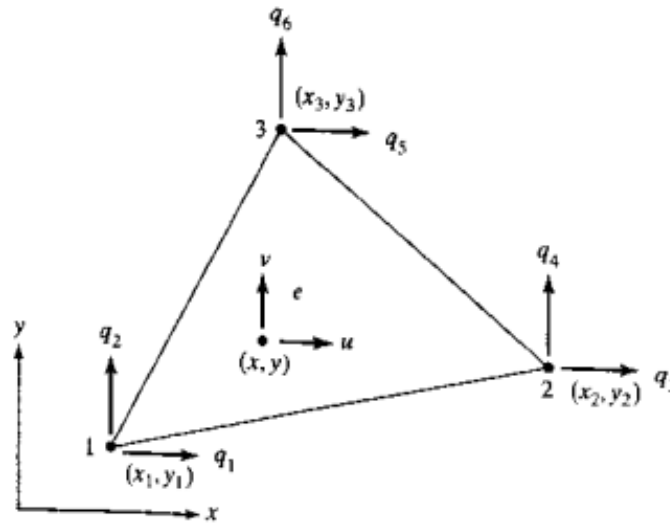
Figure 1: *6-D.O.F. Constant Strain Triangle Element [1]*

possible degrees of freedom with which the node is allowed to translate in order to deform the element under applied load. These displacement directions are denoted by the variable q_n in the figure, where subscript 'n' is the D.O.F number for that displacement. The total displacement of the element in the x and y directions, meanwhile, is denoted by the variables 'u' and 'v', respectively.

The end goal is to obtain these q_n D.O.F. displacements. This starts by defining a series of piecewise functions, known as shape functions, between each node. These shape functions

6

require a coordinate transformation to occur from cartesian to an intrinsic/natural coordinate system typically defined by the variable ξ [1]. Between any two pairs of nodes on the element, the shape functions are derived in such a way that at the starting value of ξ, N = 1, and at the ending value of ξ, N = 0. Here N is the variable representation of the shape function, and the starting and ending values of ξ correspond to the start and end nodes in the pair [1], [4]. For the constant strain triangle, these shape functions are linear in nature and are defined as shown mathematically in Equations 1-3 [1], [4] as well as pictorially in Figure 2, where η is just another natural coordinate variable.

$$N_1 = \xi \tag{1}$$

$$N_2 = \eta \tag{2}$$

$$N_3 = 1 - \xi - \eta \tag{3}$$
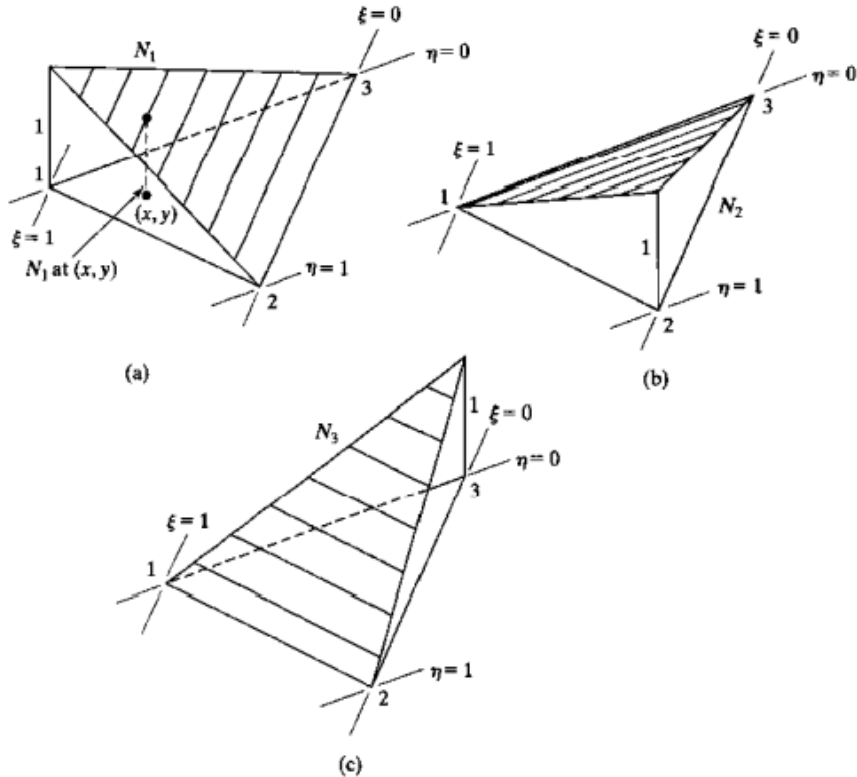
Figure 2: *Linear Shape Functions for Constant Strain Triangle Element [1]*

With these shape functions, relationships between the total u and v displacements, x and y

coordinates, and the ξ and η natural coordinates can be made, resulting in the Jacobian matrix ($\mathbf{J}$)

as shown below [1], [4]. In this matrix, upon taking the partial derivative with respect to the

natural coordinates, the values simply become the difference between x and y coordinate values

between two pairs of nodes on the element.

$$\mathbf{J} = \begin{bmatrix} \frac{\partial x}{\partial \xi} & \frac{\partial y}{\partial \xi} \\ \frac{\partial x}{\partial \eta} & \frac{\partial y}{\partial \eta} \end{bmatrix} = \begin{bmatrix} x_{13} & y_{13} \\ x_{23} & y_{23} \end{bmatrix}, where\ x_{ij} = x_i - x_j \tag{4}$$

From here, the area of the element (A_e) can be determined by calculating half of the determinant

of the Jacobian. Additionally, the element strain-displacement matrix ($\mathbf{B}$) can be determined with

the determinant of the Jacobian. Both of these are shown below as they appear in [1], [4]. The last

matrix required is the material matrix ($\mathbf{D}$) for the element, which has two forms depending on

$$A_e = \frac{|det\,\mathbf{J}|}{2} \tag{5}$$

$$\mathbf{B} = \frac{1}{det\,\mathbf{J}} \begin{bmatrix} y_{23} & 0 & y_{31} & 0 & y_{12} & 0 \\ 0 & x_{32} & 0 & x_{13} & 0 & x_{21} \\ x_{32} & y_{23} & x_{13} & y_{31} & x_{21} & y_{12} \end{bmatrix} \tag{6}$$

whether the element is modeled under plane stress or plane strain assumptions [1]. Both forms of

this matrix are shown below, with the plane stress version shown first. Since this element is two-

dimensional and under plane stress/strain assumptions, it is worth noting that the only stresses

and strains calculable are in the x, y, and xy directions. This explains why this material matrix is

only a 3 x 3 in size.

$$\mathbf{D} = \frac{E}{1-v^2} \begin{bmatrix} 1 & v & 0 \\ v & 1 & 0 \\ 0 & 0 & \frac{1-v}{2} \end{bmatrix} \tag{7}$$

$$\mathbf{D} = \frac{E}{(1+v)(1-2v)} \begin{bmatrix} 1-v & v & 0 \\ v & 1-v & 0 \\ 0 & 0 & \frac{1-v}{2} \end{bmatrix} \tag{8}$$

Through application of the total strain energy of the element, which is itself derived from the application of total potential energy for the element, the stiffness matrix of this constant strain triangle element ($\mathbf{k}_e$) as well as the final matrix equation needed to solve for the displacements ($\mathbf{Q}$) can be determined [1]. Since this element has six degrees of freedom, the resulting stiffness matrix will be a 6 x 6 matrix wherein rows and columns 1 – 6 correspond directly to degrees of freedom 1 – 6. Additionally, as mentioned earlier in this section, the constant elemental thickness (t_e) is also utilized in the calculation of this stiffness matrix in order to make up for the fact that the element is not three-dimensional. The stiffness matrix equation and FEA displacement equation are shown below [1]. In the displacement equation, the force matrix ($\mathbf{F}$) is simply a 6 x 1

$$\boldsymbol{k_e} = t_e A_e \boldsymbol{B}^T \boldsymbol{D} \boldsymbol{B} \tag{9}$$

$$\mathbf{Q} = inv(\mathbf{k_e}) * \mathbf{F} \tag{10}$$

matrix that contains the applied force components that act on each D.O.F. of the element. Importantly, the displacements can be solved only if the boundary conditions on the element are properly accounted for within the matrices in Equation 10. There are several methods of appropriately accounting for these boundary conditions at the element nodes, with one of the simpler approaches being elimination of the rows and columns corresponding to a D.O.F. where a boundary condition exists from the $\mathbf{k_e}$ and $\mathbf{F}$ matrices (implying that the deflection q_n for that D.O.F. is zero or some known quantity) [1], [2], [4].

Having solved for the displacements, the strains and stresses acting on this triangular shell element can then be found. Equation 11 shows the formulation necessary to find elemental strains while Equation 12 shows the calculation required for elemental stresses [1], [4]. In the strain equation, the distinction between the $\mathbf{Q}$ and $\mathbf{q}$ displacement matrices is that the $\mathbf{q}$ matrix

$$\boldsymbol{\epsilon} = \begin{Bmatrix} \varepsilon_x \\ \varepsilon_y \\ \gamma_{xy} \end{Bmatrix} = \mathbf{Bq} \tag{11}$$

$$\boldsymbol{\sigma} = \begin{Bmatrix} \sigma_x \\ \sigma_y \\ \tau_{xy} \end{Bmatrix} = \mathbf{D\boldsymbol{\epsilon}} = \mathbf{DBq} \tag{12}$$

re-includes those known deflections at the boundary condition degrees of freedom. Additionally, expanding the above process to multiple connected elements, all one has to do is determine the stiffness matrix for each element. At common nodes shared between elements, the D.O.F. number assignments are the same. Therefore, the full stiffness matrix is a combination of all elemental stiffness matrices, with elemental stiffnesses summed together at common D.O.F. points.

2D FEA Using QUAD Shell Elements

Rectangular shell elements have their nodal displacements solved in a fashion similar to the constant strain triangle. However, there are some more complexities that must be accounted for. The simplest form of the rectangular shell element to model is the eight-D.O.F. QUAD element. This element, being a quadrilateral, has one more node than the triangular elements (thus the reason for the additional degrees of freedom), and it is defined with a fixed horizontal length 'a' and height/width of 'b' [2]. This element is shown in Figure 3 below as it is defined in both cartesian and natural coordinate spaces. The shape functions that are formulated for this type of element are similarly linear. Since there are four nodes, however, there will also be four shape functions. Due to the fact that this element is defined with fixed dimensions, the shape functions can easily be written using cartesian coordinates, as can be seen in Equations 13-16 [1], [2].
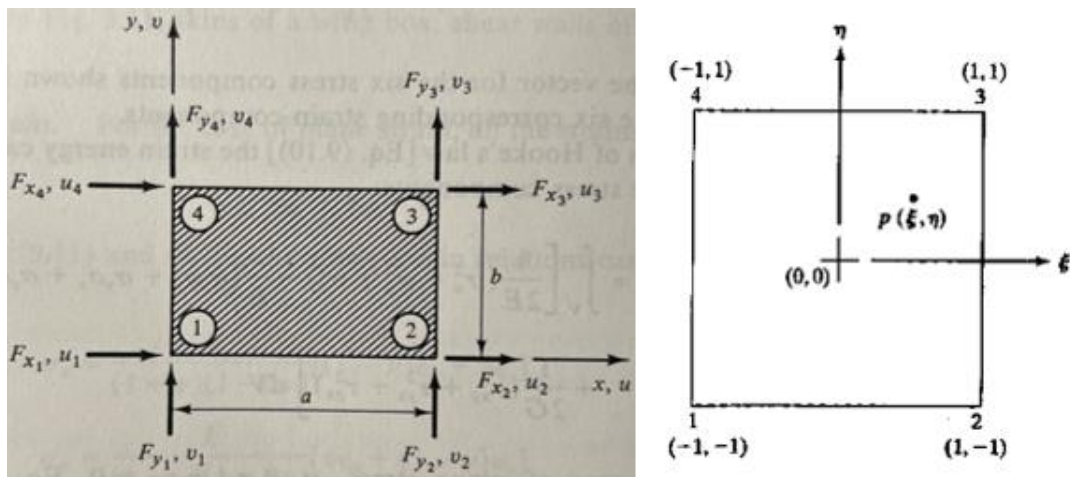
Figure 3: *8-D.O.F. Rectangular Element in Cartesian (**Left**) [2] and Natural (**Right**) Coordinates [1]*

$$N_1 = \frac{(1-\xi)(1-\eta)}{4} = \left(1 - \frac{x}{a}\right)\left(1 - \frac{y}{b}\right) \tag{13}$$

$$N_2 = \frac{(1+\xi)(1-\eta)}{4} = \frac{x}{a}\left(1 - \frac{y}{b}\right) \tag{14}$$

$$N_3 = \frac{(1+\xi)(1+\eta)}{4} = \frac{xy}{ab} \tag{15}$$

$$N_4 = \frac{(1-\xi)(1+\eta)}{4} = \left(1 - \frac{x}{a}\right)\frac{y}{b} \tag{16}$$

Observation of these shape functions reveals a major difference from those defined for the constant strain triangle elements. The shape functions are no longer defined only at the nodes of the element but rather can have a finite linear value assigned at any point between any pair of nodes. This is the case because these QUAD elements are no longer bound by the constant elemental strain assumption, but rather, strain varies linearly between any two nodes while also being independent of the specified (x, y) coordinate [2]. Since strains are no longer constant across the element, each node will have its own strain and stress solutions. Using the cartesian form of these shape functions, the element strain-displacement matrix (**B**) can be directly assembled [2].

$$\mathbf{B} = \begin{bmatrix} -\frac{1}{a}\left(1 - \frac{y}{b}\right) & 0 & \frac{1}{a}\left(1 - \frac{y}{b}\right) & 0 & \frac{y}{ab} & 0 & -\frac{y}{ab} & 0 \\ 0 & -\frac{1}{b}\left(1 - \frac{x}{a}\right) & 0 & -\frac{x}{ab} & 0 & \frac{x}{ab} & 0 & \frac{1}{b}\left(1 - \frac{x}{a}\right) \\ -\frac{1}{b}\left(1 - \frac{x}{a}\right) & -\frac{1}{a}\left(1 - \frac{y}{b}\right) & -\frac{x}{ab} & \frac{1}{a}\left(1 - \frac{y}{b}\right) & \frac{x}{ab} & \frac{y}{ab} & \frac{1}{b}\left(1 - \frac{x}{a}\right) & -\frac{y}{ab} \end{bmatrix} \tag{17}$$

Before nodal displacements can be calculated, the element stiffness matrix (k_e) must be assembled. The stiffness matrix equation is again derived from the application of total strain energy on the element. Despite this, actual assembly of this matrix is made much more complex since the strain varies linearly between nodes and is no longer constant. Instead of a straightforward multiplication of matrices, the added step of performing integration across the elemental area is required. After this integration is performed, the total stiffness matrix will be a matrix of size 8 x 8 that consists of a symmetric ordering of stiffness coefficients that require only the material Poisson ratio, Elastic Modulus, element thickness, element length, and element

width/height to be known [2]. Equations 18-27 below show this process [1], [2]. It is worth noting that the material matrix (**D**) is constant and has the same form as those shown in Equations 7 and 8 for the constant strain triangle elements. Once this stiffness matrix is assembled, the nodal displacements of the element and the strains and stresses at each node can be determined using the same approach as described for the constant strain triangle elements (Equations 9-12). Keep in mind that the stress and strain equations must be used four times for each of the element nodes, updating the x and y coordinates in the element strain-displacement matrix accordingly each time. Additionally, the concept of summing common stiffness coefficients for common D.O.F. from two or more elements to form the total stiffness matrix still applies.

$$\mathbf{k_e} = t_e \oiint \mathbf{B}^T \mathbf{DB} * det\mathbf{J} \, d\xi \, d\eta = t_e \oiint \mathbf{B}^T \mathbf{DB} \, dx \, dy \tag{18}$$

$$\mathbf{k_e} = \begin{bmatrix} C_1 & C_2 & C_4 & C_5 & -0.5C_1 & -C_2 & C_7 & -C_5 \\ & C_3 & -C_5 & C_6 & -C_2 & -0.5C_3 & C_5 & C_8 \\ & & C_1 & -C_2 & C_7 & C_5 & -0.5C_1 & C_2 \\ & & & C_3 & -C_5 & C_8 & C_2 & -0.5C_3 \\ & & & & C_1 & C_2 & C_4 & C_5 \\ & & & & & C_3 & -C_5 & C_6 \\ & & & & & & C_1 & -C_2 \\ & & & & & & & C_3 \end{bmatrix} \tag{19}$$

$$C_1 = \frac{Et_e}{1-v^2}\left(\frac{b}{3a} + \frac{a(1-v)}{6b}\right) \tag{20}$$

$$C_2 = \frac{Et_e}{1-v^2}\left(\frac{v}{4} + \frac{1-v}{8}\right) \tag{21}$$

$$C_3 = \frac{Et_e}{1-v^2}\left(\frac{a}{3b} + \frac{b(1-v)}{6a}\right) \tag{22}$$

$$C_4 = \frac{Et_e}{1-v^2}\left(-\frac{b}{3a} + \frac{a(1-v)}{12b}\right) \tag{23}$$

$$C_5 = \frac{Et_e}{1-v^2}\left(\frac{v}{4} - \frac{1-v}{8}\right) \tag{24}$$

$$C_6 = \frac{Et_e}{1-v^2}\left(\frac{a}{6b} - \frac{b(1-v)}{6a}\right) \tag{25}$$

$$C_7 = \frac{Et_e}{1-v^2}\left(\frac{b}{6a} - \frac{a(1-v)}{6b}\right) \tag{26}$$

$$C_8 = \frac{Et_e}{1-v^2}\left(-\frac{a}{3b} + \frac{b(1-v)}{12a}\right) \tag{27}$$

Pros and Cons to TRI3 and QUAD4 Shell Elements

When it comes to choosing between the two above element types for meshing of the finite element model, one finds that both have advantages and disadvantages. The obvious disadvantage of the triangular elements is that they have a constant strain across the element due to how the linear shape functions are defined [5]. This restriction causes these shell elements to become stiffer, resisting deformation from an applied load more than would actually be the case [2], [3]. This problem can persist when using four-node tetrahedron elements in 3D analyses as well [5]. With this in mind, a resulting shell mesh consisting of CST elements will be much finer than a shell mesh consisting of QUAD elements in order to get the same displacement, strain, and stress FEA solution. The more elements in a mesh, the more computing time and power are required to reach a solution, which is also not ideal. That being said, the advantage of triangular elements is that they are much easier both to model and analyze, especially if one is trying to implement this shell type into an auto-meshing routine or utilize them on a simple FEA problem [3], [5].

QUAD elements have the exact opposite attributes in that they are less stiff due to the lack of constant strain assumptions, but they are more difficult to model and analyze. The requirement to perform strain and stress calculations once for all four nodes creates a much more complicated FEA solving routine that requires keeping track of each element's nodal stresses, strains, and displacements and then combining these appropriately across common nodes between two or more QUAD elements. Because these elements are not as stiff as CST elements, however, a much coarser mesh can be generated to reach the correct FEA solution, which translates to faster computing times. Of course, some of the shortfalls among these elements can be negated by introducing extra nodes along the element edges between the corner nodes, thereby defining the shape functions in such a way that they are second order or higher [1] – [5]. In addition, adding extra nodes will increase the D.O.F. of the element while also allowing it to be contorted so that it can better conform to curved surfaces, circular edges, or other complex geometries on the part.

3D FEA Using TET Solid Elements

Finite Element Analysis can become even further detailed by extending the analysis bounds to all three dimensions. Instead of objects being idealized into infinitesimally thin shell elements, 3D FEA directly accounts for the object's thickness and volume within the model. Thus, it makes sense, then, that the previous assumptions of Plane Stress/Strain no longer apply since there is now the possibility of deformation, stress, and strain in all three cartesian directions. One of the more common solid element types utilized for 3D analysis is the tetrahedral element. The simplest form of this element consists of four nodes, each with three possible degrees of freedom, assembled in such a way that the element looks like a triangular pyramid. Since this solid has four nodes, similar to the 2D QUAD elements, there are similarly four shape functions that can be defined for the natural coordinate system transformations. This element in the natural coordinate system can be viewed below. The typical shape function variables ξ and η are again utilized. However, the extra dimension requires a third shape function variable to be defined, ζ.
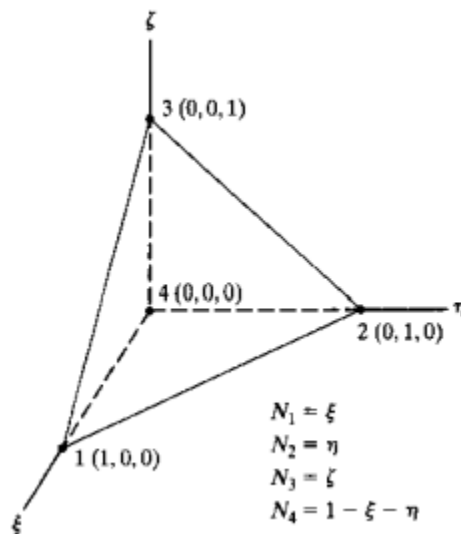
Figure 4: *3D Solid Tetrahedron Element [1]*

Solving finite element analysis around this element type follows similar steps as previously discussed for the shell elements, just with an added dimension. The shape functions and their relationships between *u*, *v*, and *w* displacements and x, y, and z coordinates allow for the

generation of a 3 x 3 Jacobian matrix ($\mathbf{J}$). This matrix is similar to that of Equation 4 but with

extra indices for the extra dimension and fourth node. The elemental volume can be found by

multiplying the determinant of the Jacobian by the volumetric integral of the element. Taking the

inverse of the Jacobian allows for the assembly of the element strain-displacement matrix ($\mathbf{B}$),

which will be a 6 x 12 matrix [1]. The stiffness matrix ($\mathbf{k_e}$) can then be assembled similarly to

those equations derived for the shell elements, with the exception that the constant element

thickness, t_e, and element area, A_e, are replaced by the elemental volume [1]. The resulting

stiffness matrix for one tetrahedral solid element will be 12 x 12. The FEA displacement solution

will similarly yield 12 solutions, corresponding to each of the four nodes being allowed to deform

in three directions. When it comes to meshing these solid elements, it is best to first divide the

object into cubes and from there, sub-divide each cube into five or six tetrahedral elements, which

share common nodes at the cube's corners [1]. This subdivision is shown in Figure 5 below for a

six-tetrahedral element cube. The same rules for assembly of the total stiffness matrix for this

combination of solid elements still applies: any common nodes shared by two or more elements

will have their corresponding stiffnesses at proper D.O.F. summed together.
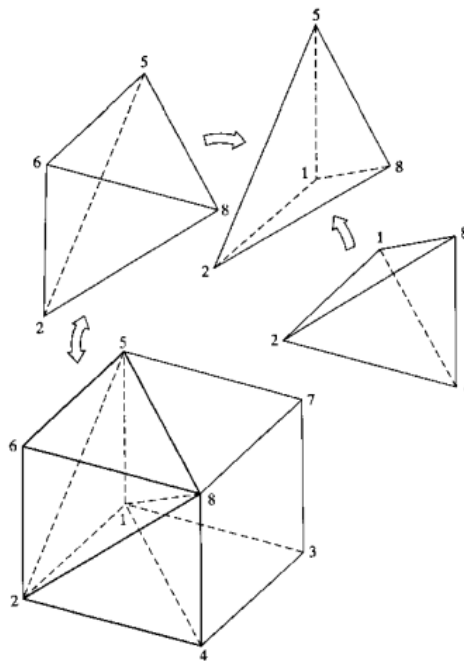
Figure 5: *Sub-Division of Solid Cube into Six Tetrahedral Elements [1]*

B. Carbon Fiber Material Properties

Of foremost importance to Finite Element Analysis is the understanding of how the various materials of the modeled component behave under load. To this end, the mechanical properties must be known for all materials in a model so that the most accurate FEA solution can be achieved. For the Unmanned Aerial Vehicles (UAV's) produced at Oklahoma State University's Design and Manufacturing Lab (DML), the wing spars on these aircraft are composed of two primary materials: unidirectional carbon tape and balsa wood, which are combined to form a composite I-beam structure. This I-beam structure can be observed in Figure 6, which depicts an instructional wing structure mock-up used by the lab, and in Figure 7, which shows a wing spar being fitted into the wing of a Speedfest capstone aircraft from 2021. The first of these two materials will be further discussed in this current section while the latter will be addressed in the following section.
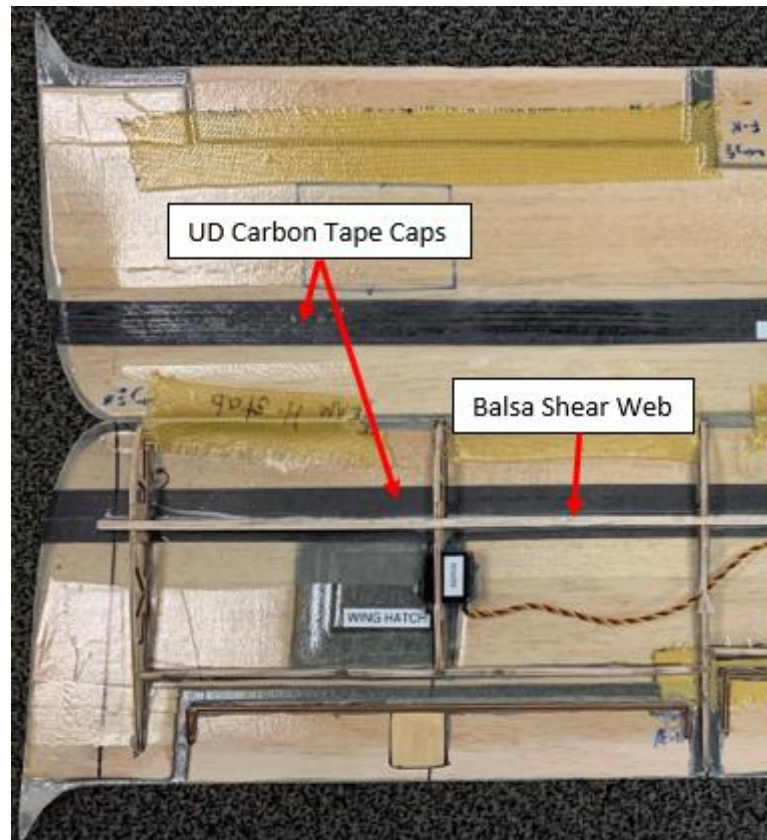
Figure 6: *Wing Structure Instructional Mock-up*

16
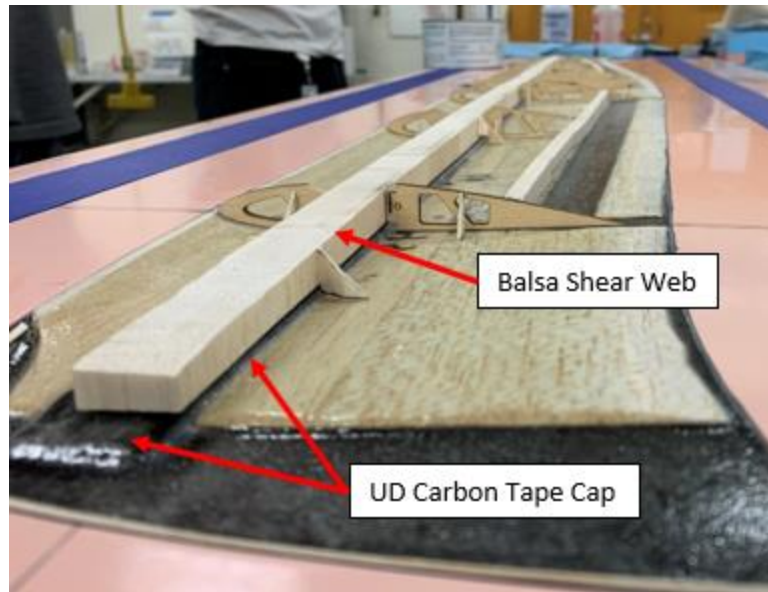
Figure 7: *Composite I-beam Spar from a 2021 Speedfest Aircraft*

Unidirectional Carbon Fiber Material Characterization

Fabric composites are a family of strong, flexible, and light-weight alternative materials that can easily be formed into complex contoured shapes. These types of materials can also have their properties specially altered for desired loading applications through the use of certain fiber weaves, fiber materials, and ply orientation patterns. Despite the many types of composite fabrics available on the market, the focus of this research effort is solely on the properties of unidirectional carbon fiber tape. This material is utilized by the DML as the spar caps for the composite I-beams constructed in the wings of most UAV's produced by the lab, as Figures 6 and 7 have shown. This material is excellent for this role due to its ability to resist large loads in bending as well as because it is thin and light, which are desirable characteristics for the kind of aircraft produced by the University. Each layer of this unidirectional tape is approximately 0.005 inches thick and weighs 3.70 oz/yd^2 after the curing cycle [11]. For Finite Element Analysis, the mechanical properties of this composite material are desired; however, certain aspects of composite terminology and laminate theory must be explored and understood before these properties can be determined.

Composites are typically created through the combination of some woven fabric material, such as fiberglass, carbon fiber, Kevlar, or others, with a bonding epoxy. When separated, the two materials may not necessarily be strong or stiff enough for most applications. However, when combined, along with the appropriate curing cycle, this material can yield remarkably strong, flexible, and lightweight parts. It is important to understand that the mechanical properties of composite materials are derived from this combination of both fabric and epoxy, which is achieved through what is referred to as the Law of Mixtures [8], [9]. Figure 8 below shows this combination of materials under a microscope while Equation 28 [8] shows an example of the Law of Mixtures for determination of the composite's longitudinal Elastic Modulus. In this figure and equation, the matrix is representative of the epoxy while the fibers are the composite fabric material. Various combinations of the fabric and epoxy properties and the area fraction of composition for each in the composite can yield all the necessary mechanical properties, such as Elastic Moduli, Poisson's ratios, and Shear Moduli in all key directions. Due to these combinations of fibers and epoxy into a laminate, composites are generally known as orthotropic materials, meaning that the mechanical properties of the material are dissimilar across the three possible planes of elastic symmetry [9].

$$E_{log} = E_F \left(\frac{A_F}{A_{total}} \right) + E_M \left(\frac{A_M}{A_{total}} \right) \tag{28}$$
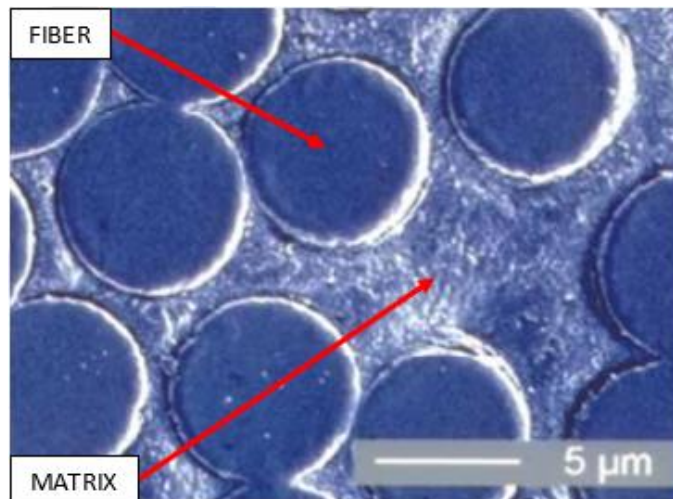
Figure 8: *Unidirectional Composite Cross-Section Showing Fibers and Epoxy Matrix [6]*

The term unidirectional carbon fiber tape aptly describes this material in that the fabric fibers run only in one direction on the tape. Accordingly, the principal material axes for unidirectional carbon fiber are shown below. In this figure, axis one is equivalently the longitudinal axis while axes two and three are equivalently the transverse axes. Regardless of the material orientation on the part, these principal axes remain fixed with the shown composite orientation. The resulting mechanical properties in these principal directions for the particular unidirectional carbon fiber utilized by the DML can be pulled from manufacturer-provided datasheets and are summarized in Table 1. Missing from this table are both the properties in the third axis direction as well as any
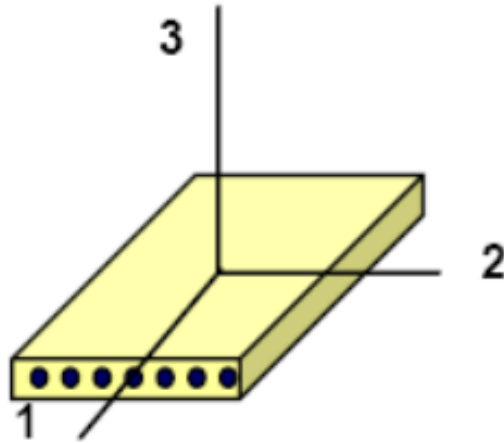
Figure 9: *Principal Material Axes for Unidirectional Carbon Fiber [6]*

Table 1: *Unidirectional Carbon Fiber Properties [10], [11]*

Unidirectional Carbon Fiber Mechanical Properties		
E_1	19580	ksi
E_2	1450	ksi
G_{12}	725	ksi
v_{12}	0.30	
$\sigma_{Ult\_T,1}$	218	ksi
$\sigma_{Ult\_C,1}$	174	ksi
$\sigma_{Ult\_T,2}$	7	ksi
$\sigma_{Ult\_C,2}$	36	ksi
$\tau_{Ult,12}$	10	ksi

information on the yield limits of the composite. The former is missing due to assumptions of transverse isotropy and plane stress on this material. Due to the uniformity of the carbon fiber, with the fibers all running the same direction, transverse isotropy applies since both principal directions two and three act perpendicular to the fibers, thereby implying that the material properties in the two and three axis directions are the same [6]. As for the plane stress assumption, this is valid due to the small per layer thickness of the carbon tape. Essentially, the minimal thickness can allow for the three axis properties to be assumed negligible, which is advantageous for further design and analysis of composite structures [6] – [9]. Finally, the lack of yield stress information is due in large part to the fact that composites typically behave like a hybrid between a brittle and ductile material. Under excessive load, the fibers and epoxy will simultaneously experience elastic and plastic deformation, with the epoxy entering plastic first due to its higher ductility [12]. Counteracting this is the fabric material, which is less ductile but stronger. Therefore, typical signs of total yield into plasticity for composites are not readily observable. Instead, composites typically behave similarly until the ultimate stress limits are exceeded, whereby total and abrupt failure of the composite will occur. As such, yield strength of composites is not a commonly defined property.

Directionality of Unidirectional Carbon Fiber Laminates

As mentioned previously, composite fabrics can be manipulated in such a way as to achieve suitable mechanical properties under specified loading conditions. This is largely achieved through utilization of rotating successive fabric layers such that the weave of each layer is oriented in pre-determined directions. Figure 10 provides a visual of such rotated layering. This layering is done in order to resist expected shear, tensile, and torsional loads exerted on the component, combinations of which a single fabric weave orientation alone may not be able to sufficiently handle. Conventional composite fabrics typically are composed of a weave pattern in which fibers are interwoven in two directions at 90 degrees to one another. Depending on the

fiber volume in each direction, the properties in these directions can be similar or one direction can be stronger than the other, which would make the fabric more suited to handle a particular load condition under specific orientations. Despite this, producing a laminate composed of many layers of this fabric (with each layer oriented such that the stronger fabric direction is dominate in the directions of expected load) will result in a specially made composite material that is pre-designed to handle loadings both on and off conventionally defined axes for the component.
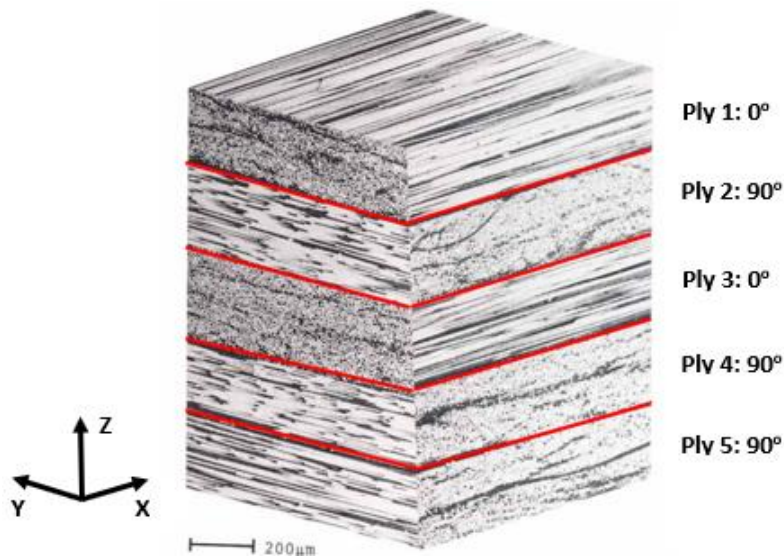
Figure 10: *Unidirectional Carbon Fiber Laminate (0º / 90º Orientation Pattern) [6]*

This directionality of composite fabric materials can best be determined once the mechanical properties in the principal axis directions, such as those listed in Table 1, are known. With these properties defined, it is possible to determine the mechanical properties at any fabric orientation using Basic Lamination Theory [7] – [9]. The first step required is to compute and assemble the components of the composite's compliance matrix. The only inputs required to conduct this computation are those mechanical properties listed in Table 1. Once this matrix is complete, the S_{11}, S_{12}, S_{22}, and S_{33} components are utilized in conjunction with the angle between the ply one principal axis and the fixed x-axis to determine a polar plot of the properties at all possible orientation angles [7] – [9]. Based on the rotation angle, the resulting lamina properties will be projected back to the fixed coordinate system to determine the rotated lamina's new x, y, and xy

21

diagonal properties. This plot will map the change in mechanical properties of the composite as its one principal axis is rotated away from the global x-axis direction. Equations 29 – 36 [7], [9] show the process required to develop these polar plot equations for a lamina. It is worth noting here that there is a distinction between a lamina and a laminate. A lamina is a singular layer of composite fabric material (otherwise known as a ply) while a laminate is the resulting composite, which is composed of multiple laminae [9]. The equations shown below are applicable only for a singular lamina. Mechanical properties for common ply orientation angles, those being 0, ±45, and 90-degrees, can easily be determined using these equations. The properties of unidirectional carbon at these angles are tabulated in Table 2 below. In addition, Figures 11 and 12 show the full Elastic and Shear Moduli polar plots for unidirectional carbon.

$$S_{11} = \frac{1}{E_1} \tag{29}$$

$$S_{12} = -\frac{v_{12}}{E_1} \tag{30}$$

$$S_{22} = \frac{1}{E_2} \tag{31}$$

$$S_{33} = \frac{1}{G_{12}} \tag{32}$$

$$E_x = [S_{11}cos^4(\theta) + (S_{33} + 2S_{12})cos^2(\theta)sin^2(\theta) + S_{22}sin^4(\theta)]^{-1} \tag{33}$$

$$E_y = [S_{11}sin^4(\theta) + (S_{33} + 2S_{12})cos^2(\theta)sin^2(\theta) + S_{22}cos^4(\theta)]^{-1} \tag{34}$$

$$G_{xy} = [2(2S_{11} + 2S_{22} - 4S_{12} - S_{33})cos^2(\theta)sin^2(\theta) + S_{33}(sin^4(\theta) + cos^4(\theta))]^{-1} \tag{35}$$

$$v_{xy} = E_x[-S_{12}(sin^4(\theta) + cos^4(\theta)) - (S_{11} + S_{22} - S_{33})cos^2(\theta)sin^2(\theta)] \tag{36}$$

Table 2: *Mechanical Properties for Unidirectional Carbon Tape at Common Ply Angles*

Rotated Unidirectional Carbon Mechancial Properties					
	0°	+45°	-45°	90°	Units
E_x	19580	1915	1915	1450	ksi
E_y	1450	1915	1915	19580	ksi
G_{xy}	725	1350	1350	725	ksi
v_{xy}	0.30	0.32	0.32	0.02	
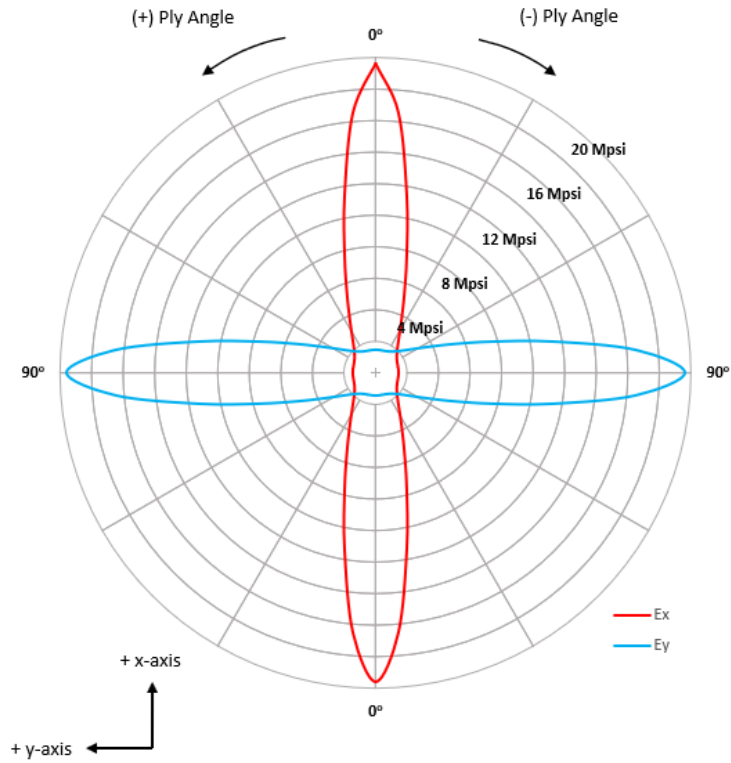
Figure 11: *Polar Plot of E_x and E_y Elastic Moduli for Rotated Unidirectional Carbon Lamina*
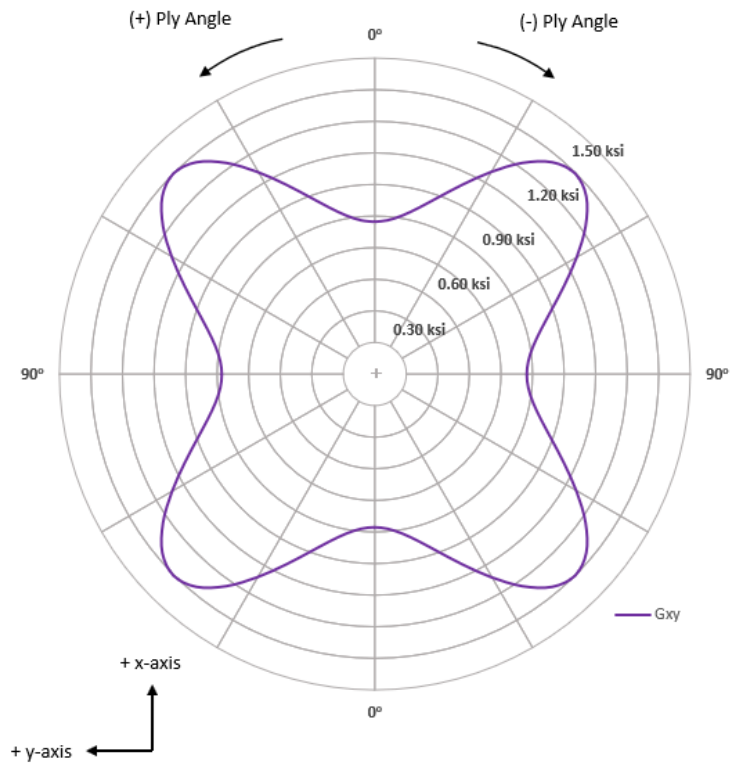
Figure 12: *Polar Plot of G_{xy} Shear Modulus for Rotated Unidirectional Carbon Lamina*

Finding the resulting composite laminate mechanical properties requires more calculations to be performed as well as a predetermined laminae stack and orientation sequence. While the details of these calculations will not be explored in full (see [7], [9]), knowledge of the general process follows. First, the transformed stiffness matrix $\bar{Q}$ must be computed for each lamina layer in the laminate. This matrix is derived from the inverse of the S compliance matrix previously discussed and is transformed by the ply angle similarly to that shown in Equations 33 – 36. A resulting force/moment matrix can then be compiled that will allow for the transformation of measured strains and curvatures on the laminate into N_x, N_y, and N_{xy} tractions as well as M_x, M_y, and M_{xy} moments. To assemble this matrix, A, B, and D component matrices must be compiled through a process of summing individual lamina $\bar{Q}$ matrices multiplied by a function that accounts for the distance of each lamina from the laminate's cross-sectional centerline. From this

$$
\begin{bmatrix} n_x \\ n_y \\ n_{xy} \\ m_x \\ m_y \\ m_{xy} \end{bmatrix} = \begin{bmatrix} A_{11} & A_{12} & A_{13} & B_{14} & B_{15} & B_{16} \\ A_{21} & A_{22} & A_{23} & B_{24} & B_{25} & B_{26} \\ A_{31} & A_{32} & A_{33} & B_{34} & B_{35} & B_{36} \\ \hline B_{41} & B_{42} & B_{43} & D_{11} & D_{12} & D_{13} \\ B_{51} & B_{52} & B_{53} & D_{21} & D_{22} & D_{23} \\ B_{61} & B_{62} & B_{63} & D_{31} & D_{32} & D_{33} \end{bmatrix} \begin{bmatrix} \varepsilon_x^0 \\ \varepsilon_y^0 \\ \gamma_{xy}^0 \\ \kappa_x \\ \kappa_y \\ \kappa_{xy} \end{bmatrix}
$$

Figure 13: *Constitutive Relationship for a Composite Laminate [7], [9]*

force/moment matrix (see Figure 13), the A matrix portion can be utilized to find the resulting laminate mechanical properties, which are an average of the mechanical properties of each rotated lamina within the composite [9]. If all laminae within the laminate are oriented to the same ply angle, the resulting laminate mechanical properties will be the same as a single lamina within the stack. Since the unidirectional carbon spar caps manufactured at the DML are all composed of laminae at the same ply orientation, the mechanical properties shown in Table 2 and Figures 11-12 can therefore be extend to the resulting unidirectional laminate as a whole.

C. Balsa Wood Material Properties

The second material incorporated in these composite I-beam spars is balsa wood. Characterization of balsa wood material properties and behavior under load has been the subject of both past and ongoing research at the DML under Dr. Andy Arena, with the goal of better understanding the material as it applies to its structural application on aircraft produced by the lab [13]. Particularly, balsa wood is used on the composite I-beam spars as the shear web between the unidirectional carbon tape spar caps. Just as the carbon fiber tape is utilized for its tensile and compressive strength (making it suitable for use as spar caps on an I-beam), balsa wood is similarly utilized for its shear properties (making it suitable for use as the shear web material on an I-beam). Additionally, as was the case for the discussion of carbon fiber, it is necessary to gain an understanding of balsa wood as a material before its mechanical properties can be characterized.

Balsa Wood Material Characterization

Wood is another material that is orthotropic in its composition. However, the organic nature of this material lends its orthotropy to be unique compared to fabricated materials. This is due in large part to the cellular makeup of the material, which is specifically tailored to support the needs of the tree from both a sustainment and structural standpoint. In particular, balsa wood is made up of a microstructure containing three main cellular structures: tracheids, vessels, and rays [14]. Tracheids are long cylindrically shaped structures oriented axially within balsa wood and are typically 600 µm in length with a hexagonal cross-section of 30-40 µm in diameter [14]. These cellular structures are primarily utilized to support the weight of the balsa tree. Similarly, vessels are cellular structures oriented axially within the wood and are otherwise known as sap channels. They are typically the larger structure within the material at a diameter of 150-250 µm [14]. Despite this, their primary function is to assist in the transfer of vital fluids vertically from the roots to the rest of the tree. Rays, however, are structures that are oriented radially within the

wood. These structures are ~30 μm in length by 20-50 μm in diameter and are primarily utilized to store carbohydrates within the wood, facilitate transfer of fluids from the sap channels radially, as well as provide increased radial structural support for the tree [13], [14]. Overall, a typical balsa wood specimen has a composition of 80-90% tracheids, 8-15% rays, and 2-5% vessels by volume [14]. Figure 14 displays this microstructure within balsa wood.
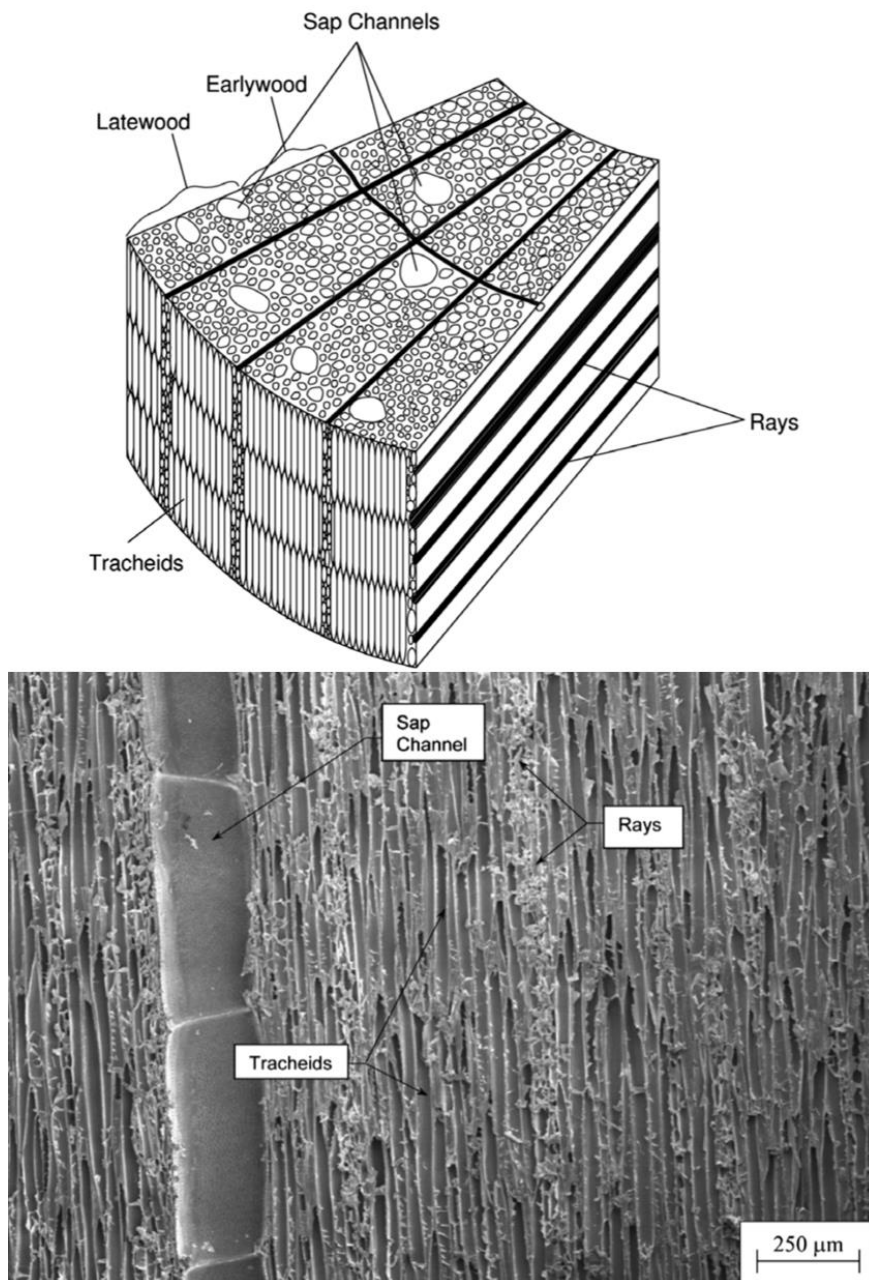
Figure 14: *Microstructure of Balsa Wood [14]*

The tracheids can further be described as the grain of the wood. When wood is harvested, the resulting lumber is cut such that the lengthwise direction of the lumber is parallel to the wood grain (see Figure 15) [15]. This is advantageous for wood utilized in construction or load-bearing roles since the tracheids are the primary load-bearing component within the wood. Balsa wood also possesses a trait that helps to determine the desired grain orientation relative to an applied loading. Balsa is much easier to cut or otherwise pull apart parallel to the grain than it is to do so perpendicular to the grain. In the context of applied bending loads on a composite I-beam spar, where balsa comprises the shear web, it is especially important to properly orient the grain direction so as to account for this fact since shear is the primary loading of concern for this material. In bending, when a load is applied vertically to an object, the resulting shear loading is applied horizontally across the component. With this in mind, orienting the balsa wood so that the grain direction is parallel to the applied load (known as cross-grain or end-grain balsa) will yield higher shear strength properties [13]. Therefore, higher bending loads can be achieved on these composite I-beams before the end-grain balsa experiences the required shear load to shear the wood perpendicular to the grain in the spanwise direction. On the other hand, orienting the balsa so that the grain is perpendicular to the applied load (known as with-grain balsa) will yield lower shear strength properties due to the grain running parallel to the applied shear load in the beam [13]. As a result, the material will more easily shear apart along the grain in the spanwise direction at lower bending loads, which is not desirable.
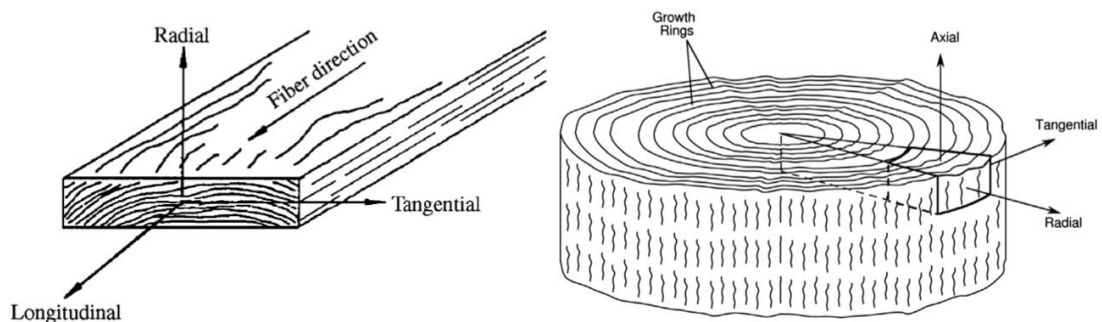
Figure 15: *Principal Axes for Balsa Wood [14], [15]*

Balsa Wood Properties

Being an orthotropic material, balsa wood has different mechanical properties depending on the material principal axis. Similar to the unidirectional carbon fiber tape, this is because the microstructure in the wood is directionally oriented. Since the tracheids are the main structural component in balsa wood and they grow in the longitudinal direction, the expectation is that the material would have higher stiffness as well as higher stress limits in this direction. The rays also provide some structural support in balsa wood, though not as much as the tracheids. One would therefore expect that the radial axis would have the second highest stiffness and stress limits out of the three material axes.

Despite these expectations, it is more difficult to characterize balsa wood's mechanical properties due to the varying inhomogeneity of the material. This lack of uniformity in material composition best exhibits itself in the form of varying density [13] – [16]. Due to the organic nature of the material, no one balsa sample will have the same microstructural composition, and the resulting wood density will depend on the varied volumetric percentage of tracheids, rays, and sap channels [13] - [16]. Extensive research into this topic has shown that this varied density has a direct impact on the mechanical properties of the material, an example of which Figure 16 shows. Further still, past research by colleagues at Oklahoma State University has found that the
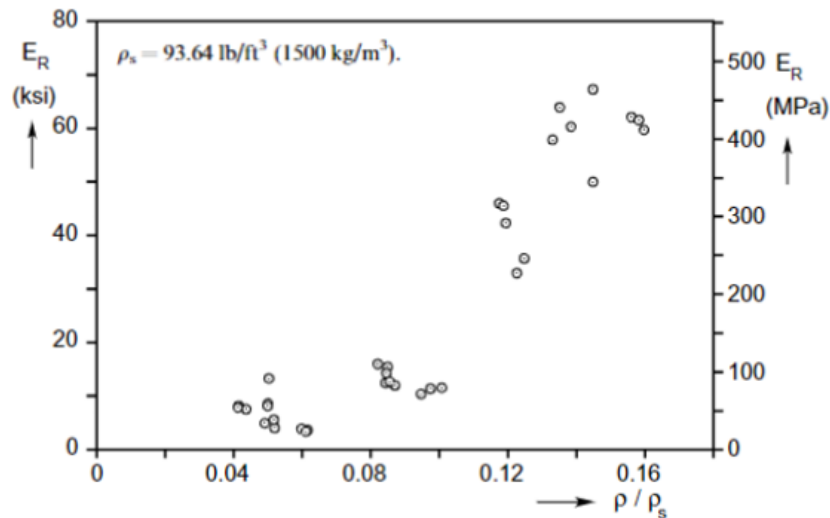
Figure 16: *Dependence of Radial Elastic Modulus on Balsa Wood Density [14]*

28

mechanical properties of balsa wood are also dependent on the thickness of the sample (see Figure 17) [13]. The trend identified here is that as the balsa sample gets thicker, the shear stress limit drops. Admittedly, the trend identified in Figure 17 was the result of a small sample size in terms of balsa density classification (mostly light and extra light) [13]. More extensive investigation of balsa properties for a larger range of densities in [57] concluded that this dependence on thickness only occurs at and above densities classified as 'heavy' (> 14 lb/ft^3).
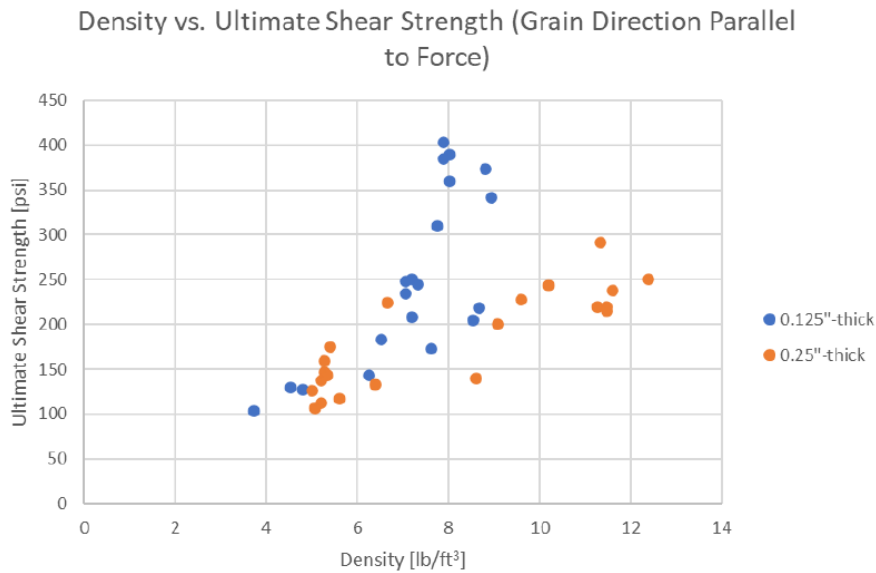
Figure 17: *Dependence of With-Grain Ultimate Shear Strength on Balsa Thickness [13]*

Even though this dependence on density causes the properties of balsa wood to vary, sufficient research has been conducted on the material to gain a reliable average of the Elastic and Shear Moduli as well as the Poisson ratios in all axes (see Table 3) [15], [16]. The first quantity to know for balsa wood is the Elastic Modulus in bending. Once this is known, the longitudinal Elastic Modulus can be determined by computing 110% of the Bending Elastic Modulus. From there, the remaining moduli can be determined through a series of ratios between the longitudinal modulus and the modulus of interest [15], [16]. These ratios are also shown in Table 3. Unfortunately, the stress limits for balsa wood, especially in tension and for cross-grain, are not as well understood. However, the most important properties for the purposes of this research, are

Table 3: *Balsa Wood Moduli Ratios and Average Mechanical Properties [15], [16]*

Balsa Wood Moduli Ratios	
E_L / E_{Bend}	110.00%
E_T / E_L	1.50%
E_R / E_L	4.60%
G_{LR} / E_L	5.40%
G_{LT} / E_L	3.70%
G_{RT} / E_L	0.50%

Avg. Balsa Wood Elastic and Shear Moduli		
$E_{Bending}$	493.13	ksi
E_L	542.44	ksi
E_T	8.14	ksi
E_R	24.95	ksi
G_{LT}	20.07	ksi
G_{LR}	29.29	ksi
G_{RT}	2.71	ksi

Avg. Balsa Wood Poisson Ratios	
v_{LT}	0.49
v_{LR}	0.23
v_{RT}	0.67
v_{TL}	0.01
v_{RL}	0.02
v_{TR}	0.23

the cross-grain shear strength and the ultimate tensile and compressive strengths of the material since these are the limits of interest in bending. Research at the DML has indicated that cross-grain ultimate shear strength can vary anywhere from 230 psi to 430 psi (on a range of $4 - 10$ lb/ft^3), depending on density [13]. The average cross-grain shear strength from this dataset is ~323 psi. As for tensile and compressive strengths, neither is well nor fully defined. The exception is the compressive strength parallel to the grain, which is 2,161 psi [13], [15], [16]. The most well-defined limit, however, is the average Rupture Modulus for balsa wood – 3,132.8 psi [13], [15], [16]. This modulus relates the dimensions of the sample to the maximum bending force that can be applied to it before failure occurs. As such, this limit will assist in determining the proper bending load to apply to the I-beams in order to avoid a balsa wood failure.

D. Previous Work on Composite Beam Analytical Modeling

Due to the specialized nature of the I-beam spars produced at Oklahoma State University, finding pre-existing research or studies into the efficacy of modeling such composite beams using FEA proved to be difficult. In fact, no previous studies matching this present research endeavor were found. Despite this, some academic works which focused on modeling other types of composite beams in bending using FEA techniques were found to be closely related enough to the present research focus to be worth mentioning. Lastly, it is worth noting that none of the findings presented in this section utilized SolidWorks as the Finite Element Modeling and Analysis

software. Instead, programs such as Abaqus were utilized, and based on the literature found that utilized FEA modeling, such programs appear to be the preferred standard. With this in mind, it is likely that the results and modeling techniques used in these studies will not completely translate to SolidWorks, especially since Abaqus is an FEA specialized program that may have more functionality for these analyses than SolidWorks.

Composite Reinforced Timber I-Beams

The focus of this research out of Australia was to investigate the bending behavior of lightweight composite timber I-beams being utilized for building construction as well as how certain reinforcement methods improved their load-bearing capacity [17]. As part of this investigation, an experimental component and an analytical component using Abaqus FEA were employed. The unmodified I-beams, as acquired from the manufacturer, consisted of laminated veneer lumber caps and a shear web composed of oriented strand board [17]. Several reinforcement techniques were devised, ranging from wrapping the timber beams in carbon fiber to applying angled shear web stiffeners (see Figure 18). Acquisition of the desired experimental data for these modified beams utilized a large 3-point bending apparatus called the Meccano testing machine, which simulates a simply supported beam with two roller supports and one applied load acting on the beam. It can be viewed in Figure 19.

Figure 18: *Composite Timber I-beam Reinforcement Techniques [17]*
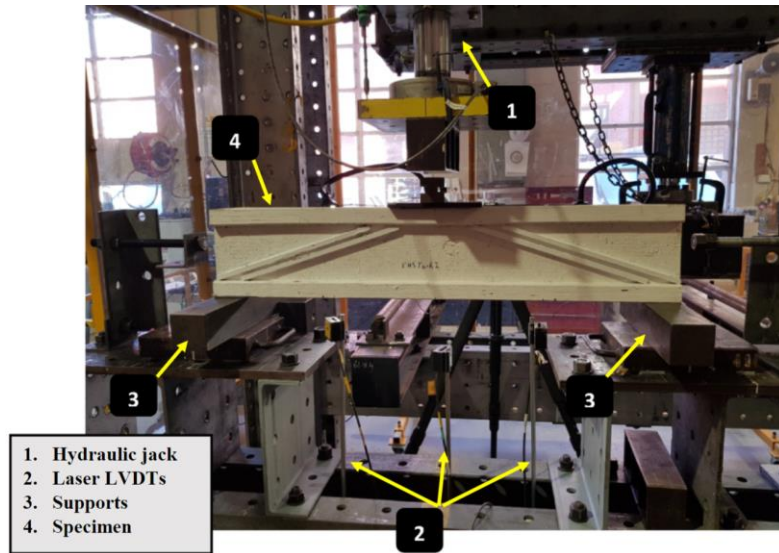
Figure 19: *Meccano Hydraulic 3-Point Bending Apparatus [17]*

All timber beams from this study were loaded until failure using the Meccano 3-point bender. The main parameters tracked for each beam were the deflection versus the applied load on the beam. The primary mode of failure for each beam varied slightly depending on the reinforcement technique; however, all failures consistently occurred in and around the shear webs [17]. With this in mind, the resulting Abaqus FEA models were primarily focused on tracking the deflection versus the applied load as well as the stress distributions in the shear webs. These models were developed using solid 8-node block elements (C3D8R) from the Abaqus element library [17]. An example of the resulting FEM solution is shown in Figure 20. Overall, these results correlated well to the failure modes observed from the experimental testing, with a computed difference of
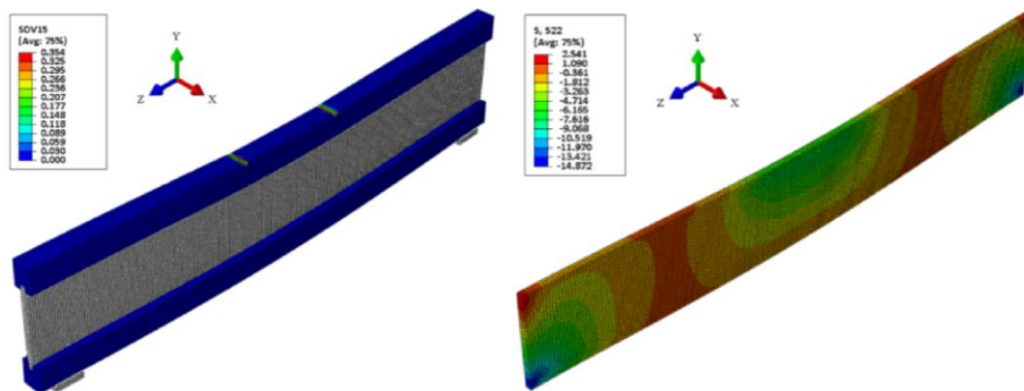
Figure 20: *Abaqus Results for SDV15 Damage Index and S_{22} Stress Tensor [17]*

11% between experimental data and the FEA solutions [17]. In addition, comparison of the load versus displacement data between these FEA models and the experimental data yielded similarly well-correlated results. Admittedly, some of the FEM solutions deviate from what was actually measured, especially as the load approached the failure limit (see Figure 21). Despite this, the general trend in the load versus displacement as well as the load at which failure occurred remained quite similar.
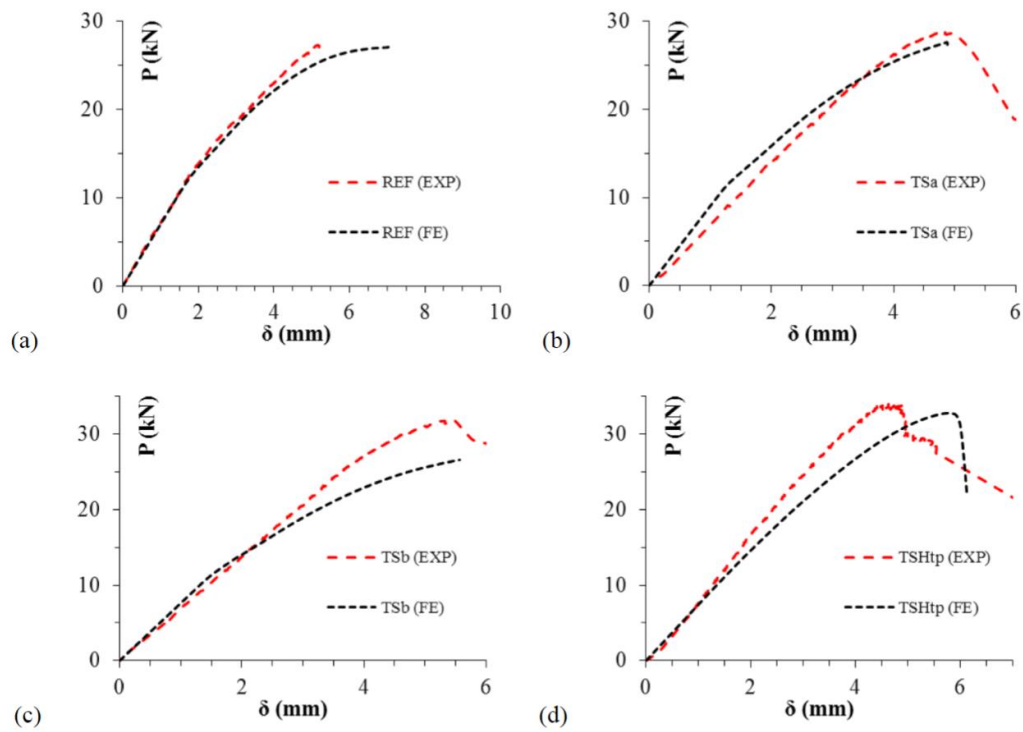
Figure 21: *Abaqus FEA Solutions versus Corresponding Experimental Measurements [17]*

This study into the bearing capacity of various structurally modified timber I-beams is relevant to this present research endeavor for two primary reasons. The first is that this study utilized an experimental loading technique to validate the FEA results that is simple to set up, easily repeatable, and readily available at the DML. Secondly, this study demonstrated that it is possible to generate reliable FEA models of multi-material composite I-beams as long as the proper meshing techniques and boundary conditions are applied. As such, some of the FEM techniques discussed in this study may become useful when developing the SolidWorks models.

Multilayer Composite Beams in Bending

Similar research from Poland has also attempted to further explore and understand the behavior of multilayered laminated composite beams for use in building construction via the use of finite element models and analysis. The goal of their research was ultimately to provide a viable FEA model with which civil and mechanical engineers could utilize to apply standard design procedures for such beam compositions [18]. As part of this study, three types of laminated beams were tested and modeled. The first beam was composed of two panels of PA-38 aluminum bonded together with a 0.5 mm thick layer of Sika®PSM polyurethane resin [18]. This beam was aptly named the '3-layer aluminum beam'. The other two beams were considered 5-layer beams. One was composed of two outer spruce wood panels with the fibers oriented lengthwise along the beam bonded to a middle layer of glued wooden panels with fibers oriented transversely [18]. The other beam was composed of three bonded layers of general plywood [18]. The layers of the two 5-layer beams were bonded using Sika®PS and Sika®PST adhesive, respectively [18]. Unfortunately, no pictures of the beams themselves were provided.

The experimental setup consisted of two separate tests, one used for the 3-layer beam and the other used for the 5-layer beams. For the aluminum beam, a similar approach to the Meccano apparatus was utilized. The three-point bending for this beam similarly involved two simple supports restricting vertical displacement and one applied load between these supports. Resulting displacements both vertically and horizontally were measured at the indicated positions in the diagram shown in Figure 22, where all dimensions listed are in millimeters. As for the 5-layer
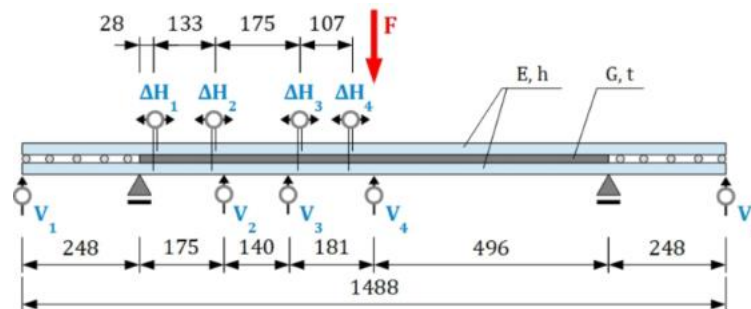
Figure 22: *3-Layer Aluminum Laminated Beam 3-Point Bending Setup [18]*
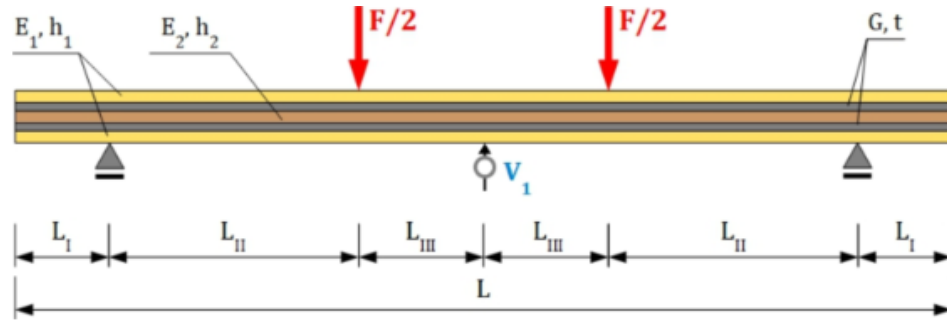
Figure 23: *5-Layer Composite Timber Beam 4-Point Bending Setup [18]*

beams, a four-point bending test was devised with the same general setup as the three-point test

applied. However, the beam is loaded at two locations between the supports, with each load

approximating half of the total load applied to the beam. This setup is shown in Figure 23. It is

unclear why different experimental bending techniques were utilized as no justification for it is

provided in the documentation.

All FEA models were again developed using Abaqus, with the preferred solid mesh element

this time being hexahedral brick elements [18]. An example of the resulting model for the 5-layer

spruce beam is shown in Figure 24. Likewise, the resulting comparison between FEM, theory,

and experiment for the vertical deflection of the 3-layer beam are shown in Figure 25. Of key

interest from these results is how well not only the FEM solution matched experimental data but

also how well the theoretical predictions matched. Similar to the results from the previous sub-

section, this again demonstrates that it is possible to accurately model such complex composition

beams using FEA techniques as long as proper meshing and boundary conditions are applied.

Figure 24: *Abaqus FEA Model for 1/4 Length of Spruce 5-Layer Beam [18]*
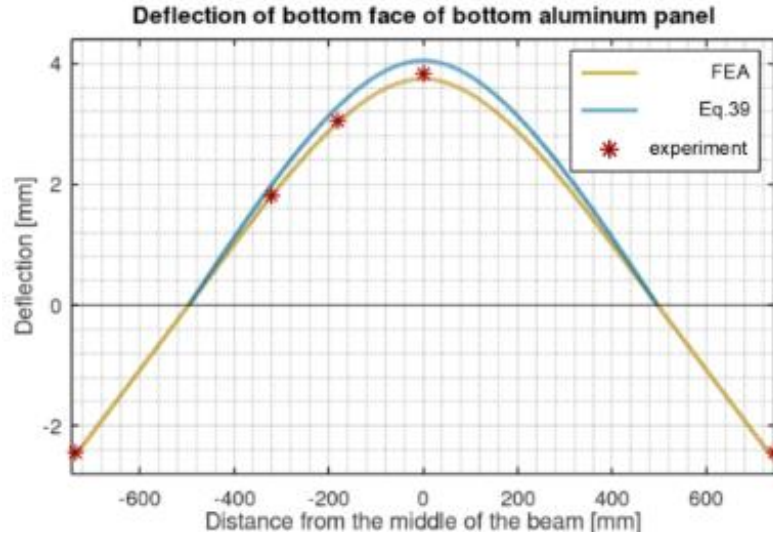
Figure 25: *Deflection Solutions Derived from Theory and FEA Compared to Experimental Data [18]*

Further still, the FEA models not only accounted for the properties of the panels but also the properties of the bonding adhesive between each panel [18]. This shows that as long as the adhesive layer thickness and properties are known, its impact on the beam can be properly accounted for using FEA. Despite this, a conclusion reached from this study stated that theoretical assumptions regarding the bond layer can remain applicable provided that the beam is slender with thin bond layers [18]. This could be interpreted to mean that the bond layers can be ignored if they are thin enough, and the only parameter to track at the bond line is the resulting shear relative to the ultimate shear load rating for the adhesive. These findings regarding bond line FEA modeling will be considered when developing the SolidWorks models.

E. Experimental Stress Measurement and Instrumentation

One of the better methods for validating finite element models is to compare the FEM solution to actual experimental data. While theoretical approximations may come close, experimental results will provide the de facto benchmark with which all FEA configurations must match since experimental testing will not fall victim to underlying assumptions as theory does. With this in mind, the most effective measurement tools for stress analysis are strain gages. These instruments allow for strain measurements to be taken straight from the surface of a loaded

component and, depending on gage orientation, the strain due to load in virtually any direction on that component can be obtained. Because strain gages are such effective tools for FEA validation, the remainder of this section will focus on what strain gages are and how they can be used for bending loads.

Strain Gage Basics

Strain gages are especially sensitive instruments that can record changes in resistance due to loading on a component, which can then be transformed into the equivalent strain experienced by the gage. These instruments consist of a thin wafer backing known as the carrier [19]. On the carrier is a metallic grid pattern composed of either fine wire or, equivalently, a thin metallic foil [19]. The start and end of this metallic grid terminates at copper solder pads, which is the point where lead wires can be attached to the gage for signal output to an appropriate data acquisition device. On the fringes of the carrier, markings to assist with alignment of the gage can be found. There are usually at least four triangles/arrows at 90-degrees from each other, and sometimes there are four rectangular tick marks also situated perpendicular to each other but rotated 45-degrees from the triangular markings. A basic linear strain gage can be viewed in Figure 26, which shows the above-mentioned components and aligning marks. In Figure 26, the rounded triangles in the corners of the gage are not part of the alignment marking system.
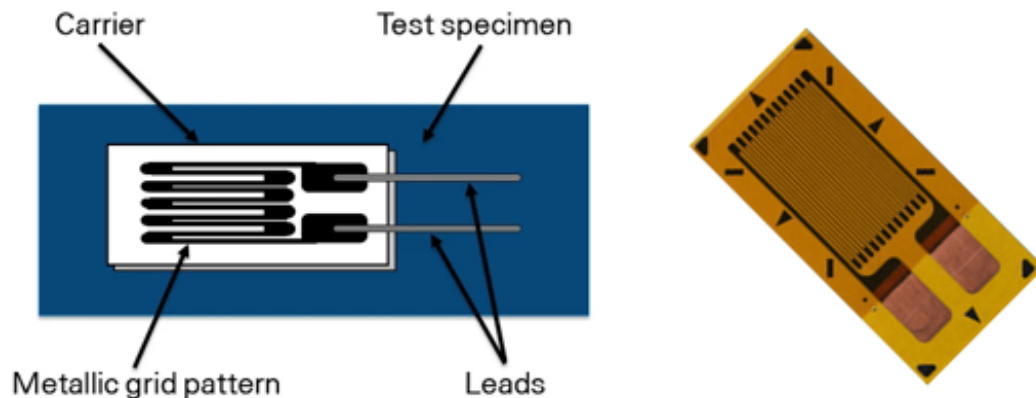
Figure 26: *Linear Strain Gage Main Components (**Left**) [19] and Actual Example (**Right**) [20]*

As mentioned previously, strain gages work by detecting changes in resistance due to an applied load on the component to which the gage is bonded. In much the same way that wire resistance is proportional to the length of the wire, changes in the metallic grid length due to stretching or compressing of the surface it is bonded to will change the overall resistance of the gage itself. Typically, these grid pattern length changes are small, and the best method of detecting this miniscule change in resistance is through the utilization of a Wheatstone bridge. A Wheatstone bridge consists of four bridge arms, each with a resistor. Half of the bridge requires two of the arms to be connected in series, which is then connected in parallel with the other half of the bridge containing the other two arms, also connected in series [21]. The start and end junctions of the parallel wiring connection for this bridge are connected to a common power supply. Likewise, between the arms connected in series is the junction utilized to measure the resulting output voltage from the bridge [21]. See Figure 27 for a pictorial reference for a general Wheatstone bridge as described.
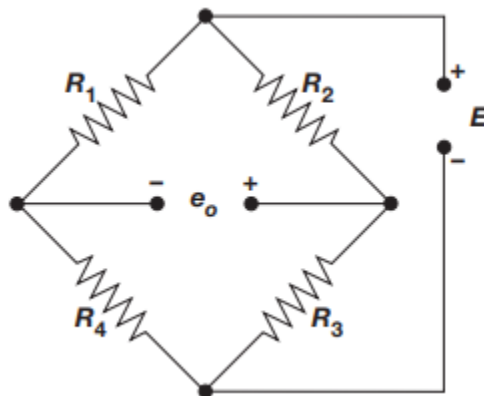
Figure 27: *Basic Wheatstone Bridge Configuration [21]*

This bridge formation is sensitive to slight changes in resistance across any one of the bridge arms, and any resistance imbalance across the bridge arms in series will generate an output voltage. The relationship between the input voltage, E, and the output voltage, e_o, is shown in Equation 37 [22]. If the resistances in each pair of series bridge arms are equivalent, the Wheatstone bridge will be balanced, and the resulting output voltage will be zero [22]. If resistor

$$e_o = E\left[\frac{R_4}{R_4+R_1} - \frac{R_3}{R_3+R_2}\right] \tag{37}$$

$$V_r = \left(\frac{e_o}{E}\right)_{strained} - \left(\frac{e_o}{E}\right)_{no\ strain} \tag{38}$$

$$\varepsilon = \frac{-4V_r}{GF(1+2V_r)}\left[1 + \frac{R_{L1}}{R_G}\right] \tag{39}$$
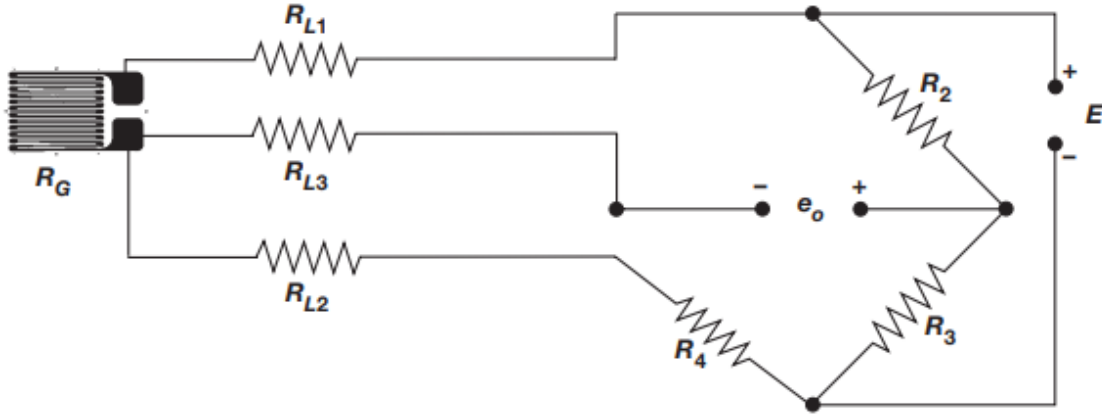
Figure 28: *Three-Wire Quarter-Bridge Strain Gage to Wheatstone Bridge Hookup [21]*

R_1 is replaced with a three-wire linear strain gage of nominal unstrained resistance R_G, as is the case in Figure 28, then changes in the gage resistance due to applied loads will unbalance the Wheatstone bridge and cause a non-zero output voltage. Equations 38 and 39 show the process required to relate this unbalanced bridge voltage to equivalent measures of strain [22]. In Equation 39, GF refers to gage factor, which is a constant value assigned to the strain gage based on its nominal resistance and properties of the metallic grid [19]. Likewise, R_{L1} is the resistance of the lead wire that is in series with the strain gage on the same bridge arm. Lead wire resistance R_{L2} is considered in series with resistor R_4 and apart of R_4's bridge arm [21]. On the other hand, lead wire resistance R_{L3} is a voltage-sensing wire only and is not considered part of any of the Wheatstone bridge arms [21]. It is worth noting that for significantly long lengths of lead wire, it is important to account for the resistance of the wire itself because the large wire resistance can effectively negate the resistance changes from the strain gage [22]. Known as lead wire desensitization, it can cause large errors in strain measurements, especially when the lead wire resistance exceeds 0.1% of the nominal gage resistance [22].

Strain Gage Configurations for Beams in Bending

When it comes to experimentally measuring these strains on a loaded specimen, there are a few options regarding the gage orientation and even the type of gage that can be used. Strain gages can be arranged on a test specimen in one of three possible configurations: quarter-bridge, half-bridge, and full-bridge, which correspond to the number of bridge arms in the Wheatstone bridge that are taken up by active strain gages. An example of a quarter-bridge strain gage connection can be viewed in Figure 28. Each of these three options has its advantages as well as its disadvantages. In the case of the quarter-bridge, only one active strain gage is required in the circuit; however, sensitivity to the voltage changes and compensation for strain due to thermal changes is reduced or non-existent [23]. For half-bridges, two active strain gages are required, which then requires more time devoted to bonding and wiring the gages to the specimen. The upside, though, is that the overall bridge sensitivity is double that of a quarter-bridge [23]. Finally, full-bridges require the most prep time because they utilize four active strain gages, meaning that all four bridge arm resistors in the Wheatstone bridge are replaced. Despite this additional prep time, this configuration has the highest bridge sensitivity, which is four times the sensitivity of a quarter-bridge [23]. Table 4 displays the necessary data, such as that discussed above, for all gage types and desired strain measurement cases.

For the purposes of this research endeavor, there are two strains (and by extension, stresses) that are of primary interest to compare with the finite element models: bending strain and shear strain. In the case of acquiring bending strain, the configuration of strain gages is straightforward, as Figure 29 shows. All gages must be bonded to the surface(s) which are perpendicular to the applied bending load. In addition, the preferred strain gage of choice for this measurement is the linear strain gage (such as the one shown in Figure 26). In Figure 29, the bending strain gage orientation is restricted to the gages being bonded in the spanwise direction along the specimen. While this is typical, the second and fourth axial strain options in Table 4 can also measure bending strain (called a type 1 half-bridge and type 2 full-bridge, respectively) [19].

40

STRAIN	BRIDGE TYPE	POSITION OF GAGES FIG. C-F	SENSITIVITY mV/V @ 1000 $\mu\epsilon$	OUTPUT PER $\mu\epsilon$ @ 10 V EXCITATION	TEMP COMP.	SUPERIMPOSED STRAIN COMPENSATED
BENDING	¼	1	0.5	5 $\mu V/\mu\epsilon$	No	None
	½	1, 2	1.0	10 $\mu V/\mu\epsilon$	Yes	Axial
	Full	All	2.0	20 $\mu V/\mu\epsilon$	Yes	Axial
AXIAL	¼	1	0.5	5 $\mu V/\mu\epsilon$	No	None
	½	1, 2	0.65	6.5 $\mu V/\mu\epsilon$	Yes	None
	½	1, 3	1.0	10 $\mu V/\mu\epsilon$	No	Bending
	Full	All	1.3	13 $\mu V/\mu\epsilon$	Yes	Bending
SHEAR AND TORSIONAL	½	1, 2	1.0	10 $\mu V/\mu\epsilon$ @ 45°F	Yes	Axial and Bending
	Full	All	2.0	20 $\mu V/\mu\epsilon$ @ 45°F	Yes	Axial and Bending
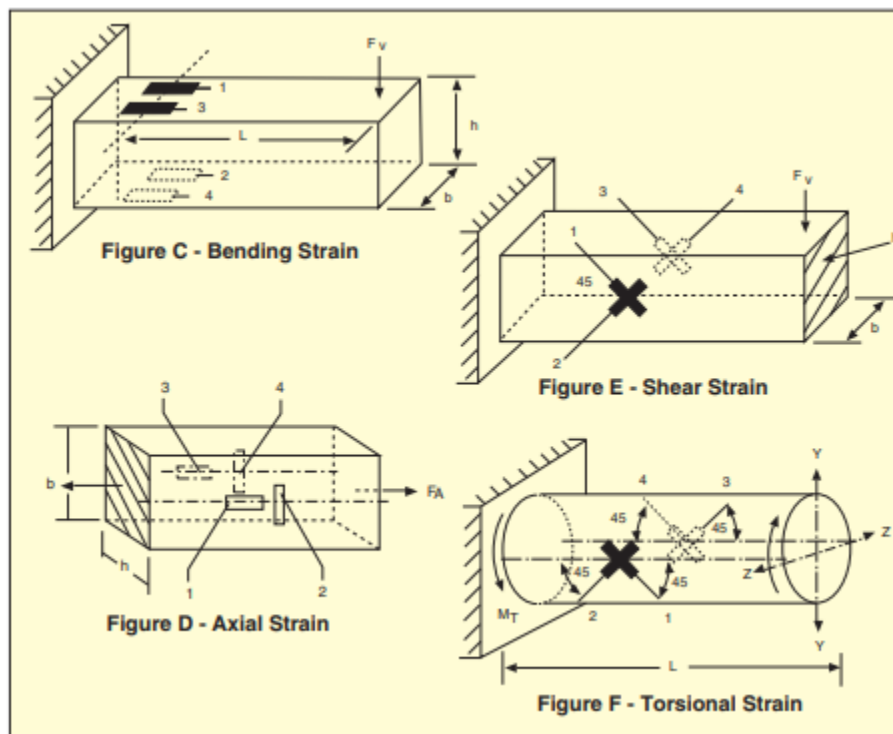
Figure 29: *Strain Gage Orientations for Various Desired Strain Measurements [23]*

Experimental measurement of shear strain in bending has more leeway in terms of possible gage types and configurations. This type of strain can be acquired directly using linear strain gages oriented on the side surface(s) of the specimen as shown in Figure 29. When utilizing this

approach, the strain measured at 45-degrees is not the true shear strain, but rather only half.

Therefore, shear strain is found by multiplying the measured strain from these gages by two [23].

The alternative method for measuring shear strain is a more direct or indirect approach,

depending on personal interpretation. For this method, a type of strain gage known as a strain

rosette can be utilized, which is typically composed of two to four individual linear gage grid

patterns rotated either 90, 45, or 60-degrees apart from each other. For the purposes of this

discussion, a 45-degree, three grid rectangular strain rosette will be considered since these are

readily available at the DML. These gages are bonded in similar fashion to the side surface(s) of

the specimen, and each of the rosette grids records a corresponding principal strain (ε_1, ε_2, and ε_3)

[24]. As long as the principal axes of the loaded specimen and the rosette's orientation relative to

these axes are known, the total shear strain can be found to be the vector sum of the two shear

bisectors (γ_A and γ_B) between the rosette grids [24]. This fact, along with an example image of a

45-degree rosette gage, is shown in Figure 30 and is represented mathematically by Equation 40.

$$\gamma_{MAX} = \sqrt{2}\sqrt{(\varepsilon_1 - \varepsilon_2)^2 + (\varepsilon_2 - \varepsilon_3)^2} \tag{40}$$
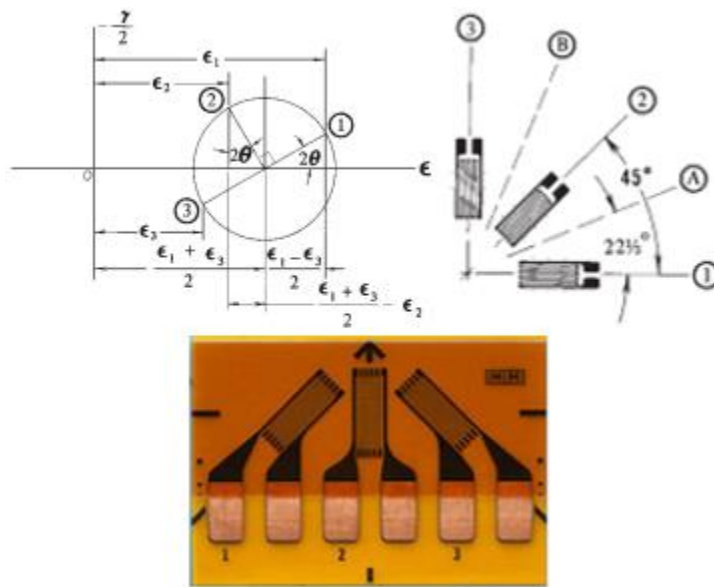
Figure 30: *45-Degree Rectangular Rosette Strain Gage [20], [24]*

CHAPTER III

METHODS OF VALIDATION REVIEW

A. Empirical Data Measurement

As discussed in the previous chapter, the best approach to validating a finite element model is to directly compare the model's predicted solution to that of actual experimentation. This section will seek to provide an overview of all of the required testing equipment, programs, and methods of measurement utilized to collect the data for FEM comparison. The content of this section will not focus on the specifics of experimental testing procedures conducted. This is due to the varying nature of tests performed using this testing setup. These details can be found in the subsequent chapters, wherein discussion of each experiment performed for this research endeavor occurs.

Vernier Structures and Materials Tester

The Vernier Structures and Materials Tester is a versatile platform that allows the user to perform a variety of tests for the purposes of evaluating a structure or the behavior of a material. One of the key uses of this platform at the DML has been to perform tensile tests on balsa samples for the purposes of material characterization [13]. While this has been most useful for research regarding balsa wood or other materials, the tensile test configuration for this platform is not optimal for testing the behavior of beams subjected to bending loads. It is instead more advantageous for the purposes of this research to utilize this tester as a three-point bending

apparatus in much the same way that the Meccano three-point bender from the literature review was utilized. Figure 31 below shows the assembled Vernier Structures and Materials Tester as well as its three-point bending configuration.
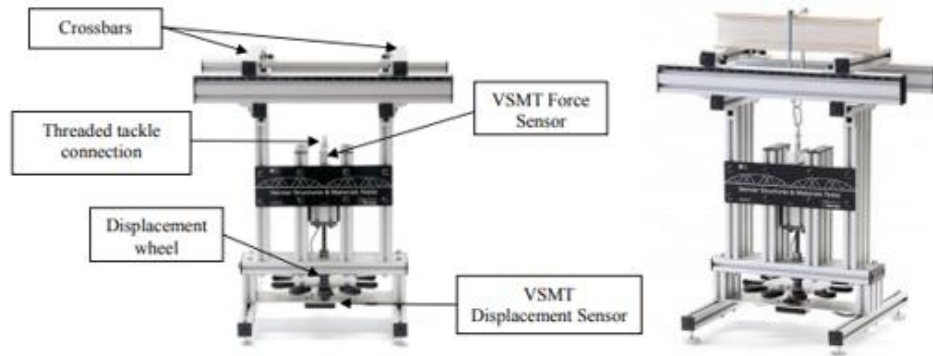
Figure 31: *Vernier Structures and Materials Tester [25]*

This testing platform is primarily composed of 80/20 aluminum slotted framing and comes equipped with both a displacement and a force sensor. The displacement sensor operates by correlating the number of revolutions completed by the hand crank displacement wheel to vertical displacement of the threaded loading rod. This sensor is capable of taking only one displacement measurement with this displacement being that experienced by the structure at the point of the applied load. In addition, the tester is capable of displacing a structure up to 2.75 inches vertically and has a measuring resolution slightly above $1/32^{nd}$ of an inch (this resolution corresponds to 22.5 degrees of rotation on the hand crank displacement wheel) [25]. The force sensor rests atop the threaded load rod and has an eyelet connection for the attachment of chain links and the U-bolt load strap. This sensor is a typical load cell that is optimized for measuring applied tensile loading as the hand crank slowly pulls downward on the sensor and increases the tensile load in the chain links connected to the test specimen. This force sensor has an operational limit of up to 224.8 lb of applied load with a working resolution of 0.225 lb [25]. Damage to this sensor will occur if the applied load exceeds 292.3 lb [25]. Both of these sensors can have their output data directly compiled and displayed using a Vernier LabPro Data Acquisition Interface (see figure below), which is connected to a laptop with the proper version of Logger Pro 3 installed.

44
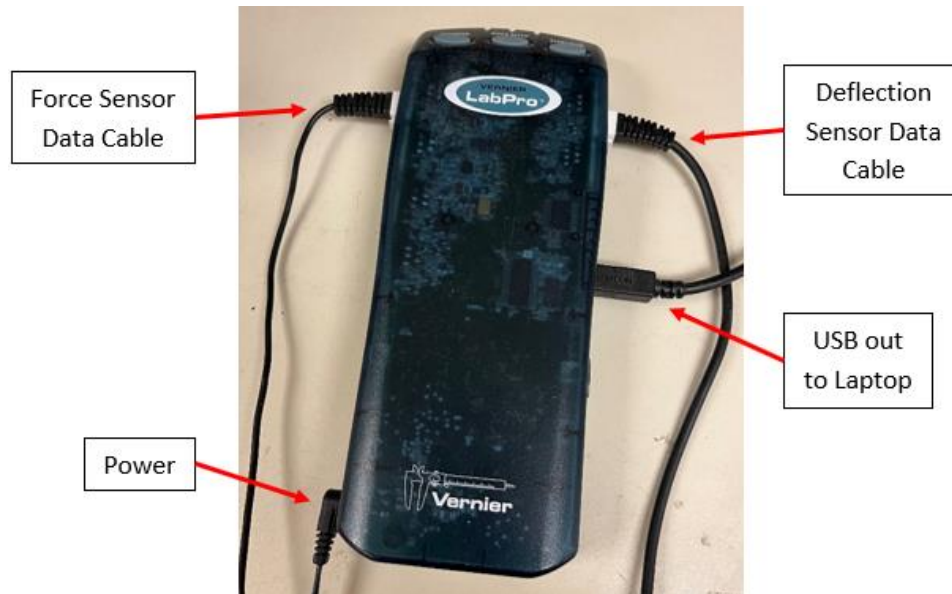
Figure 32: *Vernier LabPro Data Acquisition Interface*

For the purposes of three-point bending, the stock structures tester has a slide rail upon which two crossbars are attached via bolts with t-nuts inserted in the slot on the top of the slide rail. These crossbars are 1" x 1" in cross-section and have a length of 8.0625" (which is also the distance between the front and rear slide rails). They act as the beam supports for the three-point bending configuration, and they can be positioned symmetrically or asymmetrically up to 7.875 inches from the applied load via the load U-bolt [25]. Despite this, the utilization of 80/20 slotted framing allows this testing platform to be quite modular. Therefore, it is not difficult to modify the original platform construction such that longer beams and a larger span between the crossbar supports can be achieved. For the purposes of this research, such modifications were deemed necessary and are documented in the following sub-section.

Bending Deflection Measurement

As was mentioned in the previous sub-section, the Vernier Structures and Materials Tester is capable of capturing only one deflection measurement at the point of the applied load. This limitation would only allow for comparison between FEA and experimental maximum deflection values. While the maximum deflection values might match well, it is possible that properties in

45

the physical beam specimen could cause the deflection curve across the beam span to vary from that found through FEA. As a result, it was more desirable to devise a method of obtaining deflection measurements at multiple set points along the beam length in order to capture these possible spanwise discrepancies.

Given how cramped the tester is below the slide rails due to the sensors, hand crank mechanism, and support structure, the best method of obtaining these multiple deflection measurements was from above the beams. Such measurements could be taken from above at a predetermined height above the bent beams, and this, in turn, would require the development of a platform modification to the original tester platform structure. A survey of measuring equipment was conducted using the following criteria: must have a high measurement fidelity, must be reliable, must be reasonably compact, and measurements taken with the instrument should be easily repeatable. Using these criteria, a few options presented themselves as contenders. Ultimately, however, a depth gauge, more specifically a Fowler Electronic Depth Micrometer, was selected as the measuring instrument most capable for the required task.

This gauge has a maximum dimension of four inches on the measurement interface and is capable of taking depth measurements between 0-6 inches in increments of $0.00005" \pm 0.0001"$ [26]. Due to the instrument's compactness, this measuring capability is further divided between six measuring rods, each capable of measuring a one-inch increment (0"-1", 1"-2", etc.) [26]. This presents a downside to the use of this instrument in that if a deflection exceeds an inch (plus the height to the reference datum), then the next highest rod increment must be installed and the measurement taken again. Despite this, the three-point bending experiments can be designed in such a way that the applied load does not deflect the beams beyond this threshold. Therefore, the same measuring rod can be installed for the duration of the testing. This depth gauge can be viewed in Figure 33 below.

Figure 33: *Fowler Electronic Depth Micrometer*

With the measuring device selected, the proper modifications to the Vernier Structures and Materials Tester were developed. Ideally, this depth gauge should straddle the gap between the slide rails (just as the crossbar supports do) so its measuring rod can be lowered to the point of interest on the beam's upper surface. The reference datum platform it rests on needs to be smooth and as level as possible to allow this gauge to be moved along the span of the beam in order to take measurements at multiple spanwise locations. In addition, this modification must be implemented without interfering with the tester's sensors or the bending behavior of the beam under load so as not to skew the experimental results. Under these requirements, the following modification to the structures tester using 80/20 slotted aluminum depicted in Figures 34-35 was devised and implemented. In these figures, components shaded red are original to the stock structures tester while all other components are part of the modified addition. The decision to replace the stock slide rails for longer ones was based purely on the desire to accommodate longer beams and a larger separation distance of the support crossbars from the load point.

This modification to the structures tester allows the depth gauge to sit atop a level platform with approximately a two-inch gap for the measuring rods to be extended to the beam's surface. In addition, this platform allows as many deflection measurements as is required along a two-foot span of the beam, which is an improvement over the original tester's deflection measuring

47

Figure 34: *CAD Rendering of Modification to Vernier Structures Tester*
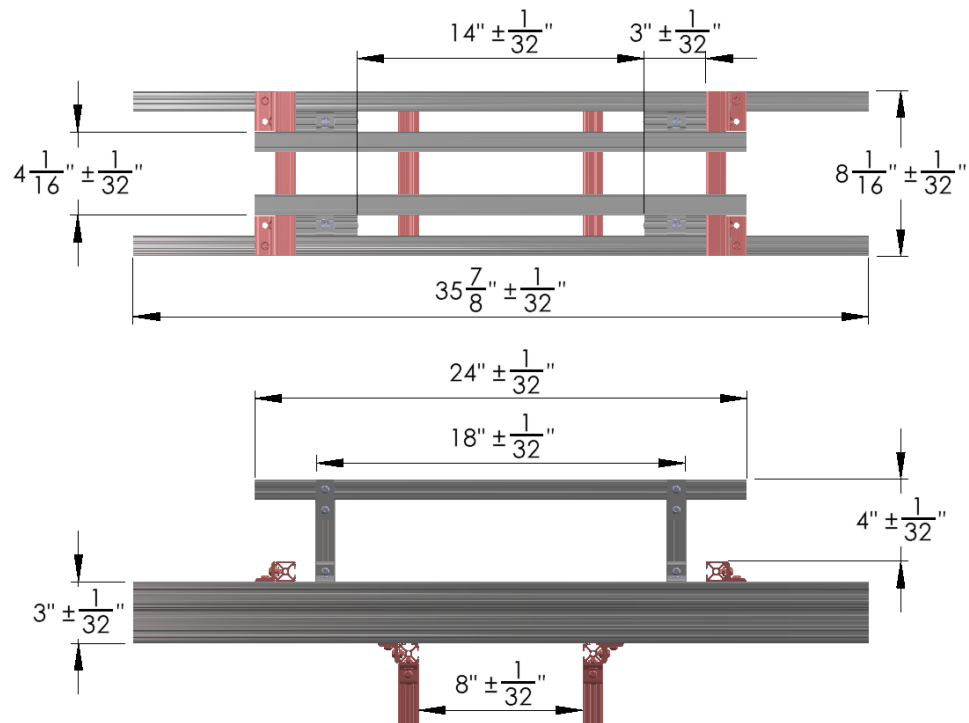
Figure 35: *Modified Vernier Structures Tester Dimensions*

capabilities. The platform itself is height adjustable but it is designed to remain within five inches

of the top face of the crossbars so that the six-inch measuring limit of the depth gauge is not

exceeded. It can be raised to a maximum of four inches above the crossbars and lowered until it

touches the upper surface of the crossbars. Utilization of half-inch slotted rails for the platform

vertical supports allows sufficient free space around most beams, thereby reducing the risk of

interfering with the three-point bending results. Lastly, as mentioned previously, the addition of the longer slide rails is intended to accommodate longer beams and larger crossbar support separation. Since the load capacity of the structures tester is only 224.8 lb, having larger support separation will assist in achieving greater beam deflections for beams composed of stiffer/stronger materials. Figure 36 shows an example of beam deflection being measured utilizing this modification to the Vernier structures tester.

Figure 36: *Beam Deflection Measurement Technique Using Depth Gauge*

Beam Stress Measurement

Another desired parameter to compare with FEA predictions is the bending stresses in the beams as they are subjected to a three-point bending load. As discussed in the literature review, the best tool for capturing stresses in a loaded object is through the use of strain gages. Similar to how the structures tester requires a data acquisition interface for the force and displacement

instruments, strain gages require such an interface in order to relay their strain measurements to the user. The selected instrumentation for this requirement is the National Instruments NI cDAQ-9185 chassis with NI-9237 + NI-9923 add-ons (both with DSUB pinouts). The cDAQ-9185 chassis is a modular data acquisition platform capable of supporting several types of data measurement. Its four-slot capacity allows for support of multiple modular specialized instrumentation add-ons [27]. The complete cDAQ chassis with the above-mentioned add-ons can be viewed in Figure 37.
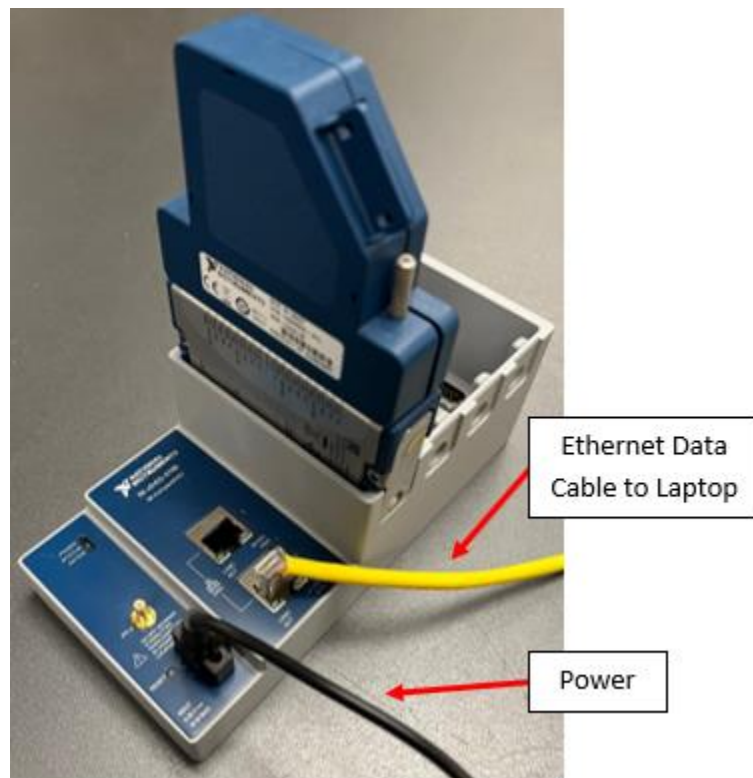
Figure 37: *NI cDAQ-9185 Chassis with NI-9237 + NI-9923 (w/ DSUB) Strain Instrumentation*

The NI-9237 add-on is an instrument that acts as the completion Wheatstone bridge for strain gages. The DSUB pinout port on top of the NI-9237 has markings to indicate what each pin connects to in the internal bridge. This instrument is capable of handling up to four separate strain gage connections at once, and as such, the DSUB pinout is divided into four separate channels (see Figure 38). These channels are denoted by a number between 0 and 3 after each pin

description on the unit. The limitation of this completion bridge is that it is capable of internally

completing only half and full-bridge gage configurations [28]. If a quarter-bridge setup is utilized,

the strain gage must be connected in series with either a dummy resistor or additional unstrained

gage of the same nominal resistance, thus completing half of the Wheatstone bridge externally

from the unit [28]. Lastly, the power limitation for this instrument is 150 mW, meaning that the

input excitation voltage is dependent on external bridge gage resistance [28]. For example,

simultaneous measurement from four 120 Ω half-bridges is limited to an EX-input of 2.5 volts

[28]. Likewise, simultaneous operation of four 350 Ω full-bridges is limited to an EX-input of 3.3

volts [28].
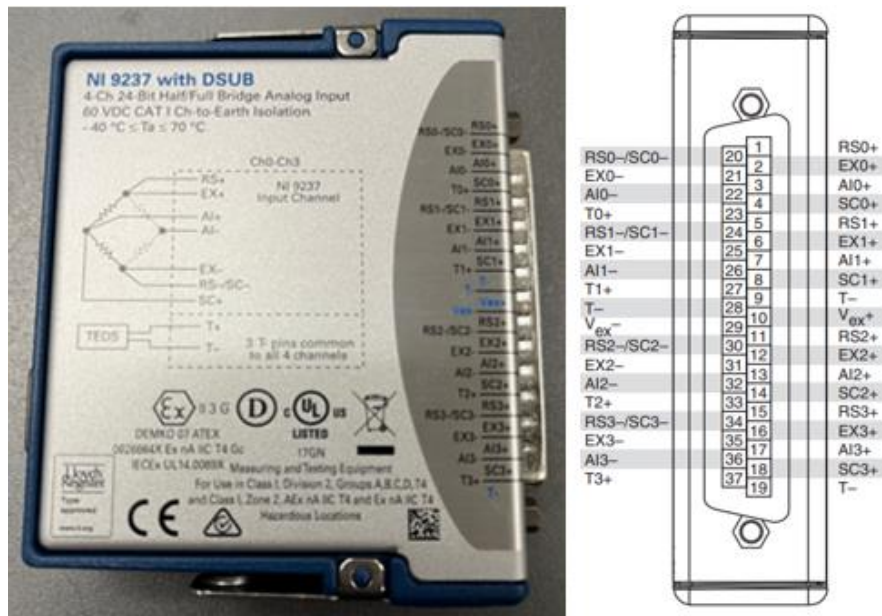
Figure 38: *NI-9237 Completion Bridge and Accompanying Pinout Guide [28]*

The final add-on for this instrumentation is the NI-9923 screw terminal to DSUB pinout.

Attaching this terminal to the DSUB pinout port of the NI-9237 unit allows for ease of connection

of the strain gage lead wires to the cDAQ. Each terminal has the corresponding DSUB pinout

number it is tied to which, in turn, can indicate which wire should be connected by cross-

referencing the terminal number with the pinout map from Figure 38. This screw terminal unit, as

well as an example of lead wires connected to the fully assembled cDAQ chassis, are shown in the following figures. This fully connected cDAQ unit, shown in Figures 37 and 40, can transmit the measured output signal from the NI-9237 completion bridge and external strain gages to a LabVIEW readout program to be properly compiled and displayed. This readout program will be discussed in the following sub-section.

Figure 39: *NI-9923 Screw Terminal to DSUB Pinout Unit*

Figure 40: *Four Half-Bridge Strain Gage Configurations Connected to NI cDAQ-9185 Chassis*

LabVIEW Strain Readout Program

In order to properly view and process the analog output signals from channels A0-A3 from the cDAQ-9185, a LabVIEW visual instrument file (VI) had to be developed. Interfacing a VI with a cDAQ device requires certain specific drivers to be installed in addition to the base

LabVIEW software. Chief among these additional drivers is the NI-DAQmx series. Once installed, these drivers allow the cDAQ instrumentation to communicate directly with VI's developed in LabVIEW through the addition of specialized program blocks, which will be discussed later in this sub-section. The remainder of this sub-section focuses on the functionality of the LabVIEW programs developed to read strain measurements taken using the cDAQ-9185. Lastly, the base structure of the VI to be discussed draws heavily from the strain VI tutorial covered in [29].

The front panel of the strain readout VI developed for this research is shown in Figure 41. This front panel contains many useful sources of data output as well as data measurement parameters. An example of this is a plot that can simultaneously display the time history of a measured strain signal from each of the four available cDAQ channels. As will be discussed later, the data presented by this plot is the raw strain signal output from each channel. Below the plot are indicator displays that take the raw strain signal from each analog channel and average it over a set time interval as well as compute the standard deviation of the strain signal over this same time interval. Above the plot, there are two signal measurement parameters: sampling rate and number of samples to be taken per time interval. Trial and error upon initial development and testing of this VI found that a sampling rate of 1000 Hz paired with 250 samples taken per time interval produced the best output signal data free from aliasing or other prominent sources of noise. In addition, to the right of what is shown in the figure, there is a control interface to command the VI to write all data collected to an output file. The operation of this interface is self-explanatory and requires that only one button be toggled either ON or OFF. There is also a STOP button that, when pressed, will terminate the operation of the VI.

The details of how this VI operates to display data in the front panel is best understood by examining the block diagram. The following discussion focuses on the two main sections of the block diagram, with the first being the processing and display of the strain data read into the VI from the cDAQ. Shown in Figure 42, this portion of the block diagram can further be sub-divided
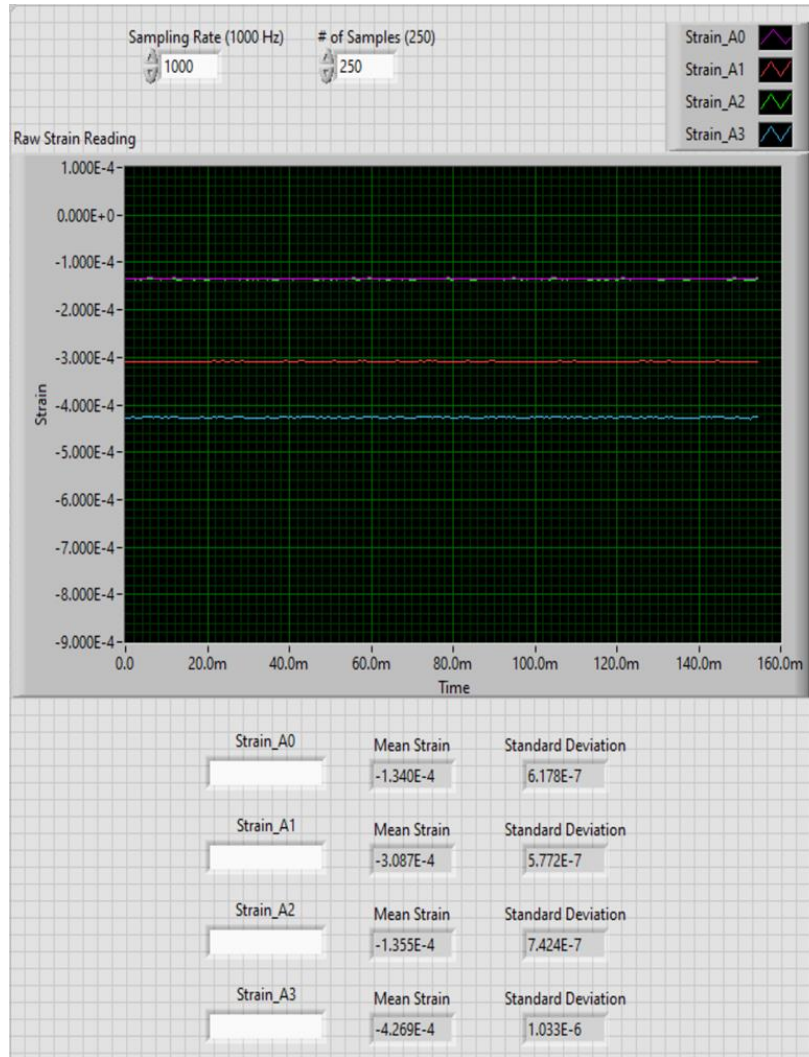
Figure 41: *Example Front Panel Strain Data Readout (75 lb Load in 3-Point Bending Config.)*

into four main components. The first component, denoted by the red numerical indicator in the

figure, is the specialized program block mentioned previously, which is known as the 'DAQ

Assistant' block. Adding this block and then double clicking it when the cDAQ is powered and

connected will then open the interface window shown in Figure 43. This is the main window

through which control over the cDAQ from LabVIEW occurs. There are a few steps omitted

regarding the initial setup and pairing of this block with the cDAQ. However, [29] does an

excellent job of explaining these steps. Within this interface, the user can toggle between all four

analog channels from the cDAQ and update the proper strain gage parameter based on gage type
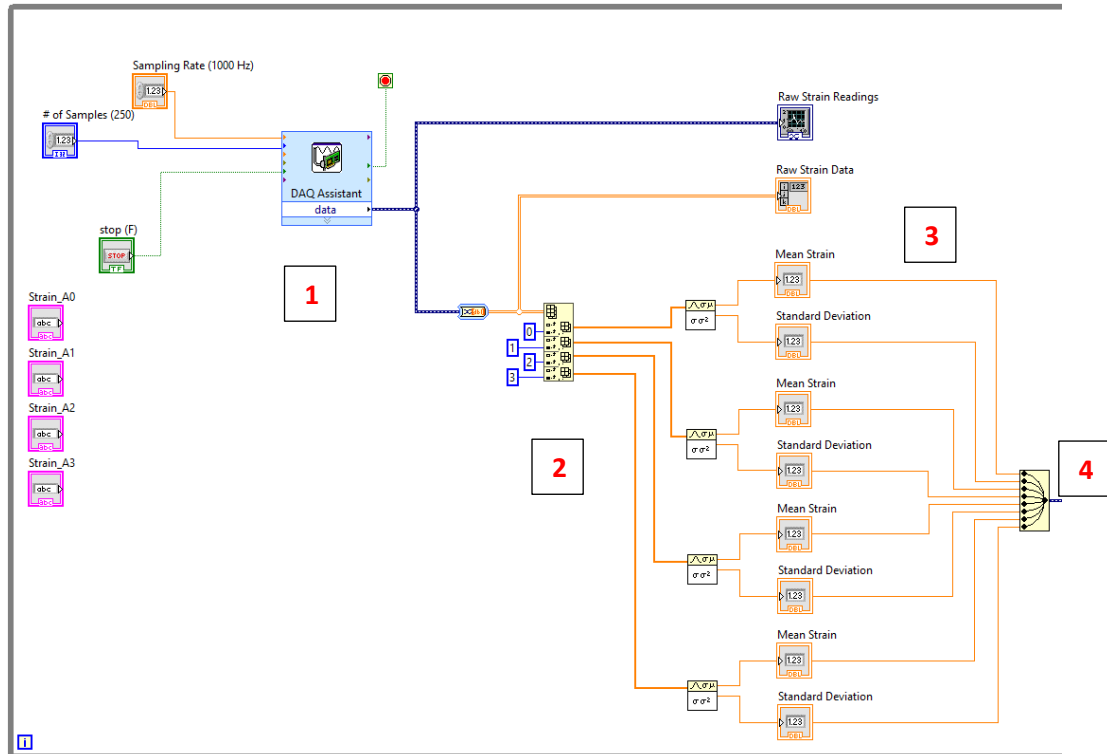
Figure 42: *Strain Data Processing and Display Portion of VI Block Diagram*
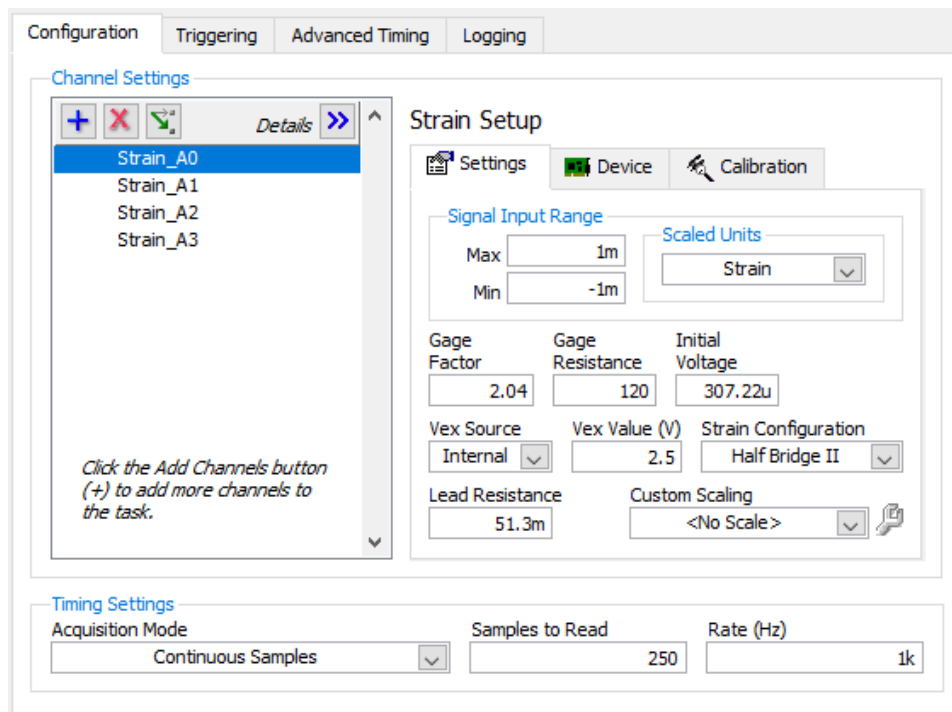
Figure 43: *DAQ Assistant Block Main Interface Window*

and configuration connected to each respective channel. These fields include the gage factor, gage resistance, Vex voltage, strain configuration, and lead resistance. All other fields should display as shown in Figure 43 (initial voltage will vary, however). Once this data is properly entered, clicking the 'Device' tab and then the 'Strain Calibration' button will allow the user to zero the strain signal measured from the gages. This process is also well covered by [29]. Once all channels are updated and calibrated, clicking the 'OK' button in the bottom right of the interface window will apply these parameter settings to the remainder of the VI.

The second component of importance is an indexing array. This block takes the combined output signal from the 'DAQ Assistant' block and divides the data into four separate signals (one for each analog channel from the cDAQ). This then allows the 'standard deviation and variance' blocks, the third component of interest, to average as well as compute the standard deviation of the strain data for each channel. Additionally, the raw signal data is sent to a graph block, which generates the strain data plot shown in the front panel. The resulting average strains and their accompanying standard deviations for each analog channel are then concatenated into one signal using a 'merge signals' block (the fourth component of interest). This recombined signal is then sent to the second half of the VI.

The second half of the VI focuses on generating an output .txt file containing the mean strain and standard deviation of this mean for each of the active analog channels from the cDAQ. The recombined signal from the 'merge signals' block is subsequently passed through a series of 'set dynamic data attributes' blocks. These blocks allow the user to assign meaningful titles to each individual signal, as well as specify which signal that title is assigned to. The numbering system for these signals starts at zero, which is counted from the first signal input at the top of the 'merge signals' block. There are as many 'set dynamic data attributes' blocks as there are combined signals. In this case there are four mean strain signals and four standard deviation signals, thus requiring eight 'set dynamic data attributes' blocks. Once all signals have been assigned an appropriate name, the merged signal is then passed to the 'write to measurement file' block.
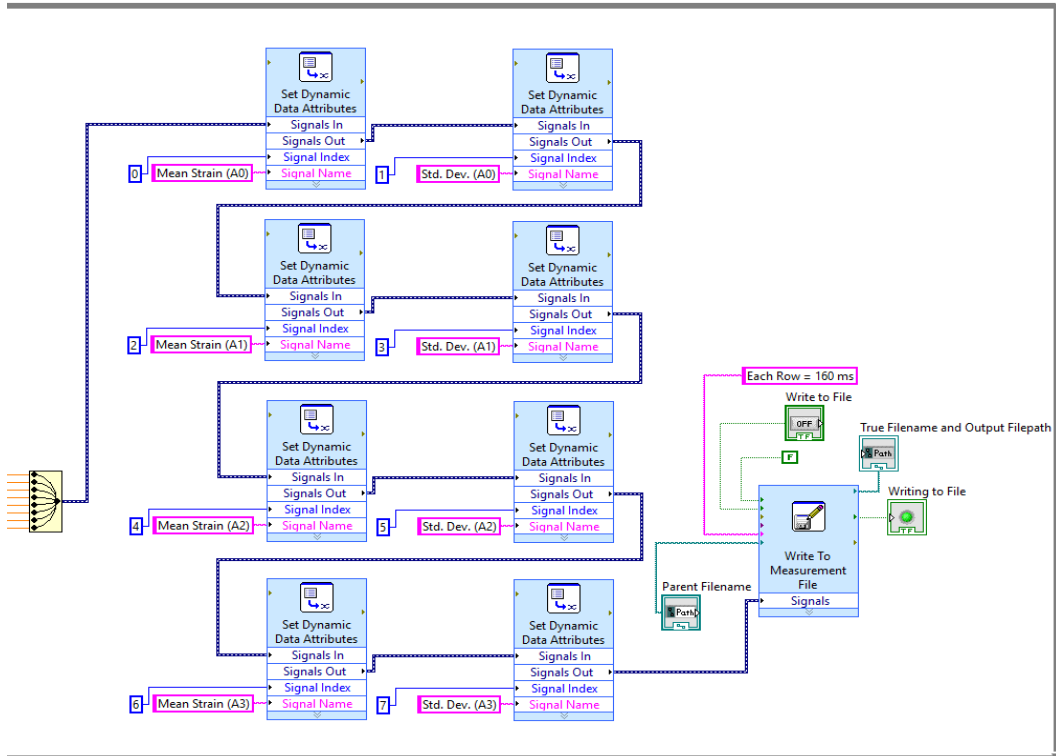
Figure 44: *Write-to-File Portion of VI Block Diagram*

One major difference between the VI developed in [29] and this version is that this version allows continuous strain measurement to occur. This is accomplished by enclosing the block diagram in a while loop structure (the gray outline in the figures). Due to this while loop, strain measurements with this VI will only stop once the VI is terminated. Lastly, for the purposes of this research two versions of this VI were created. The version shown in Figures 42 and 44 is configured for normal strain due to bending while the other version handles shear strain due to bending. Both strain readout VI's maintain the same core bock structure, and there are only minor differences between the two.

B. Euler-Bernoulli Beam Theory

In addition to experimental testing, other methods of theoretical evaluation can be utilized for comparison to the finite element model solutions. The three-point bending configuration of the Vernier Structures and Materials Tester can be idealized to a simply supported beam with a center

loading condition. Due to this idealization, less rigorous theoretical evaluations than FEA can be computed on such bending configurations with reasonable success. For the purposes of this research, the theoretical methodology utilized for an additional point of comparison with the FEA results is Euler-Bernoulli Beam Theory. The remainder of this section will focus on the application of this theory to the idealized simply supported three-point bending model.

Single Material Composition Beams

Before application of this theory can occur, the idealized model previously mentioned must be defined. The Vernier Structures and Materials Tester can be simplified to the basic case of a simply supported beam with a center load. Since this is a popular loading condition, mathematical representations of the bending loads and displacements are well defined and readily accessible [30]. In the case of the structures tester, the simple support model of the three-point bending configuration can be defined as shown in Figure 45. In this figure, the 80/20 crossbars from the structures tester are reduced to the simple triangular supports. These supports restrict the vertical
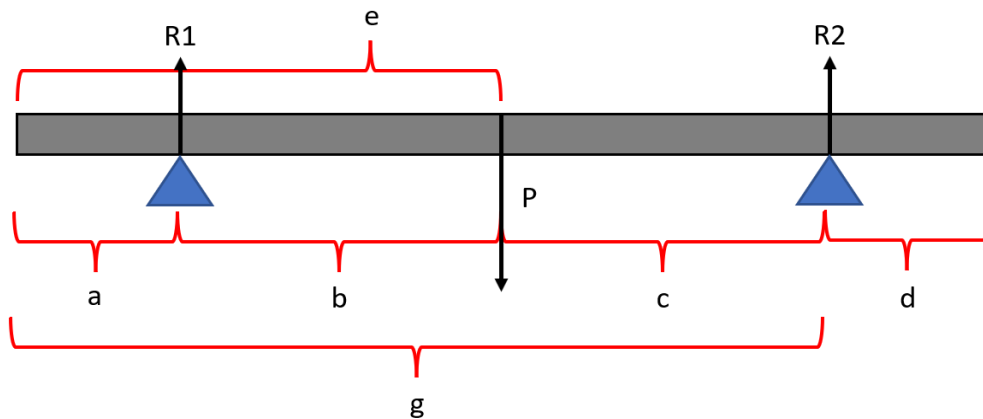
Figure 45: *Idealized Beam Theory Model for Beams in Three-Point Bending Apparatus*

displacement of the beam but do not hinder any lateral movement when under load. Likewise, the load U-bolt is reduced to a simple point load, P, which acts at the center of the beam's length. While most three-point bending tests apply the load in the center of the beam's length and equidistant from the beam supports, this idealized Beam Theory model is defined such that

58

asymmetrical support or load application positioning can be easily accounted for through changes in distances a-e. Additionally, this model is designed to consider a known amount of excess beam overhang, distances a and d, on either side of the supports. If no overhang is present, a = d = 0 in the following equations.

Knowing the Beam Theory model, mathematical equations can be developed through the use of Singularity Functions to define the shear force, bending moment, deflection, bending stress, and transverse shear stress distribution across the beam's length [30]. These functions operate by dividing the beam into specified sections, with transitions between consecutive sections occurring at locations of applied loads or reaction forces imparted by the supports. In the case of this model, there are four unique sections: segment a, segment b, segment c, and segment d. The corresponding Singularity Functions that define the shear force, bending moment, and bending deflection across each of these segments (including calculation of necessary constants) are defined in Equations 41-46 below. In this model, x is positive from left to right with the origin located at the left end of the beam. These functions work by requiring any term in the angled brackets to be positive and greater than zero. Therefore, the x distance must be greater than the constant value subtracted from it for that term to contribute. Lastly, each equation from 42-44 is an integral of the previous equation, with the equation of the beam curvature (the integral of the bending moment equation) omitted.

$$R_1 = \frac{Pc}{b+c} \qquad R_2 = \frac{Pb}{b+c} \tag{41}$$

$$V(x) = R_1 \langle x - a \rangle^0 - P\langle x - e \rangle^0 + R_2 \langle x - g \rangle^0 \tag{42}$$

$$M(x) = R_1 \langle x - a \rangle^1 - P\langle x - e \rangle^1 + R_2 \langle x - g \rangle^1 \tag{43}$$

$$\delta(x) = \frac{1}{EI_{zz}} \left[\frac{R_1}{6} \langle x - a \rangle^3 - \frac{P}{6} \langle x - e \rangle^3 + \frac{R_2}{6} \langle x - g \rangle^3 + k_1 x + k_2 \right] \tag{44}$$

$$k_1 = \left(\frac{1}{g-a} \right) \left[\frac{P}{6} (g - e)^3 - \frac{R_1}{6} (g - a)^3 \right] \tag{45}$$

$$k_2 = \left(\frac{-a}{g-a} \right) \left[\frac{P}{6} (g - e)^3 - \frac{R_1}{6} (g - a)^3 \right] \tag{46}$$

The resulting bending stress and transverse shear stress can then be calculated once the spanwise distribution of shear force and bending moment are known for the beam. For bending stress, this idealized model assumes uniaxial loading of the beam, meaning that there is only one applied load, and that load is applied in one specified direction. The resulting bending stress can be calculated using Equation 47. In this equation, the bending stress is dependent on two parameters: the spanwise bending moment distribution along the beam and the vertical distance from the neutral axis of the beam. The neutral axis parameter will influence whether the bending stress is zero, tensile, or compressive. Likewise, for transverse shear stress, dependency on the spanwise shear force distribution along the beam as well as vertical distance from the neutral axis of the beam are necessary. Under the uniaxial loading assumption and these dependencies, transverse shear stress can be computed using Equation 48. In this equation, Q is the first moment of the area (which accounts for the vertical position relative to the neutral axis) while w is the width of the cross-section at the vertical position from the neutral axis. Regarding the experimental and FEA results, it is usually standard to compare the strains instead of the stresses, especially for more complex materials or load cases. Conversion to bending and transverse shear strain is accomplished using the Beam Theory assumption that all materials involved are linearly elastic. Therefore, in conjunction with the uniaxial loading assumption, the relationship between stress and strain follows the simplified form of Hooke's Law: σ = Eε and τ = Gγ.

$$\sigma_{Bend} = \frac{M(x)*y}{I_{zz}} \tag{47}$$

$$\tau = \frac{V(x)*Q}{I_{zz}w} \tag{48}$$

Multi-Material Composition Beams

As discussed in the previous sub-section, the model applies only to beams composed of one singular homogenous material. In the case of the composite I-beams utilized by the DML, this Beam Theory model is inadequate for capturing the deflection and stresses in the beams. This

60

inadequacy can be rectified through the application of the transformed area method to the beam

cross-section. This transformation method will transform the cross-section of the beam to an

equivalent representation composed of the material with the higher Elastic Modulus. This is

accomplished by modifying the less stiff material's cross-sectional width such that the original

composite beam's bending stiffness is preserved [31]. This modification of the beam cross-

section requires the calculation of the transformation factor, n, which is simply a ratio of the less

stiff material's Elastic Modulus to the stiffer material's Elastic Modulus. In the case of this

research, n is defined by Equation 49.

$$n = \frac{E_{Balsa}}{E_{Carbon}} \hspace{3cm} (49)$$

The thickness of the balsa shear web is then multiplied by this factor to transform its cross-

section to an equivalent composition of carbon fiber. From this point, utilization of the previous

sub-section's mathematical equations is valid. The only exception is that the Elastic Modulus

utilized for the deflection calculations will be that of the carbon fiber (the stiffer material).

Additionally, the moment of inertia will be that of the transformed material beam due to the fact

that modifying the balsa shear web width by the transformation factor will modify the overall

beam moment of inertia. The resulting bending stresses computed will be for the transformed

beam. These stresses will be accurate only where carbon fiber exists on the original beam. To get

the stresses in the balsa shear web, the transformed bending stress in this region must be

multiplied by the transformation factor [31]. Shear stress will not be influenced by multi-material

beam cross-sections. Therefore, the original moment of inertia and cross-sectional dimensions

can be utilized in this calculation.

C. OSU Wing Spar Mathcad Analysis Tool

The final method of validation to be utilized for this research is the DML's proprietary Wing

Spar Mathcad analysis tool. This tool was developed by Dr. Arena mainly to assist undergraduate

Aerospace students participating in the annual Speedfest design/build/fly capstone, though it is also utilized by graduate students conducting research for Dr. Arena. Currently, this spar analysis program is the sole pre-prototype design tool available to initially size one of the more structurally significant components of UAVs being built at the DML. Ultimately, successful development of a method for modeling and analysis of these composite wing spars using SolidWorks FEA would pave the way for this Wing Spar program's eventual retirement from use. At the very least, however, complimenting the design and analysis capabilities of this program with a viable FEA model would serve to greatly expand the lab's structural analysis resources.

Program Functionality and Applicability

This program operates by first requiring the user to input information regarding the proposed wing geometry and airfoil cross-section along with an expected worse case flight condition. This information is then passed into a vortex lattice routine which, among other parameters, computes the expected lift distribution along the wing. The remaining information to enter into this program is the desired spar geometrical dimensions and mechanical properties of the spar cap and shear web materials. Following what can sometimes be a lengthy iteration process, a final composite I-beam spar geometry can be sized for the expected flight loads of the UAV wing design. In the structural analysis routines of this program, deflections and stresses are computed using the same Beam Theory approach as discussed in the previous section, though this program ignores the possibility of beam overhang beyond the supports (causing the Singularity Functions to be slightly different). What makes this current version of the program unsuitable for 3-point bending analysis, however, is the fact that it analyses the wing spars under a more realistic spanwise distributed lifting load instead of a point load at the wing root. With this in mind, this version of the Wing Spar analysis tool required modification in order to be compatible.

Fortunately, all of the necessary modifications required to make this analysis tool suitable for 3-point bending were already completed during research conducted by [13]. While a copy of this

modified Wing Spar program no longer exists, enough detail regarding its structure and logic was included in this Thesis such that it was easily replicated for this research endeavor. In summary, the portion of the program that linked the beam bending load to the calculated aerodynamic lift distribution was removed and replaced with a user input variable for the point load at the wing root. The Beam Theory calculations still utilize the transformed area method for dealing with composite sections, with the only required mechanical properties being the carbon fiber E_1 modulus and ultimate load limits as well as balsa wood cross-grain modulus (E_T) and cross-grain ultimate shear limit. The remaining program inputs such as beam length and cross-sectional dimensions remained unchanged. An example of the inputs provided to this program can be viewed in the figure below.
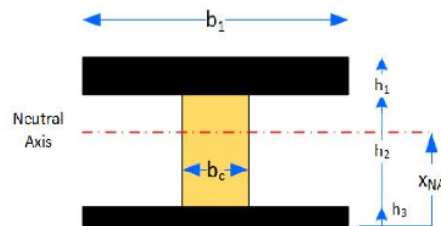
SPAR GEOMETRY INPUTS:

$h_1 \equiv 12 \cdot 0.005 = 0.06$ Top spar cap thickness [in] (each uni-carbon layer approx. 0.005" thick)

$h_2 \equiv 1.118$ Balsa shear web height [in]

$h_3 \equiv 12 \cdot 0.005 = 0.06$ Bottom spar cap thickness [in] (each uni-carbon layer approx. 0.005" thick)

$b_c \equiv 1.217$ Spar cap widths [in]

$b_w \equiv 0.125$ Balsa shear web width [in]

$E_{Balsa} \equiv 7614$ Balsa Elastic Modulus [psi] (perpindicular to grain)

$E_{Carbon} \equiv 1000 \cdot 19580.1 = 1.958 \times 10^7$ Uni-Carbon Elastic Modulus [psi] (parallel to fibers)

$\sigma_{ult\_c} \equiv 1000 \cdot 174.05 = 1.74 \times 10^5$ Uni-Carbon Ult. Compressive Strength [psi]

$\sigma_{ult\_t} \equiv 1000 \cdot 217.56 = 2.176 \times 10^5$ Uni-Carbon Ult. Tensile Strength [psi]

$\tau_{ult} \equiv 323.20$ Balsa Avg. Ult. Shear Strength [psi] (perpindicular to grain)

$R_1 \equiv -49.96$ Point load input [lb]

$L \equiv 20$ I-Beam Length [in]

$R_2 \equiv \dfrac{R_1}{2}$ Support Reaction force calculation [lb]

Figure 46: *Example Wing Spar Mathcad Inputs*

63

Similar to the independently developed Beam Theory analysis tool, which utilizes the Singularity Functions from the previous section, this Wing Spar program outputs important structural parameters such as shear and moment diagrams, beam deflection, and maximum tensile and compressive bending stress as a function of beam length. Where this program differs in outputs is that, instead of calculating the cross-sectional shear stress distribution in the beam, only the maximum shear stress in the balsa shear web as well as the shear stress at the balsa-carbon bond line are determined and output to the user. For all stress plots generated, the ultimate limits for the materials in bending and shear are concurrently plotted in order to indicate to the user when the design iteration is approaching failure limits. A beam status output is also generated to provide further feedback on the beam condition and to identify the likely failure mode it will experience. In addition, the Wing Spar program also generates cross-sectional profiles of the I-beam geometry before and after the Area Transformation Method is applied to the beam. An example of this output can be viewed below. In order to adequately compare the results from this program with the Beam Theory from the previous section as well as to experimentation, the beam length input into the Wing Spar program will be the equivalent length of the beam between the supports.
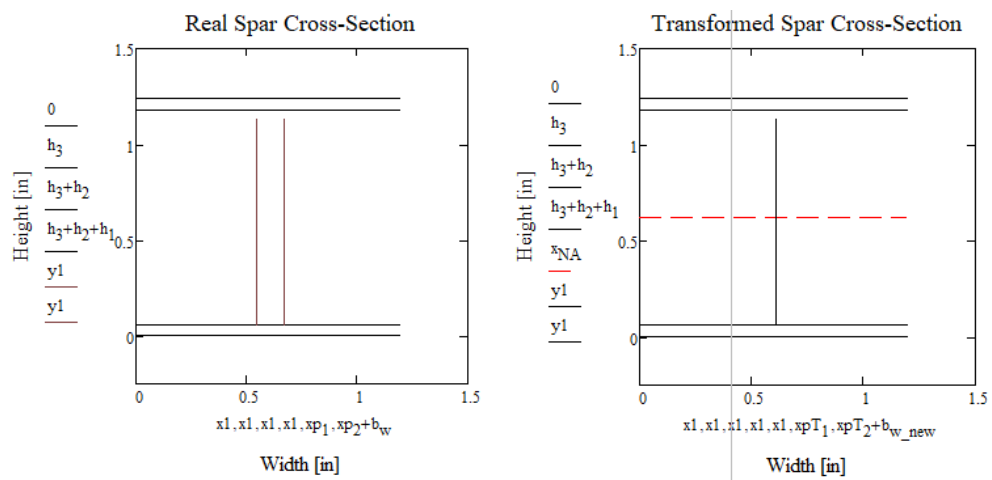
Figure 47: *Wing Spar Area Transformation to Equivalent Cross-Section Composed of Carbon Fiber*

CHAPTER IV

ISOTROPIC BEAM TESTING, MODELING, AND RESULTS

A. Testing and Modeling Objectives

Before moving forward with testing and modeling of the composite I-beam spars, it was first prudent to establish a baseline test case with a simpler beam composition. Thus, this first experiment utilized two metal test specimens (described in the following section) whose mechanical properties allowed them to be classified as isotropic materials. These simpler beam geometries and properties would be quite useful for establishing the capabilities and functionality of the SolidWorks FEA solver program, especially since not much was known about its capabilities at the outset of this research. Furthermore, this test case would also be useful in establishing the proper experimental testing procedure regarding bending of the test specimens in the Vernier Structures and Materials Tester in a 3-point bending configuration. The main emphasis here would be on the correct application, arrangement, and measurement of strain gages and the resulting strain data. The procedures for this portion of structures testing were not well established within the DML at Oklahoma State University at the time of this writing. The results of the SolidWorks FEA predictions compared to empirical data for these beams, whose properties also readily allow for satisfactory prediction of deflections and stresses via Beam Theory, will provide insight into the expected performance of this FEA program for the more complex composite I-beams.

The objectives and subsequent focus for testing and modeling of these isotropic metal beams are summarized as follows:

8) Establish proper experimental testing procedure for beams in 3-point bending configuration with an emphasis on procedures/recommendations for strain gages.

9) Explore methods to properly generate FEA models within SolidWorks, especially as it relates to application of loading conditions, boundary conditions, and model meshing.

10) Establish a baseline for the capabilities of the FEA solver in SolidWorks for both 2D and 3D FEA models of the isotropic metal beam test specimens so that expectations for its solving capabilities on the composite I-beams can be hypothesized.

B. Beam Experimental Setup

Much of the instrumentation and equipment required to perform a 3-point bending test are covered in Chapter III, Section A. All documentation discussed there represents the finalized experimental equipment and programming needs for the testing performed for this current chapter. Not covered in Chapter III, however, was the choice and arrangement of strain gages on the test specimens for strain measurements as well as the specifics of both metal test specimens utilized for this experiment. Both of these previously omitted topics are covered in detail in the following sub-sections. The end goal for the empirical data gathered from bending these metal beams is to compare the true beam deflections, normal strains, and transverse shear strains to those obtained from a SolidWorks FEA model approximating the experimental testing conditions. The following sub-sections, coupled with the discussion from Chapter III, Section A describe these experimental testing conditions and procedures.

Square Beam Cross-Section

The first of the two test specimens utilized was a square cross-section Al 6061-T651 metal

beam. The supplier rated this beam to have a cross-sectional width and height of 0.75 ± 0.014"

and a length of 24" (accompanied by a length tolerance listing of 'plus') [32]. Verifying

measurements performed on the acquired beam revealed the height and width measurements to be

outside of the stated tolerance range while the beam length specifications listed were within

tolerance. With the true dimensions of the beam known, all necessary beam cross-sectional

properties could be determined. Along with Tables 5 and 6, Figure 48 details these beam cross-

sectional properties as well as the mechanical properties for 6061-T651 aluminum (as obtained

from [33]). Apart from this beam's isotropic mechanical properties, it was selected as a test

specimen for its simplistic cross-sectional geometry. This simple geometry would be a fitting

starting point for generating the desired SolidWorks FEA baseline.
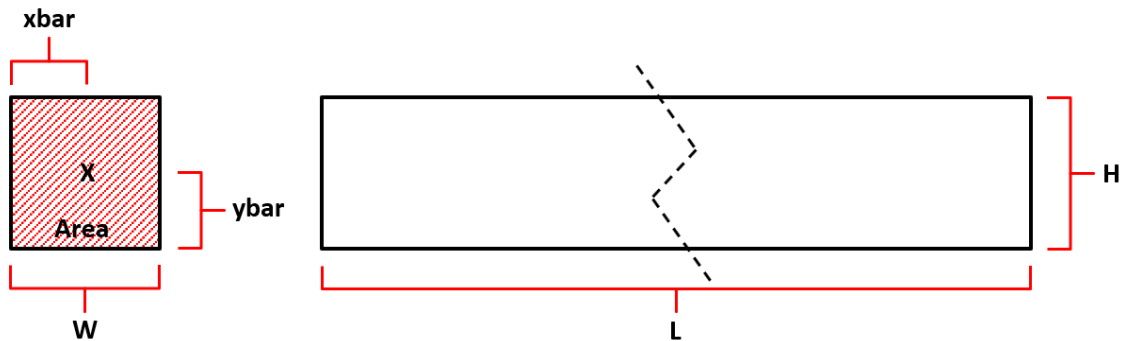
Figure 48: *Square Beam Dimensions and Cross-Sectional Properties Reference*

Table 5: *Square Beam Dimensions and Cross-Sectional Properties*

Square Beam Dimensions and Cross-Sectional Properties				
L	24.0625	±	0.0156	in
W	0.811	±	5.00E-04	in
H	0.815	±	5.00E-04	in
Area	0.661	±	5.75E-04	in²
ybar	0.407	±	2.50E-04	in
xbar	0.406	±	2.50E-04	in
I_{zz}	0.037	±	7.10E-05	in⁴

Table 6: *Aluminum 6061-T651 Mechanical Properties [33]*

Aluminum 6061-T651 Mechanical Properties		
E	10000	ksi
G	3770	ksi
ν	0.33	
$\sigma_{yld.\_T}$	40	ksi
$\sigma_{Ult.\_T}$	45	ksi
$\tau_{Ult.}$	30	ksi

The lengthwise centerlines on this beam, along the width and height faces, were marked with a fine-point Sharpie. The same Sharpie was utilized to mark every two inches in length along the beam for deflection measurement, with 0" starting at the left of the beam when placed in the Vernier Structures and Materials Tester. Additionally, four locations along the length of the beam on the upper and lower faces were marked for placement of strain gages intended for measuring bending strain. Another location for strain gage placement was marked along the length of the beam on the side faces for gages measuring shear strain. With the exception of the normal strain gage at the beam length midpoint, all of these gage location markings were placed at odd distances from the left end of the beam so as not to interfere with the deflection measurements to be taken with the depth micrometer. Further information on the use of strain gages for this beam is provided in the Strain Gage Configurations sub-section.

Following completion of necessary markings and bonding of strain gages in desired locations along the length of the beam, this beam was placed in the Vernier Structures and Materials Tester and configured for a 3-point bending test. Figures 49 and 50 display the square beam specimen as it was tested within the Vernier Structures and Materials Tester (note the implementation of the modified shelf assembly for beam deflection measurements as discussed in Chapter III, Section A). In addition, in these figures, the presented configuration shows that the strain gages attached to the NI cDAQ-9185 are those intended for measuring bending strain for this beam. Initially, this testing configuration lacked some of the positional markings present in Figures 49 and 50. Upon
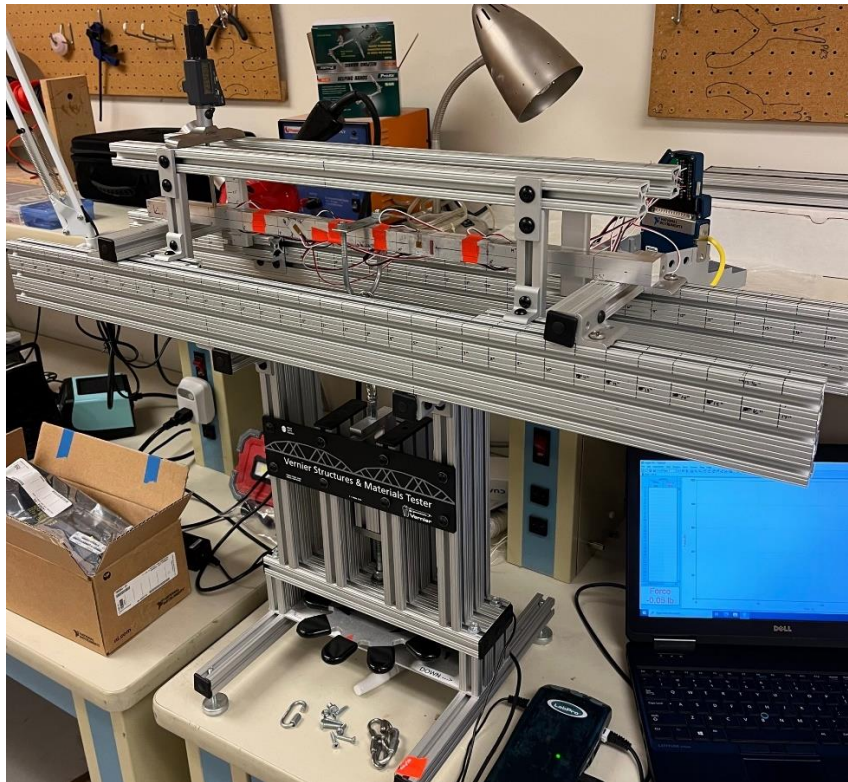
Figure 49: *Square Beam 3-Point Bending Configuration (pt. 1)*
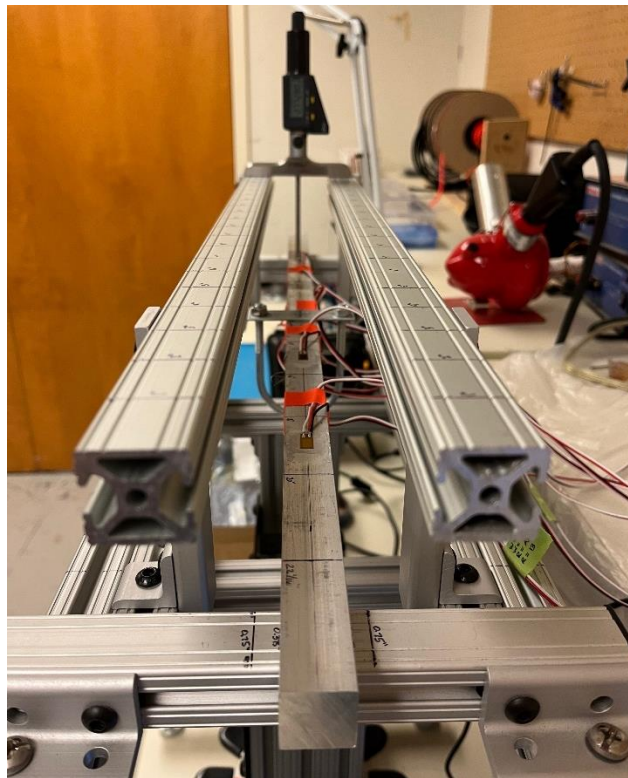
Figure 50: *Square Beam 3-Point Bending Configuration (pt. 2)*

conducting test bending trials to prove that this 3-point bending configuration worked as expected, it was found that the lack of these markings had an adverse effect on the collection of deflection and strain data for the square beam due to support and/or load U-bolt misalignment. Addition of these position markings on the structures tester, as well as ensuring that the modified shelf assembly was as level as possible, greatly reduced the observed errors from the testing trials, improving the quality of data collected in the process. Lastly, for this test configuration, the modified shelf assembly was located ~2.78" above the top face of the beam under no load conditions, necessitating the use of the 2-3" measuring rod on the Fowler Depth Micrometer.

In the experimental configuration as shown in the above figures, the necessary constants for generation of the Beam Theory model could be determined. All of the unknown variables from Beam Theory Equations 41-48 for this square beam were measured according to the diagram depicted in Figure 45 (also from Chapter III). These variables are tabulated in Table 7 below. The applied load P was determined during testing and is the average load over time for all testing trials conducted with this square beam. Likewise, the R_1 and R_2 reactions and k_1 and k_2 constants were determined by simply substituting the appropriate variables for Equations 41, 42, 45 and 46 and solving.

Table 7: *Square Beam 3-Point Bending Beam Theory Constants*

Square Beam 3-Point Bending Beam Theory Constants				
a	2.0313	±	0.0625	in
b	10.00	±	0.0625	in
c	10.00	±	0.0625	in
d	2.0313	±	0.0625	in
e	12.0313	±	0.0625	in
g	22.0313	±	0.0625	in
P	150.09	±	0.112	lb
R_1	75.05	±	0.336	lb
R_2	75.05	±	0.336	lb
k_1	-3.752E+03	±	49.210	lb-in^2
k_2	7.622E+03	±	177.712	lb-in^3

I-Beam Cross-Section

The second test specimen chosen for this experiment was a thin-walled I-beam composed of Al 6063-T5 metal. From the supplier, this beam was rated as having beam caps of thickness 0.055 ± 0.008" and width 1.5 ± 0.024" [34]. Additionally, the overall height of the cross-section was listed as 2.110" (with no tolerance given) while the beam length was rated as 36" (again with a length tolerance designation of 'plus') [34]. Verifying measurements were again taken on the acquired beam, and the measurements for the wall thickness and cross-section height were within the provided tolerance ratings. The length measurement, however, was outside of the provided tolerance at a length of 35.875". Knowing the true dimensions of the I-beam, all necessary beam cross-sectional properties could be calculated in a manner similar to those calculated for the square cross-section beam. Along with Tables 8 and 9, Figure 51 details these calculated cross-sectional properties as well as the mechanical properties for 6063-T5 aluminum (as obtained from [35]). This beam was chosen as a test specimen due to the I-beam cross-section. Since the composite spars utilized by the DML are typically thin-walled I-beams, establishing a baseline for SolidWorks FEA solutions on an isotropic thin-walled I-beam is a desirable and logical increase in geometrical complexity compared to the square beam cross-section baseline.
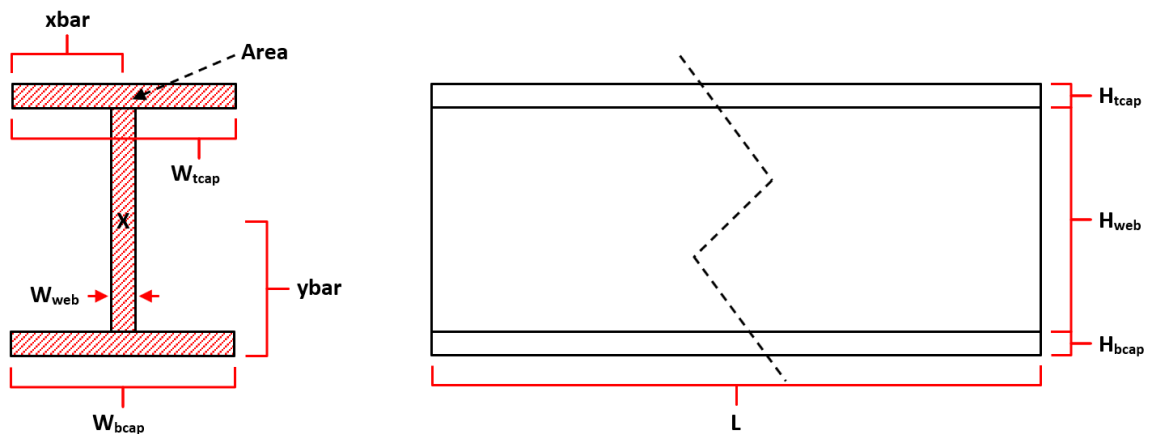
Figure 51: *I-Beam Dimensions and Cross-Sectional Properties Reference*

Table 8: *I-Beam Dimensions and Cross-Sectional Properties*

I-Beam Dimensions and Cross-Sectional Properties			
L	35.875	±	0.0156	in
W_{bcap}	1.485	±	5.00E-04	in
H_{bcap}	0.055	±	5.00E-04	in
W_{tcap}	1.485	±	5.00E-04	in
H_{tcap}	0.056	±	5.00E-04	in
W_{web}	0.048	±	5.00E-04	in
H_{web}	1.997	±	8.66E-04	in
H_{TOTAL}	2.108	±	5.00E-04	in
Area	0.261	±	1.43E-03	in^2
ybar	1.060	±	3.90E-03	in
xbar	0.743	±	1.88E-04	in
I_{zz}	0.205	±	1.07E-03	in^4

Table 9: *Aluminum 6063-T5 Mechanical Properties [35]*

Aluminum 6063-T5 Mechanical Properties		
E	10000	ksi
G	3740	ksi
ν	0.33	
$\sigma_{yld._T}$	21	ksi
$\sigma_{Ult._T}$	27	ksi
$\tau_{Ult.}$	17	ksi

The lengthwise centerlines along the width and height faces were marked on this I-beam using a fine-point Sharpie just as was done for the square beam. Each two-inch increment along the I-beam's length was also similarly marked (keeping the same position convention of 0" starting at the left of the beam when in the Vernier Structures and Materials Tester). Four locations along the beam's length on the upper and lower faces were again identified for placement of strain gages to measure bending strain. Another location was identified on the side faces for strain gage placement to measure transverse shear strain. These gage locations were again placed at odd distance increments from the left end of the beam to avoid interfering with

deflection measurements (with the exception, again, of the gage placed at the beam's length midpoint). Further information regarding strain gage configurations on this I-beam can be found in the Strain Gage Configurations sub-section.

Once the I-beam was appropriately marked and all strain gages satisfactorily bonded to the beam at the designated locations, this beam was placed in the Vernier Structures and Materials Tester for its 3-point bending test. Figures 52 and 53 display this I-beam specimen in the desired 3-point bending configuration within the structures tester. As was the case in Figures 49 and 50, these figures show that the strain gages connected to the NI cDAQ-9185 are those to be utilized for measuring bending strain. In Figure 52, the shear strain bridge configuration for this I-beam specimen is indicated by the white circle (unfortunately obscured by the vertical 80/20 member). This shear configuration is the same as can be observed on the square beam in Figure 49. Lastly, for this test configuration, the modified shelf assembly was located ~1.49" above the top face of the I-beam under no load conditions, necessitating the use of the 1-2" measuring rod on the Fowler Depth Micrometer.
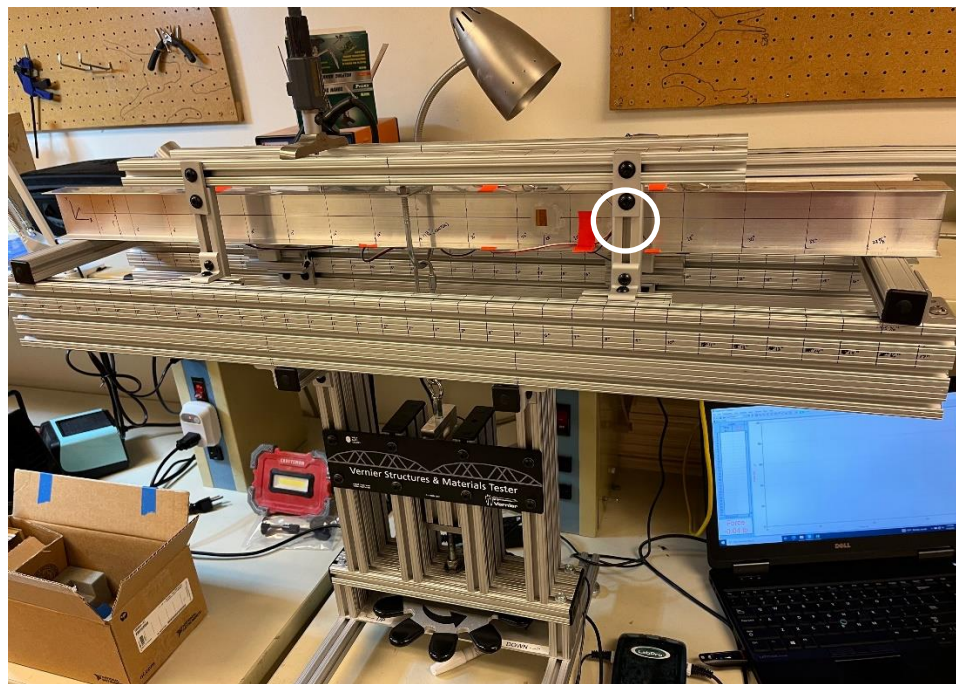
Figure 52: *I-Beam 3-Point Bending Configuration (pt. 1)*
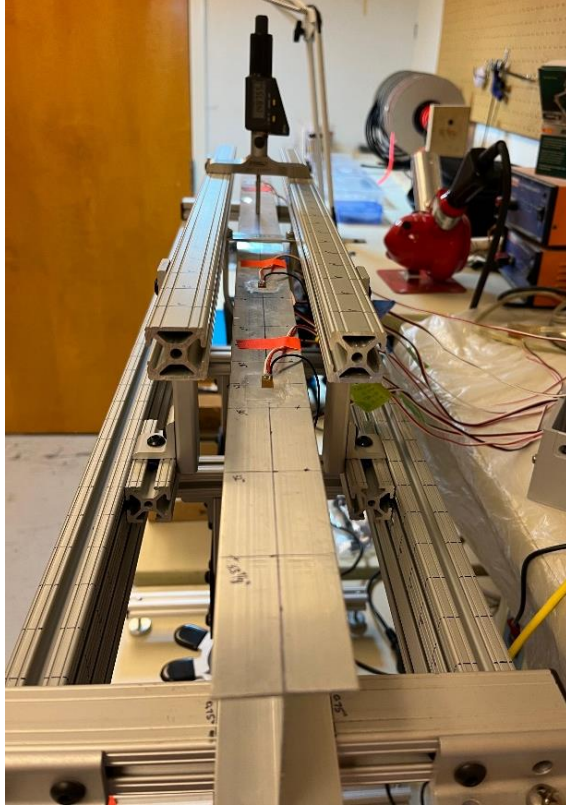
Figure 53: *I-Beam 3-Point Bending Configuration (pt. 2)*

Table 10: *I-Beam 3-Point Bending Beam Theory Constants*

I-Beam 3-Point Bending Beam Theory Constants				
a	1.969	±	0.0625	in
b	15.969	±	0.0625	in
c	15.969	±	0.0625	in
d	1.969	±	0.0625	in
e	17.938	±	0.0625	in
g	33.906	±	0.0625	in
P	149.96	±	0.112	lb
R_1	74.98	±	0.215	lb
R_2	74.98	±	0.215	lb
k_1	-9.560E+03	±	78.711	lb-in^2
k_2	1.882E+04	±	498.975	lb-in^3

Similar to the square beam, the 3-point bending Beam Theory model constants for Equations 41-48 were obtained from this testing configuration for the I-beam. Recalling again Figure 45, the necessary constants were measured according to the diagram depicted in this figure. Table 10 has all of these Beam Theory constants tabulated. The applied load P was again determined by taking the average load over time for all testing trials conducted with this I-beam. Likewise, reactions R_1 and R_2 along with constants k_1 and k_2 were again determined by substituting the appropriate variables into Equations 41, 42, 45, and 46.

Strain Gage Configurations

As can be seen in Figures 49-50 and 52-53, both test specimens were instrumented with strain gages such that both bending strain and transverse shear strain could be measured during the 3-point bending tests. Overall, three strain gage bridge types were utilized on both of these beams: half-bridge type I, half-bridge type II, and a shear half bridge [19], [23]. Figure 54 shows how these gages were arranged on both test specimens as well as each gage type, where dimensions in parentheses are for the I-beam. From Beam Theory, the resulting bending strain curve should resemble a pyramid, and placement of the type I and type II half bridges along these beams was intended to capture bending strain along the length such that the resulting data could be compared to this expected strain trend. These bending strain gage configurations were placed as closely as possible to each beam's horizontal centroid location. Additionally, from Beam Theory, everywhere along the beam length between the supports (apart from directly in line with the applied load or the reactions) has a constant shear force applied. Therefore, the shear strain curve along the beam height is constant in this region on these beams. Since maximum shear stress is of primary concern for the composite I-beams (and due to the small size of these beams), only one shear strain gage sight was applied to each beam. This gage configuration was placed as closely as possible to each beam's vertical centroid location in order to best capture the maximum shear strain experienced by the beams during bending.

75
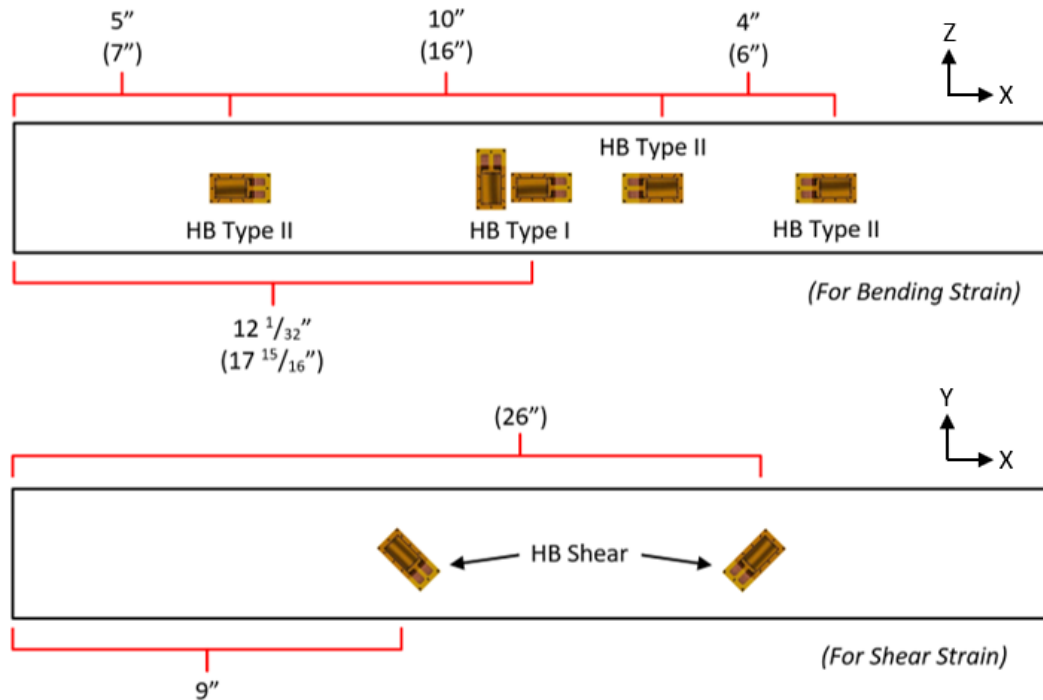
Figure 54: *Strain Gage Types and Locations for Both Beam Test Specimens*

Determination of the appropriate gage configurations for capturing bending strain data was relatively straightforward. Since the spanwise direction of the beam will either stretch or compress during pure bending (depending on vertical location relative to the centroid of the beam), bending strain must be measured in the spanwise direction [23]. Due to this fact, the gage grids must be oriented as shown in the upper portion of Figure 54. Because the load U-bolt is located on the upper surface of the beams at the spanwise midpoint, the type I half-bridge was utilized so that both gages in this configuration could be placed on the bottom surface of the beams to avoid interference. This allowed for the maximum bending strain in the beams to be measured. The remaining type II half-bridges have one strain gage on the upper surface and one on the lower surface on each beam. For either configuration, the strain gage utilized was a Micro-Measurements CEA-06-240UZA-120 gage [36]. In terms of bridge type, the half-bridge configuration was chosen because the half-bridge has satisfactory bridge sensitivity while requiring fewer gages than a full-bridge configuration [23]. This is desirable largely due to the

76

fact that the beams being tested are small and, therefore, do not have much space for multiple gages to be placed next to each other (as is also typically the case for the composite I-beam spars constructed at the DML). General wiring diagrams for these half-bridge configurations are found in the Appendix, Section A. These wiring schemes were based on the half-bridge wiring diagrams presented in [37].

Unlike the bending strain gage layout, determination of the proper shear strain gage configuration was more tedious. In fact, determining the proper gage arrangement to measure shear strain constituted a large portion of research and testing for this experiment. As discussed in the literature review, there are two primary gage types used for measuring shear strain. Initially a 0º-45º-90º rectangular rosette gage was utilized for this task. A Micro-Measurements CEA-06-120CZ-120 rosette gage was bonded to the square beam, as Figure 55 shows, and testing was performed to ensure the gage was operating correctly. This rosette was wired in a quarter-bridge type I configuration with each gage grid on the rosette wired to a precision dummy 120 Ω resistor. For testing of this gage, the square beam was loaded to a set load and the resulting rosette strains were pulled from LabVIEW into Equation 40 to obtain the shear strain measured by the gage. This measured value was then compared to the Beam Theory shear strain solution for that location on the beam under the same loading condition. Almost immediately, this gage presented issues. When unloaded, the two diagonal gages registered that they were reading a load of up to 10 με different from the middle gage grid. More significant was the fact that all three grids, when
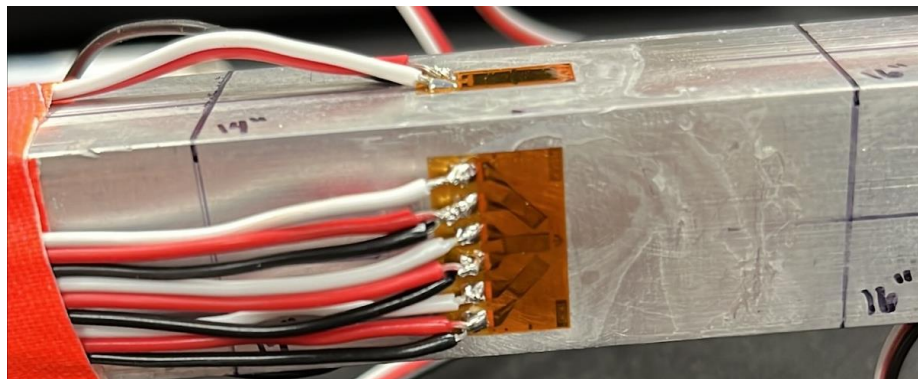
Figure 55: *CEA-06-120CZ-120 Rectangular Rosette (Shear Strain Attempt #1)*

77

unloaded, registered a measured strain signal that would slowly oscillate between ± 30 $\mu\varepsilon$. At first, it appeared that this was simply noise in the instrumentation that would be less influential as the measured strain signal grew under load. Unfortunately, this turned out not to be true. Under load, sometimes the measured strains from the grids would not change at all from the no load condition while other times, these strains would change, but the resulting shear strain was not even reasonably close to Beam Theory estimates. Moreover, after unloading the beam from a test, the rosette gage would not return to its originally calibrated no load condition but would register a significant strain reading as if it were still under load.

Attempts at diagnosing the cause of this issue were unsuccessful. All of the grid resistances were within acceptable tolerances for this particular rosette, and cold solder connections or incorrect wiring connections to the dummy resistors and NI-9237 were ruled out via continuity checks. Further research on rosettes offered a potential cause. Technical Note 515 from Vishay discusses that a major disadvantage of using a rosette like the one in Figure 55 is its size [38]. Essentially, if the surface the rosette is bonded to experiences a large strain gradient and that rosette covers a considerable portion of that surface, then none of the grids on the rosette will be measuring the same local strain field, thus contributing to large measurement errors [38]. From Beam Theory, the shear strain curve for this square beam does experience a significant strain gradient between the beam centroid and the upper/lower surfaces of the beam. In Figure 55, the rosette can be observed to be covering nearly the entirety of the side face of the beam. Thus, it is indeed plausible that the size of the rosette was the cause of the problem.

According to [38], the solution was to utilize a stacked rosette where strain gradients are known to be large due to its smaller size as well as because the centers of all three gage grids are stacked on top of each other to further assist in ensuring measurement of the same local strain field. An Omega SGD-2/350-RY51 tri-axial stacked rosette was acquired and bonded to the square beam (see Figure 56). This rosette was wired in a quarter-bridge type II configuration, utilizing another stacked rosette bonded to an aluminum plate as the 'dummy' resistor. The same
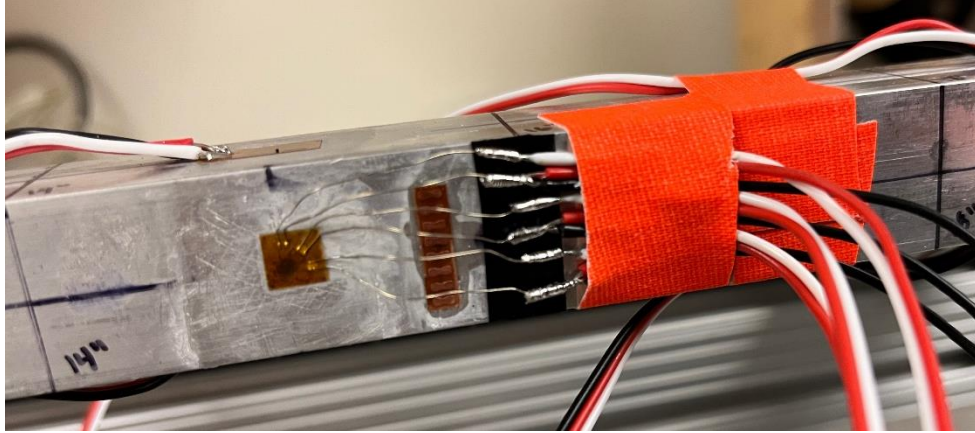
Figure 56: *SGD-2/350-RY51 Tri-Axial Stacked Rosette (Shear Strain Attempt #2)*

testing performed on the rectangular rosette was repeated. Unfortunately, the same measurement problems occurred. While the no load strain oscillations were smaller, the amplitude of oscillation was still not approximating zero strain. Under load, however, this rosette did obtain shear strains closer to Beam Theory estimates, but successive measurements were not consistent. Further issues with loss of calibration also plagued this gage, with instances causing the gage to measure shear strains approximating 10 psi when Beam Theory estimated a maximum shear stress of 3.25 psi for the applied load on the system. Checks of the gage grid resistances and wiring continuity turned up no anomalies.

Following yet more research into alternative methods of measuring shear strain with strain gages, technical document [23] from Omega offered a solution. Instead of using rosettes, this document recommended using regular axial gages in a half or full-bridge configuration angled at 45º from horizontal [23]. To obtain shear strain, the strain measured from these gages must be multiplied by two. Utilizing the same Micro-Measurements CEA-06-240UZA-120 linear gages used to measure bending strain, a shear strain half-bridge type II configuration was bonded to the square beam and tested similarly to the rosettes. This configuration can be viewed in Figure 57. This shear bridge far exceeded the performance of the rosettes. Measurements were consistently close to Beam Theory estimates for the loading condition, and the gages never lost their calibration nor did they experience the unloaded strain oscillations. This gage configuration was

79

added to both beams for the purpose of measuring shear strain. Despite this successful

implementation of a shear strain gage configuration, measurement of shear strain in this manner

has one distinct disadvantage. As is discussed in [39], axial gages are the most sensitive to

measurement errors due to small angular misalignment of the gage when at 45° angles to a

principal axis. As will be seen later in this chapter, this sensitivity will be a significant contributor

to the overall uncertainty of the shear strain measurements on these metal beams.
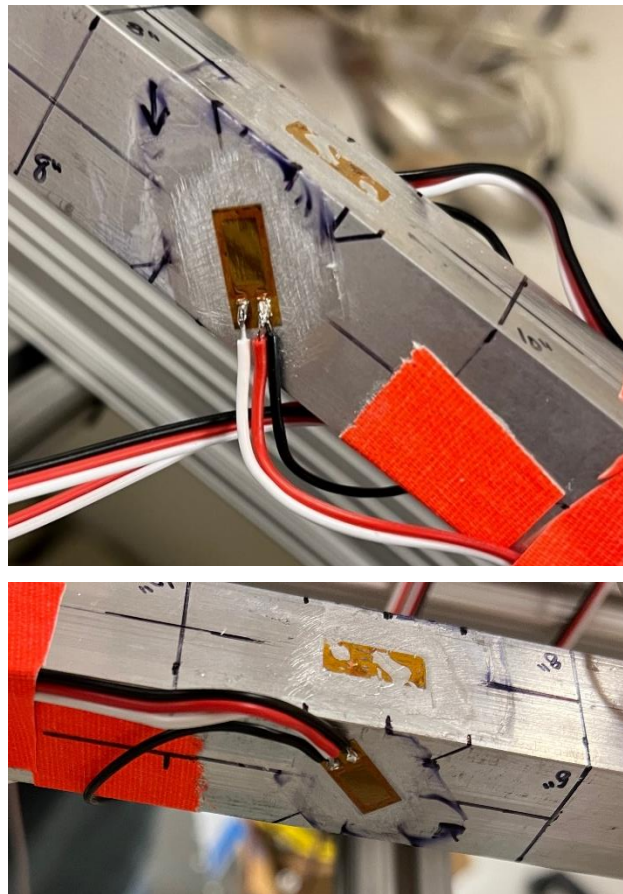
Figure 57: *CEA-06-240UZA-120 Shear Half-Bridge (Shear Strain Success)*

Testing Methodology

This sub-section will cover the steps taken during experimentation to properly prepare the test

specimens as well as those taken to acquire the necessary data from each of the beams. In an

effort shorten the preparation side of the following procedure, some steps will refer to tutorial

videos or other documentation that was used to accomplish the particular task. It is advisable to view all external documentation relating to strain gages before proceeding, especially if not experienced in strain gage use, application, or measurement techniques.

1) Using a fine-point black Sharpie, mark the following on the beams:
   a. Every 2 inches along the beam length
   b. Each beam's length midpoint
   c. The xbar centerline on the top and bottom faces
   d. The ybar centerline on the side faces
   e. All locations and orientation markings for desired strain gage placement

2) Acquire 10 CEA-06-240UZA-120 strain gages (per beam) and the following materials:
   a. Strain gage application tape
   b. Loctite 496 adhesive
   c. 3-wire 24 AWG servo wire (recommended at least 20 feet per beam)
   d. Wire strippers
   e. Tweezers
   f. Soldering iron and solder

3) Prep beam surface, apply strain gages, and connect servo wires according to [40] and Section A of the Appendix.
   a. Surface degreasing can be accomplished with isopropyl alcohol.
   b. Replace catalyst bonding adhesive with Loctite 496 – apply pressure firmly with thumb for 6 minutes before tape removal.
   c. Draft lines can be accomplished through fine-point black Sharpie markings from Step 1d.
   d. Ensure no M-Prep Neutralizer residue remains on the surface – gages WILL NOT bond if residue remains.

4) Replace the stock support rails on the Vernier Structures and Materials Tester with the modified 80/20 shelf assembly as discussed in Chapter III, Section A and shown earlier in this current chapter.
   a. Ensure the shelf assembly is level and at some height between 1" and 6" above the beam's upper surface.

b. Insert the appropriate measuring rod length into the Fowler Depth Micrometer.

5) Move support crossbars such that the inside face is ~2" from each end of the beam.
   a. For the square beam, this should correspond approximately to the 2" and 22" Sharpie markings.
   b. For the I-beam, this should correspond approximately to the 2" and 34" Sharpie markings.

6) Center the load U-bolt at the intersection of each beam's length midpoint and top surface xbar centerline.

7) Plug in the LabPro DAQ, open the LabPro 3 application, and connect to the VSMT Force Sensor.
   a. Set force units to lb.
   b. Slowly rotate crank screw until the load U-bolt is firmly seated on the top surface of the beam but minimal load is registered in the LabPro 3 readout.
   c. Once Step 7b is accomplished, zero the sensor.

8) With the NI cDAQ-9185 unplugged, do the following:
   a. Connect the ethernet cable to the computer containing the LabVIEW strain gage readout program discussed in Chapter III.
   b. Connect all four half-bridge strain gage configurations for bending strain to channels A0-A3 (one per channel) of the cDAQ (see Appendix, Section A).
   c. Plug in the cDAQ and open the 'Bending Normal Strain Readout' LabVIEW VI.

9) Open the DAQ Assistant Block, connect to the cDAQ, and enter appropriate strain gage parameters similar to that shown in Figure 43 for each channel.
   a. Calibrate each channel's half-bridge connection by following the calibration procedure in [29], click OK in lower right corner of the DAQ assistant window when finished.

10) Using the Fowler Depth Micrometer, take initial undeflected depth measurements every 2" along the beam length for each 2" marking between the support crossbars.
   a. For the square beam – start at 4", end at 20".
   b. For the I-beam – start at 6", end at 30".

11) Run the front panel of the LabVIEW strain readout program, ensure four strain measurements appear (set sample rate to 1000 Hz and take 250 samples per time interval).

    a. Ensure that the Write to File button is set to OFF (red) initially before running.

12) Slowly turn the crank screw until a load of 150 lb is achieved.

    a. At this load, record the load over time in LabPro and turn the Write to File button to ON (green) in LabVIEW simultaneously. Allow to run for 30 seconds then stop recording.

    b. Stop running the LabVIEW front panel to successfully generate a strain data output '.txt' file (each file should contain ~188 lines of strain data per channel).

    c. Copy 30 seconds worth of load data from LabPro into an Excel file for future reference.

13) Using the Fowler Depth Micrometer, take final deflected depth measurements every 2" along the beam length for each 2" marking between the support crossbars.

    a. For the square beam – start at 4", end at 20".

    b. For the I-beam – start at 6", end at 30".

    c. Overall beam deflection is determined by taking the difference between Steps 13 and 10.

14) Return the beam to its initial unloaded state and repeat Steps 10-14 two more times.

    a. Once third pass is completed, return beam to initial unloaded state, and continue.

15) Unplug the NI cDAQ-9185 and do the following:

    a. Disconnect the bending strain half-bridges from the cDAQ.

    b. Connect the shear strain half-bridge to channel A0.

    c. Open the 'Shear Strain Readout' LabVIEW VI.

    d. Re-plug in the NI cDAQ and repeat Step 9 for channel A0.

16) Repeat Steps 11 and 12 three times, returning the beam to its unloaded state between passes.

C. SolidWorks FEM Generation

Model generation is an important step for FEM analysis in that it is crucial to replicate the physical system so that the resulting model solution best represents what would and should be expected. This includes modeling the correct geometry, applying the proper mechanical and material properties, and replicating the loading and constraint conditions. Depending on the system to be modeled, the resulting FEM can be as complex or as simple as is deemed necessary. Once a model is sufficiently detailed, further complexity becomes unnecessary and only causes the solving time and required computing power to increase. Insufficient model detail or incorrect aspects of the model, however, can be detrimental to the resulting FEA solution. The sub-sections that follow detail the generation of the Finite Element Models for both beam test specimens.

Square Beam Cross-Section 3D FEM

Before Finite Element Analysis can be performed, the solid model must be created and prepared for analysis. For the square cross-section beam, this was accomplished by first creating a sketch of the cross-section as is shown in Figure 58. To keep continuity with the defined axial directions on the physical model, this sketch was defined on the Right Plane such that the x-axis is parallel to the length of the beam while the y-axis points up and is parallel to the beam's height. Upon ensuring that the sketch was fully defined, the sketch was finished and model generation could continue. The next requirement was to extrude this cross-sectional sketch to the length of the beam as provided in Table 5. This extrusion can be viewed in Figure 59. The final step required for creation of the model was to apply the appropriate material definition to the solid part. Navigating to the Feature Manager Design Tree, right clicking the row labeled 'Material <not specified>', and selecting 'Edit Material' will open a built-in Material Properties library within SolidWorks. Via either the search bar or manually, this library can be utilized to find property files for most common materials.
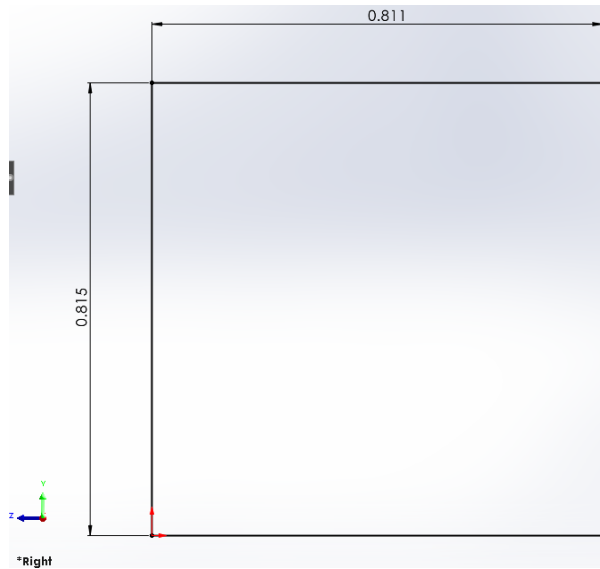
Figure 58: *Square Beam Cross-Section SolidWorks Sketch*
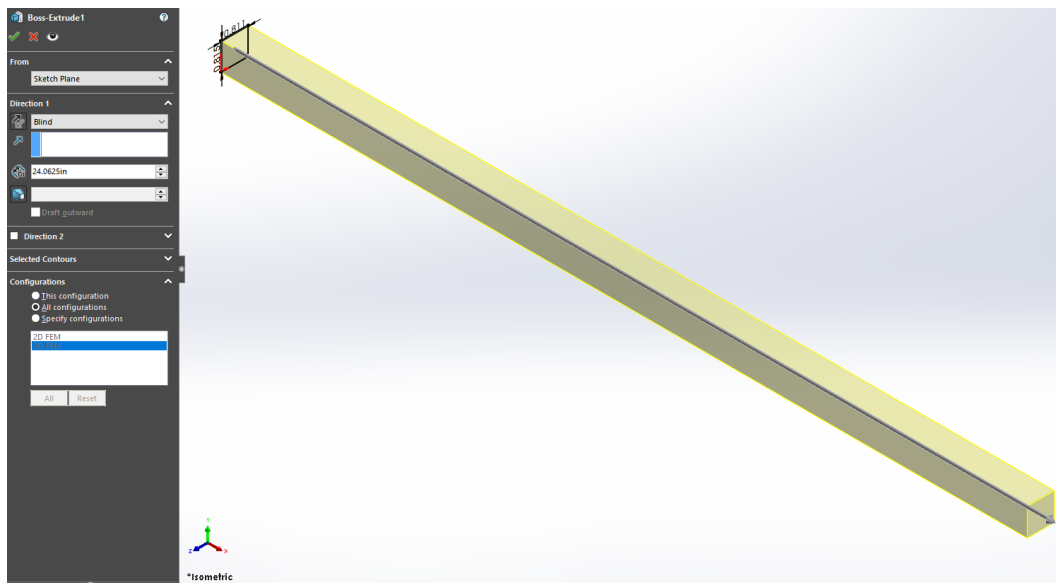
Figure 59: *Square Beam Extrusion for Solid Part Creation*

Fortunately, 6061-T6 Aluminum was included in this library (see Figure 60). No further steps had to be taken apart from ensuring that the properties on file in this library matched those listed in Table 6 (which they did). Clicking 'Apply' in the bottom right corner of the materials window applied the selected material to the solid part. This, in turn, caused the 'Material <not specified>' label to be replaced with a label identifying the material that had been applied.
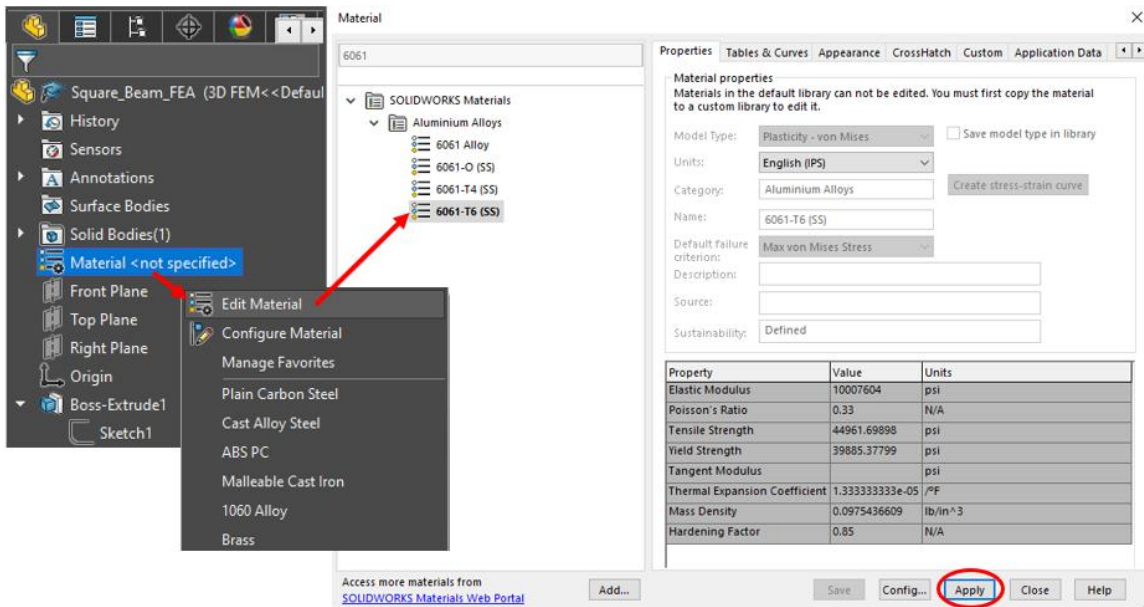
Figure 60: *Procedure for Material Application*

Following completion of the solid part, this virtual beam was prepared for FEA and post

analysis. The model to be generated from this solid part will consider only the beam itself and not

the Vernier Structure from the physical system. As such, markings must be made on this beam for

the application locations of boundary and loading conditions (application of which will be

discussed in a later sub-section). In addition, to alleviate the frustration of selecting multiple

elements and/or nodes across one of the beam faces to acquire necessary deflection or strain data,

further markings should be made at points of interest on the beam for post-analysis data sampling.

Both of the above can be achieved through the use of either the Split Tool or the Split Line Tool.

The Split Tool will separate the original solid part into two or more smaller solid parts at areas of

intersection with the beam (with these intersections generally defined by planes or sketches).

After splitting the body, this tool will then globally fix the split solid parts together, but an edge

will be present at the location of the split. Similarly, the Split Line Tool 'splits' the geometry at

designated intersections with the beam (again denoted by planes or sketches). However, it only

projects a line onto the selected part faces and does not actually split the part at these locations.

For this portion of research, use of the Split Line Tool was the more convenient method.

To utilize the Split Line Tool, desired locations along the solid part first required some type of geometrical entity to intersect one or more faces of the beam at these locations. As mentioned, this can be accomplished in a myriad of ways, such as creating sketches on one or all of the beam faces at the desired location. The chosen geometrical entity here, however, was planes. In total, six plane/part intersections were created, as Figure 61 depicts. Two planes were projected from the Right Plane to locations along the solid part approximating the location of the crossbar supports – dimensions a and g in Table 7. Another plane was projected from the Right Plane to the location of the shear strain gage placement. Two more planes were projected from the Right Plane to the location of the applied load on the beam. From the physical system, the metal strap that spans the load U-Bolt and applies the load to the beam was measured to be 0.75" wide. These two planes bound this width at the beam's length midpoint. In other words, one of the two planes is projected to a location 0.375" before the length midpoint, and the other is projected to a location 0.375" after the length midpoint. The final plane was projected off one of the side faces of the solid part to the location of the beam's measured x-centroid location. Split lines were then added at these plane/part intersections on the appropriate part faces. The load split lines were added to the top face while the boundary condition split lines were added to the bottom
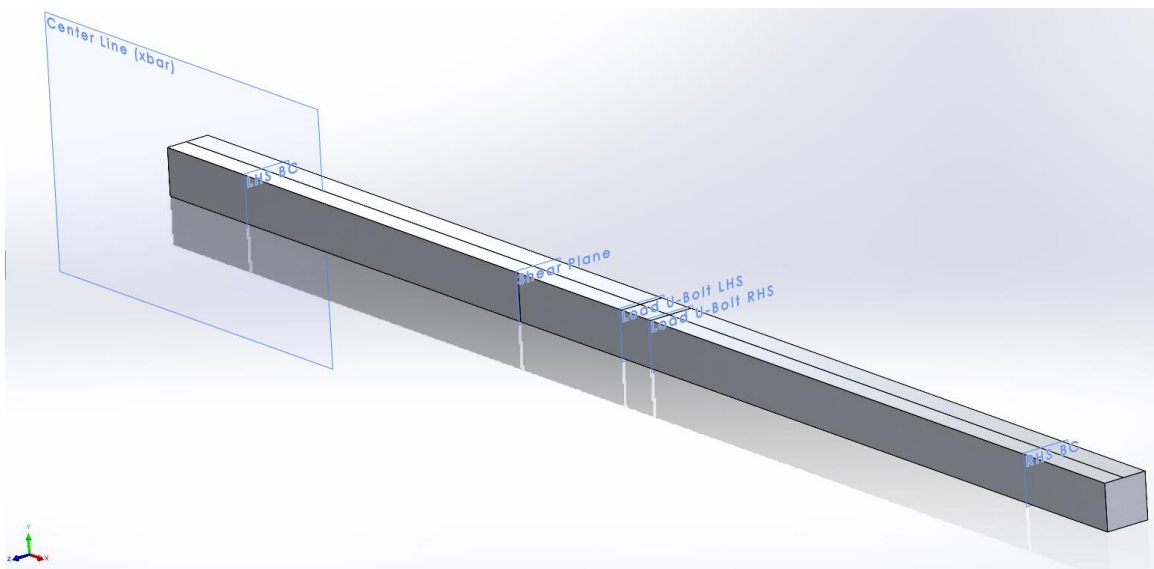
Figure 61: *Square Beam Split Line Intersection Planes*

face. The shear strain split line was added to one of the side faces, and the x-centroid split line was added down the entire length of the beam on both the top and bottom faces. To declutter the model visually, these planes were hidden after the split lines were created.

After this preparation was completed, the final step was to insert the model into the SolidWorks FEA Simulation program so that the actual FEM analysis parameters could be generated. This was done by navigating to the Simulation tab and selecting the 'New Study' option displayed on the far left. A series of study options will appear on the left of the screen. The study type desired for this FEM was 'Static'. The 'Use 2D simplification' checkbox that appears when selecting the 'Static' option was left unchecked. Upon naming the study and clicking the green check mark, a new simulation tab will be generated at the bottom of the screen, and the user will be allowed to access the SolidWorks FEA Simulation space.
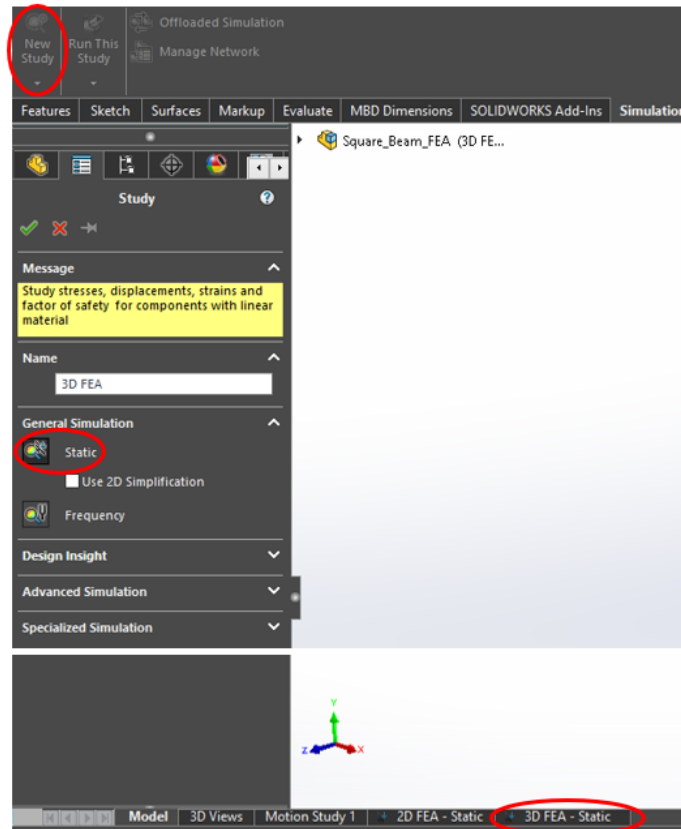
Figure 62: *SolidWorks FEA Study Creation Procedure*

I-Beam Cross-Section 3D FEM

The I-Beam model similarly first required the cross-section sketch to be generated. To maintain axes definitions from the physical system, this sketch was again created on the Right Plane and can be viewed in Figure 63. Once the sketch was fully defined, it was then extruded to the length measured for the beam (indicated in Table 8). This extrusion is depicted in Figure 64. As was the case for the square beam, the final step was to apply the proper material properties. The same process as depicted in Figure 60 applies for this solid part, with the only difference being that the material to be applied was Al 6063-T5, instead of Al 6061-T6. Fortunately, the SolidWorks Material Library contains a material properties file for 6063-T5 Aluminum, though the values listed for Elastic Modulus and Shear Modulus are slightly higher than those properties obtained for this I-beam as they are displayed in Table 9. In addition, the yield and ultimate stresses are not the same. Despite this, the Moduli properties are considered close enough to warrant minimal solution impact. Moreover, this research endeavor is not investigating FEM predictions in the plastic region, so yield and ultimate limits are of no concern.
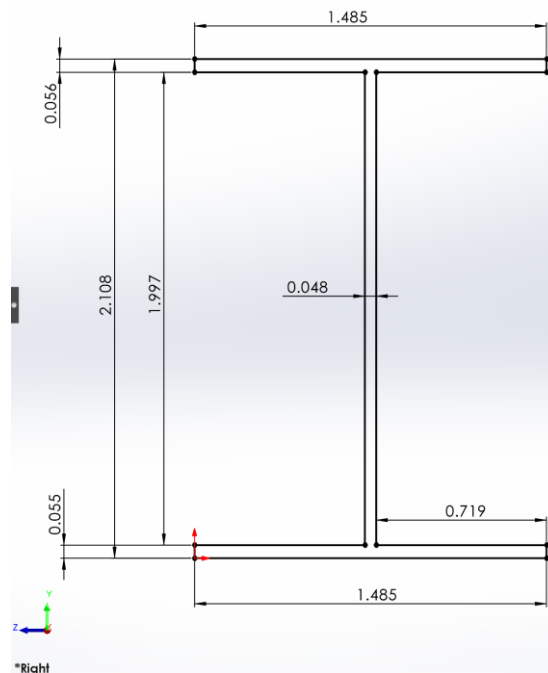
Figure 63: *I-Beam Cross-Section SolidWorks Sketch*
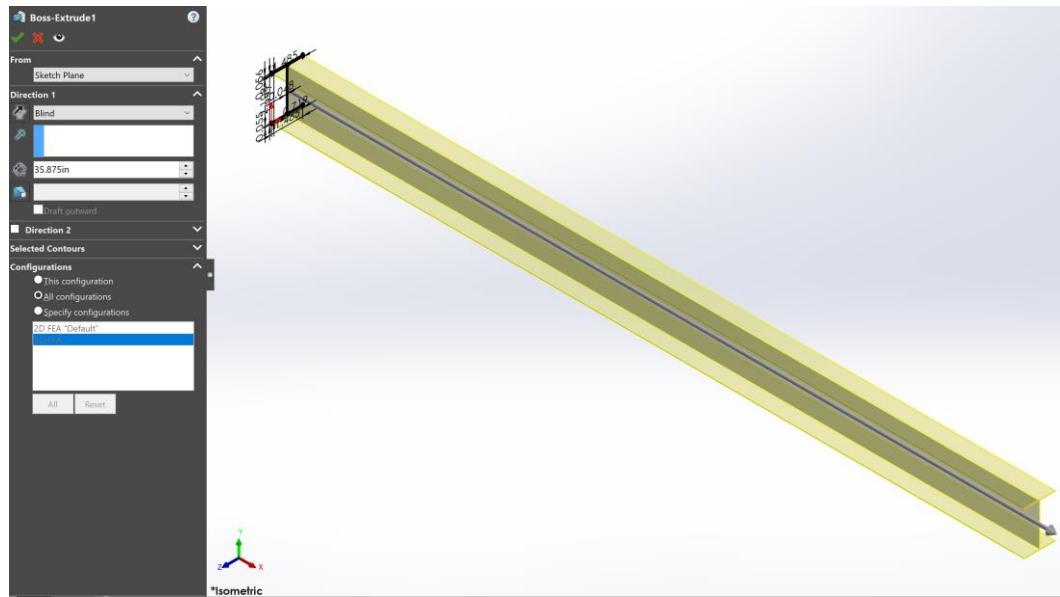
Figure 64: *I-Beam Extrusion for Solid Part Creation*

Final preparation of the I-beam FEA model required the placement of the split line

intersection planes similarly to those on the square beam. Once more, six planes were utilized.

Two of the planes were placed at the approximate locations of the crossbar supports for the

physical system – distances a and g in Table 10. A further two of these planes were positioned to

straddle the beam's length midpoint to approximate the 0.75" width of the metal spanner strap

that spans the load U-bolt and applies the load to the beam. Again, this means that one of these

two planes is positioned 0.375" before the length midpoint while the other is positioned 0.375"

after the midpoint. The fifth plane was placed at the location of the shear strain gage

configuration for this beam, which is 26" from the beam's left end. The sixth and final plane was

positioned at the I-beam's x-centroid location. This plane arrangement can be viewed in Figure

65. For the planes at the supports, the split lines were added to the bottom face of the beam.

Likewise, the applied load planes had their split lines applied to the beam's top face. The shear

plane's split line was applied to one of the I-beam's side faces on the shear web only. As for the

x-centroid plane, its split line was applied across the beam's length on the bottom face only.
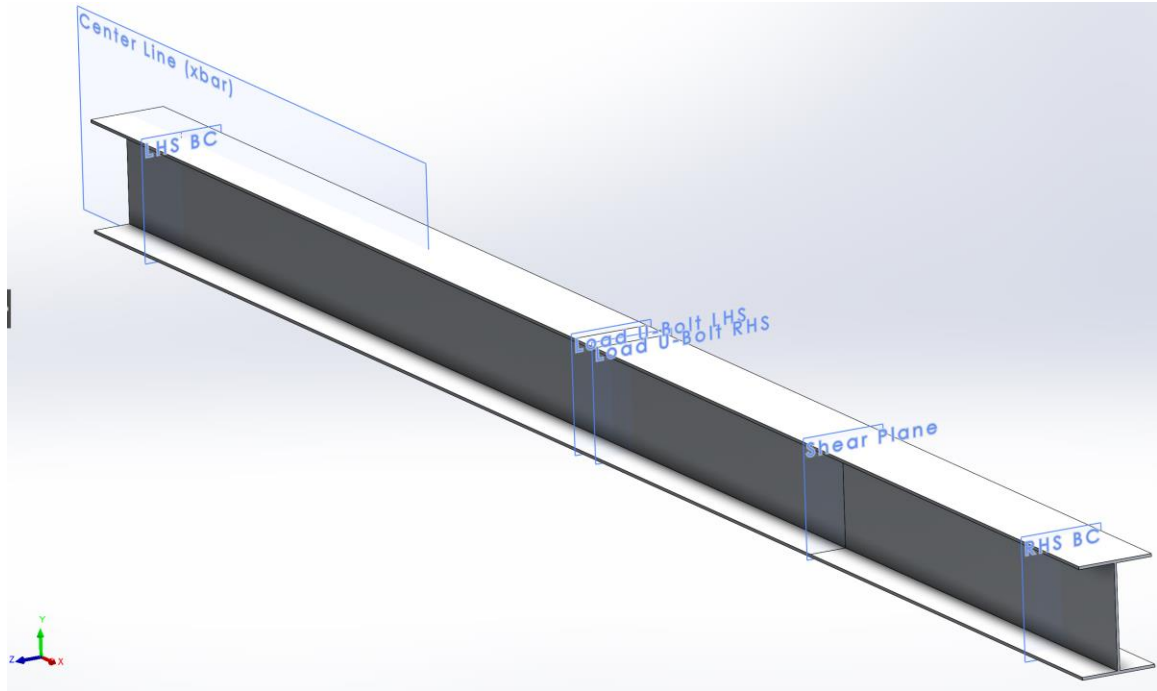
Figure 65: *I-Beam Split Line Intersection Planes*

The completed I-beam model could now be imported into the SolidWorks FEA Simulation

space. The same procedure applies for accessing the simulation program for this task as is

described at the end of the previous sub-section. Reference Figure 62 for a visual reminder of

how to access the FEA simulation tools and be sure to again select 'Static' as the study type and

leave the 'Use 2D simplification' checkbox unchecked. Upon clicking the green arrow, the 3D

FEM study for this I-beam was generated, and this FEM could be accessed through the newly

created simulation tab at the bottom of the SolidWorks screen.

Requirements for 2D FEM Generation

At this point, all discussion relating to FEM generation has focused on the procedures

required to generate a 3D FEA model. It is also necessary, however, to generate 2D FEM

solutions for comparison with the empirical data. Model preparation for creation of a 2D FEA

study in SolidWorks requires additional steps. The first of these is to create the solid part model

as one would for a 3D FEM (as described in either of the previous two sub-sections). Before

generating the simulation study, the 3D solid model must be idealized to an equivalent 2D geometrical representation. Accomplishing this idealization requires utilization of the Surfaces toolkit within SolidWorks. Much of the following discussion borrows from 2D FEM preparation techniques as covered in [41].

Following creation of the base 3D solid model, it is best practice to create separate 2D and 3D FEM configurations of the solid part. This will not only assist in keeping modeling features properly assigned to either the 2D or 3D versions of the beams, but it will also allow multiple FEM configuration studies to be generated off the base SolidWorks part or assembly file. To create separate model configurations, navigate to the Configuration Manager on the left side of the screen. Initially, there will only be one configuration present in the manager named 'Default'. Right clicking on this configuration title and going to properties, the name was changed from 'Default' to '3D FEA'. Once this configuration was re-named, a new configuration was added by right clicking on the configuration parent label at the top of the manager and then clicking 'Add Configuration'. This new configuration was named '2D FEA'. This process of adding a new configuration is shown in Figure 66.
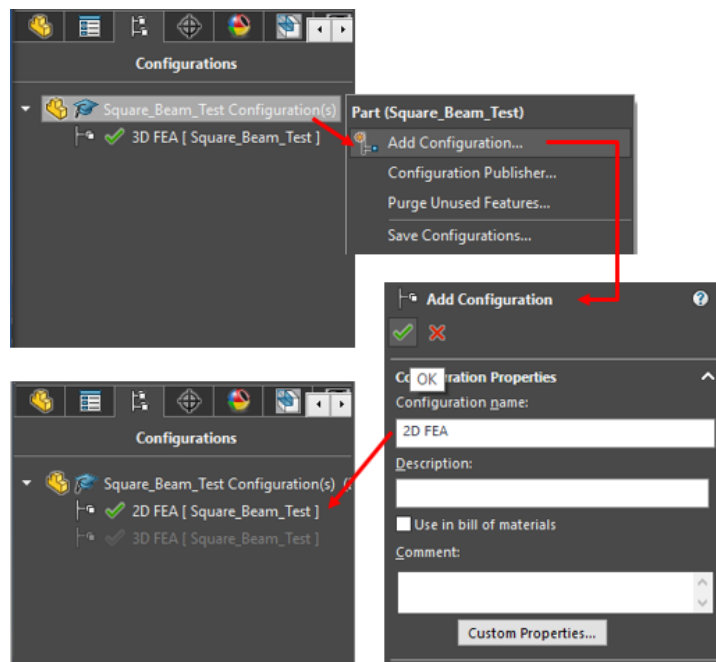
Figure 66: *Addition of Model Configurations Procedure*

To switch between configurations, one must double click on the desired configuration from the list in the Configuration Manager. Conversely, the configuration currently in use for the model is indicated by whichever option is not grayed out in the list. It is worth noting here that FEM studies generated from configurations other than the one currently selected in this manager will not work. In this case, a 2D FEM and 3D FEM study were generated using the 2D FEA and 3D FEA configurations respectively. If the 2D FEA configuration is enabled and the user attempts to open the 3D FEM study, SolidWorks will register an error and essentially claim the FEA model is broken. Only when the 3D FEA configuration is enabled will the 3D FEM study work properly.

The next step is to assign any sketches, solid features, or reference geometry to their respective configurations. As discussed in the previous two sub-sections, since the base beam models were already set up for 3D FEA, the 3D FEA configuration was selected first. To assign a modeling item to particular configurations, navigate to the item, right click on it, and select the 'Configure Feature' option. The resulting window will display all configurations of the base model along with a column of check boxes next to each configuration listed. Selecting the checkbox for a configuration will suppress the modeling item for that particular configuration, thereby not including that modeling item in that configuration. See Figure 67 for reference. For the 3D FEA configuration, all split lines originally added to the 3D model were suppressed for the 2D FEA configuration option. All of the reference geometry planes inserted into the model as well as the feature extrusion remained unsuppressed for both configurations. When this was complete, the 2D FEA configuration was enabled and the 2D FEM could be generated. The following discussion will refer only to the process required to generate the 2D I-beam FEM since idealizing its geometry is more involved. Idealizing the square beam to 2D follows a similar process.
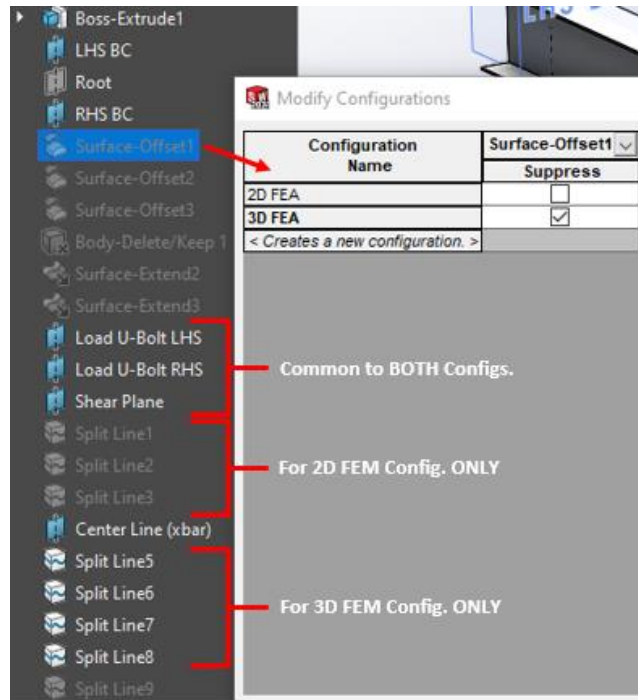
Figure 67: *Feature Configuration Management*

The first step for 2D geometry simplification is to replace the solid body of the beam with planar surfaces. This was accomplished through the use of the 'Offset Surface' tool. On the I-beam, visually divide it into three solid components – the bottom spar cap, the shear web, and the top spar cap. Each of these solids must be replaced with a representative 2D surface. Utilizing the 'Offset Surface' tool three times and selecting the bottom face, a side face, and the top face, respectively, for each of the three solid components, a surface could be projected to the middle thicknesses of each of these solids. Removal of the solid body altogether, following the creation of these surfaces, required the use of the 'Delete/Keep Body' tool (which is found in the Analysis Preparation tab). For this tool, the 'Delete Bodies' option was enabled, and the original feature extrusion of the beam cross-section sketch was selected. This feature was then removed from the 2D FEA configuration, leaving only the offset surfaces as shown on the left of Figure 68. Inspection of these surfaces revealed a gap between the cap and web surfaces where they do not connect. To remedy this issue, the 'Extend Surface' tool was utilized. Using this tool, either the top or bottom edges of the shear web could be selected. Choosing the 'Up to Surface' option and

94

selecting the corresponding spar cap surface will cause the shear web surface to extend until the gap was closed. The end result is shown on the right of Figure 68. Coincidentally, Figure 67 displays the features and tools mentioned here in the order they were implemented and discussed for the I-beam 2D idealization.
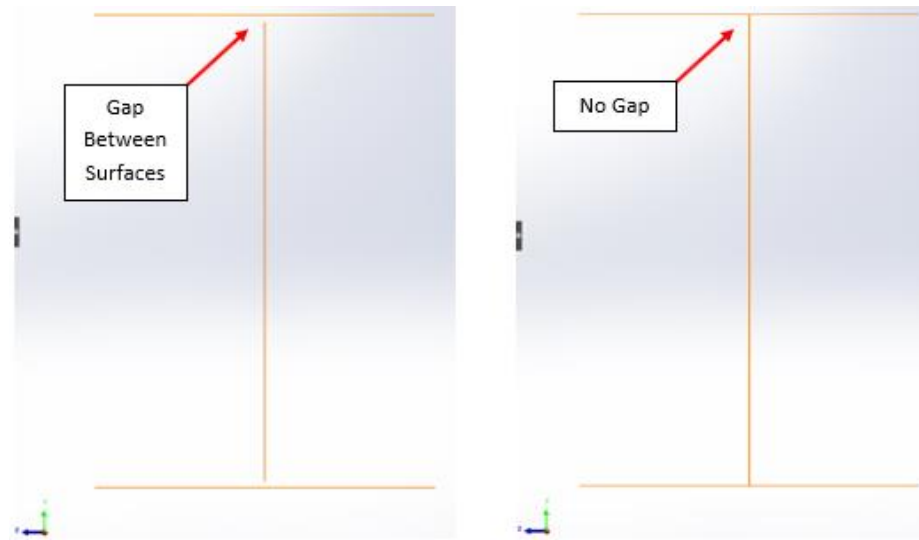
Figure 68: *Surface Offset and Extension for I-Beam 2D Idealization*

Once all of the surfaces were connected, the same split lines were added to the 2D I-beam model that were added to the original 3D model (and the same is true for the 2D square beam model). This concluded the idealization process required to generate the 2D FEM of the beam test specimens. However, one final step must be taken after the 2D FEA simulation study is created. Opening the 2D study and navigating to the left of the screen, at the top of the FEM options list displayed will be a short component list containing all three 2D surfaces. Each of these surfaces must have a thickness and an element solving method (either thin, thick, or composite) assigned to it. Right clicking on each surface in the list and selecting the 'Edit Definition' option allowed these assignments to be made. For these 2D FEM studies, the thin element solving method was selected for all surfaces (as is shown in Figure 69) due to the beam length to thickness ratios exceeding 20 [42]. Following each assignment, an icon appeared to the left of the surface listing with a green checkmark, indicating it was fully defined for analysis.
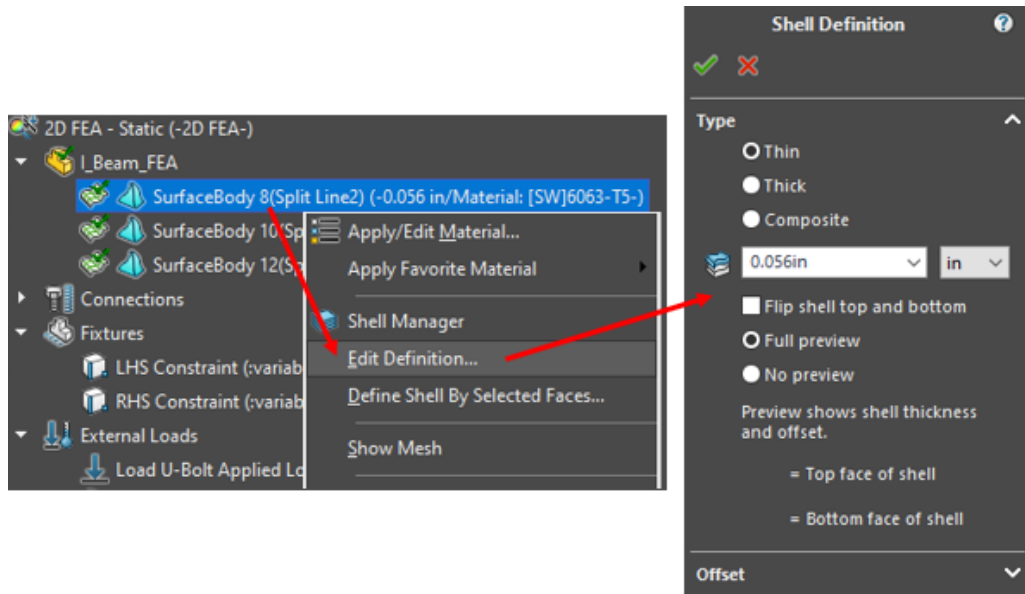
Figure 69: *Bottom Spar Cap Surface Shell Element Definition*

Boundary and Load Condition Implementation

Assuming the geometry and material properties of the FEM model correctly represent the

physical system, the key components that determine if the overall model is good or bad is the

application of the loading and boundary conditions. As stated previously, the goal of FEM

generation is to replicate the physical system virtually as best as possible. This is especially true

for boundary condition implementation. By reducing the number of idealizing assumptions and

unknown contributors to the boundary conditions on the system, the resulting model accuracy

will be much improved, and it will better represent reality.

The following discussion will explore the process taken to arrive at the correct model

boundary conditions as well as highlight an example of an incorrect boundary condition

candidate. In order to properly model the boundary conditions for FEA, one must first gain a

better understanding of the forces that resist the movement of the beam at the contact interface

between the beam and the 80/20 crossbar supports from the structures tester. When the beam is

unloaded and resting atop the crossbars, there will be a distributed reaction force applied to the

beam by the supports parallel to the y-axis. This distributed reaction counteracts vertical

movement of the beam at this interface. Additionally, there will be some frictional force in both

the x-axis and z-axis directions at this contact interface that will resist the beam's sliding in either

the x or z directions along the crossbar. When unloaded, these forces will have the entirety of the

contact area between the beam's lower face and the upper face of the crossbar to resist beam

movement. The same cannot be said when the beam begins deflecting due to an applied load.

Under load, the beam will begin to pivot along one of the corners of the crossbar, effectively

reducing the load path between the beam and the support to a singular point, as Figure 70

demonstrates. Since the corners on the 80/20 crossbars are rounded, this singular point of contact

will occur at the point of tangency between the beam's lower surface and the rounded edge of the

support. The resulting vertical and horizontal forces that resist the beam's movement will be a

combination of the normal force exerted on the beam perpendicular to the point of tangency and

the frictional force parallel to the point of tangency. The frictional force in the z-axis will remain

the same, just applied in the z-direction through the point of tangency.
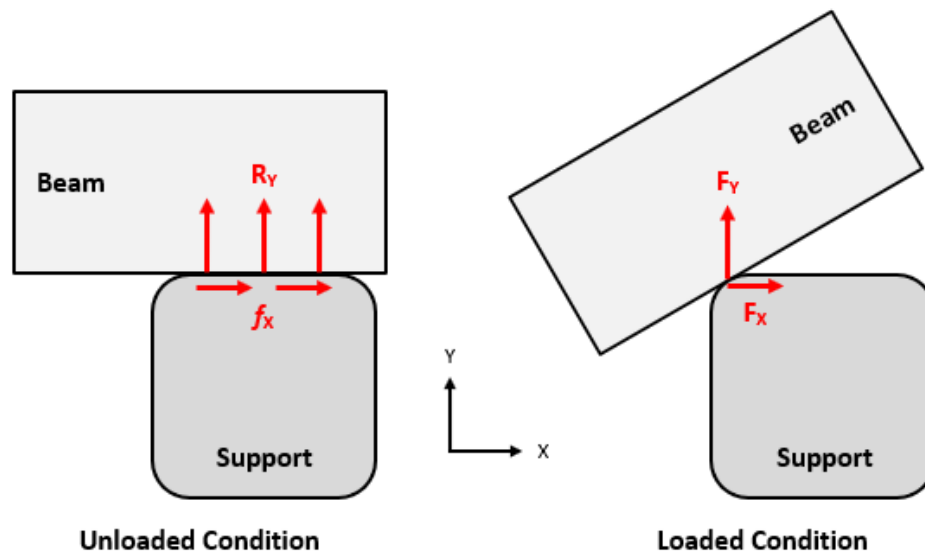
Figure 70: *Boundary Condition Transition of Physical System*

This knowledge of the boundary conditions' transition under an applied load is ultimately very beneficial. For the simple FEA models that focus only on modeling the beam, the boundary conditions can be assumed to be applied along a line spanning the thickness of the lower face of the beam. In this manner, two split lines can be positioned at both lengthwise locations of the supports from the physical system, and the appropriate boundary conditions can be applied directly to those lines. These split lines were already introduced into the FEA models so no additional split lines were required. Technically, Figure 70 implies that there is a full (x,y,z) boundary condition fixing the line of contact on the beam at both supports. Trial and error of various boundary condition permutations revealed that direct application of such a boundary condition at both supports did not yield the proper beam behavior, as is depicted in Figure 71. As mentioned elsewhere, the Beam Theory solutions for deflections and stresses should well approximate the actual response of the physical system for these isotropic metal beams. Knowing this, resulting FEA solution curves from applied candidate boundary conditions were compared to their Beam Theory counterparts. If the trend of the curves and general magnitude along the beam length for each curve were near equivalent, the boundary condition was considered to be correct.
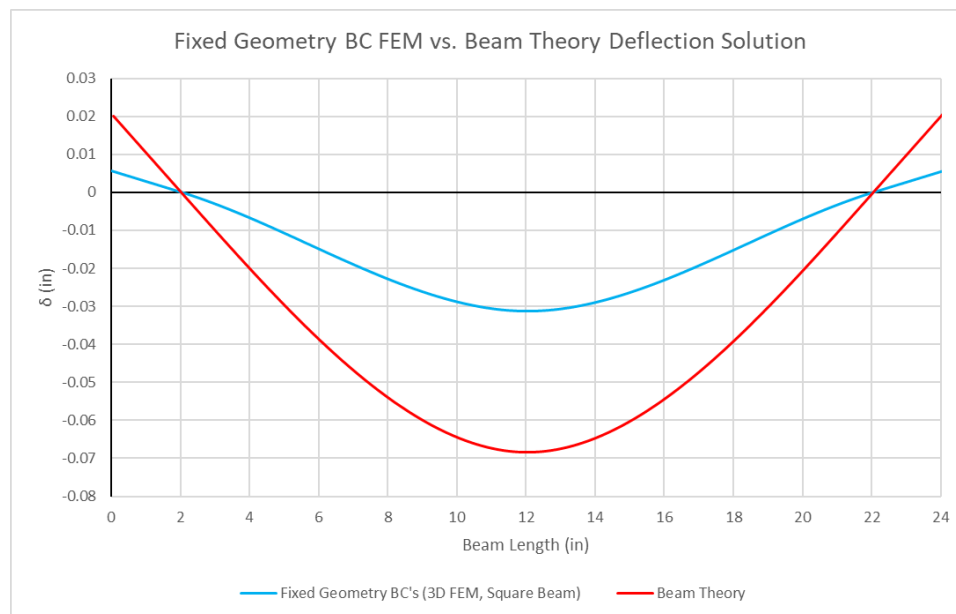
Figure 71: *Incorrect Boundary Condition FEM Compared to Beam Theory Solution*

98

As is evident in Figure 71, application of the 'Fixed Geometry' boundary condition at both

support split lines did not yield the proper beam deflection trends or magnitudes when compared

to Beam Theory estimates for the square cross-section beam. According to [49], 'Fixed

Geometry' constrains full translation as well as full rotation. This is not desirable for replication

of 3-point bending as the beam should be free to rotate. It is worth noting here that the 3D FEM

for the square cross-section beam was utilized for all boundary condition testing. Since it is the

simplest cross-section of the two beams, its deflection and stress curves should closely match the

trends and magnitudes of Beam Theory when the correct combination of boundary conditions are

applied to the model.

Following further investigation into various boundary condition combinations, the proper

implementation was eventually determined. For the purposes of replicating beam behavior under

the scenario of three-point bending, only one of the support split lines (in this case the right

support) can have a full translational boundary condition. The left-hand side support split line, on

the other hand, only requires being fixed in the y and z-directions. This constraint scheme

emulates one support being fixed by a static hinge while the other is placed on a frictionless roller
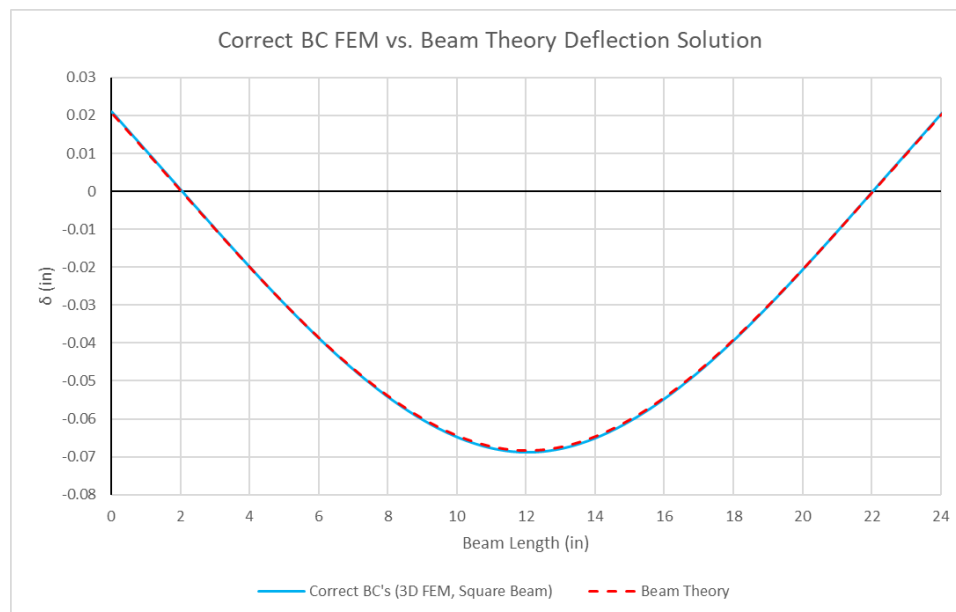
Figure 72: *Correct Boundary Condition FEM Compared to Beam Theory Solution*
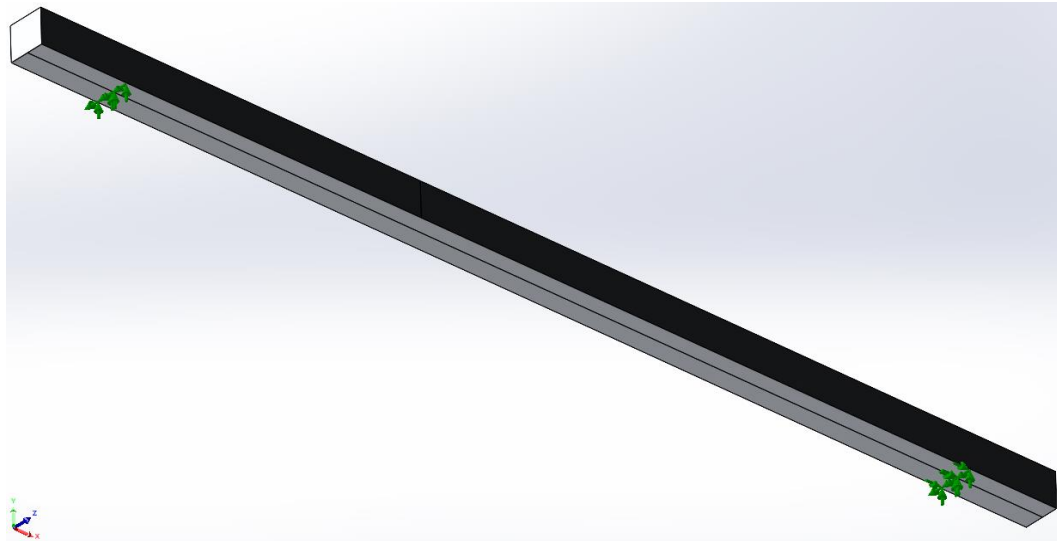
Figure 73: *Correct Model Boundary Conditions Applied to the Supports*

that is only capable of moving in the x-axis in response to applied bending loads. Figures 72 and

73 show the resulting beam deflection curve compared to Beam Theory as well as these boundary

conditions implemented on the square beam model. The bending stress curves matched equally

well, further confirming this combination as the proper implementation of model boundary

conditions. Further testing also confirmed that switching which support had the static hinge

boundary condition (adding the full translational constraint to the left support and moving the

roller constraint to the right support) had no effect on the resulting FEM curves as compared to

their corresponding Beam Theory Solutions.

Implementation of this correct boundary condition combination will now be discussed. The

boundary conditions as shown in Figure 73 required the utilization of the 'Advanced Fixtures'

tool. This tool allows the user more freedom with implementation of more complex model

constraint configurations by allowing for constraint application on a per axis basis as well as

selecting if the constraint type is rotational or translational [49]. Upon selecting this tool, for the

static hinge constraint, the only task required was to select the split lines representing the location
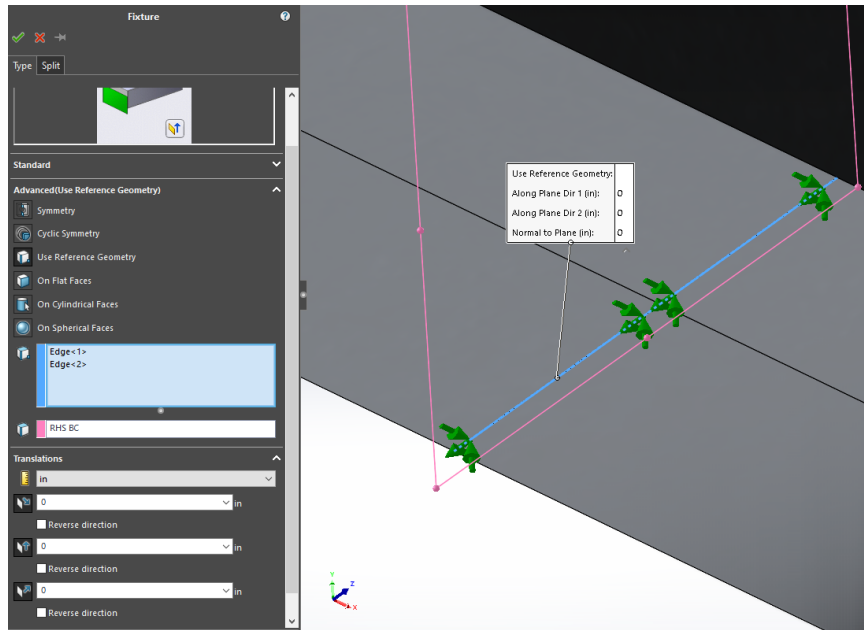
Figure 74: *Application of 'Advanced Fixture' X, Y, and Z Constraint to Right Support Split Line*
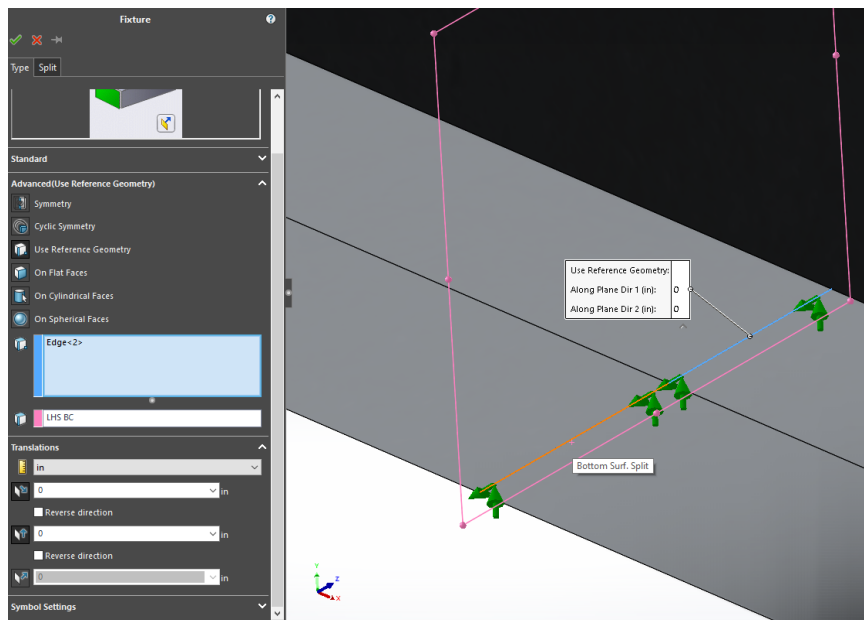
Figure 75: *Application of 'Advanced Fixture' Y and Z Constraint to Left Support Split Line*

of the right-hand side crossbar support as depicted in Figure 74 as well as a reference geometry

for support orientation. For the static hinge, full translational restraint was desired, so all three

translational directions were selected and the allowable translation for each direction was entered

as 0". For the frictionless roller restraint on the left-hand side of the beam, only translational

restraints in the y and z axes were required as the beam is free to deform in the x-axis as it deflects under load. Similar to Figure 74, a reference geometry was selected for constraint orientation, and a 0" allowable translation constraint was enforced in only the y and z directions (see Figure 75). Note that, for both Figures 74 and 75, the direction of the axial constraints using this tool are dependent on the reference geometry chosen. Therefore, the fixture directions required to achieve the proper boundary conditions may differ from the selections shown in these figures for a different reference geometry.

This boundary condition scheme was successfully implemented on three of the four FEA models, yielding similar results to Beam Theory estimates. Interestingly, the 2D FEM for the square cross-section beam did not yield comparable results under this scheme but instead exhibited beam behavior again similar to that shown in Figure 71. Luckily, the solution was rather simple. Instead of utilizing the 'Advanced Fixtures' tool as described above, both support split lines were configured with advanced fixture constraints in the y and z axes. Utilizing advanced fixtures once more, the x-axis constraint was then moved to an added split line that
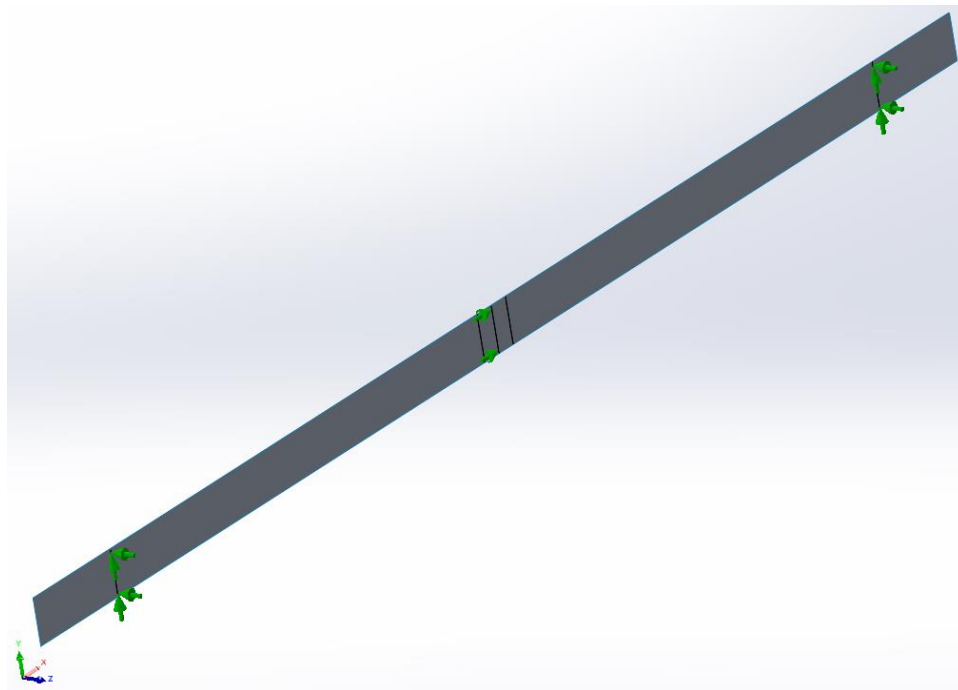
Figure 76: *2D Square Beam FEM Unique Boundary Condition Scheme*

denoted the length midpoint of the beam. Upon making this correction, the 2D FEM for the square beam yielded comparable results to Beam Theory and its 3D FEM counterpart. This different boundary condition scheme can be viewed in Figure 76.

Unlike boundary condition implementation, application of the loading condition for these beams was much less complicated. As mentioned in a previous sub-section, the metal spanner strap that spans the load U-bolt and applies the load to the top face of the beams was measured to be 0.75" wide. Corresponding split lines were positioned on all FEA models to approximate this width straddling the length midpoint of each beam. Depending on if there is an additional split line marking the length midpoint (as was the case for the 2D square beam FEM), these split lines will 'split' either one 0.75" wide face or two 0.375" wide faces around the beam length midpoint. Selecting the 'Force' option from the drop-down menu under the External Loads Advisor allowed for designation of load direction, magnitude, and location of application. First, the face(s)
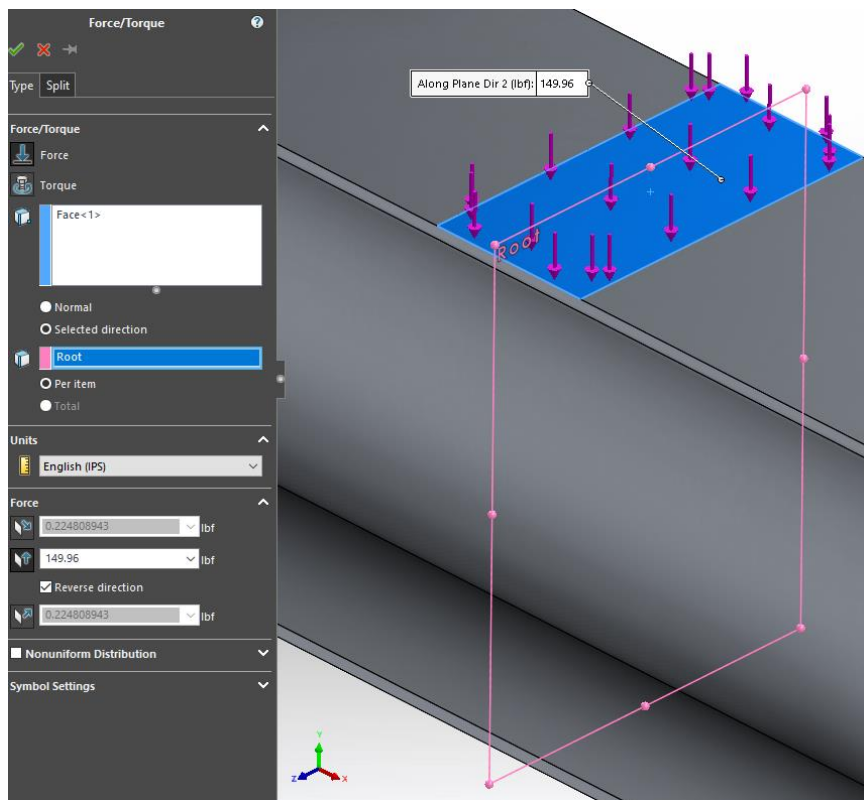
Figure 77: *Implementation of the Three-Point Bending Loading Condition*

between the load split lines were selected for the desired load application position. Then the 'Selected Direction' option was marked, and the reference geometry was any of the split line intersection planes. If selecting more than one face between the load split lines, the 'Total' option must also be checked. If this is not selected, then the input load magnitude will be applied to each face selected, effectively doubling the load applied to the model. Finally, the load units, magnitude, and direction were selected and input. Figure 77 depicts this process for the 3D I-beam FEA model. All of these FEA models also had the load due to gravity implemented. This was accomplished simply by selecting the gravity load from the same drop-down menu as the 'Load' option and then ensuring gravity was applied in the same direction as the applied load. It is worth noting that the Beam Theory model does not account for the effects of gravity. However, as is evident in Figure 72, the effect of gravity on these beams is of negligible impact due to their small mass.

Meshing Preferences for Solution Convergence

Another key factor in determining the validity of an FEA model is the fineness of the element meshing. Even if the entirety of the model is built correctly, a really coarse mesh can result in the FEA solution converging to deflections and stresses that are either higher or lower than they should be for the model. This is typically the case because a significantly coarse mesh does not lend the solver much fidelity. If, for example, on the square beam a mesh was generated using two elements (each spanning half the beam length), the solver would be computing deflections and stresses over a 12-inch-long section of the beam. Determination of each element's deflections and stresses, then, would be widely distorted as the averaging of the solutions at the element nodes would register minimal values on one end and maximum values on the other. The perfect FEM would ideally be composed of an infinitesimally fine grid element mesh. However, computing power limitations restrict just how fine the mesh can actually be. The goal, then, is to

apply an adequately fine grid mesh to the model such that the resulting solution is no longer significantly dependent on the element size or number of elements in the model.

One method built into SolidWorks Simulation that is intended to assist in determining the proper mesh element size is an automated mesh refining routine. This routine comes with two iterative solvers called h-adaptive and p-adaptive. The h-adaptive iterative solver automatically increases the mesh fineness iteratively between FEM solving loops until the change in minimum strain energy of the model between successive loops exceeds a user specified accuracy threshold [43]. The p-adaptive iterative solver, on the other hand, works to increase the order of the elements (thereby increasing the order of the elemental shape functions) iteratively between FEM solving loops until the change in strain energy falls below a user defined threshold percentage [43]. Ideally, either of these iterative meshing routines will determine the perfect amount of mesh fineness. This was not found to be the case for the FEA models generated for this research endeavor. When attempting to utilize either solver to automatically refine the model mesh, the routine would either 'converge' after one pass, quit working before fully converging, or encounter strain energy divergence and enter into a loop of never-ending mesh refinement. As a result, the element meshes that would be output by these solvers would be too coarse to be considered reliable or altogether non-existent because the solver diverged and/or failed.

With these iterative meshing routines ruled out, the only alternative available was refining the mesh manually. In order to gage at what level of fineness the mesh was to be considered acceptable, the resulting maximum deflections and bending stress at a fixed location along the beam's semi-span were compared to the corresponding results from Beam Theory. Starting with a very coarse mesh element size of one inch, the mesh fineness was increased iteratively. This continued until the resulting bending stress and maximum deflection solutions between successive solving loops experienced minimal change at or nearby the Beam Theory target values. Once this criterion was met, the mesh would be considered adequately fine since the resulting solution would not be as sensitive to element size. In Figures 78 and 79, as was also the

case for the I-beam models, the 2D model was especially sensitive to the element size in the mesh. Only after passing a mesh element size of 1/8" did the sensitivity to element size drop considerably. Likewise, the 3D model did not experience quite as much volatility to the element size and, in fact, essentially converged on the deflection solution immediately. The 3D bending stress did not display minimal change until an element size of 1/8" or smaller was achieved.
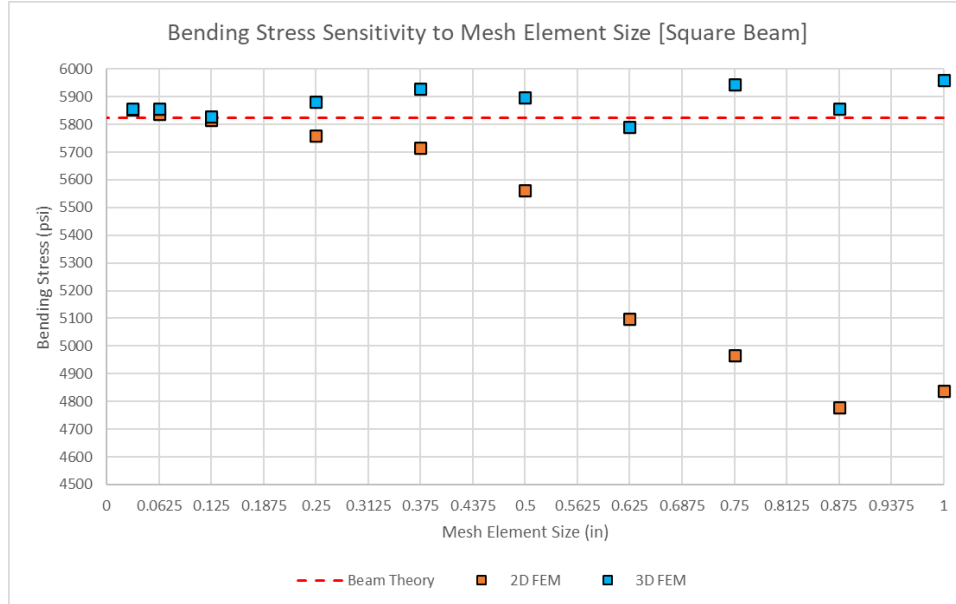
Figure 78: *Bending Stress Sensitivity to Mesh Fineness (Measured 9-inches from Left End)*
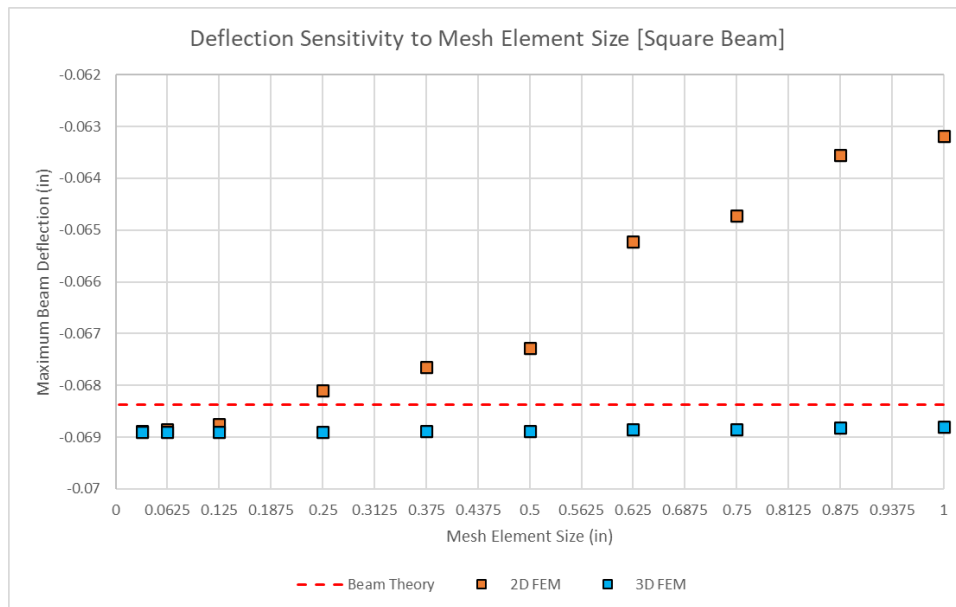
Figure 79: *Deflection Sensitivity to Mesh Fineness (Measured at Length Midpoint)*

In light of this data, a relatively fine grid mesh was implemented on all four FEA models

generated in this chapter, with the mesh element sizing controlled to be consistently 1/8". Control

of the mesh element size was achieved through either numerical or slider input in the manual

mesh generation window (see Figure 80). Additionally, in this manual mesh interface, there is an

option to manually control the element quality. SolidWorks utilizes only TRI and TET elements

for shell and solid FEA models, respectively. Despite this, two types of each base element are

offered by SolidWorks to provide solving quality control. Setting the element type is accessible

through the 'Mesh Quality' tab in Figure 80. The first element type is called a draft element,

which is an element that has nodes only in the element corners like those discussed in the

literature review [43]. The second element type is called a high-quality element, which places

nodes along the element edges between the corner nodes, thus increasing the element's shape

function order [43]. When high quality elements were enabled for the 3D FEA models, an option
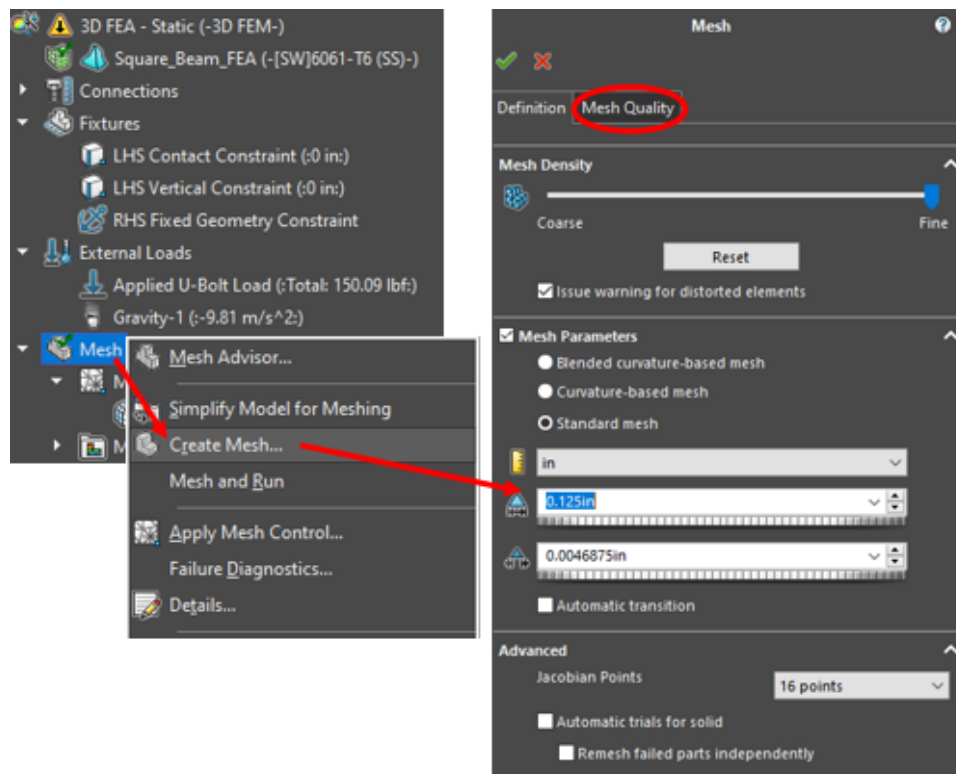
Figure 80: *Procedure for FEM Mesh Generation*

became available in the mesh generation window wherein the number of Jacobian Points (nodes) could be manually set. In order to avoid some of the pitfalls of lower order shape function elements, all four FEA models had meshes generated using high-quality elements. For the 3D models, these high-quality elements were generated with 16 Jacobian Points per element. The resulting fine grid 2D and 3D mesh for both the square cross-section beam and the I-beam can be viewed in Sections B and C, respectively, of the Appendix.

Another tool available to assist in manual mesh refinement is an option called Mesh Control. This tool allows the user to manually select faces, edges, points, or split lines along the solid part where a certain mesh element size is desired. In this way, this tool can be utilized to manually fulfill the roll of the h-adaptive iterative solver by locally coarsening or refining the mesh grid as needed. This tool is most useful for smoothing areas of high stress concentration on a part, especially if those concentrations exist around sharp corners or holes in the part. Due to the reduction of the support boundary conditions to two lines on the bottom face of the beams, there did exist high bending stress concentrations at these locations. However, attempts to utilize mesh controls to generate a locally finer mesh in these areas did not alleviate the concentrations. Further discussion of these stress concentrations is covered in the next sub-section. Where Mesh Control was found to be useful was for the split line on the side face of the beams, which would be used to sample shear stresses and strains. Application of a locally finer mesh grid along this split line greatly assisted in producing consistently smooth shear stress and strain data plots.

Added FEM Complexity for Model Verification

Finally, as a check against the simplified models generated as discussed throughout this section, a more complex 3D FEM was generated for each of the beam test specimens. This model was made more complex through the addition of solid parts approximating the geometry of the 80/20 crossbars as well as the metal spanner strap attached to the load U-bolt. Along with the solid models of the beams, these components were placed into a SolidWorks assembly and the

crossbars and load U-bolt were positioned along the beams using a combination of parallel, coincident, and distance mates. When pulling this model into the Simulation space, the vertical boundary condition that was originally applied to split lines at the support locations was replaced with a contact connection constraint (see Figure 81). When generating FEA models from an assembly, SolidWorks automatically makes these connection constraints based on the mates applied to the components. The only required modification was the contact set type. SolidWorks automatically generated bonded connections with all touching parts, so this connection definition was edited so that it was a contact connection instead. Additionally, since the solution for the
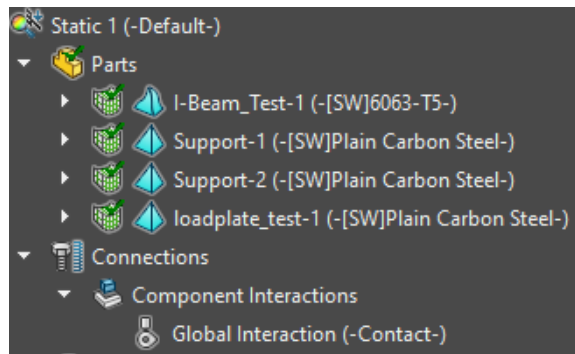
Figure 81: *Application of Vertical Boundary Condition Through Contact Connections*
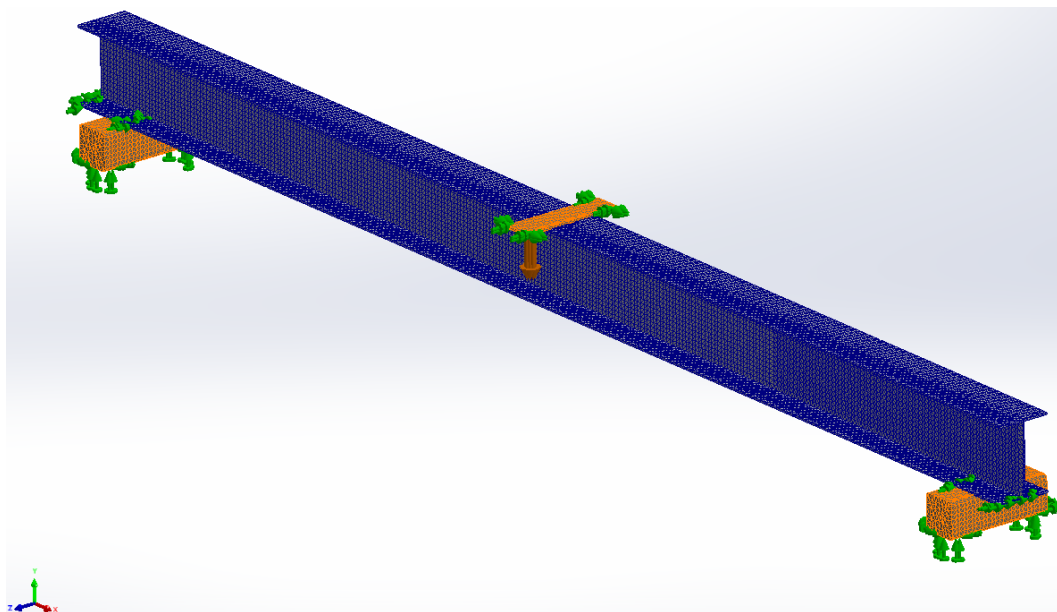
Figure 82: *Complex 3D FEM Generated for the I-Beam*

beams themselves were of importance, only the beam solid parts had high quality mesh elements applied to them. The crossbar and load U-bolt parts had draft quality mesh elements applied to them. An example of the final complex FEA model (which was produced for the I-beam) can be observed in Figure 82. In this figure the blue elements are high quality, and the orange elements are draft quality.

The reasoning behind the generation of these more complex 3D models was twofold. First, by replacing the vertical boundary constraints with an actual model of the support crossbars, the boundary condition assumption that all load flowed through two lines approximating the support locations along the beam could be verified. In addition, replacing the load condition on the top of the beam with a solid part approximating the load U-bolt spanner plate geometry would further allow for verification of the proper loading condition applied to the simple models. Secondly, as was briefly mentioned in the previous sub-section, there were some concerns with the simple beam FEMs due to the large stress concentrations that occurred at the support locations. It was likely that the boundary conditions at the supports had been too idealized, resulting in these concentrations. Therefore, the more complex model would indicate if this was the correct assumption based on if the stress concentrations persisted.

As Figure 83 shows, the bending strain curves generated from both the simple and the complex 3D models for the I-beam experienced nearly identical trends, maximum values, and magnitudes of stress concentrations at the supports. The same was observed when comparing the simple and the complex 3D models of the square beam. With this in mind, since the area of contact is quite small between the beam's lower face and the rounded corner of the crossbar, it is likely that some magnitude of stress concentration does, in fact, occur on the physical system since the load path is reduced to flowing through interface areas approximating that of a line [44]. Observing no meaningful change between the complex and the simplified FEA models for both beams, the simplified versions as discussed earlier in this section were deemed sufficiently complex such that they would yield reasonably reliable deflection and stress solutions.
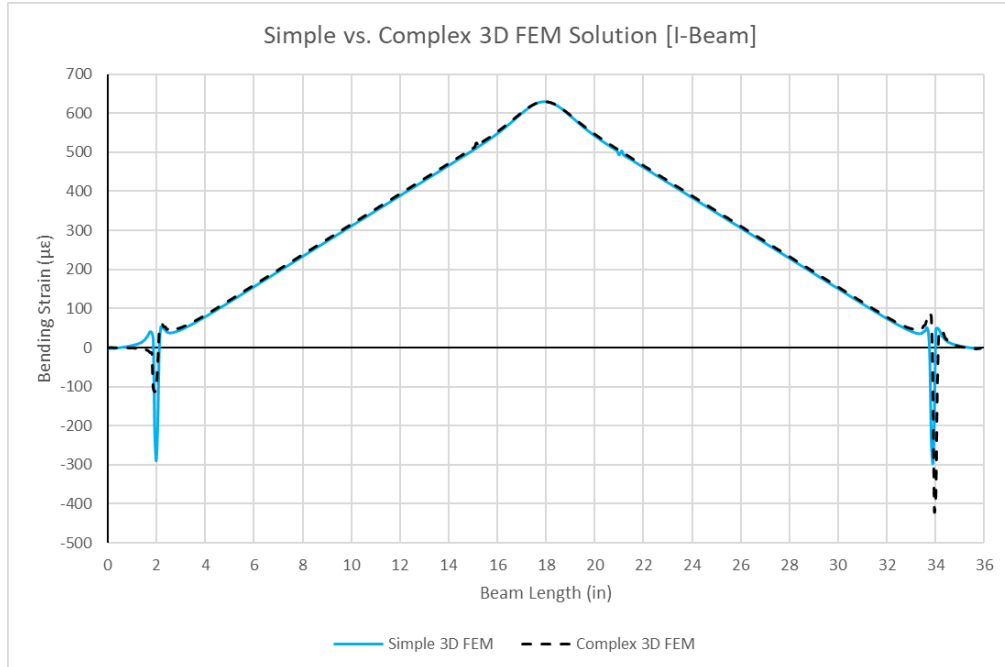
Figure 83: *Comparison of Bending Strain Solutions for Simple and Complex 3D FEA I-Beam Models*

D. SolidWorks FEM Results and Comparison

With the Finite Element Models for both beam test specimens generated and the experimental

data gathered with which to compare, the FEA solving capabilities of SolidWorks Simulation

could be characterized. The end goal of this characterization is to establish a performance

baseline for simple material properties and beam geometries. From this baseline, expectations

about how SolidWorks will handle modeling and solving of the orthotropic material composition

of the I-beam spars produced at the DML can be extrapolated. The remainder of this section

focuses on evaluating the performance of SolidWorks FEA Simulation. As is also the focus of

designing the composite I-beam spars, this evaluation will center around SolidWorks' ability to

predict beam deflection, bending stress, and shear stress. The latter two criteria will be presented

in the form of strains since this was the parameter that was empirically measured, and it can be

easily extrapolated from the Finite Element Models in place of the stress values. Note that the

experimentally measured data for both beams can be found in Sections B and C of the Appendix.

111

Square Beam Cross-Section Results

For beam deflection predictions, both the 2D and 3D FEA models modeled the same deflection trends and magnitudes as the solution from conventional Beam Theory. This is evidenced by all three predicted deflection curves lying atop one another in the upper portion of Figure 84. For a beam of isotropic mechanical properties and simple cross-sectional geometry, this outcome was anticipated, as has been mentioned and shown elsewhere in this chapter. Comparison of Beam Theory and the FEA models to those deflection values obtained from experimental testing for this beam further displays that the general trend among the predicted deflection curves matches well with the apparent trend of the measured data. Calculation of the correlation coefficients between the models and the empirical data supports this observation, with both 2D and 3D models yielding a strong correlation coefficient of +0.99.

To get a better idea of how well the FEA models were able to predict the true beam deflections, the plot shown in the lower portion of Figure 84 was generated. In this plot, the diagonal red line indicates a perfect match between the FEA model deflection data and the experimentally measured deflection data. In an ideal scenario, the plotted datapoints would fall right on this red line, indicating that the FEA models perfectly predicted the deflection behavior of the beam under load. As is evident, however, this was not the case. Instead, both the 2D and 3D models were found to consistently underpredict beam deflections. This is indicated by the fact that all of the datapoints fall above the diagonal red line. Quantifying this consistent underprediction, the magnitudes of the FEA deflections were found to have an average Root Mean Squared Error (RMSE) of 0.0059 inches compared to the real deflections. Factoring in the measurement uncertainties associated with the experiment, this RMSE between datasets could be as small as 0.0044 inches or as large as 0.0074 inches. This range is somewhat significant compared to the magnitude of the deflection data. Overall, however, considering that this amounts to a difference of at most 1/128th of an inch between actual and model values, it can be inferred that these FEA models accurately predicted the true deflection of this beam.
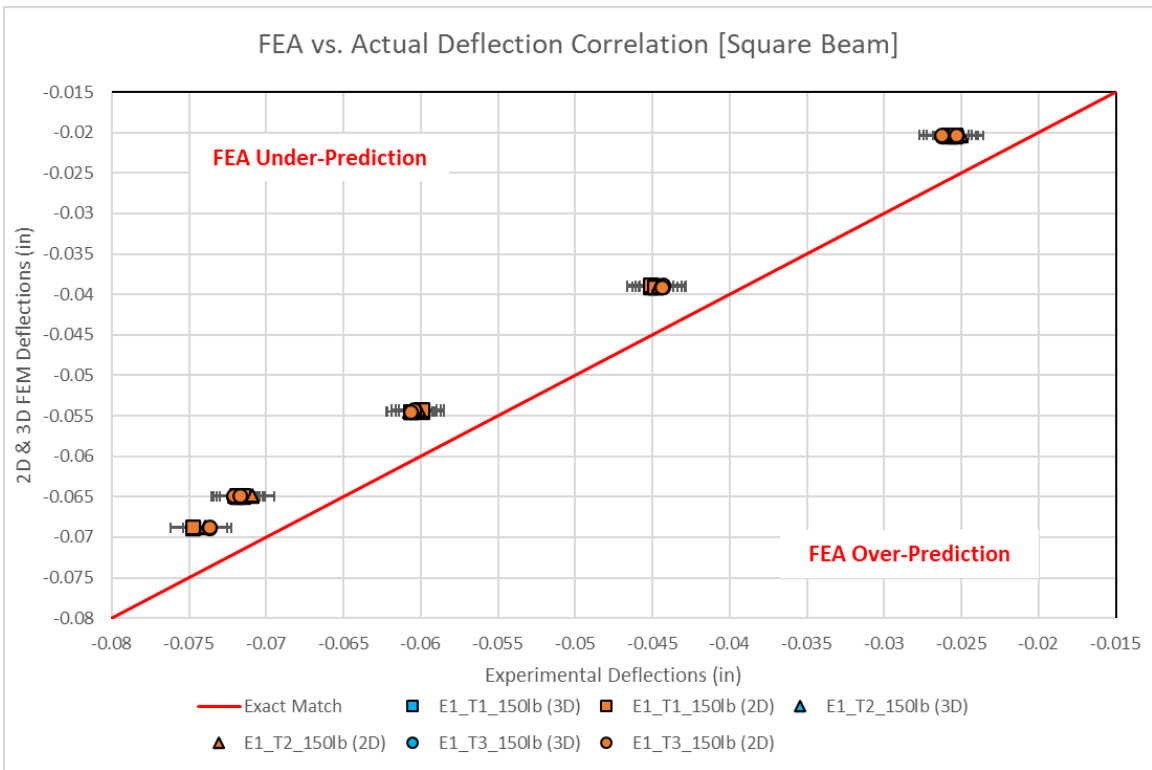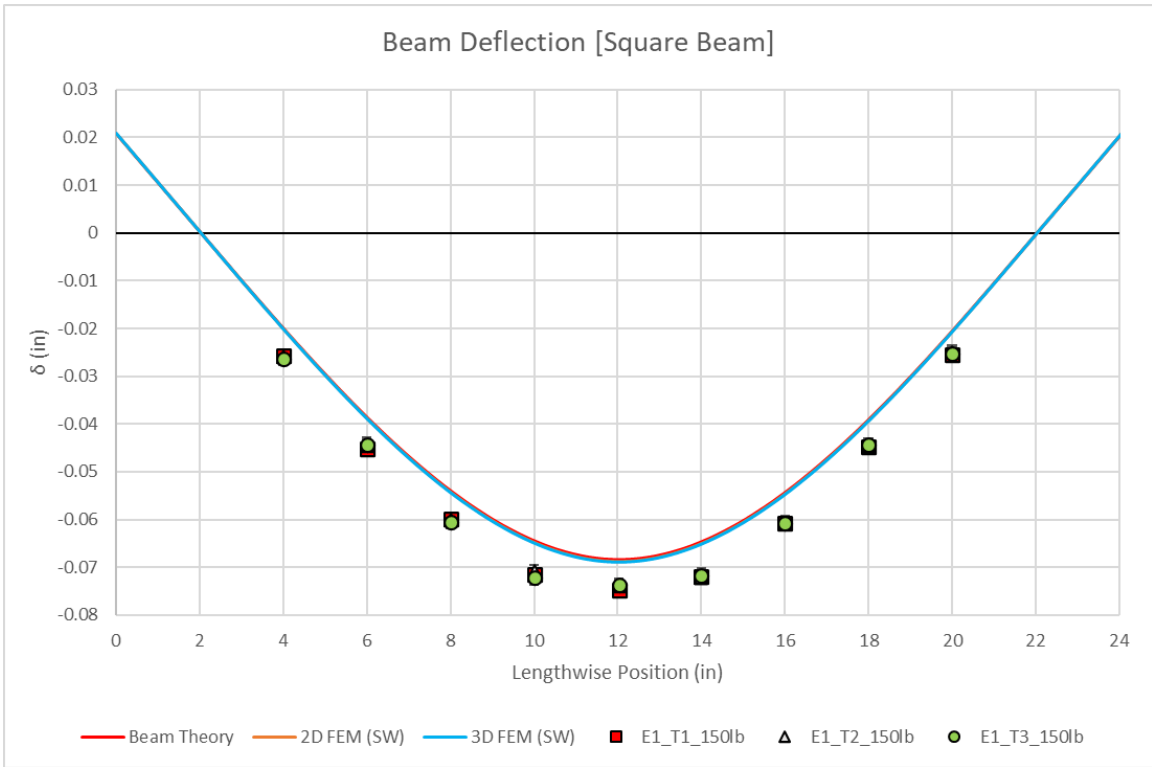
Figure 84: *Square Beam Deflection Results*

For bending strain data, similar overall FEM performance can be observed in Figure 85. Once more, the 2D and 3D FEA models were agreeable with the bending strain solution obtained from Beam Theory. Unlike the deflections, though, the 3D model adhered better with Beam Theory than the 2D model did as evidenced by the 2D model's slope being less than the other two. Further still, the 2D model struggled to predict the strains (and by extension the stresses) near the length midpoint of the beam. Viewing Figure 85, the 3D model produced a smooth strain curve in this region while the 2D model curve is jagged. The likely culprits are the split lines that populate this region of the 2D square beam model. When building the FEA models, it was intermittently observed that placing split lines in certain locations along the beam resulted in the bending strain curves having a sudden magnitude joggle at the split line's location, which is similar to what appears for this 2D model. Despite this, both models produced stress trends that correlated well with the experimentally determined values, with both models again having correlation coefficients of +0.99 with the measured dataset.

As was done for the deflection data, the plot shown in the lower half of Figure 85 was produced to better gage FEA's ability to predict the stresses in the beam. Both the 2D and 3D models were found to underpredict what was observed in the physical system by an average RMSE of 26.18με. Factoring in measurement uncertainties again, this RMSE could be as high as 44.34με or as low as 9.18με. What is different from the deflection data is that the lower uncertainty bound would shift nine of the twelve experimentally measured strain datapoints onto the desired perfect match line for both the 2D and 3D models. Further, recalling the mesh sensitivity plot in Figure 78, the FEA solutions were converging to stresses equivalent to 30 – 40με higher than Beam Theory at mesh sizes finer than the chosen 1/8th of an inch. A finer mesh would have certainly placed both of the FEA strain curves within the uncertainty ranges of all of the experimentally measured data. Therefore, these models are similarly found to accurately predict the bending stresses for the square cross-section beam.
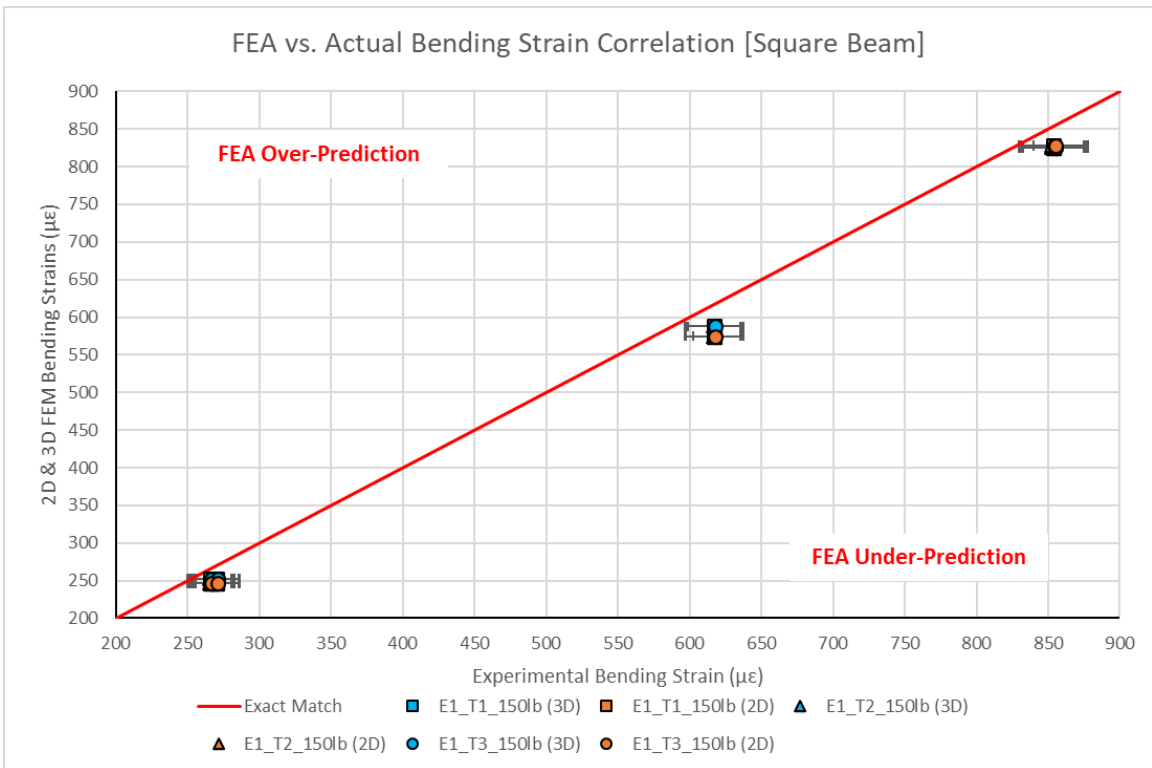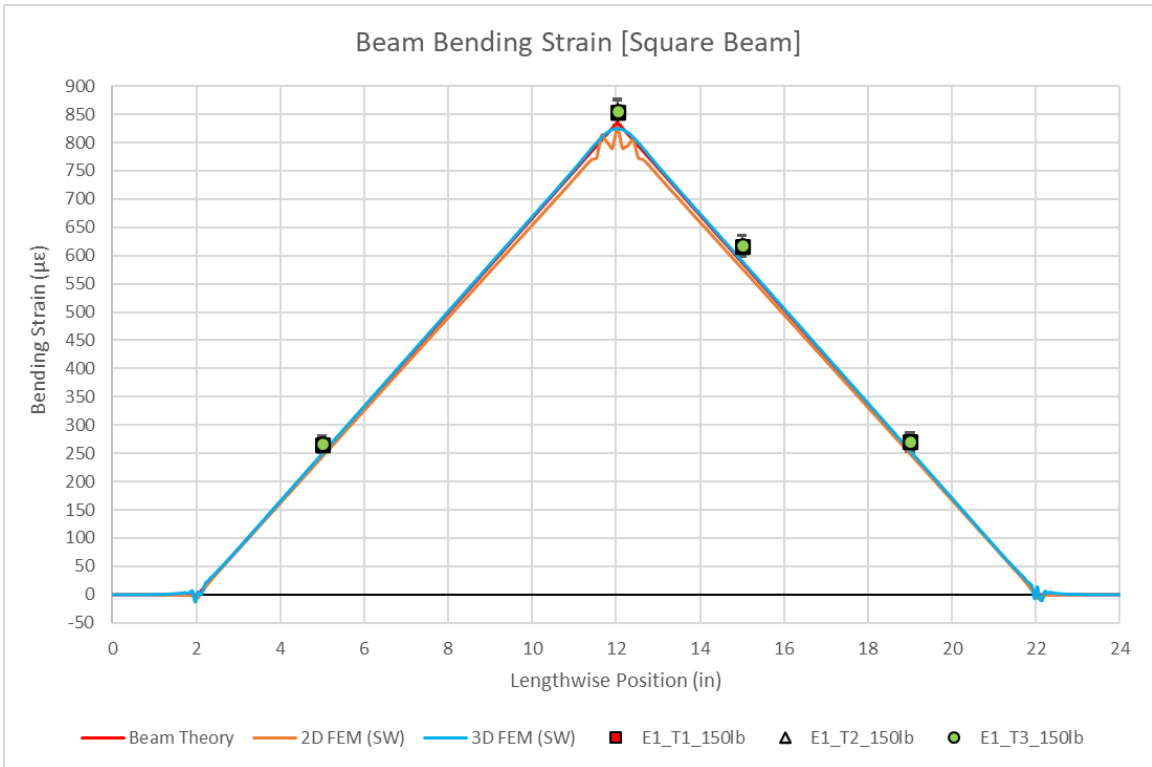
Figure 85: *Square Beam Bending Strain Results*

Unlike the deflection and bending stress data, shear stress in this beam proved to be more difficult for SolidWorks FEA to capture. In Figure 86, it is apparent that all three prediction models (Beam Theory, 2D FEA, and 3D FEA) again underpredicted the actual values obtained for shear strain. Despite this, the 3D FEM had more success in its shear solution than the others. Part of the cause for such a noticeable discrepancy between the 2D and 3D solutions is the model simplification applied to the shell model. Just like Beam Theory, the 2D FEM was idealized such that the thickness of the beam was represented as a singular surface that was in line with the beam's x-centroidal plane. As such, all deflections and stresses were similarly calculated along this same centroidal axis just as is done in Beam Theory. This explains why these two datasets coincide. On the other hand, the solid model does not make this assumption but rather determines the stresses as a function of the distance in the z-axis away from this centroidal plane. This relationship becomes more influential as z-axis material thickness increases.

As a result, shear measured on the outer face of the beam (which is where the shear strain gages were placed experimentally) is different than the shear measured at the beam's centroid. This is depicted for the 3D model in Figure 86, where the dotted blue line is the shear strain curve sampled along the beam's centroid while the solid blue line was sampled on the outer face. This stress variation along the z-axis of the beam is further supported by the experimental shear measurements, which the 3D FEM outer face shear solution comes closer to matching out of the two models. To quantitatively assess both model's performance, the RMSE was again calculated. On average, the 2D FEM had an RMSE of 15.84μγ. Considering measurement uncertainty, this RMSE could be as small as 11.36μγ or as large as 20.33μγ. Likewise, the average RMSE was found to be 8.49μγ for the 3D FEM. The range due to measurement uncertainty here could make this error fall between 4.01 and 12.98μγ. Even at this higher bound, the 3D FEM is just barely further from the true measurement than the 2D FEM is at its smallest possible error. For the case of shear stress prediction, the 3D model is more accurate while the 2D model represents an idealized case that is subject to assumptions similar to those used for Beam Theory.
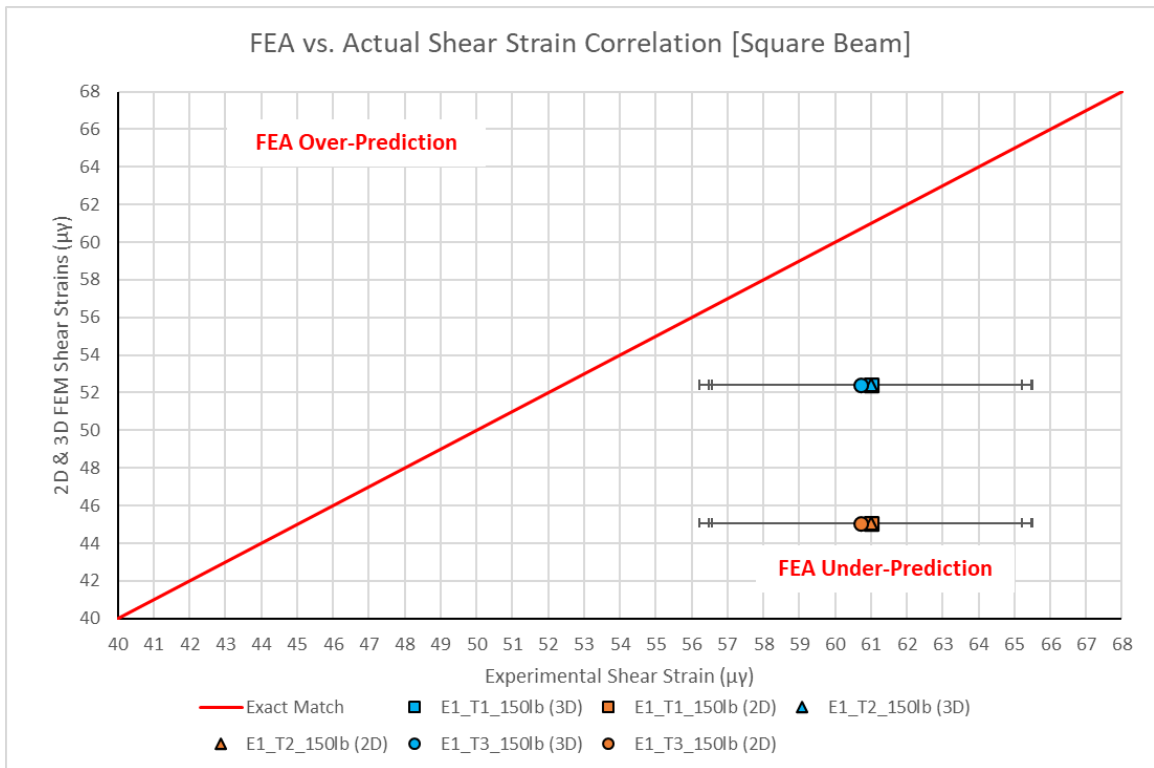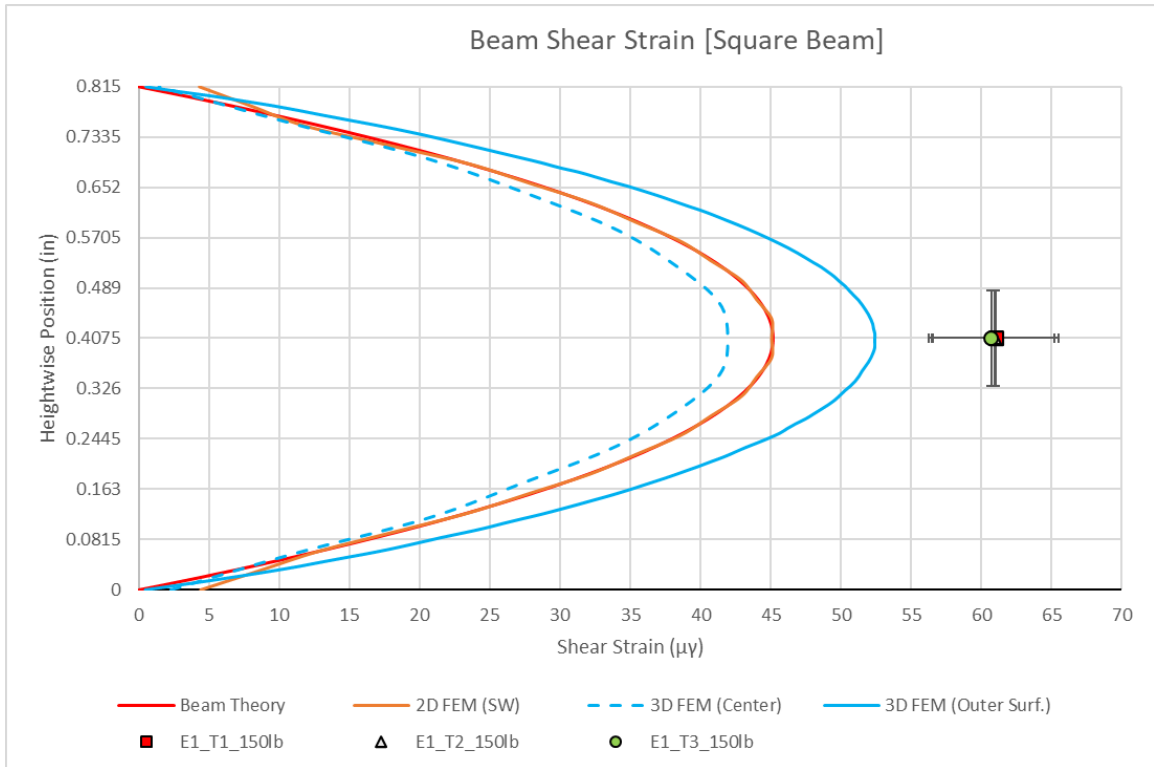
Figure 86: *Square Beam Shear Strain Results*

I-Beam Cross-Section Results

For the I-beam, the deflection predictions between the FEA models were again very similar as was the case for the square beam. Despite this, both models yielded deflection predictions slightly higher than the solution obtained from Beam Theory, as is evident in the upper portion of Figure 87. Even so, the recurring trend of SolidWorks FEM underprediction when compared to empirical data becomes evident once more. The magnitude of this underprediction has increased when compared to the trends for the square beam's deflection in Figure 84. At maximum deflection, the square beam models were on average five thousandths of an inch off from the experimental measurement. For the I-beam, this gap between the FEA models and the experiment just more than doubles at eleven thousandths of an inch. This constitutes a significant increase in model underprediction, especially since the overall deflection magnitudes for both beams are similar. The general trend between the models and the empirical data still match well, as was expected, with both the 2D and 3D models again yielding a strong correlation coefficient of +0.99 with the actual data.

Further quantification of this larger underprediction when compared to the square beam becomes evident through the Root Mean Squared Error of this data. On average, the RMSE between the FEA models and the actual data was found to be 0.0097 inches. Factoring in measurement uncertainties, the possible error range extends from 0.0089 to 0.0105 inches. Considering that the upper bound of possible error for the square beam FEM deflections was 0.0074 inches, this increase in model underprediction becomes quite clear. There is the possibility that unforeseen properties of the experimentally tested beam (such as inadvertent torsion lowering the inertia due to an uncentered load or a non-constant cross-section) could have played a role in these increased deflections. However, replication of such possible discrepancies in the FEA models yielded no significant deviation from the FEM solutions shown. Overall, the models still predict the deflections well, but this data indicates that SolidWorks Simulation may be struggling to properly deal with the added geometrical complexity of the I-beam.
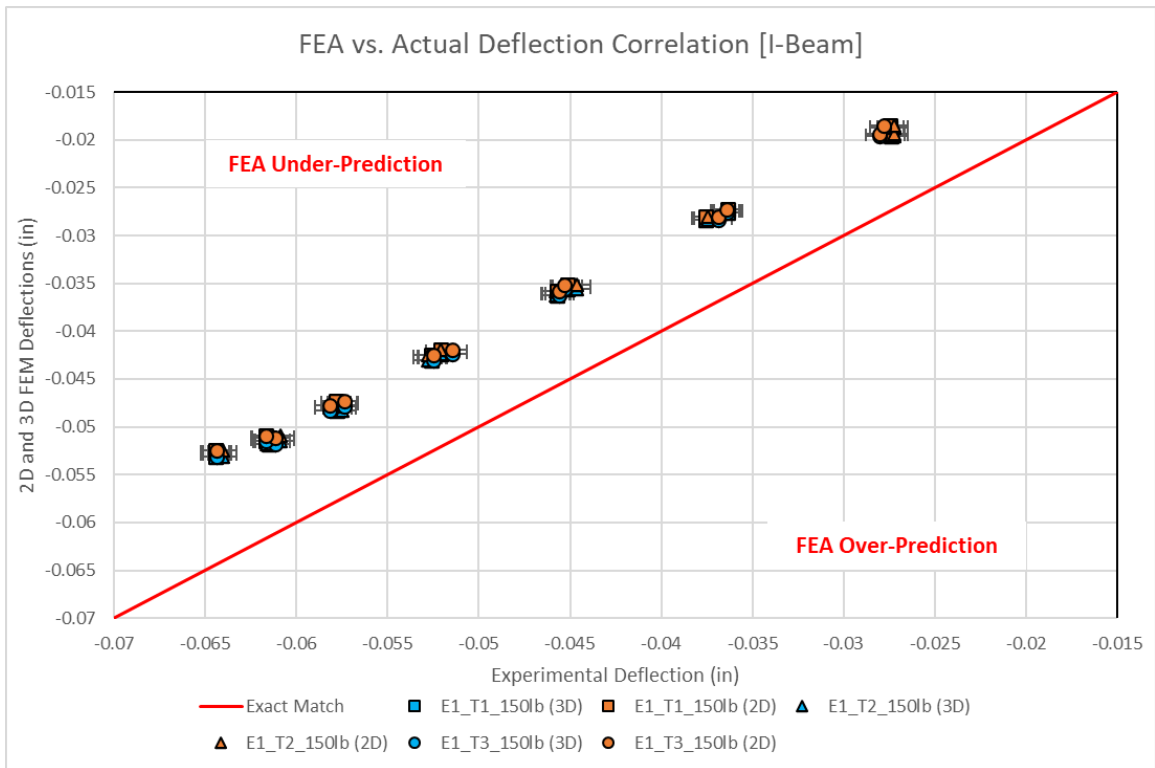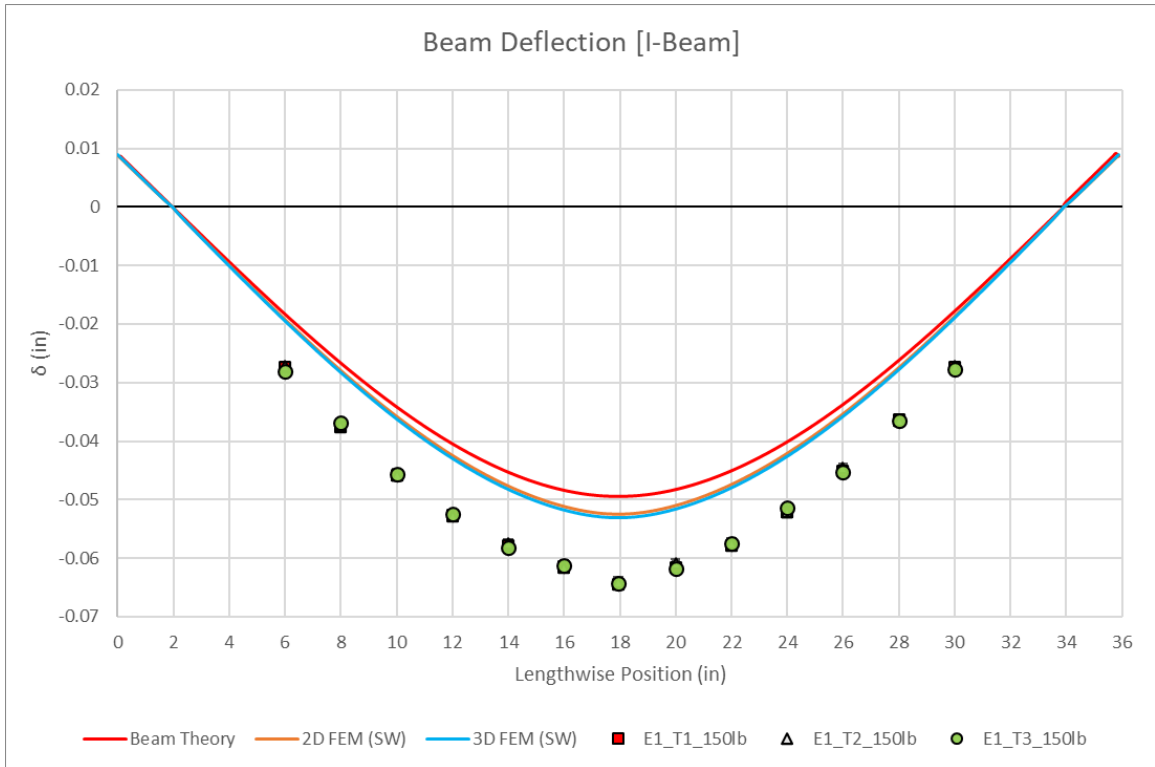
Figure 87: *I-Beam Deflection Results*

For bending strain on this I-beam, despite the increase in FEA deflections compared to Beam Theory, the resulting strain curves for theory and the models still match quite well in trend and overall magnitude. Compared to the square beam bending strain curves, the FEA solutions for the I-beam also follow a similar trend. For the square beam, when the 2D and 3D models predicted similar deflections to theory, the resulting 3D bending stress magnitudes (especially near the peak stresses at the length midpoint) were on the order of ~10$\mu\epsilon$ higher than the 2D solution if the jaggedness is ignored. This similar trend for the I-beam models is evident. The model deflections were similar and the resulting stress data, as shown in Figure 88, indicates that the 3D FEM stress data near the peak beam stresses are again on the order of ~10$\mu\epsilon$ above that of the 2D solution. Also present in the upper plot of this figure are the FEM stress singularities that were discussed in the previous section. Considering that these concentrations are much more prominent for the I-beam models than they were for the square beam ones, further support is garnered that SolidWorks FEA struggles to deal with this added geometric complexity.

Quantitative evaluation of the FEM predictions compared to the experimentally gathered data further reveals the uptick in FEA underprediction similarly to the I-beam deflections. The RMSE on average for the 2D and 3D FEA models was found to the be 37.60$\mu\epsilon$ off from the measured data. With added uncertainties, the range of possible strain error shifted as low as 26.93$\mu\epsilon$ and as high as 48.45$\mu\epsilon$ for these models. Comparatively, this range of errors is not far off from those found for the square beam, especially on the upper bound, but the lower bound and average error for the I-beam is noticeably higher. Observation of the lower portion of Figure 88 shows that both FEA solutions begin to drift further away from the 'perfect match' line as well as each other at higher stresses. There remains the likelihood that a finer mesh grid size than 1/8th of an inch would produce FEM stress curves peaking at ~30$\mu\epsilon$ higher than shown (as Figure 78's trends suggest), but this would barely move the curves inside the experimental uncertainty bounds for the models. Regardless, the 3D model is slightly better at making this stress prediction.
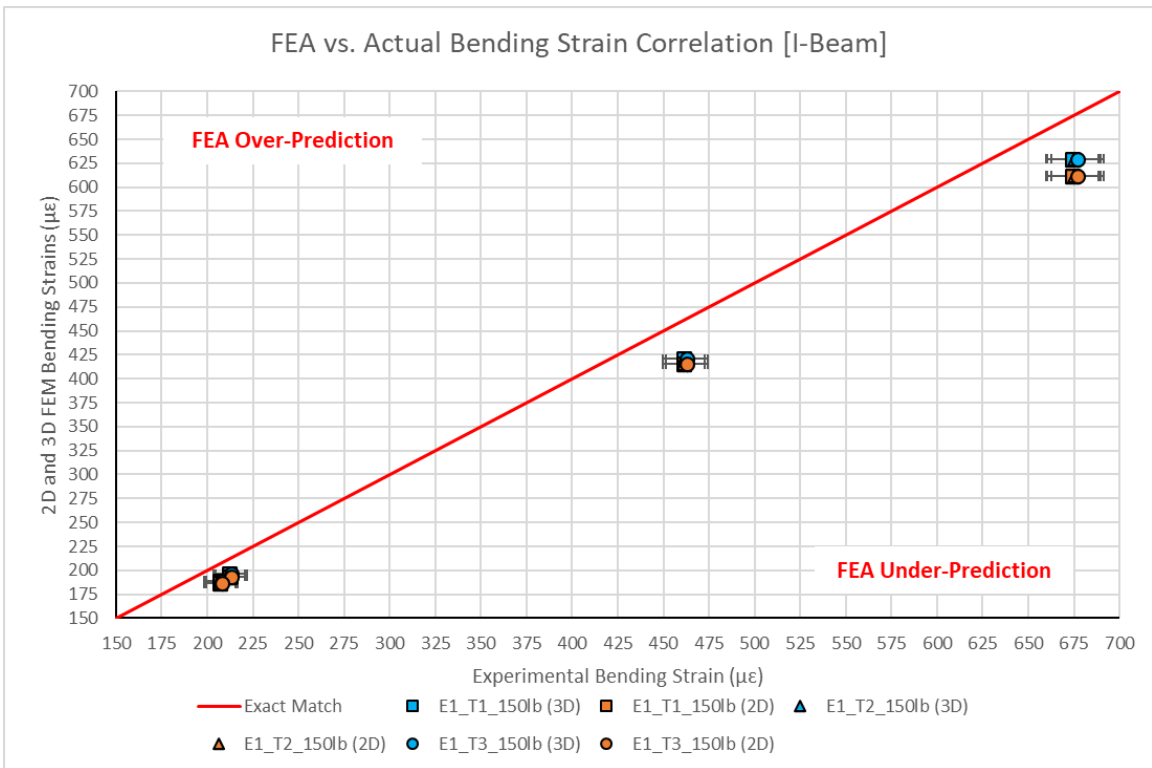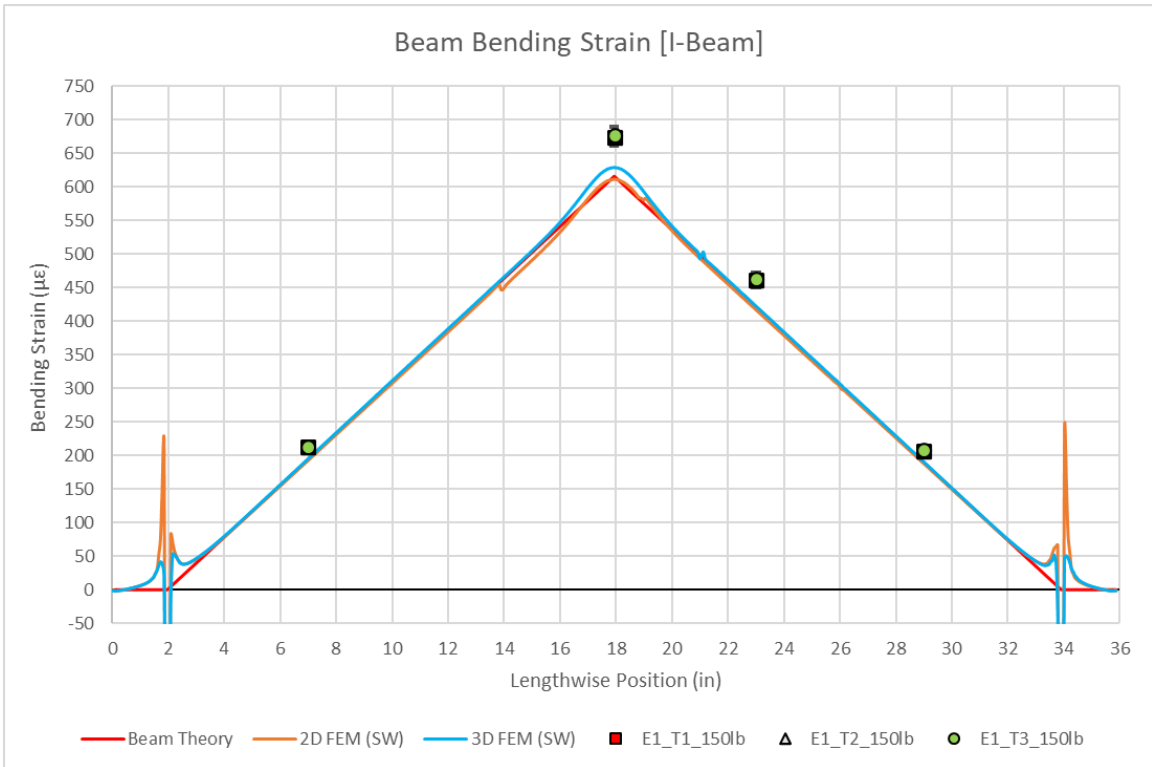
Figure 88: *I-Beam Bending Strain Results*

In contrast to the shear strain trends presented for the square cross-section beam, Figure 89 illustrates that the I-beam shear strains for all three prediction models matched quite well in overall trend and magnitude. For the 2D and 3D FEA, the shear strain was sampled only along the height of the I-beam's shear web, which is why the data curves abruptly end while the Beam Theory curve continues to plot shear strain through the height of the I-beam caps. Just as was the case for the square beam, the 2D model is still idealized such that it assumes that the I-beam web thickness is applied as a flat shell along its x-centroidal plane. For the 3D model, though, the true thicknesses of the caps and shear web are so small that this I-beam qualifies as a thin-walled structure. When performing the 3D analysis, the calculation of shear stress as a function of thickness in the z-axis (extending out from the centroidal plane) results in the same data as the 2D FEM and Beam Theory due to the minimal change in thickness between the centroidal plane and the outer surface of the shear web. At this small of a thickness between the two at ~0.024", the influence of the web thickness is not enough to cause a noticeable change in shear strains between the 2D and 3D models as it was for the thicker square beam.

Further deviation from the previously established norm is presented in this data as it is the only dataset where the models overpredicted the experimental data, as the lower portion of Figure 89 indicates. The average RMSE between the FEA models and the experimental shear strain dataset was determined to be 24.09μγ. With measurement uncertainty, the bounds of overprediction extend to between 14.62μγ and 33.55μγ. As is also the case for the square beam, much of the error associated with the experimental shear measurements stems from sensitivity to angular misalignment of the 45° shear bridges [39]. Even so, this result further reinforces SolidWorks Simulation's difficulty in precisely predicting the shear stress in these isotropic beams. In the simpler but thicker square beam geometry, SolidWorks FEA underpredicted shear stresses in the beam. Here, for the thinner but more complex I-beam geometry, SolidWorks FEA overcompensated and thus overpredicted the overall shear stress in the beam. Despite this, both I-beam FEA models still adequately predicted shear stress in the vicinity of the true value.
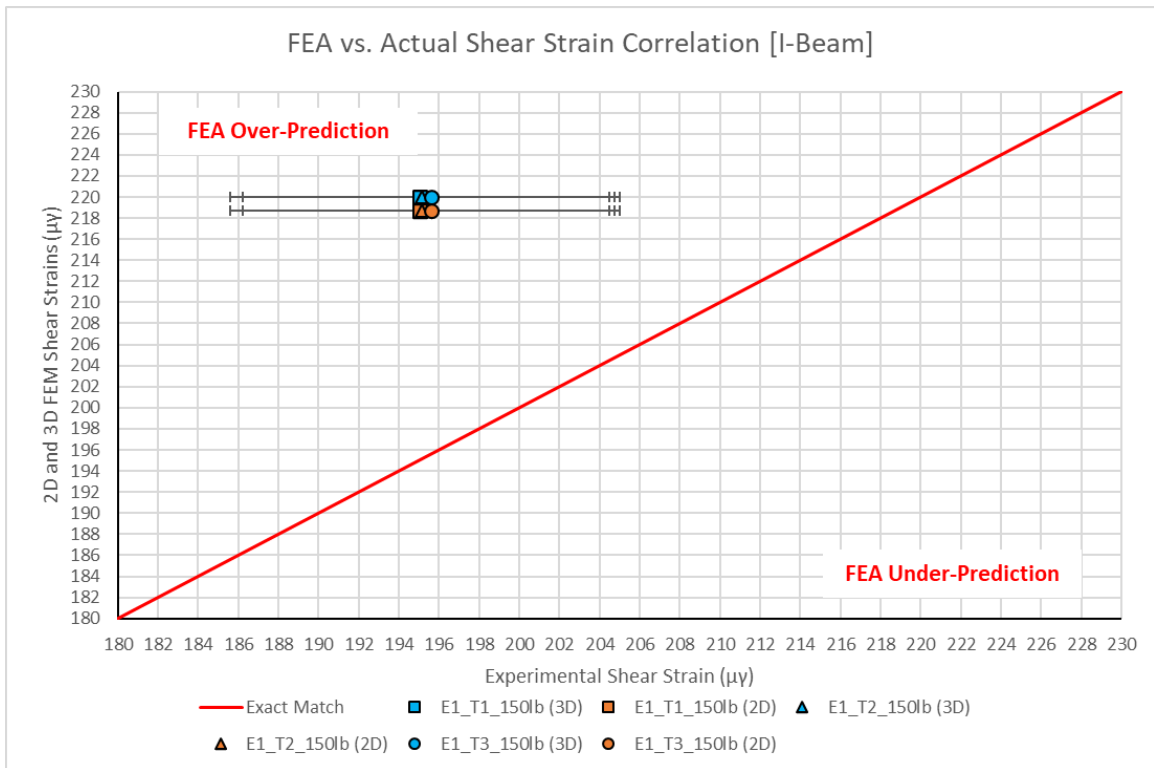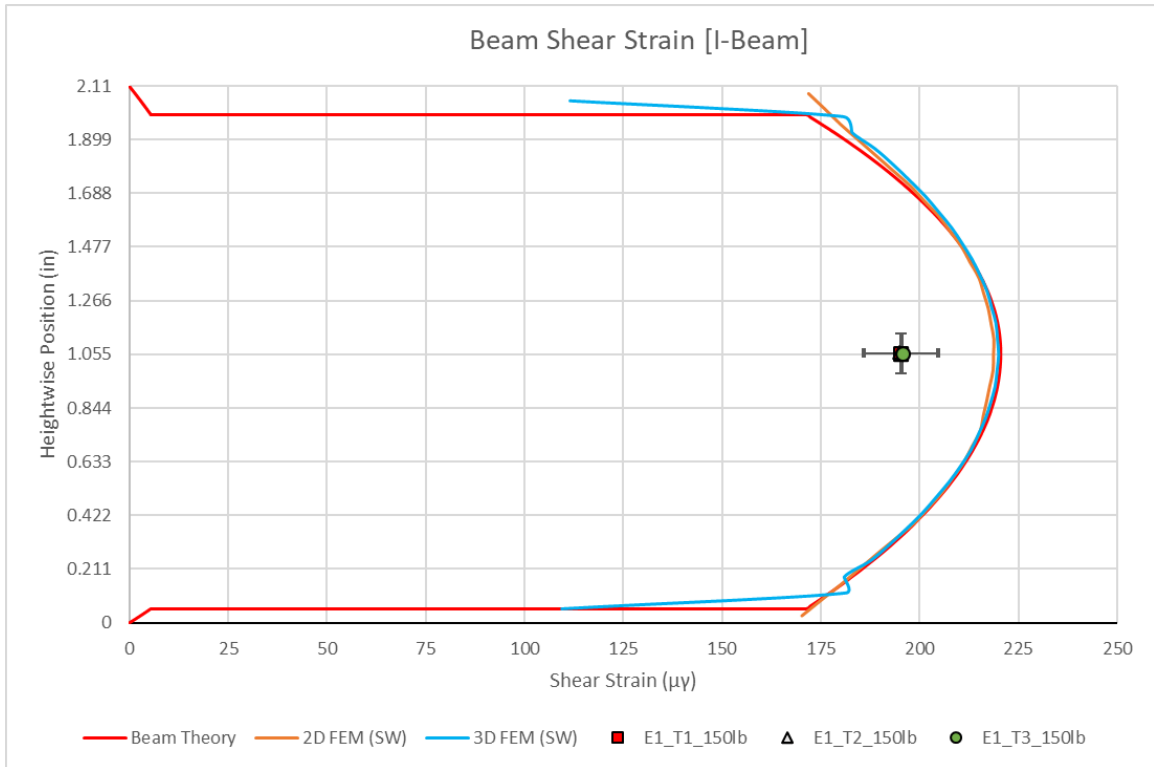
Figure 89: *I-Beam Shear Strain Results*

E. Isotropic Beam FEA Performance Summary

Based on the data gathered both experimentally and through the Finite Element Models in SolidWorks, the consensus is that SolidWorks FEA will consistently underpredict both beam deflections and bending stresses. SolidWorks' limited variety of available mesh element types (those being TRI and TET elements) cause both the 2D and 3D Finite Element Models to be stiffer than what was found to be the case via experiment. These elements are known to be among the stiffer element options available for FEA meshing, and their utilization, especially if they are lower order TRI's and TET's, will artificially stiffen a model for the case of bending analyses [3], [45]. Were the option to switch element types to other common but less stiff element geometries available, such as QUAD and HEX elements, it is likely the FEA results would better predict beam deflections and bending stresses [3], [45]. Since this is not an option for SolidWorks, the only available course of action to attempt further refinement of the models would be to continue increasing the number of elements in the mesh. In other words, the element size would need to be decreased below 1/8th of an inch, which will sacrifice computing power and computing time as the mesh becomes further refined.

Considering the data that was acquired from these models as they were generated in this chapter, further support for the assertion that SolidWorks struggled with the added geometric complexity of the I-beam compared to the simpler square beam becomes evident. For added ease of comparison of the 2D and 3D FEM performances between both beams, the previously discussed RMSE values for the models were normalized into error percentages with the experimental measurements in Table 11. As can be seen, the deflection and bending strain errors and error bounds, which factor in experimental uncertainty, are consistently lower for the square beam compared to the I-beam. In all cases for these datasets, the error is found to nearly double for the I-beam models. This increase in underprediction could be influenced by the combination of the stiffer TRI and TET elements with the more complex model geometry of the I-beam.

Table 11: *Normalized Errors for SolidWorks 2D and 3D FEA Models*

Metal Beam Normalized RMSE Values					
		2D FEM		3D FEM	
Category	Uncertainty Bounds	Square Beam	I-Beam	Square Beam	I-Beam
Deflection	Actual	11.20%	20.59%	10.93%	19.63%
	Max	13.57%	21.84%	13.30%	20.89%
	Min	8.71%	19.30%	8.44%	18.32%
Bending Strain	Actual	5.77%	10.77%	4.67%	8.54%
	Max	9.03%	13.18%	8.03%	11.03%
	Min	2.55%	8.27%	1.25%	5.95%
Maximum Shear Strain	Actual	26.01%	12.00%	13.94%	12.67%
	Max	31.08%	17.71%	19.85%	18.41%
	Min	20.13%	6.82%	7.10%	7.46%

As for shear strain, the 2D I-beam model was found to better predict shear than its square beam counterpart. Considering the previous discussion of how SolidWorks FEA calculates shear as a function of distance in the z-axis from the x-centroidal plane of the beam, this is a reasonable outcome. Since the square beam was much thicker than the shear web of the I-beam, the simplification of the beams to a surface along the centroidal plane resulted in a larger shear stress distortion for the square beam. On the other hand, the 3D models were rather similar in their prediction error as they both predicted the maximum shear strain for their respective beams with errors within two percent of each other. Likewise, the resulting error bounds due to measurement uncertainty were also very similar to one another. Granted, the error percentages for the square beam indicates an underprediction while the percentages for the I-beam indicate overprediction.

In light of these findings, the baseline for SolidWorks is complete. From this baseline FEA performance on isotropic material beams, the following expectations for SolidWorks FEA's ability to model the composite I-beam spars can be formulated:

1) The resulting spar FEA models will continue the trend of underprediction for beam deflections and bending stresses.

2) The continued trend of struggling with consistently either over or under approximating shear stress in the beams will persist, though the solid model will likely produce the more precise solution.

3) Based on the I-beam results from Table 11, it should be possible to obtain a consistent solution for deflections and stresses in either a 2D shell model or a 3D solid model of the composite spar, especially since overall cap and web thicknesses will be similar.

4) Errors of underprediction and overprediction are likely to be closer to those percentages computed for the I-beam in Table 11, though the addition of material orthotropy could cause errors to further increase.

5) Introduction of material orthotropy will further cause the FEA solutions to stray from solutions computed using Beam Theory techniques and assumptions.

CHAPTER V

COMPOSITE I-BEAM TESTING, MODELING, AND RESULTS

A. **Testing and Modeling Objectives**

With experimental testing and FEA modeling procedures satisfactorily established from the

previous chapter's baseline testing, research efforts shifted focus to the composite I-beam spars.

For this second round of experimentation, three composite I-beam spars were constructed

utilizing similar manufacturing methods as are typically employed when fitting these spars into a

wing. Further discussion of these beams' construction will occur in the following section.

Because experimental and modeling procedures were established from baseline testing, as

aforementioned, the resulting composite spar FEA models can be evaluated on their ability to

account for the orthotropic nature of both the unidirectional carbon laminate spar caps and the

balsa wood shear web. The FEA results for these composite beams will be directly compared to

empirical data to determine model validity. Unlike the previous chapter, the addition of material

orthotropy and the overall composite nature of these I-beams present additional complexity that

Beam Theory may not fully account for, even with the transformed area method. As such,

utilization of Beam Theory to determine FEA model validity is not advisable due to the

possibility of errors between Beam Theory and experimental data being greater than desirable.

However, it is still expected that general trends from Beam Theory will persist, such as the U-

shaped deflection curve and V-shaped bending stress curve.

In light of the above, the resulting objectives and focus for testing and modeling of these composite I-beams are summarized below:

1) Utilize established testing procedures from the previous chapter to acquire necessary deflection, bending strain, and shear strain data in order to validate SolidWorks FEA models.

2) Explore methods to properly generate composite FEA models within SolidWorks, especially as it relates to accounting for material orthotropy.

3) Evaluate the efficacy of these FEA models based on their agreement with experimental data first and then also with Beam Theory.

B. Beam Experimental Setup

Similar to the previous chapter's experimental setup, the composite beams were loaded in a 3-point bending configuration on the Vernier Structures and Materials Tester. For reference, much of the information regarding this experimental setup, such as required instrumentation and equipment, is covered in Chapter III, Section A. Further, most information regarding the required strain gage configurations for measuring shear and bending strains on beams in this configuration was determined during the baseline testing and can be found in Chapter IV, Section B. For these composite beams, the same 3-point bending procedures discussed in Chapter IV will be utilized here. The main difference, however, is that three composite beams were manufactured for testing. This was done to account for variance in the mechanical properties of both the carbon fiber and balsa wood. In addition, this will reduce the impact of bad data collected from a test specimen with either material or manufacturing defects. The following sub-sections detail the manufacturing process, experimental testing configuration, and preparation and testing procedures for these composite beams.

Composite Beam Construction

Typical procedure at the DML for implementation of a composite I-beam spar into a UAV wing is a two-step process. The first step takes place as the last process during the wing skin layup. After the final layer of fabric composite is wetted into the wing mold, unidirectional carbon fiber tow is layered along the span of the wing at the location of the main wing spar with the fibers oriented in the spanwise direction. After up to a 24-hour cure time under vacuum at room temperature and post-processing of the skin halves for bonding, the second step occurs. During this step, internal structure for the wing, including the balsa shear web, is approximately positioned in one of the wing skin halves with small, thin balsa wood triangles. Refer to Figure 7 in the literature review for a visual reference. This structure is then sanded until the gap between the skin halves at the wing parting line is closed. Lord 310 A/B bonding epoxy is utilized as the bonding adhesive. All locations where internal structure is to be placed is scored with low grit sandpaper and cleaned before the adhesive is applied. Once the halves are placed together, they are secured in order to minimize shifting and left to cure for another 24 hours.

Unlike the process as described above, the composite I-beam spars built for the purposes of this research were constructed as a separate entity without a wing skin being manufactured. Building these spars external to a wing presented some obstacles, especially as it relates to bonding the carbon spar caps and the balsa shear web together. This jigging deficiency was addressed while waiting for ordered spar materials to arrive. The ultimate goal for these bonding jigs was to maintain straightness of the beam as well as to ensure that the spar caps were perpendicular to the balsa shear web during bonding. Additionally, these jigs needed to be easy to apply pre-bond and easy to remove post-bond while also being modular such that varied beam lengths could be accounted for. This would be important due to the likely variability in beam dimensions as a result of the manufacturing process. Initially, a jigging design utilized by a colleague during his research, which involved these composite spars, was considered [13]. This design, however, was intended to bond composite beams of no more than ~8-10 inches in length.

The planned length of the I-beams for this research endeavor was intended to be much longer at ~24 inches in length. Therefore, this jigging design was deemed inapplicable.

Despite ruling out this established design, the method with which they were produced (that being additive manufacturing via 3D printing) was similarly utilized for the design of the jigs used for this research. The intended maximum spar cap width was to be 1.25" while the intended shear web width and height was to be 0.125" and 1.125" respectively. This prototype design, as shown in Figure 90, was developed in order to determine the correct tolerancing of the SolidWorks model such that the resulting 3D print adhered to the jig requirements listed previously. The basic tenets of this prototype design were found to perform well, especially after
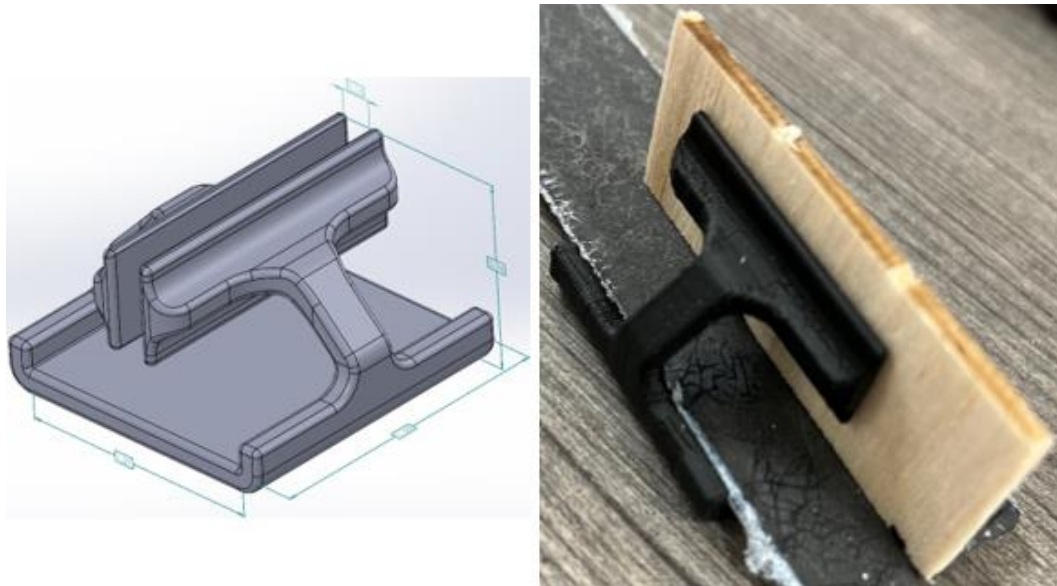
Figure 90: *Bonding Jig Prototype Design*

initial tolerancing issues were sorted out. Stemming from this prototype, two improved jig designs were developed (see Figure 91). The first of these improved designs was just a lengthened version of the prototype. The length of this version, viewable on the left of Figure 91, was doubled to 3" in length and three of these jigs were intended to be used per beam. The second improved design was a modification of the prototype for alignment of the ends of the beam. As is shown in the right of Figure 91, this jig has a flat reference face that the spar cap and shear web

can be pushed against to ensure a flush alignment of the beam end. Additionally, a hole was cut out of this face to account for possible adhesive squeeze-out during bonding. The length of this design was only 2" in length, and two were intended to be used per beam. To expedite the bonding process, two sets of these jigs were printed so that two beams could be bonded simultaneously. In total, six of the left jig design and four of the right jig design from Figure 91 were printed.
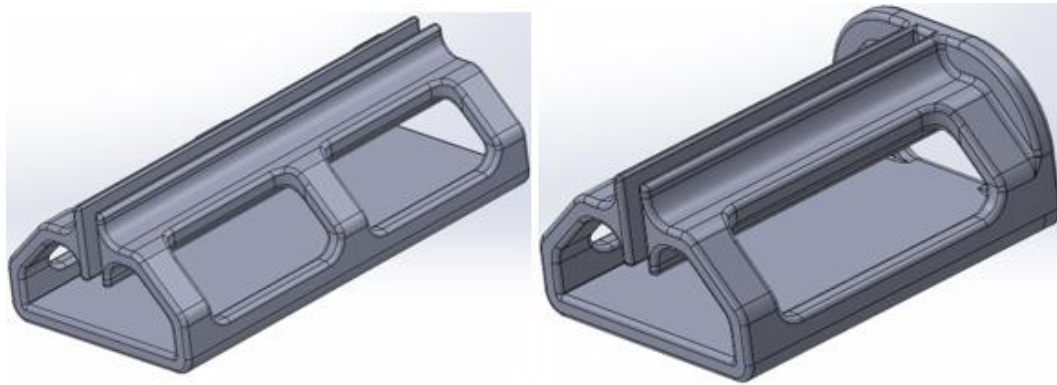
Figure 91: *Finalized Bonding Jig Designs*

Materials for these composite beams were acquired from professional companies so as to limit manufacturing defects. This was especially important for the unidirectional carbon fiber. From composite laminate theory, having successive fiber layers oriented at different angles can significantly impact the resulting mechanical properties of the laminate [6], [7], [9]. For the composite beams, it is essential that the unidirectional fibers be oriented such that they run parallel to the length of the beam. With this in mind, a 36" x 12" x 0.06" unidirectional carbon fiber laminate sheet was acquired from CSTSales. The approximate mechanical properties of this laminate are the same as those listed in Table 1 of the literature review. This sheet was squared off and marked so that six 1.25" x 24" spar caps could be cut from it.

Initial inspection of this sheet before the spar caps were cut revealed some interesting characteristics. Chief among these was that, to the naked eye, it was impossible to tell which direction the fibers were oriented. This was likely a result of the curing process utilized for this

laminate, which is believed to have been either an oven cure or an autoclave cure. The only way to confirm was to break off a piece of the laminate and inspect the thickness section under a microscope (see the left of Figure 92). Comparing this section view to Figure 10 from the literature review, the fiber orientation of this laminate was determined to be parallel to the 36" length dimension. This was further confirmed when cutting out the spar caps as fiber fraying

Figure 92: *Unidirectional Carbon Laminate Fiber Direction and Surface Texture*

would occur only when cutting the laminate along the 36" length direction. The other significant characteristic was the epoxy texturing applied to the outer surfaces of the laminate. Once more, to the naked eye, this laminate appeared as though there was a 0/90 fiber weave on the outer surfaces. Despite this, there was a noticeable surface texture that could be felt by rubbing a finger across these surfaces. Placing part of the laminate under a magnifying glass confirmed that a zig-zag epoxy surface texture pattern had been applied to the laminate during curing (see the right of Figure 92). It was this texture that made the laminate appear to have a weave fiber pattern.

For the shear webs, a 12" x 36" sheet of 0.125" thick balsa wood was acquired from Specialized Balsa, which specializes in balsa wood products. It is possible to order wood from this company with specified grain orientations and overall density ranges. Under the advisement of a colleague at the DML who was continuing research into material characteristics of balsa

wood at the time of this writing, this balsa sheet was requested to have a B-grain orientation with a medium density range [57]. This density range was further requested to be refined to a range between 11 lb/ft^3 and 13 lb/ft^3 so that density variation of the balsa wood for each composite beam would not cause large changes in mechanical properties [14], [57]. Due to these requests, the resulting balsa sheet consisted of multiple balsa strips that were laminated together primarily to achieve the density range. An example of this laminated sheet can be viewed on a laser cut shear web piece in Figure 93, where four distinct strips of balsa are visible.

Figure 93: *Example of Laminated Balsa Strips to Achieve Requested Density*

Since the width of this sheet was only 12" and the grain direction ran perpendicular to the sheet width, it was decided that the shear web would be composed of three 8" x 1.125" x 0.125" balsa pieces. These pieces were laser cut, and a total of nine 8" long pieces were required for the three beams' shear webs (though more were cut as backups). To prepare for bonding, each of these pieces' edges were sanded lightly until the burned char from the laser was removed. For each beam, three of these 8" long pieces were glued together with CA. The bonding jigs were utilized to maintain proper alignment of the shear web pieces while they were glued together, as Figure 94 depicts.

Figure 94: *Process for Assembling Balsa Shear Web with CA*

Before these shear web pieces were glued together, they were divided into groups of three with each group designated for one of the three composite beams. Each of these groups was weighed on a scale and that weight was divided by the approximate volume of the three pieces to obtain the density of each of the three beams' shear webs. Each group of three weighed 10 grams, resulting in a shear web density of ~11.29 lb/ft^3 for all three beams (which is a testament as to how well Specialized Balsa hand selected each balsa strip that was laminated into the resulting balsa sheet). Considering the resulting mechanical properties of this balsa wood, the density is higher than the density at which the balsa properties listed in Table 3 are assigned. Despite this, [14] has a convenient tabular breakdown by density of all of the important balsa mechanical properties. Using this table and the determined shear web density, the resulting mechanical properties of balsa wood at 11.29 lb/ft^3 was linearly interpolated and can be viewed in Table 12 below. The Poisson ratios remain the same as those listed in Table 3, however.

Table 12: *Balsa Mechanical Properties for a Density of 11.29 lb/ft^3 [14]*

Balsa Wood Elastic and Shear Moduli		
ρ	11.29	lb/ft^3
$E_{Bending}$	659.10	ksi
E_L	725.01	ksi
E_T	9.71	ksi
E_R	33.20	ksi
G_{LT}	16.80	ksi
G_{LR}	28.93	ksi
G_{RT}	36.25	ksi

During final preparation for bonding of the balsa shear web to the carbon fiber spar caps, both the caps and shear web were marked with lengthwise markings every two inches as well as a centerline mark at the x-centroid for the spar caps and at the y-centroid for the shear webs. Additionally, the carbon fiber spar caps had centering markings added to one side that straddled

the x-centroidal line as well as markings placed at odd distances from the left end of the beam for placement of bending strain gages. These centering marks were intended to ensure that the shear webs were properly centered on the spar caps in the bonding jigs as well as to provide a reference for where the Lord 310 A/B bonding epoxy needed to be applied. Lastly, on the balsa shear webs, additional 45° markings were added at the location designated for the placement of the shear strain gages. Once these markings were applied, the carbon fiber spar caps were scored with low grit sandpaper along the center markings to make a more bondable surface. The resulting accumulated carbon dust was removed from the surface using alcohol and a rag, and the surface was allowed to dry.

The process of bonding the balsa shear web to the carbon spar caps is detailed in the following discussion. First, a bead of Lord 310 A/B epoxy was applied to one spar cap along the centering marks. This spar cap was then carefully inserted into the bonding jigs to avoid smearing the Lord bead. The balsa shear web was then carefully pressed into the alignment slot of the bonding jigs. This alignment slot was exactly 0.125" wide so as to generate desired clamping forces to hold the balsa shear web against the spar cap. Because of this zero-tolerance slot, applying too much pressure when pressing the balsa into the jigs would break the shear web. Before pressing the shear web into the Lord epoxy bead, both the spar cap and the shear web were pressed firmly against the flat wall of one of the beam end jigs. Upon visually inspecting that this end of the beam's components was flush and that the alignment markings along the length of each component lined up, the shear web was pressed into the epoxy. Because two sets of jigs were printed, two beams were bonded in this fashion simultaneously. These two bonding beams were pressed against each other, and three 2.5 lb weights were added on top of the shear webs to ensure that the balsa was firmly pressed into contact with the Lord epoxy and the spar cap. The Lord epoxy was allowed to cure for 16 hours before the jigs were removed and the process repeated for the remaining spar cap on each beam. Figure 95 depicts this process.
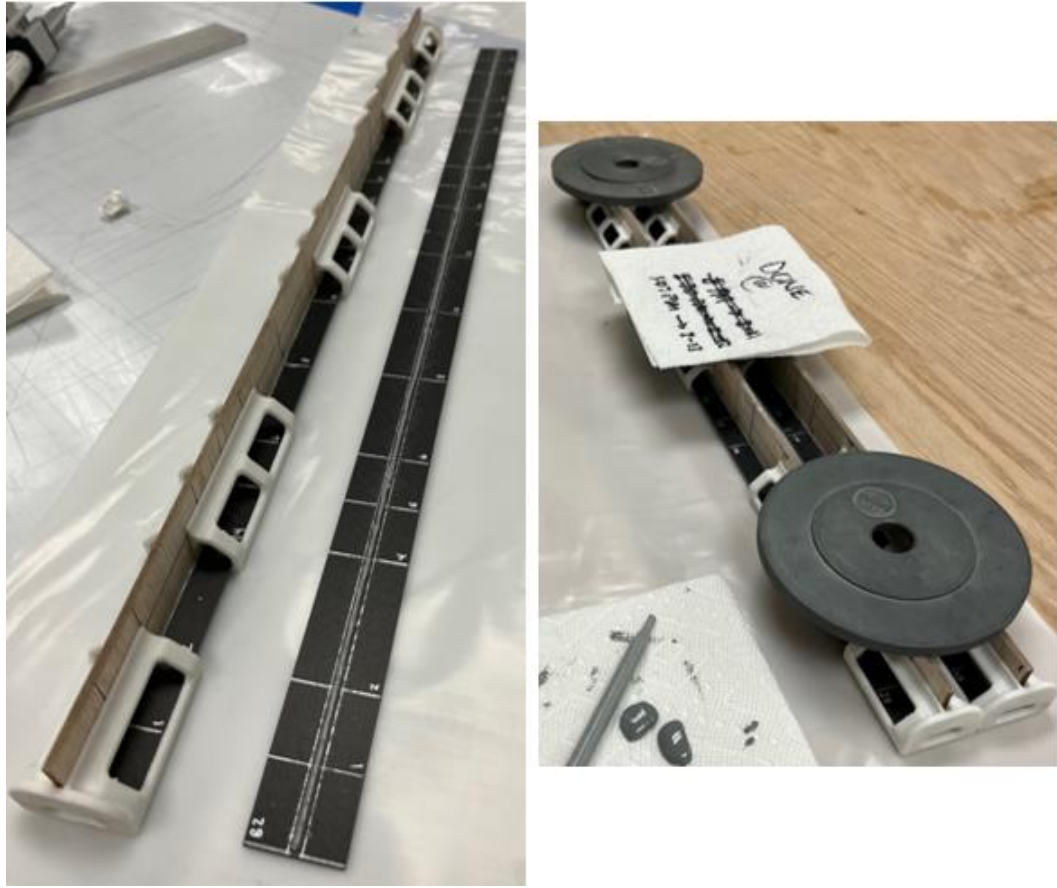
Figure 95: *Bonding Procedure Utilizing 3D Printed Bonding Jigs*

The resulting dimensions and cross-sectional properties for each of the three manufactured composite I-beams can be viewed in Table 13. If needed, refer to Figure 51 in Chapter IV for a visual reference of the variables listed in the leftmost column of this table. As is evident in Table 13, parameters such as the spar cap widths and shear web heights varied between each beam. In all cases these dimensions were slightly below the previously listed target dimensions for the beams, and this is a direct result of the manufacturing process. Despite this, variation between these dimensions for each beam was minimal and was not expected to adversely affect experimental data trends. The resulting FEA and Beam Theory models to be generated for this chapter will have cross-sectional dimensions that are the average of those values listed in Table 13. Additionally, Figure 96 shows all three composite I-beam test specimens with their bending strain gages already bonded. In this figure, the shear strain gages had not yet been attached.

Table 13: *Composite I-Beam Dimensions and Cross-Sectional Properties*

	Beam #1			Beam #2			Beam #3			
Composite I-Beam Dimensions and Cross-Sectional Properties										
L	24.000	±	0.0313	24.000	±	0.0313	24.000	±	0.0313	in
W_{bcap}	1.219	±	5.00E-04	1.215	±	5.00E-04	1.217	±	5.00E-04	in
H_{bcap}	0.060	±	5.00E-04	0.060	±	5.00E-04	0.060	±	5.00E-04	in
W_{tcap}	1.219	±	5.00E-04	1.217	±	5.00E-04	1.217	±	5.00E-04	in
H_{tcap}	0.060	±	5.00E-04	0.060	±	5.00E-04	0.060	±	5.00E-04	in
W_{web}	0.125	±	5.00E-04	0.125	±	5.00E-04	0.125	±	5.00E-04	in
H_{web}	1.118	±	5.00E-04	1.122	±	5.00E-04	1.115	±	5.00E-04	in
H_{TOTAL}	1.238	±	8.66E-04	1.242	±	8.66E-04	1.235	±	8.66E-04	in
Area	0.286	±	9.57E-04	0.286	±	9.57E-04	0.285	±	9.55E-04	in^2
ybar	0.619	±	1.54E-03	0.622	±	1.54E-03	0.618	±	1.53E-03	in
xbar	0.610	±	1.97E-04	0.609	±	1.97E-04	0.609	±	1.97E-04	in
I_{zz}	0.065	±	2.57E-04	0.066	±	2.58E-04	0.065	±	2.55E-04	in^4
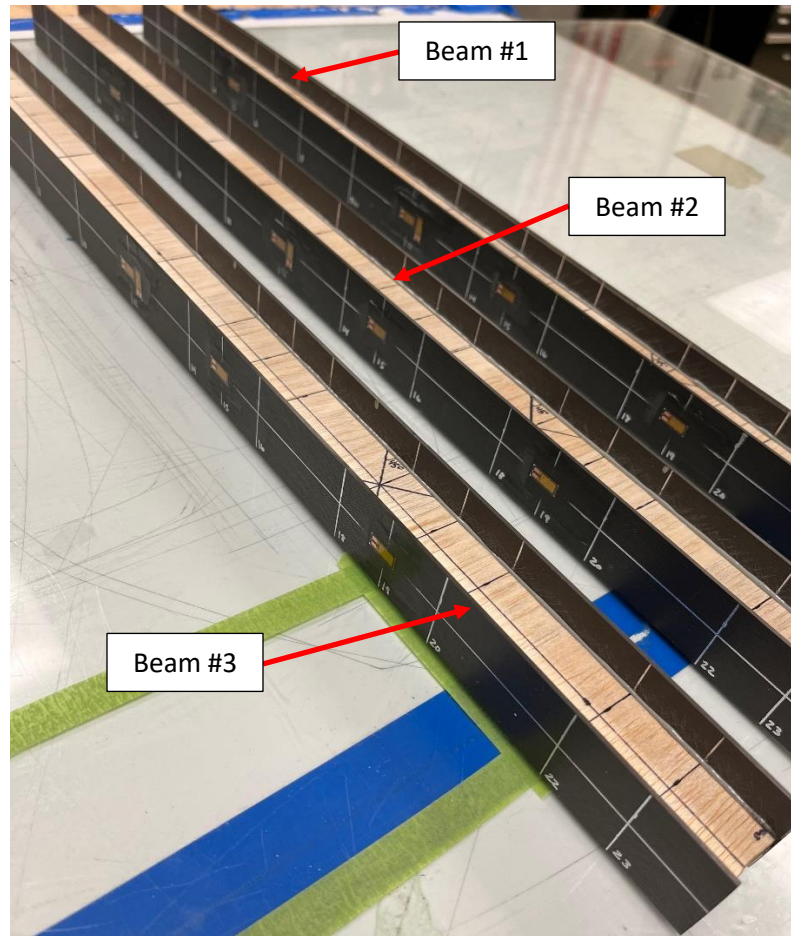
Figure 96: *Finished Composite I-Beam Test Specimens*

Experimental Configuration

Once the composite beams were completed and all of the required strain gages had been

bonded onto them, each beam was placed in the Vernier Structures and Materials Tester. Just as

was done for testing with the metal beams from the previous chapter, each of these composite

beams was configured for a 3-point bending test. The general configuration of this test for these

beams mirrors that of the testing setup utilized for the square cross-section 6061 aluminum beam

due to their similar overall beam lengths. The 80/20 support crossbars were positioned such that

the inside face was 10 inches away from the load U-bolt, which also meant that there would be 2"

of beam overhang at both supports. The load U-bolt was straddled across the length midpoint of

each composite beam, with this length midpoint being 12 inches from either end of the beams.

For the deflection measurements, the top face of the upper spar cap for all three beams was

approximately 2.375 inches below the reference datum of the modified shelf assembly. As a

result, the 2-3" measuring rod was utilized in the depth micrometer for all testing conducted with
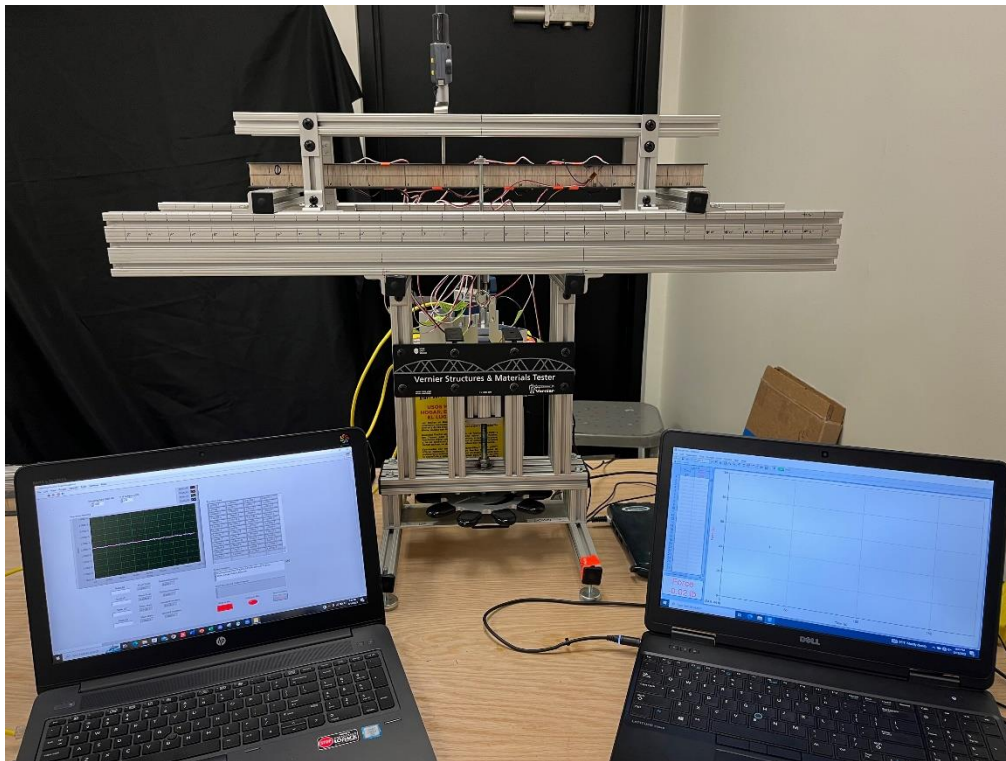
Figure 97: *Composite I-Beam 3-Point Bending Configuration (pt. 1)*
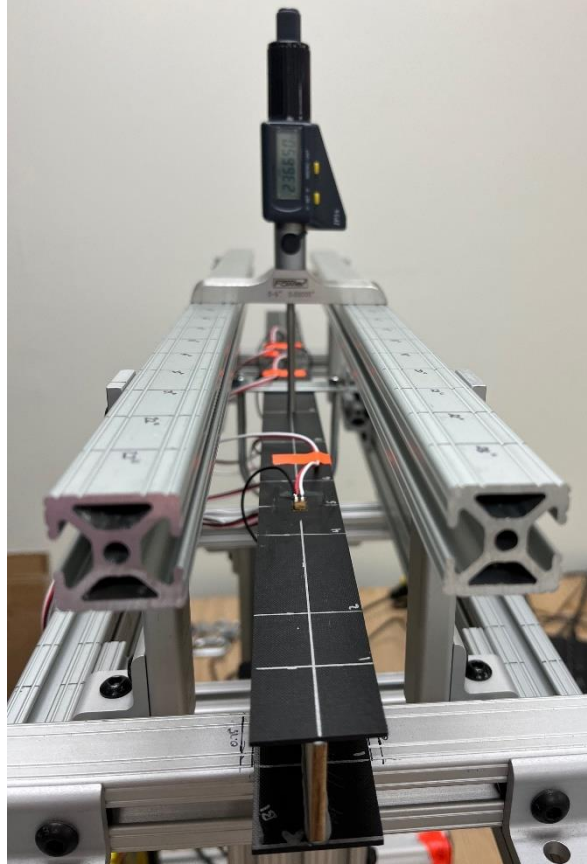
Figure 98: *Composite I-Beam 3-Point Bending Configuration (pt. 2)*

these beams. Figures 97 and 98 display this testing setup for composite I-beam #1. The same

configuration was utilized for I-beams #2 and #3 as well. Each beam was loaded only to ~50 lb in

bending so as to prevent the beams from breaking during data collection since loading the beams

to failure is not the subject of this research endeavor.

Similar to the metal beam testing, the necessary constants required for generation of both the

Beam Theory and WingSpar Mathcad models could be measured from the configuration as it is

shown in the above figures. Because there is significant overlap between these two theory

models, only the constants required for Beam Theory Equations 41-48 will be presented in Table

14. The applied load variable P in this table is the average bending load applied over time during

all testing cycles for all three beams. Refer to Figure 45 in Chapter III for a visual reference of

what these constants represent. Additionally, as was discussed in the previous sub-section, the

theory models are to utilize the average cross-sectional dimensions of the three composite I-beams. Therefore, Table 14 also contains these averaged values. Lastly, both of these theory models require an Elastic Modulus of the carbon fiber laminate and the balsa wood to be known for the purposes of determining the area transformation constant 'n'. These models consider the Elastic Modulus parallel to the beam length as the only contributors in bending for each material. For the carbon fiber spar caps, this modulus is equivalently the E_1 modulus, which is parallel to the fiber orientation. As for the balsa wood, this modulus is equivalently the cross-grain E_T modulus. Both of these moduli are also listed in Table 14.

Table 14: *Composite I-Beam 3-Point Bending Beam Theory Constants and Average Properties*

Composite I-Beam 3-Point Bending Beam Theory Constants and Average Properties							
E_{Carbon}	19580.101	ksi	a	2.000	$\pm$	0.0625	in
E_{Balsa}	9.708	ksi	b	10.000	$\pm$	0.0625	in
L	24.000	in	c	10.000	$\pm$	0.0625	in
W_{bcap}	1.217	in	d	2.000	$\pm$	0.0625	in
H_{bcap}	0.060	in	e	12.000	$\pm$	0.0625	in
W_{tcap}	1.217	in	g	22.000	$\pm$	0.0625	in
H_{tcap}	0.060	in	P	49.96	$\pm$	0.112	lb
W_{web}	0.125	in	R_1	24.98	$\pm$	0.079	lb
H_{web}	1.118	in	R_2	24.98	$\pm$	0.079	lb
			k_1	-1.249E+03	$\pm$	8.643	lb-in^2
			k_2	2.498E+03	$\pm$	30.136	lb-in^3

As far as strain gages are concerned, the same CEA-06-240UZA-120 linear strain gages used in the previous chapter were also utilized here for both bending and shear strain measurements. Following consultation with Micro-Measurements Applications Engineering Manager Darryl Peterson via email, it was determined that these 240UZA gages would be suitable for use on carbon fiber and wood [46]. The main parameter that is important for strain gages on composites and wood is the overall size of the gage. This is so because the fibrous nature of both of these materials leads to the possibility of localized strain gradients across successive fibers [46]. Therefore, a larger gage will, in effect, output the average strain across a large area of fibers. A

smaller gage, on the other hand, would output a distorted strain measurement since it would be measuring strain on a smaller area of fibers, which means the localized strain gradient between fibers is more prominent [46]. The relative size of these 240UZA gages is comparable to other composite rated gages recommended by Mr. Peterson, and he confirmed that they should be suitable for measurement on these composite I-beam materials [46].

The same strain gage configurations utilized on the aluminum beams in Chapter IV were used here as well. For bending strain, a combination of half-bridge type I and half-bridge type II's were applied on the upper and lower faces of the composite I-beams. All type II's were placed at odd distance intervals from the left end of the beam in order to avoid interference with the designated deflection measurement locations along each beam's length. The type I configuration was placed on the lower face of the bottom spar cap at the length midpoint of each beam due to the load U-bolt spanning the upper face of the top spar cap at this location. The shear bridges were also half-bridge type II's. They were placed on the balsa shear web straddling the y-centroidal line at 18 inches from the left end of each beam. Care was taken to ensure that these
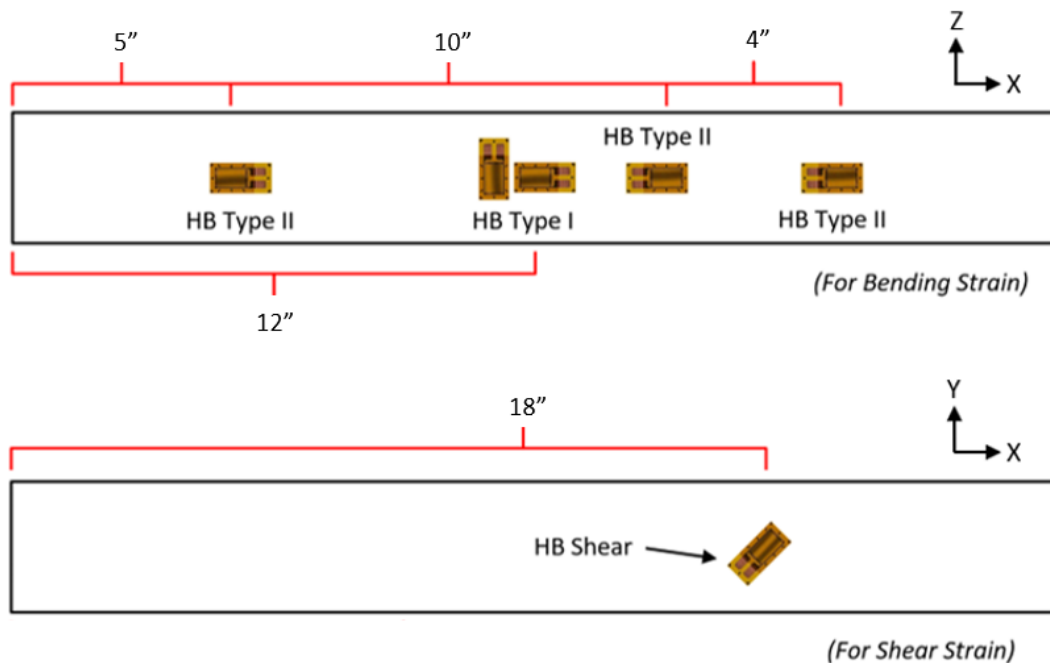
Figure 99: *Composite I-Beam Strain Gage Types and Locations*

shear bridges were not applied over either a CA joint or a lamination joint between two balsa strips. Figure 99 depicts the approximate gage location and configuration along the span of these composite beams. If needed, Section A of the Appendix also contains useful information regarding these gage configurations.

Testing Methodology

This sub-section will cover the steps taken during experimentation to properly prepare the test specimens as well as those taken to acquire the necessary data from each of the beams. With minor modifications, much of the procedure listed here is the same as what is listed for testing conducted with the metal beams in the previous chapter.

1) Refer to Steps 1 and 2 from the procedures listed in Chapter IV.
    a. On carbon fiber, replace fine-point Sharpie with a fine-point silver paint pen.

2) Prep beam surface, apply strain gages, and connect servo wires according to the following and Section A of the Appendix.
    a. Fully sand away the epoxy texture pattern on the carbon fiber laminate around the gage application sites. This texture can cause errors in gage measurements.
    b. For carbon fiber, refer to the application tutorial video cited as [47].
    c. For balsa wood, refer to the application tutorial video cited as [48].
    d. Replace M-Bond AE-10 bonding adhesive with Loctite 496 – apply pressure firmly with thumb for 6 minutes before tape removal.
    e. Draft lines can be accomplished through fine-point pen markings from Step 1.

3) Replace the stock support rails on the Vernier Structures and Materials Tester with the modified 80/20 shelf assembly as discussed in Chapter III, Section A.
    a. Ensure the shelf assembly is level and at some height between 1" and 6" above the beam's upper surface.
    b. Insert the appropriate measuring rod length into the Fowler Depth Micrometer.

4) Move support crossbars such that the inside face is ~2" from each end of the beam.

5) Center the load U-bolt at the intersection of each beam's length midpoint and top surface xbar centerline.

6) Plug in the LabPro DAQ, open the LabPro 3 application, and connect to the VSMT Force Sensor.
    a. Set force units to lb.
    b. Slowly rotate crank screw until the load U-bolt is firmly seated on the top surface of the beam but minimal load is registered in the LabPro 3 readout.
    c. Once Step 7b is accomplished, zero the sensor.

7) With the NI cDAQ-9185 unplugged, do the following:
    a. Connect the ethernet cable to the computer containing the LabVIEW strain gage readout program discussed in Chapter III.
    b. Connect all four half-bridge strain gage configurations for bending strain to channels A0-A3 (one per channel) of the cDAQ (see Appendix, Section A).
    c. Plug in the cDAQ and open the 'Bending Normal Strain Readout' LabVIEW VI.

8) Open the DAQ Assistant Block, connect to the cDAQ, and enter appropriate strain gage parameters similar to that shown in Figure 43 for each channel.
    a. Calibrate each channel's half-bridge connection by following the calibration procedure in [29]. Click OK in lower right corner of the DAQ assistant window when finished.

9) Using the Fowler Depth Micrometer, take initial undeflected depth measurements every 2" along the beam length for each 2" marking between the support crossbars.
    a. For the composite beams – start at 4", end at 20".

10) Run the front panel of the LabVIEW strain readout program, ensure four strain measurements appear (set sample rate to 1000 Hz and take 250 samples per time interval).
    a. Ensure that the Write to File button is set to OFF (red) initially before running.

11) Slowly turn the crank screw until a load of 50 lb is achieved.

    a. At this load, record the load over time in LabPro and turn the Write to File button to ON (green) in LabVIEW simultaneously. Allow to run for 30 seconds then stop recording.

    b. Stop running the LabVIEW front panel to successfully generate a strain data output '.txt' file (each file should contain ~188 lines of strain data per channel).

    c. Copy 30 seconds worth of load data from LabPro into an Excel file for future reference.

12) Using the Fowler Depth Micrometer, take final deflected depth measurements every 2" along the beam length for each 2" marking between the support crossbars.

    a. For the composite beams – start at 4", end at 20".

    b. Overall beam deflection is determined by taking the difference between Steps 12 and 9.

13) Return the beam to its initial unloaded state and repeat Steps 9-13 two more times.

    a. Once third pass is completed, return beam to initial unloaded state, and continue.

14) Unplug the NI cDAQ-9185 and do the following:

    a. Disconnect the bending strain half-bridges from the cDAQ.

    b. Connect the shear strain half-bridge to channel A0.

    c. Open the 'Shear Strain Readout' LabVIEW VI.

    d. Re-plug in the NI cDAQ and repeat Step 8 for channel A0.

15) Repeat Steps 10 and 11 three times, returning the beam to its unloaded state between passes.

16) Once the above procedure has been completed, remove the current beam test specimen and place the next beam into the structures tester. Repeat the procedure for this new beam.

    a. The full testing procedure should be completed three times in total (once for each of the three composite I-beam test specimens).

C. SolidWorks Orthotropic FEM Generation

The following section details the process of generating fully orthotropic composite Finite

Element Models for the composite I-beams. For these orthotropic models, much of the initial

model generation and preparation procedure for a 2D shell model and a 3D solid model are the

same as that discussed in Chapter IV. Discussion of the model generation procedure pertaining to

the metal I-Beam from that chapter is especially applicable here. Therefore, the following sub-

sections highlight only the new requirements necessary to implement material orthotropy into a

shell and solid FEA model within SolidWorks. If needed, refer to Section C of Chapter IV for

greater detail regarding model creation. Lastly, evaluation of SolidWorks' performance with this

orthotropic model is discussed at the end of this section.

SolidWorks Material File Creation

The first step required before the FEA models could be created was to generate the

appropriate custom material files within the SolidWorks material library. This is necessary

because orthotropic material files for balsa wood or unidirectional carbon fiber do not exist within

the material database. An isotropic balsa wood material file does exist in this database, but the

properties listed in this file are for the same density as those average properties listed in Table 3.

Because it is isotropic, however, the elastic modulus utilized in this file is the modulus in bending

from Table 3. Regardless, this pre-existing material file is unusable here because it is isotropic.

As for carbon fiber, there is a pre-existing set of carbon fiber and fiber glass material files within

the SolidWorks database. The only property listed in any of these files, however, is the lamina

density. These files are similarly defined as isotropic materials, making them equally unusable.

The following discussion will focus on the procedure required to generate custom

SolidWorks material files. In order to create custom material files, a custom material library

database must be created. To do this, one must first open the SolidWorks material library by

navigating to the feature tree on the left side of the screen, right clicking 'Material < not specified

>', and selecting the 'Edit Material' option from the drop-down menu. This is the same process discussed in Chapter IV to access the material library to apply a material to the solid part. Once in the material library, right-clicking anywhere in the window that displays all of the SolidWorks material files will give the user an option to create a new material library. Selecting the 'New Library' option from the drop-down menu then opens a File Explorer window and the user is prompted to save the new material library [49]. It is recommended that this new library be saved within the 'Custom Materials' sub-folder of the current version of SolidWorks installed on the user's computer. Once saved, this file will appear at the bottom of the materials library list, and its folder color is blue. See Figure 100 for a visual reference of the above steps.
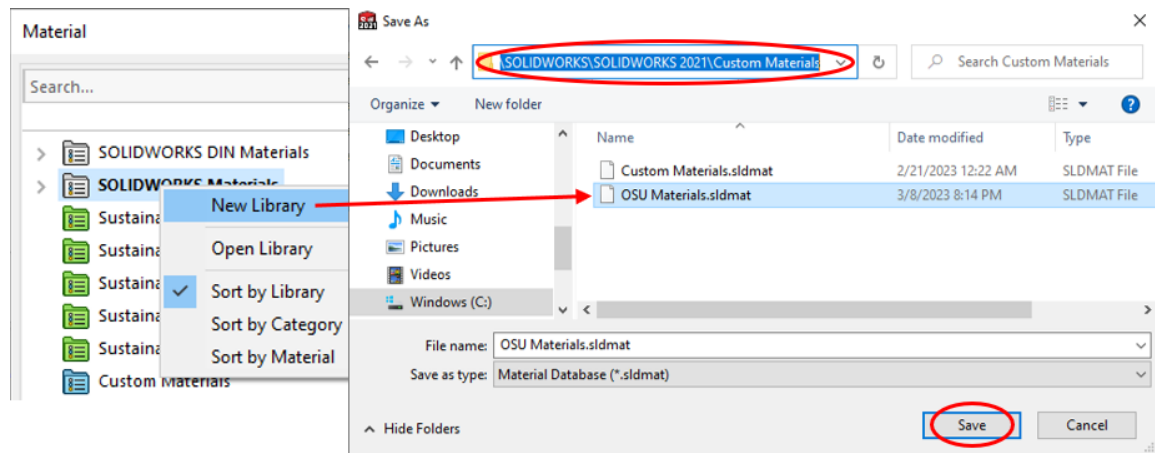
Figure 100: *Process for Generating a Custom SolidWorks Material Library*

After this custom material library has been created, material categories can be added to it. This is achieved by right-clicking on the newly created material library folder and selecting the 'New Category' option from the drop-down menu [49]. A new sub-folder will be created, and it can be renamed to whatever material type will be added to it. For this research, two new material category files were created. One was labeled 'Wood' and the other 'Composites' as Figure 101 displays. To populate these sub-folders with material files, one must again right click on the sub-folder. This time, however, the 'New Material' option must be selected. For this research, a Balsa material file was generated under the 'Wood' category, and a unidirectional carbon fiber material

146

file was generated under the 'Composites' category. Figure 101 also depicts the addition of these material files, which are highlighted in the figure.
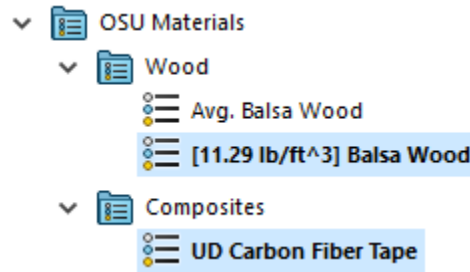
Figure 101: *Custom Library Material Category and File Population*

With these material files created, the orthotropic mechanical properties for each material on the composite I-beam could be entered into the corresponding material file. Initially, a newly created material file will default to a 'Linear Elastic Isotropic' model type. To access the orthotropic property entries, this model type must be changed. This can be accomplished by selecting the new material file, navigating to model type, and selecting 'Linear Elastic Orthotropic' from the drop-down menu [49]. Once this is selected, it is important to click the checkbox next to the model type selection menu and then click the save button at the bottom of the material library window. If this is not done, SolidWorks will automatically default the material file to the original isotropic model type. The orthotropic model can still be accessed by manually selecting the orthotropic model from the menu when applying the material, however.

After the file is configured, the orthotropic properties for the material can be added to it. Figure 102 displays the fully populated material files for both the balsa wood and unidirectional carbon fiber laminate materials, which compose the composite I-beam test specimens. Some key aspects of these material files are worth noting here. The version of these files as they appear in Figure 102 is how they appear when applying the material for FEA. The mechanical properties listed in red text are properties that must be defined for the FEA solver to properly account for the material orthotropy [49]. Those in blue text are suggested but not required unless performing either analyses involving yielding, failure, or thermal inputs [49]. The properties for balsa wood

147

Properties Tables & Curves Appearance CrossHatch Custom Application D ◀

Material properties
Materials in the default library can not be edited. You must first copy the material to a custom library to edit it.

Model Type: Linear Elastic Orthotropic ▾   ☐ Save model type in library
Units: English (IPS) ▾
Category: Wood
Reference geometry
Balsa (3D)
Name: [11.29 lb/ft^3] Balsa Wood
Default failure criterion: Max von Mises Stress ▾
Description: Balsa Wood Mechanical Properties for ~11.3 lb/ft^3
Source: Specialized Balsa
Sustainability: Balsa in SOLIDWORKS Materials : Wo   Select...

Property	Value	Units
Elastic Modulus in X	725043.6506	psi
Elastic Modulus in Y	9717.528424	psi
Elastic Modulus in Z	33213.64193	psi
Poisson's Ratio in XY	0.009	N/A
Poisson's Ratio in YZ	0.229	N/A
Poisson's Ratio in XZ	0.231	N/A
Shear Modulus in XY	16824.37757	psi
Shear Modulus in YZ	36259.43442	psi
Shear Modulus in XZ	28862.5098	psi
Mass Density	0.0065321053	lb/in^3
Tensile Strength in X		psi
Tensile Strength in Y		psi
Compressive Strength in X	129.0835865	psi
Compressive Strength in Y	2161.062291	psi
Shear Strength in XY	323.434155	psi
Yield Strength	2161.062291	psi

Properties Tables & Curves Appearance CrossHatch Custom Application D ◀

Material properties
Materials in the default library can not be edited. You must first copy the material to a custom library to edit it.

Model Type: Linear Elastic Orthotropic ▾   ☐ Save model type in library
Units: English (IPS) ▾
Category: Composites
Reference geometry
Carbon (3D)
Name: UD Carbon Fiber Tape
Default failure criterion: Max von Mises Stress ▾
Description: 3.07 oz/in^2 / 120 deg. Celcius epoxy cure cycle / Lay
Source: ACP Composites Std. Modulus CF UD
Sustainability: Undefined   Select...

Property	Value	Units
Elastic Modulus in X	19580094.58	psi
Elastic Modulus in Y	1450377.377	psi
Elastic Modulus in Z	1450377.377	psi
Poisson's Ratio in XY	0.3	N/A
Poisson's Ratio in YZ	0.554	N/A
Poisson's Ratio in XZ	0.3	N/A
Shear Modulus in XY	725188.6883	psi
Shear Modulus in YZ	997134.4465	psi
Shear Modulus in XZ	725188.6883	psi
Mass Density	0.0578036509	lb/in^3
Tensile Strength in X	217556.6065	psi
Tensile Strength in Y	7251.886883	psi
Compressive Strength in X	174045.2852	psi
Compressive Strength in Y	36259.43442	psi
Shear Strength in XY	10152.64164	psi
Yield Strength	174045.2852	psi

Figure 102: *Full Orthotropic Balsa and Unidirectional Carbon Fiber SolidWorks Material Files*

were entered using the properties listed in Table 12, the Poisson Ratios from Table 3, and the

failure limits determined by [13] – [16]. On the other hand, the carbon properties were entered

using the values listed in Table 1 as well as the failure limits listed in [10]. For the carbon fiber,

the 3-direction properties (or globally, the z-direction) were determined via transverse isotropy

assumptions, meaning $E_2 = E_3$, $G_{12} = G_{13}$, and $\nu_{12} = \nu_{13}$. General trends in the relationship

between the 12 and 23 Shear Moduli and Poisson ratios for typical carbon fiber materials as listed

in [9] further determined the G_{23} and ν_{23} entries in this file. The reference geometry selection box

at the top of both material files will be addressed in subsequent sub-sections.

Another point of interest is the ordering of mechanical properties within these files. When

attempting to enter data into these files, it was discovered that SolidWorks will not save the file

unless the E_x Elastic Modulus entry corresponds to the largest Elastic Modulus of the orthotropic

material. This was an issue for the balsa material file, requiring the E_L and E_T moduli to swap

their initial global coordinate assignments, which also caused the corresponding Poisson ratios and Shear Moduli tied to the L and T balsa axes to swap global coordinate definitions. Fortunately, this was not an issue for the carbon fiber as the desired convention that the E_1 fiber modulus be parallel to the global x-axis resulted in the largest Elastic Modulus being assigned to the x-direction. Figure 103 shows how each material's locally defined axis system is defined globally in SolidWorks within these material files. In addition, the file also cannot be saved if the Yield Stress limit for the material is left blank. Since neither of these materials actually experiences yielding before failure, this issue was resolved by entering the lowest ultimate limit parallel to the length of the I-beam for each material. For the carbon fiber, this was the ultimate compressive limit in the 1-direction. For the balsa wood, this was the ultimate compressive limit in the cross-grain T-direction.
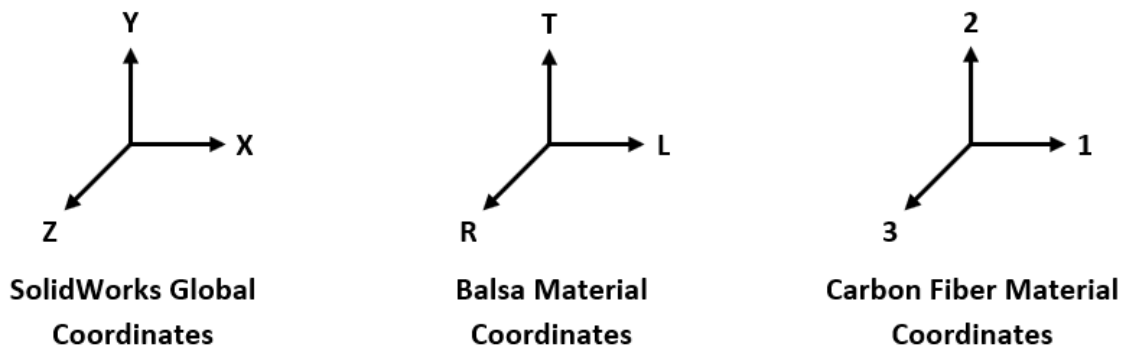
Figure 103: *Material Axes Defined in Terms of the SolidWorks Global Coordinate System*

Composite I-Beam 3D FEM

Following the creation of the material files, the orthotropic Finite Element Models for the composite I-beam were generated. Just as was done for the metal beams in Chapter IV, both a 3D solid model and a 2D shell model were generated for the composite I-beam. This current sub-section will cover the procedure taken to generate the orthotropic solid model while the following sub-section will explore the procedures for the orthotropic shell model. As was stated previously, these models were generated using the average of the experimentally measured cross-sectional

dimensions for the three composite I-beams that were tested. Figure 104 shows the resulting average cross-sectional sketch of the I-beam model. Moreover, the majority of the procedures followed to generate these orthotropic models borrow directly from the steps taken to generate the metal I-beam models from Chapter IV. As such, only relevant additions to this established procedure will be covered in detail in the following sub-sections.
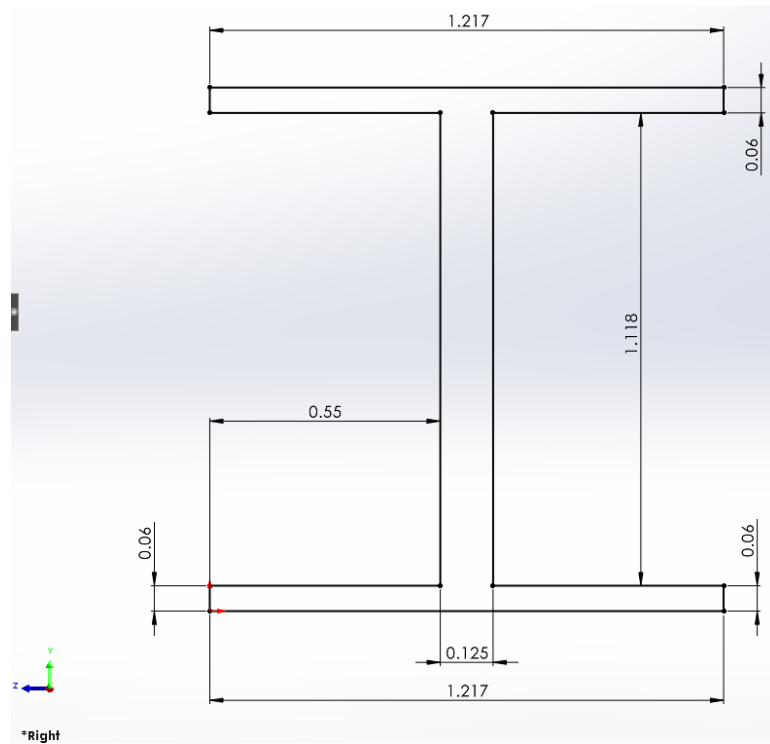
Figure 104: *Composite I-Beam Average Cross Section*

After extruding the cross-section as shown in the above figure to a length of 24", the first of the new model preparation requirements can be addressed. The beams utilized in Chapter IV were all composed of one singular material, but this is no longer the case for these composite I-beams. If attempting to apply materials for FEA to this model after extruding the cross-section to length, only one material can be applied to the entire beam model. This is not suitable for these beams where the spar caps and the shear web are two different materials, thus requiring the spar caps and the shear web to be separate entities from each other in the model. It was determined that the Split Tool was best suited for this task. This tool was discussed in Chapter IV as an alternative to

the Split Line Tool, but it was passed over in favor of the Split Line Tool then. As was covered in

Chapter IV, the Split Tool works by using some reference geometry to split a solid body into two

or more smaller solid bodies. The resulting split bodies become independent of each other,

allowing the user to assign unique material properties to each of these split bodies. For this

model, a reference plane was added that was parallel to and coincident with the lower face of the

top spar cap and another plane was added that was parallel to and coincident with the upper face

of the bottom spar cap. These two planes were used as the splitting geometry for the Split Tool, as

Figure 105 demonstrates.
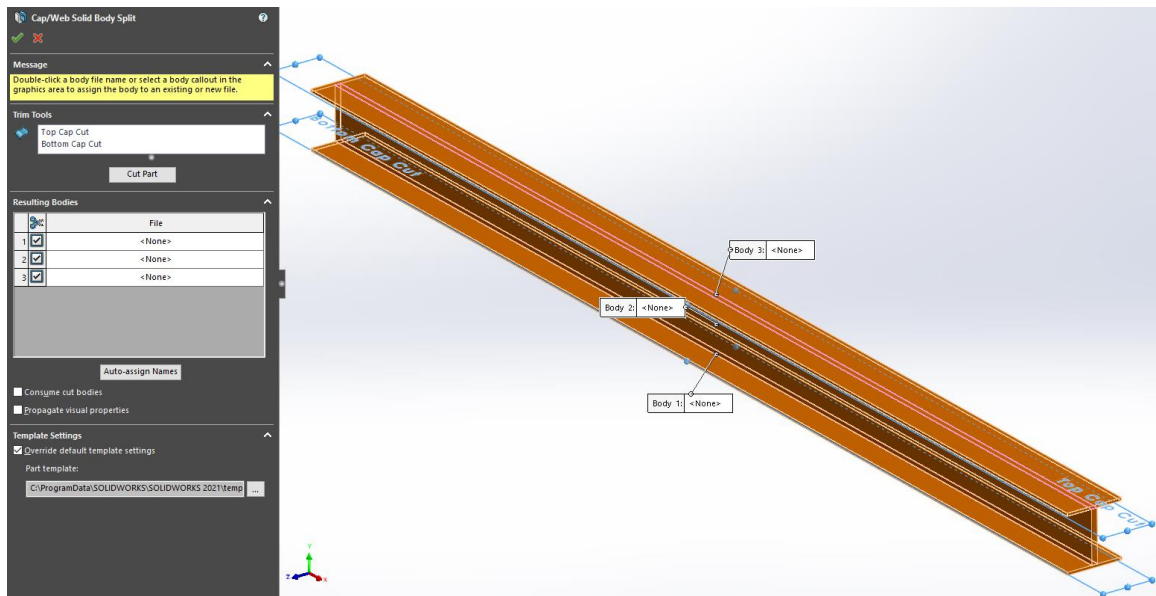
Figure 105: *Splitting the Composite I-Beam Using the Split Tool*

Upon splitting the beam into three solid bodies (the upper spar cap, the shear web, and the

lower spar cap), the necessary model split lines could be added in a similar fashion to how they

were applied in Chapter IV. The boundary condition split lines were placed on the lower face of

the bottom spar cap at lengthwise positions of 2" and 22" from the left end of the beam. The load

split lines were placed on the upper face of the top spar cap such that one was 0.375" before the

12" midspan of the beam while the other was 0.375" after this midspan location. The shear split

line was positioned on a side face of the shear web at a lengthwise position of 18" from the left

end of the beam. A final split line was added to the bottom face of the lower spar cap which runs the length of the beam. The purpose of this split line was for lengthwise sampling of bending stresses/strains and beam deflections.

Before importing this model into the SolidWorks Simulation space, one final new model preparation technique was required. As was mentioned in the previous sub-section, when attempting to apply an orthotropic material to a solid part, the material window asks the user to select a reference coordinate system, which can be seen in Figure 102. If a reference coordinate system is not selected, SolidWorks does not know on which axis to apply the mechanical properties and, therefore, cannot solve the FEA [49]. In the case of the material files as defined in Figures 102 and 103, this reference coordinate system cannot be the default global (x,y,z) system in SolidWorks. For the balsa wood, if this were the chosen system, the with-grain L properties would be defined along the length of the I-beam while the cross-grain T properties would be defined along the height of the beam, which is the opposite of how the balsa shear webs are constructed for the composite beams. In the case of the carbon fiber, the 2-direction must be defined on a horizontal plane perpendicular to the 1-direction, which is not how it would be defined using the global coordinate system. In order to properly adjust the coordinate systems for
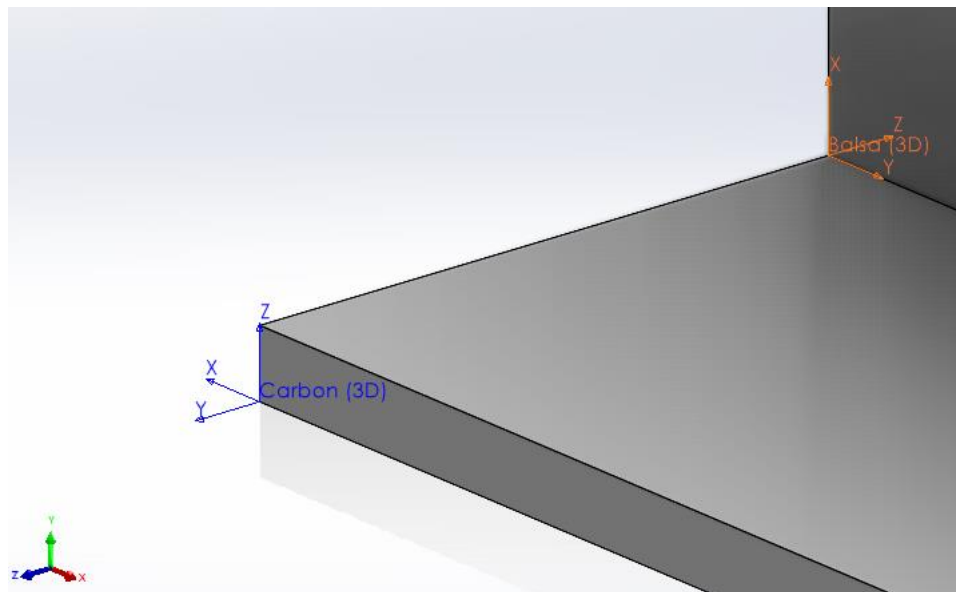
Figure 106: *Reference Coordinate Systems for Balsa Wood and Carbon Fiber Orthotropy*
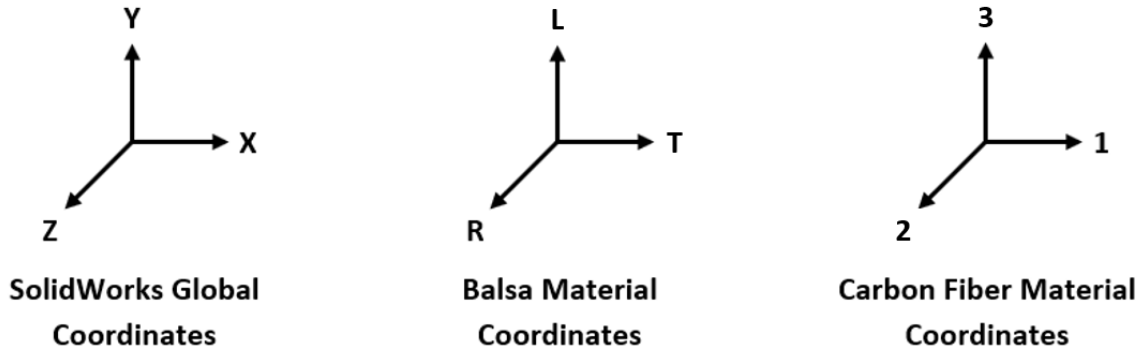
Figure 107: *Corrected Material Global Coordinate System Definitions*

each material, custom reference coordinate systems were inserted into the model (see Figure

106). The resulting adjusted material coordinate systems relative to the SolidWorks global system

is depicted in Figure 107. With these coordinate systems correctly defined for both materials, the

model could be imported into the FEA Simulation space. In preparing the model here, when

applying the orthotropic balsa material to the shear web, the 'Balsa (3D)' reference coordinate

system must be selected. Likewise, when applying the unidirectional carbon fiber material to the

spar caps, the 'Carbon (3D)' coordinate system must be selected.

The final preparation step was to ensure that the automatically generated bonded contact set

was properly applied to the model. Because the split tool was utilized, the original solid part I-

beam essentially became an assembly composed of three solid parts. When importing these split

bodies into the Simulation space, it automatically identified that there were individual bodies in

contact with each other, and SolidWorks generated a globally bonded contact set as a result.

When testing this orthotropic model initially, it was found that this globally bonded contact set

was not always applied correctly, resulting in the spar caps clipping through the shear web

following the completion of trial FEA runs. From [49], the most effective method to utilize in

order to ensure the contact set was applied properly was to define the contact set manually.

Therefore, the global contact set that was generated automatically was deleted and replaced with

a 'Local Interaction' contact set. This tool is straightforward to use as long as the user selects the

'automatically find local interactions' option, selects all three solid bodies, and changes the

contact type to 'Bonded' [49]. SolidWorks will then automatically define the areas of contact

between two or more bodies and will display a list of found contact interactions in the 'Results'

window. Clicking on the button with the green plus sign will generate the selected contact set

from this 'Results' window. Figure 108 demonstrates this process.
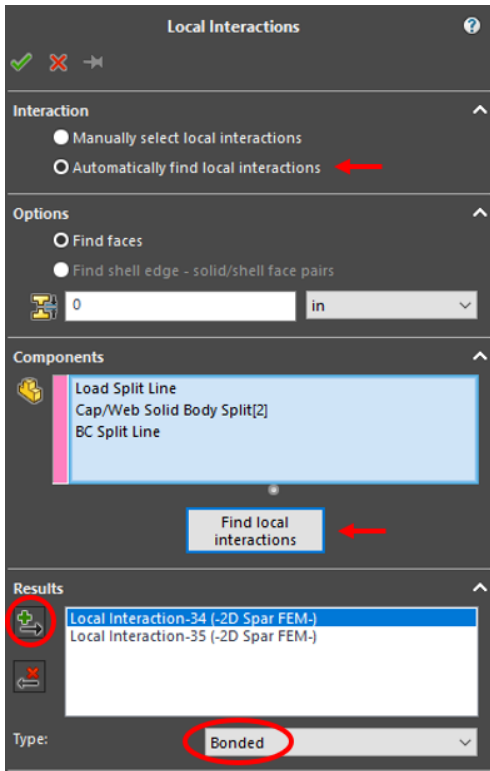
Figure 108: *Procedure for Utilizing the Local Interactions Connections Tool*

After these contact sets were properly defined, the remainder of the necessary model setup,

such as applying boundary and loading conditions as well the meshing, all followed established

procedures from Chapter IV. Boundary conditions were applied using the 'Advanced Fixture'

tool such that one end of the beam was on a frictionless roller free to translate in the x-axis while

the other end was pinned on a static hinge and was only free to rotate. A load of 49.96 lb was

applied between the load split lines on the upper face of the top spar cap. This loading is the

average load exerted on the test specimens during experimentation. Finally, manual meshing

again confirmed that a mesh element size of 1/8" or smaller was sufficiently fine such that the

resulting FEA solution was no longer dependent on the mesh size. The resulting orthotropic solid model is viewable in Figure 109 with a high-quality mesh of element size $1/8^{th}$ of an inch applied.
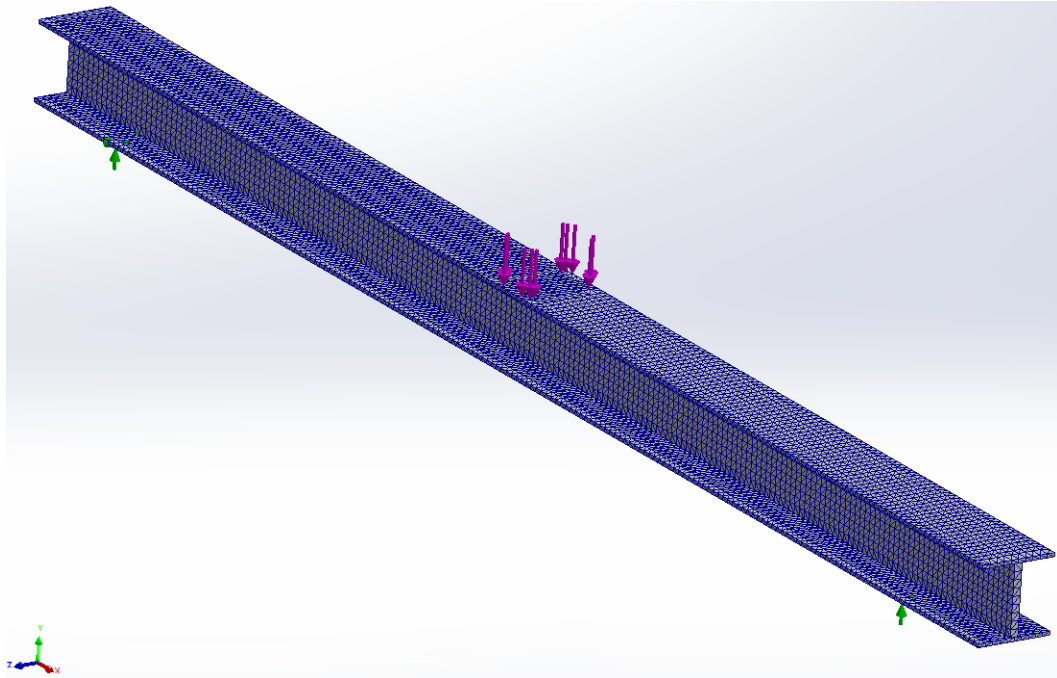
Figure 109: *3D Orthotropic FEM I-Beam SolidWorks Model*

Composite I-Beam 2D FEM

Generation of the orthotropic 2D shell model began by following the procedure from Chapter IV pertaining to the creation of the metal I-beam shell model. A new model configuration was added and corresponding features, reference geometry, and sketches were configured for either the 3D solid model as discussed in the previous sub-section or this newly created 2D shell model. The 2D surface idealization of the 3D geometrical cross-section shown in Figure 104 was accomplished using the same steps covered in [41]. The same split line locations discussed in the previous sub-section for boundary and loading conditions as well as for post analysis data sampling were re-introduced to this 2D FEM. Once all of the above was completed, the first of the new shell model preparation requirements could be addressed.

Similar to the orthotropic solid model, custom material coordinate systems needed to be defined for the FEA solver. For the 2D FEM, however, only one reference coordinate system for the balsa wood had to be created. This system was oriented the same as the 'Balsa (3D)' system shown in Figure 106, but it was given the name 'Balsa (2D)' to distinguish it from the 3D model coordinate systems. As for the carbon coordinate system, there is no need to define a custom system when dealing with a fabric composite material applied to a shell model. The reasons for this will be discussed shortly. After importing the model into the simulation space, the same procedure as was followed in Chapter IV for configuring the shells for analysis was again followed here. The shear web had the orthotropic balsa wood material applied to it with the 'Balsa (2D)' reference coordinate system chosen for mechanical property orientation. The 'thin shell' solving method was chosen for the same reasons covered in Chapter IV, and a shell thickness of 0.125" was applied.

For preparation of the unidirectional carbon spar cap surfaces, instead of again applying a thin shelled solving methodology, there is an option in the shell manager to apply a composite shell type to a surface. This shell type allows the user to define a laminate with specified ply orientations, thicknesses, and material properties [49]. Because the spar caps are, in fact, a fabric composite laminate, each composed of 12 layers of 0.005" thick unidirectional carbon fiber, this shell element type is applicable for this model. What is convenient about this shell type is that it automatically defines the correct coordinate system for the composite shells as Figure 110 depicts. In this figure, the composite shell type is applied to the top spar cap, and the tool automatically adjusted the coordinate system for the material to be similar to the custom coordinate system inserted for the solid model's carbon fiber in Figure 107. This automatically defined coordinate system is circled in Figure 110. On this coordinate system, the global laminate x-direction is equivalently the red arrow while the y-direction is equivalently the green arrow. The gray/white arrow that also appears is the fiber orientation arrow [49]. As a demonstration, ply 1 in this figure was adjusted to have the fibers (the material1-direction) rotated 40-degrees off the

global laminate x-axis, which is what the white arrow indicates. However, for this shell model, all

12 laminae for both spar caps were defined with a thickness of 0.005" and a fiber orientation

parallel to the global laminate x-axis. This caused the white orientation arrow to coincide with the

red axis arrow for all laminae in the laminate. The 'Carbon (2D)' custom coordinate system

present in the below figure was never used.
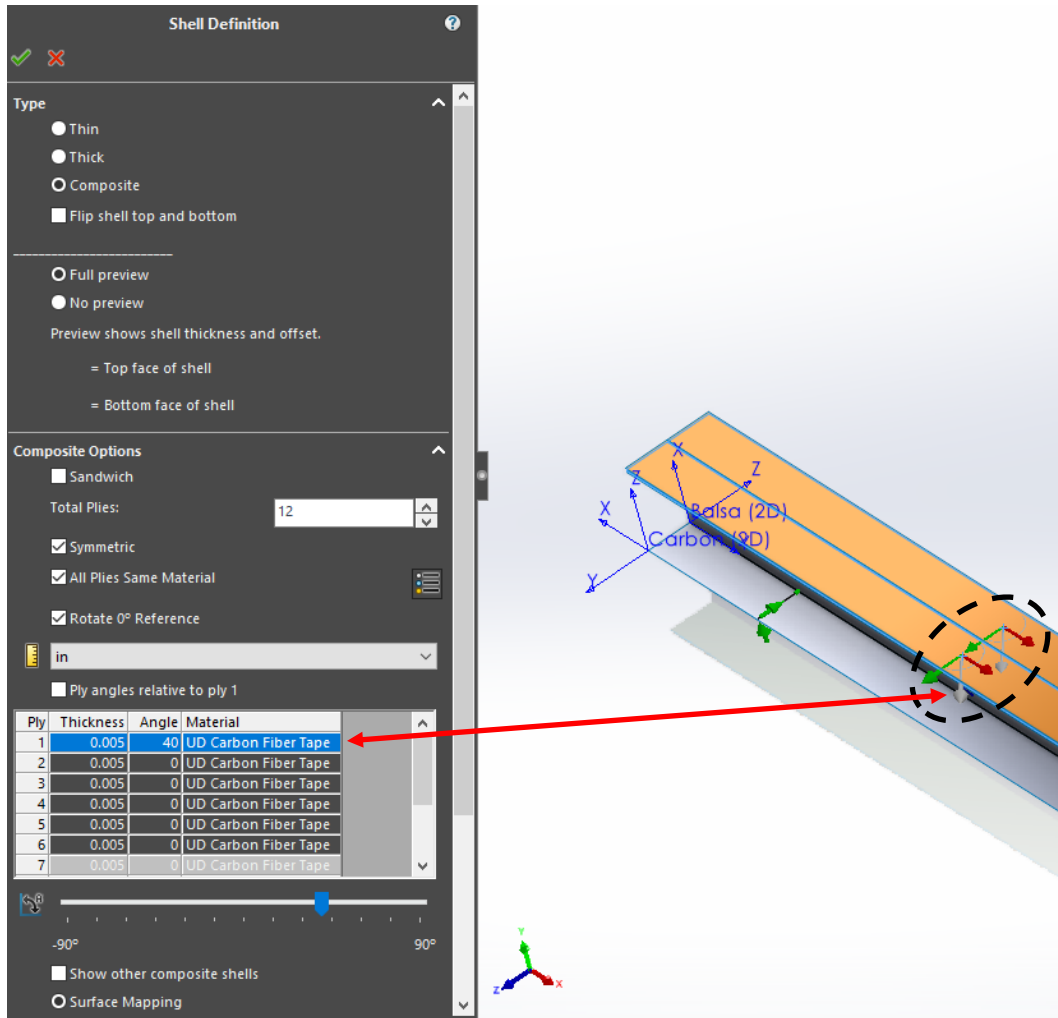
Figure 110: *Defining a Composite Laminate for Orthotropic Shell Models*

Once the spar cap laminate shells were fully defined, the remainder of the model preparation

was the same as for all previous FEA models discussed in this document. The same 49.96 lb

loading condition applied to the solid orthotropic model was again applied between the load split

lines for this shell model. Additionally, the same boundary conditions applied to the solid model
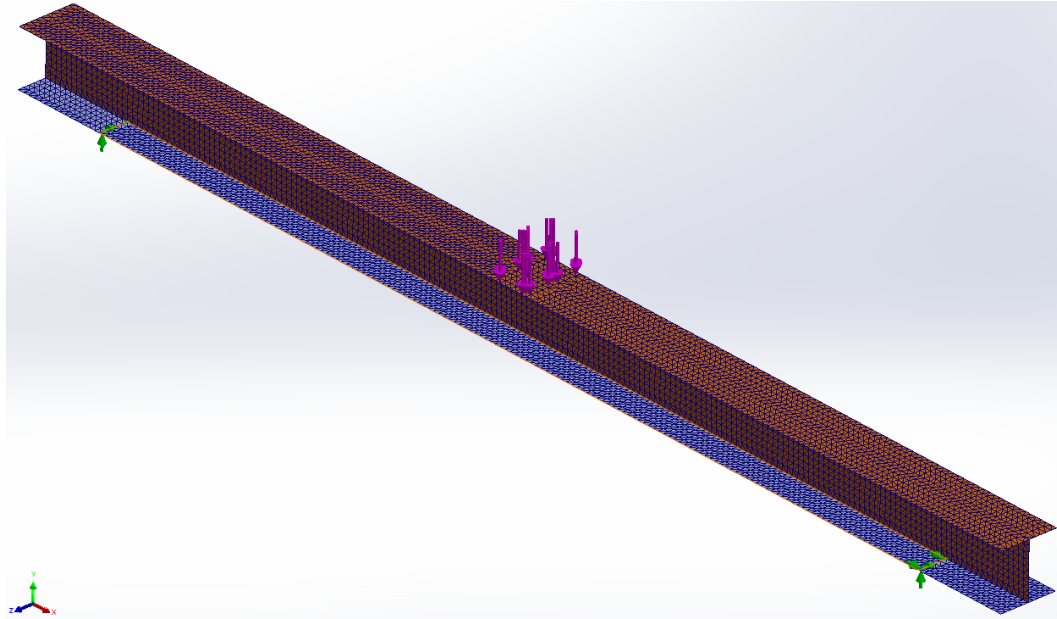
Figure 111: *2D Orthotropic FEM I-Beam SolidWorks Model*

were similarly applied to this shell model's constraint split lines. The resulting orthotropic 2D

Finite Element Model can be viewed in Figure 111 above. Regarding this finalized model, the

orange faces are equivalently the bottom shell thickness while the gray faces are equivalently the

top shell thicknesses [49]. In terms of the composite shells applied to the spar caps, orange

signifies the first ply in the laminate while gray signifies the 12th ply. Especially for the composite

shell surfaces, it is important to know this relationship, as any FEA model with a composite shell

applied to it will automatically output stresses and strains in terms of either the first ply, last ply,

laminate membrane, or the overall max/min across all plies in the laminate. Since stresses and

strains are to be experimentally measured on the outer laminate surfaces (corresponding to the

orange faces on the spar caps in the figure), all stress and strain FEA solutions must be in terms of

the stresses and strains on ply #1. This definition can be adjusted by right-clicking on the stress or

strain result option at the left of the screen and selecting 'Edit Definition' from the drop-down

menu. The first menu that appears will allow the user to select the 'Bottom Shell' for solution

output, and for composite shells, the exact ply number desired can be entered.

Orthotropic Model Evaluation

Before any data sampling from the model or comparison with empirically acquired data took place, it was evident that both the shell and solid models did not converge on expected solution trends for a beam in three-point bending. For one, the overall beam's deflection curve did not maintain the expected U-shape but rather took on more of a V-shape between the supports (see Figure 112). Moreover, the typical constant slope of the beam beyond the supports was not maintained. Instead, the beam overhang beyond the supports behaved as though the ends of the beam were clamped. Given that the same boundary conditions applied to these models were applied to the previous chapter's metal beam models (where good correlation between the empirical and FEA data was found), this behavior in the orthotropic models was surprising. To get an idea of how well (or not) these current models predicted the experimental data, their deflection and bending strains were compared first as the number of data points acquired experimentally for these parameters was the largest. As can be seen in Figures 113-114, these orthotropic models did not model the physical composite I-beams well. Interestingly, however, neither did the Beam Theory approaches, at least in terms of deflection. Discussion into why these theory approaches also did not perform well will be covered later in this chapter.
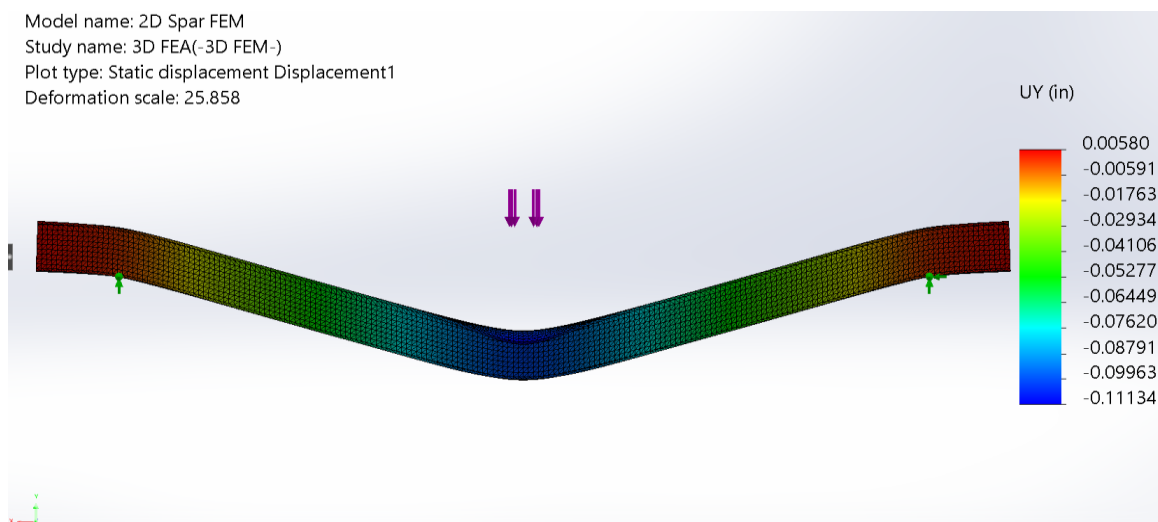
Figure 112: *Orthotropic Solid Model FEA Solution*
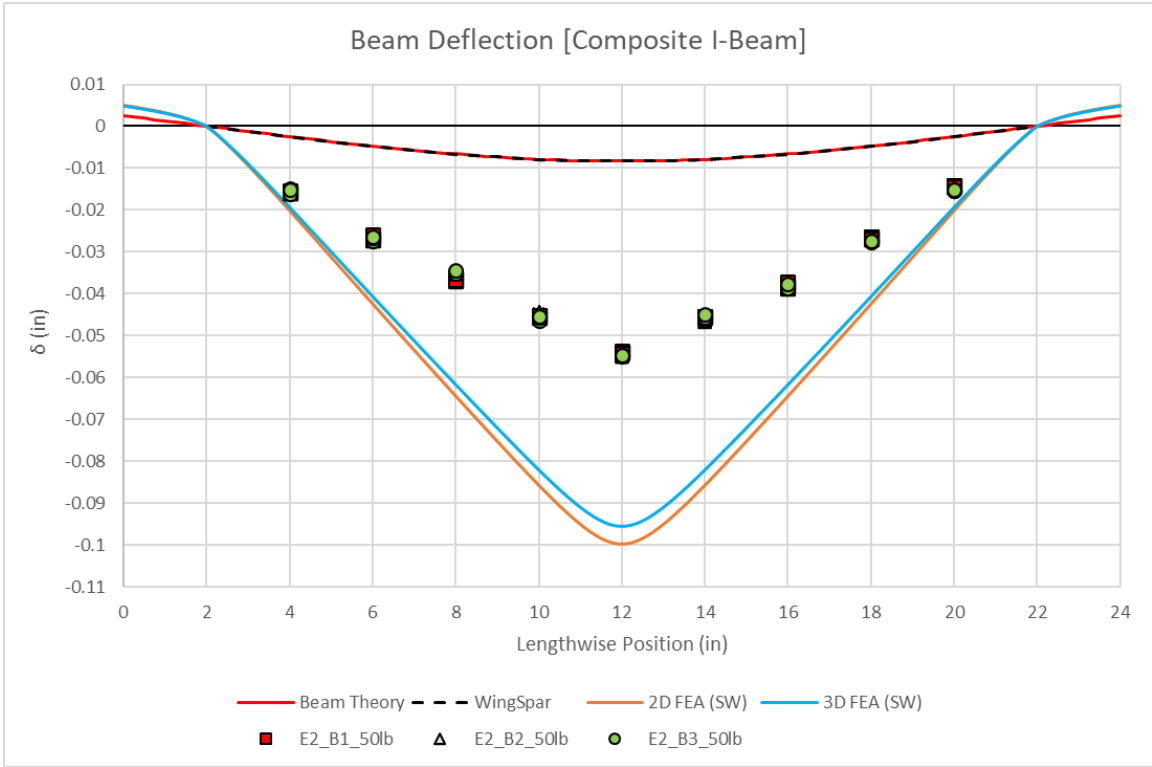
Figure 113: *Orthotropic Models' Deflection Results*
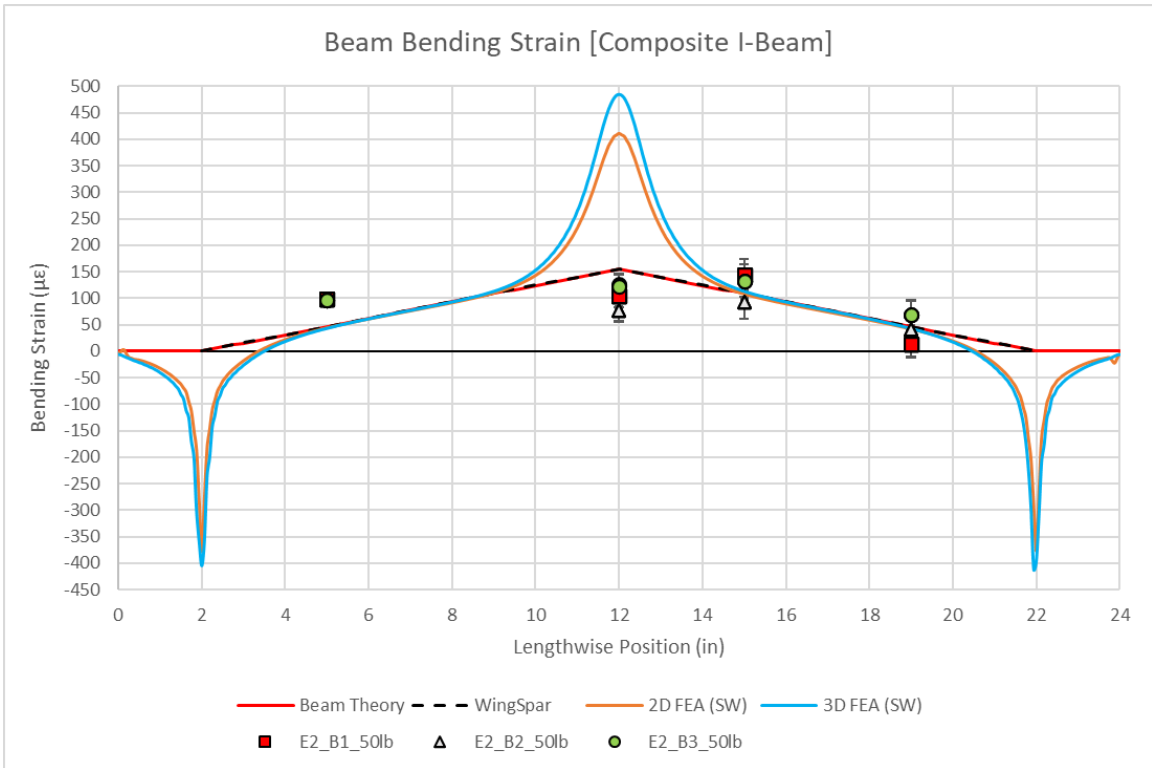
Figure 114: *Orthotropic Models' Bending Strain Results*

160

Deflection-wise, both SolidWorks FEA models of the composite I-beam can be observed to be approximately two times less stiff than was actually found to be the case through experimental testing. The datapoints plotted for the empirically acquired deflections represent each of the three test I-beams constructed as detailed at the beginning of this chapter. A total of nine lengthwise stations along each beam were sampled for deflection under load, with each beam being sampled in this manner a total of three times. This method of testing resulted in 81 deflection datapoints gathered from the physical model. All 81 of these points are present in Figure 113. Given how all 81 datapoints are coincident or near coincident is a testament to the meticulous care that was taken when manufacturing the physical test specimens while also lending support to the validity of these experimental deflection measurements over FEA.

Considering the comparison of bending strains in Figure 114, the stress concentration issue in the I-beam models that was identified in Chapter IV persisted and even got worse. Instead of being localized within roughly an inch of the beam supports, these models' concentrations distort up to five inches of the FEA bending strain curves on either end of the beam. Additionally, another concentration was generated at the point of the applied load in the models, which greatly exaggerated the resulting maximum bending stress in the I-beam. In fact, the Beam Theory approaches did much better at predicting the lengthwise bending stress distribution. Similar to the deflection data, four lengthwise stations were sampled for bending strain on each of the three beams, and each beam was again tested three times. The resulting 36 bending strain datapoints acquired are represented in Figure 114. Despite the variability in these datapoints (causes of which will be addressed later in this chapter), it is evident that the trend of these points more closely resembles the expected linear V-shaped bending strain curves of the Beam Theory approaches than the non-linear stress curves generated from the FEA models. Despite this, there is a brief region between the supports where the FEA model results coincide with the Beam Theory models, indicating that SolidWorks was at least trying to appropriately solve the bending stresses in these beams.

Given how poorly the deflection and bending strain FEM solutions predicted the physical behavior of the beam in three-point bending, it is no surprise, then, that the FEA shear strain predictions do not correlate well to either of the Beam Theory approaches or to the empirical data. This is evidenced by the FEA shear strain curve not adhering to typical shear stress trends for an I-beam in the figure below. Despite yet another poor performance here, it should be worth noting that not much else can be gained from the shear strain comparison below. As can be observed, the experimentally measured shear strains in the balsa wood are considerably lower than what was expected to be the case (based off NRMSE trends established in Chapter IV). As will be addressed later in this chapter, it is likely that unavoidable error due to instrumentation use is to blame. Apart from this, the WingSpar beam theory solution only calculates the maximum shear stress experienced in the balsa shear web. This maximum stress output is represented by the black dotted line plotted in Figure 115 below.
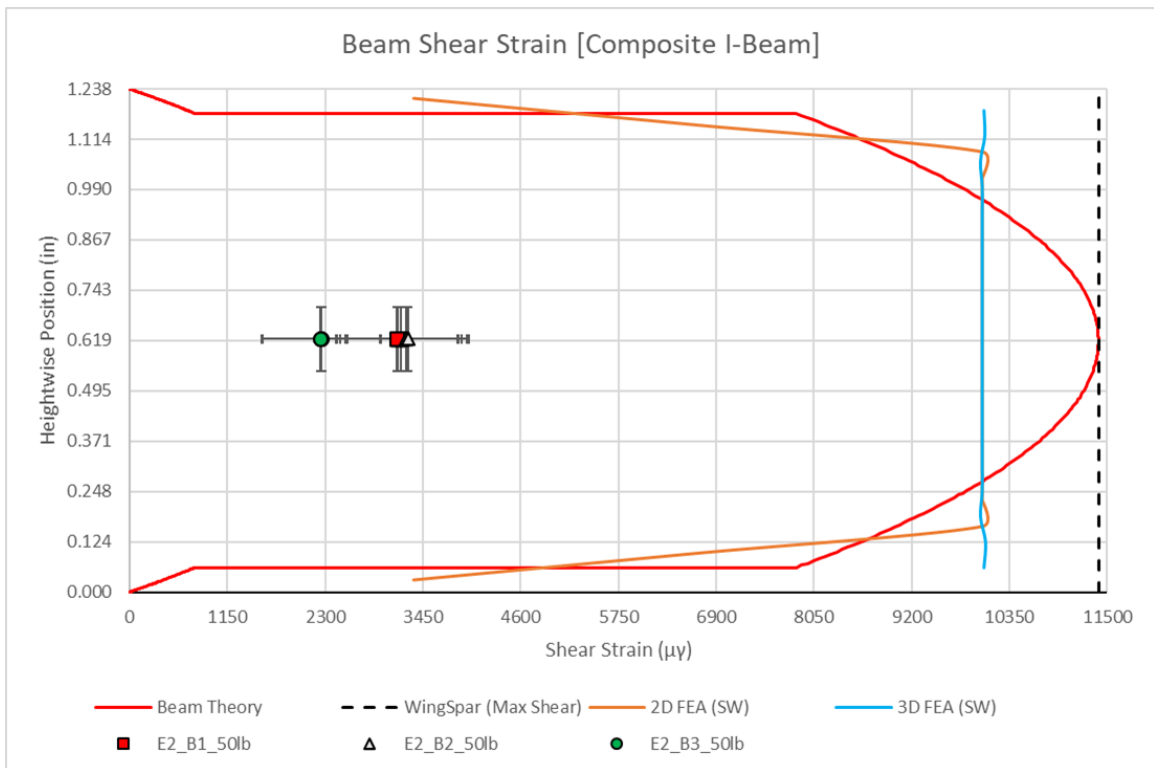
Figure 115: *Orthotropic Models' Shear Strain Results*

Following the above comparison, an investigation into the orthotropic models was undertaken to determine what, if anything, was causing such an obvious deviation from the physical system. Initially, suspicion was placed on the bonded contact set as well as the boundary conditions implemented in the models. If these were implemented incorrectly, it could explain why the beam ends acted as though they were clamped. Additionally, as was found in Chapter IV, incorrect boundary conditions/model interactions greatly affected the resulting beam deflection solution. If the boundary conditions were indeed wrong, this could also explain why the FEA solutions represented a beam that was much less stiff than the physical I-beams. A simple two step check was devised to determine the validity of the boundary conditions and the bonded contact set. The first step would check these constraints against the same exact I-beam, except the material definitions were changed so that the shear web and the caps were composed of Aluminum 6061. The resulting FEA deflection solutions reverted to the U-shaped curve, as would be expected for the case of three-point bending (see the top of Figure 116). The second step would check the exact same I-beam model, but with the shear web material being changed to Plain Carbon Steel such that the bonded contact set was enforced on an isotropic composite beam. Once more, as the bottom of Figure 116 indicates, this test again resulted in the expected U-shaped deflection curve. It was then concluded that neither the boundary conditions nor the bonded contact set were to blame for the trends observed in Figures 113-114.

Having ruled out the applied constraints on the models, attention turned to the orthotropic nature of the materials applied to these I-beams. The material files shown in Figure 102 and the source data from which each material's mechanical properties were acquired were meticulously reviewed. Unfortunately, no obvious error could be found in how the properties were determined, input into SolidWorks, or applied to the shell and solid models. In a final effort to validate the material file creation and application process applied to these models, it was decided to change the material definitions to some other combination of orthotropic materials pre-defined in the SolidWorks material library. Reversion of the FEA models to the expected U-shaped deflection

Model name: 2D Spar FEM
Study name: 3D FEA(-3D FEM-)
Plot type: Static displacement Displacement1
Deformation scale: 156.313
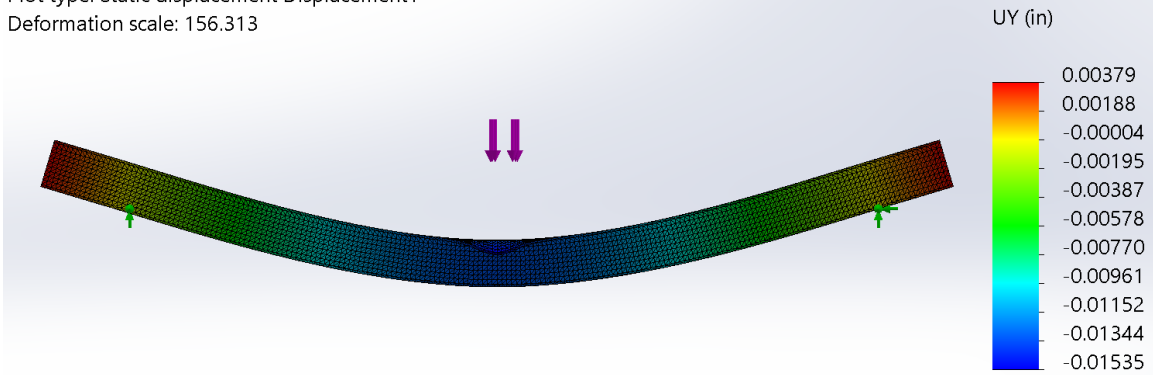
UY (in)

0.00379
0.00188
-0.00004
-0.00195
-0.00387
-0.00578
-0.00770
-0.00961
-0.01152
-0.01344
-0.01535

Model name: 2D Spar FEM
Study name: 3D FEA(-3D FEM-)
Plot type: Static displacement Displacement1
Deformation scale: 220.67

UY (in)

0.00261
0.00126
-0.00009
-0.00144
-0.00279
-0.00413
-0.00548
-0.00683
-0.00818
-0.00953
-0.01088
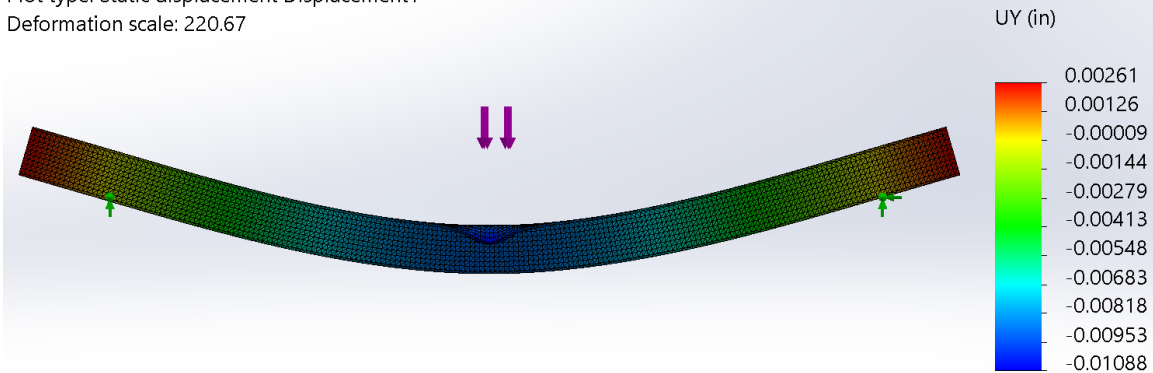
Figure 116: *Constraints Check Using Identical Cross-Section of Isotropic Homogenous Composition (**Top**), Isotropic Composite Composition (**Bottom**)*

trend under this new combination of orthotropic materials would indicate that the modeling error involved the custom orthotropic material files. Surveying the list of materials in the base SolidWorks material library revealed that not a single material listed in this database has an orthotropic material definition. Even for materials listed in this database that should be orthotropic, such as woods or fabric composites, no such orthotropic definition existed. All materials in the SolidWorks material library are either defined as isotropic or, in the case of the fabric composite materials, they simply do not have any mechanical properties defined other than the density of the material. This discovery, unfortunately, constituted a dead end for this effort. Despite this, the results from Figure 116 did suggest that something regarding the introduction of material orthotropy to the FEA models was to blame for its poor performance.

Having exhausted probable causes with the SolidWorks models that could be fixed, if needed, it was decided to determine if SolidWorks FEA's handling of orthotropic composite beams in general was the issue. For this, the exact same model was replicated using Ansys. Ansys, for the purposes of FEA, affords the user greater control over model preparation, such as providing a larger library of available mesh element types. In order to reduce potential additional causes of error, the model here was generated using TET elements with an element size of 1/8th of an inch, just like the SolidWorks models. The boundary and loading conditions were replicated as accurately as possible using Ansys loads and fixtures. The resulting solution from Ansys displayed the exact same V-shaped deflection trend with similar magnitudes of deflection, bending stress, and shear stress as was found using SolidWorks. See Figures 117-118 for examples of this similar result. In the case of the deflection data as shown in Figure 118, the Ansys model was stiffer than either of the SolidWorks models. Regardless, the Ansys model predicted deflections and stresses more in agreement with the SolidWorks models than the experimentally acquired data. With this result, two possible conclusions regarding either program's ability to model the orthotropic composite I-beam were formulated. First, the same issue in the creation and definition of the orthotropic carbon and balsa material files was unknowingly replicated for the Ansys model. Or, secondly, the fact that both programs reached
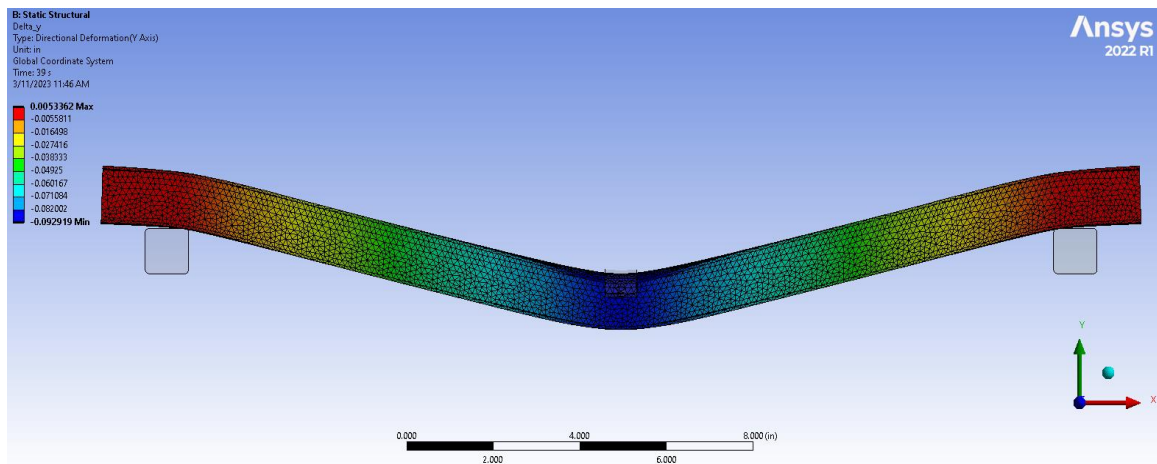
Figure 117: *Orthotropic Solid Model FEA Deflection Result from Ansys*
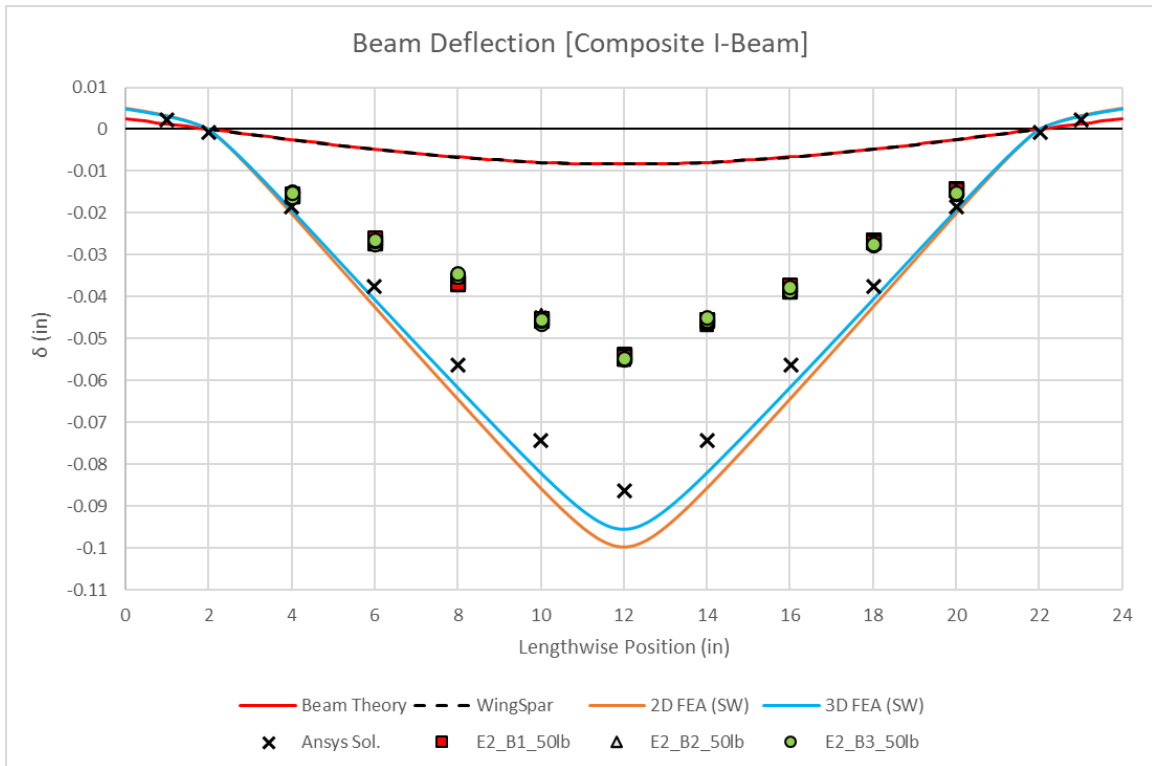
Figure 118: *Ansys FEA Deflection Compared to SolidWorks FEA Deflection*

the same result indicates that this is simply how FEA deals with orthotropic composite beams. It

was then decided to investigate the validity of the latter conclusion so as to rule it out.

For this portion of the investigation, considerable time was spent surveying both Ansys and

Abaqus FEA program user forums as well as journals discussing similar modeling trends. The

goal was to find proof that would either validate or invalidate the possibility of a fundamental

flaw in FEA's ability to model orthotropic composite sections. Due to the specialized nature of

the composite I-beams being analyzed for this research, the closest comparable composite section

found that was modeled in FEA for three-point bending were composite sandwich panels [50],

[51]. These panels are similar to the composite I-beams in that they are both composed of thin

fabric composite laminates separated by some less rigid filler material. Where they differ,

however, is that the outer composite and the filler material typically have the same width in a

sandwich panel, which is not the case for the composite I-beams. Nonetheless, the information

found for modeling of these sandwich panels in three-point bending in both Abaqus and Ansys

166

were quite interesting. Modeling of orthotropic composite sandwich panels in three-point bending in these programs results in near identical V-shaped deflection trends in the panel along with the reflexed overhang beyond the support [50], [51]. The behavior of these sandwich panels in these other FEA programs is consistent with the beam behavior observed from both the Ansys model in Figure 117 and the SolidWorks Model in Figure 112. All discussion surrounding the FEA results for these panels did not focus on this uncharacteristic deflection behavior of the panel under load, and the consensus from [50] was that the panel was modeled correctly following a few boundary condition corrections.

Based on the above findings, it was concluded that the orthotropic shell and solid models as generated earlier in this chapter were indeed modeled correctly. The poor FEA performance compared to experimental data was not caused by an error in the boundary conditions nor was it caused due to solving limitations unique to SolidWorks. Instead, the Finite Element Method in general appears to struggle in dealing with composite sections whose individual component materials are orthotropic in nature. This might explain why no pre-existing material files within SolidWorks are defined as orthotropic, despite the material type option being available. Due to this, modeling of a fully orthotropic composite beam in SolidWorks is not recommended as the preferred approach, especially given the large errors present between the above FEA results and the results obtained from experimentation. Based on results from SolidWorks' ability to reliably model isotropic beams in Chapter IV and its ability to better handle isotropic composite beams in Figure 116, a better FEA modeling approach may result from utilizing an idealizing method such that the orthotropic nature of these beams can be represented under isotropic material assumptions.

D. Equivalent Isotropic FEM Approach

An initially considered method for achieving isotropic composite representation of these orthotropic composite I-beams was the Area Transformation Method already being utilized by both the independently developed Beam Theory model and the WingSpar Mathcad model. As is evident in the previous sub-section, however, this approach assumed a much stiffer beam, resulting in a noticeable underprediction of beam deflection compared to empirical results. While the theory strain data was either nearby the experimental results or, in the case of the shear strains, adhering to expected through-the-thickness trends, this shortfall in deflection prediction eliminated this method from contention for FEA model reduction. As such, other methods for reducing the orthotropic and composite nature of the I-beams to isotropic were pursued. The remainder of this section will detail two similar methods found for idealization of a composite cross-section as well as resulting FEA solutions generated from them.

Methods of Equivalent Axial and Bending Stiffness

The first of these two methods is referred to as either the Equivalent Axial Stiffness Method or the EA-Equivalent Method [52], [53]. The emphasis is to compute an equivalent isotropic Elastic Modulus such that the resulting axial stiffness of the composite section as well as the original cross-sectional dimensions are maintained [52], [53]. This equivalent (or effective) Elastic Modulus can be computed by dividing the composite section into sub-components along boundaries of differing materials within the cross-section. From there, each sub-component's cross-sectional area and representative Elastic Modulus can be multiplied together to obtain each component's axial stiffness. Each of these axial stiffnesses can then be summed together and normalized by the total cross-sectional area to obtain the effective Elastic Modulus of the composite section. This calculation is performed in the same way that one might solve for cross-sectional centroid locations. This effective Elastic Modulus for the composite section should then provide satisfactory representation of the overall stiffness of the composite beam, which is the

main deficiency identified with both the orthotropic FEA and Beam Theory models. The key

equation necessary for this method is shown as Equation 50 below [52], [53].

$$E_{Eff.} = \frac{\sum E_i A_i}{\sum A_i} \tag{50}$$

In much the same way, the second method proposed by [52] and [53] is to compute the

equivalent bending stiffness of the composite section. This method is similarly referred to as the

Equivalent Bending Stiffness Method or the EI-Equivalent Method [52], [53]. As was the case for

the EA-Method, the goal is to compute an effective Elastic Modulus for the composite cross-

section such that the resulting bending stiffness of the section as well its cross-sectional

dimensions are maintained. Once more, this is achieved by sub-dividing the composite cross-

section along boundaries of differing materials. However, instead of computing each

component's area, the resulting inertia of each component as computed using parallel axis

theorem must be determined [53]. Once these inertias are known, each component's bending

stiffness can be determined by multiplying the inertia of the component by the corresponding

representative Elastic Modulus. From there, summing each component's bending stiffness and

normalizing it by the total inertia of the composite cross-section will again yield an effective

Elastic Modulus for the section. Equation 51 displays the key equation of this method [52], [53].

$$E_{Eff.} = \frac{\sum E_i I_i + \sum E_i A_i y_i^2}{\sum I_i + \sum A_i y_i^2} \tag{51}$$

For cases of bending loads on a component, it is usually customary to maintain the bending

stiffness of the component. This would imply for composite sections that the effective Elastic

Modulus of the section should be computed utilizing the EI-Method as described above. Despite

this, [52] demonstrated that utilization of either the EA or the EI-Methods resulted in similar

analysis performance for the maximum deflection of a steel-timber composite beam subjected to

a four-point bending load. Due to their findings, both methods will be further considered below.

Even though the above methods can allow for a composite section to be represented by an effective isotropic Elastic Modulus, there remains the predicament of determining which of the orthotropic moduli from the carbon laminate and the balsa wood should be used for the EA and EI summations. As established previously, assuming that the Elastic Moduli parallel to the length of the beam results in I-beam models that are much too stiff (see the WingSpar and Beam Theory curves in Figures 113 or 118). To get an idea of how much stiffer these theory models were compared to the experimental deflection data, deflection values at one lengthwise location along the beam from the theory and physical models were compared. This was chosen to be the deflection at six inches from the left-hand side of the I-beam for two reasons. The first is that the empirical deflection data was consistently around -0.02745" for this location. The second is that this general location along the beam should have roughly a constant slope of deflection, meaning that decreasing the stiffness of the beam should cause the deflection curve to become coincident with an imaginary line drawn through the experimental datapoints between the lengthwise positions of 4" and 8".

At this location, theory predicted a deflection of -0.00476" while empirically, as aforementioned, the deflection was measured to be -0.02745". Dividing these two deflections revealed that the theory models were ~5.77x stiffer than what was observed during experimentation. Summing the equivalent bending stiffness of the I-beam from theory resulted in an $EI = 993$ kip-in^2. Knowing that the deflection data needed to be ~5.77x larger in magnitude and that from theory $\delta \propto 1/EI$, the actual bending stiffness of the composite I-beams could be estimated according to Equation 52 below. Further still, using the EI-Method, an estimate

$$EI_{Actual} = \left[\frac{5.77}{(993 \; kip-in^2)} \right]^{-1} = 172.2 \; kip - in^2 \tag{52}$$

for the effective isotropic Elastic Modulus of the I-beam can be computed. Using the EI calculated in Equation 52, this effective modulus was determined to be ~2.64 Mpsi.

Comparing this effective Elastic Modulus to the modulus used for Beam Theory, which was equivalently the E_1 modulus of the carbon fiber laminate (~19.58 Mpsi), it becomes clear that the theory is not accounting for certain characteristics of these orthotropic materials, which are causing the physical beams to be more flexible.

In light of the above, focus was directed at finding a method through which an equivalent isotropic modulus could be computed for orthotropic materials such that this representative modulus accounted for the directionality of the material. By accounting for the orthotropy in the calculation of a representative modulus, it was believed that the resulting effective beam stiffness would become closer to the estimate determined in Equation 52. Fortunately, such a method indeed exists and is referred to as the Geometric Mean Isotropic (GMI) material equivalent [55]. Essentially, this method works by taking the geometric mean of the directional mechanical properties of an orthotropic material in order to determine the effective isotropic material equivalent [53], [54], [55]. Not much information could be found as to why this method works apart from a brief mention that someone found that it correlated well with testing data [54]. Regardless, the GMI Elastic Modulus of the carbon laminate could be determined according to Equation 53. This equation assumes that plane stress applies due to the small thickness of the laminate [55]. As for the balsa wood, such assumptions are not applicable, so its GMI modulus was determined according to Equation 54.

$$\overline{E_{Carbon}} = \sqrt{E_1 E_2} = 5.33 \; Mpsi \tag{53}$$

$$\overline{E_{Balsa}} = \sqrt[3]{E_L E_T E_R} = 61.59 \; ksi \tag{54}$$

These GMI Elastic Moduli for the balsa wood and the carbon fiber laminate were then utilized for the EA and EI-methods of computing an equivalent isotropic Elastic Modulus for the composite I-beams. The results of these calculations are summarized in Table 15 (see the Appendix, Sections D and E for the full calculation of each method). As can be seen, both the EA

Table 15: *Composite Beam Theory Stiffnesses Compared to the GMI Equivalent Stiffnesses*

	E_{Carbon} (Mpsi)	E_{Balsa} (ksi)	$\sum EA$ (kip)	$\sum EI$ (kip-in^2)	$E_{Eff.\_EA}$ (Mpsi)	$E_{Eff.\_EI}$ (Mpsi)
Beam Theory	19.58	9.71	2860.83	993.01		19.58
GMI Equivalent	5.33	61.59	786.86	271.12	2.75	4.15

and EI-methods result in an effective Elastic Modulus for the I-beams that is much lower than the Beam Theory assumption that $E = E_1$. The EA-method resulted in an equivalent modulus that is very close to the estimated modulus of ~2.64 Mpsi, as determined earlier, while the EI-method produced an equivalent modulus that was ~1.5x larger. From [52], these results are consistent with their findings in that the EI-method predicted a stiffer beam than the EA-method did. Despite this, the two methods resulted in near identical deflection predictions in [52], though it is acknowledged that the sample size of test results with which these methods were compared was small and that further research into their accuracy was required. For the composite I-beam FEA models, the equivalent isotropic Elastic Modulus as determined by the EA-method should result in acceptable prediction of the beam's deflection. Regardless, FEA results from both methods will be considered in the following sub-section.

Equivalent E Model Generation and Evaluation

For both of the previously discussed methods, a shell and solid FEA model was generated. Because these methods idealize the composite and orthotropic nature of the I-beams to an isotropic material equivalent, all models generated for these two methods were built according to the modeling procedures developed and discussed for the metal I-beam models in Chapter IV. All loading and boundary conditions are the same for these models as previously covered elsewhere in this document, and the same applies to the 1/8th-inch sizing of the mesh elements. With these models built, the only task remaining was to generate the appropriate material files for each method. The same procedure discussed for development of the orthotropic material files from the

previous section of this chapter were applied to generate the equivalent isotropic material files for the EA and EI-Methods. The only difference, however, is that these material files were defined using the "Linear Elastic Isotropic" material type as opposed to the "Linear Elastic Orthotropic" designation for the orthotropic carbon and balsa files developed previously.

For these files, four properties are required for SolidWorks FEA to properly analyze the model. These four parameters are the Elastic Modulus, Poisson Ratio, density, and yield strength. As discussed in the previous sub-section, the Elastic Modulus was determined from either the EA or EI-Methods. The Poisson Ratio is assumed to be 0.33 as it is only necessary for determining the material Shear Modulus through isotropic relations. It will have no influence on material stiffness, nor the resultant bending or shear stresses developed on the I-beam. The equivalent density of the composite I-beams was determined by taking the area-weighted average of the density for the unidirectional carbon fiber and the balsa wood. This calculation is shown in Sections D and E of the Appendix. The yield strength value chosen was the ultimate compressive load limit for the unidirectional carbon laminate. The resulting EA and EI-Method SolidWorks material files can be viewed in Figure 119.
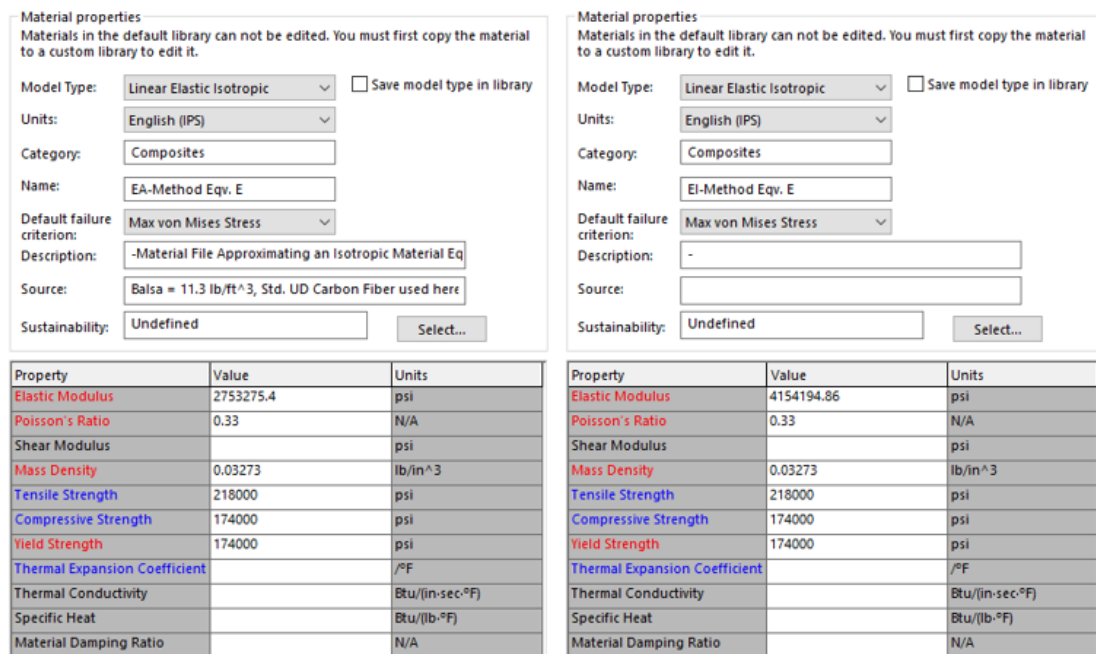
Figure 119: *SolidWorks Material Files for the EA-Method (**Left**) and EI-Method (**Right**)*

173

The resultant FEA solutions for I-beam deflection, bending strain, and shear strain for both methods were then compared to the empirically acquired data as well as the models generated from theory. For added ease of visual comparison between the EA and EI equivalent models, only the 3D FEM results will be shown graphically. From trends between the 2D and 3D FEA results as established in Chapter IV, it can be inferred that the 2D FEM solutions from both methods resulted in similar spanwise trends and magnitudes as their respective solid model counterparts. The shell model results for each of these methods, however, will be further considered in the following section.

The main deficiency as identified in both the theory models and the fully orthotropic models was the inability to properly model the stiffness of these composite I-beams, which directly impacted the deflection solutions. Both of the equivalency methods discussed here are directly tailored towards correcting this modeling deficiency and should better predict the deflections observed during experimentation. As Figure 120 demonstrates, these methods indeed do a better
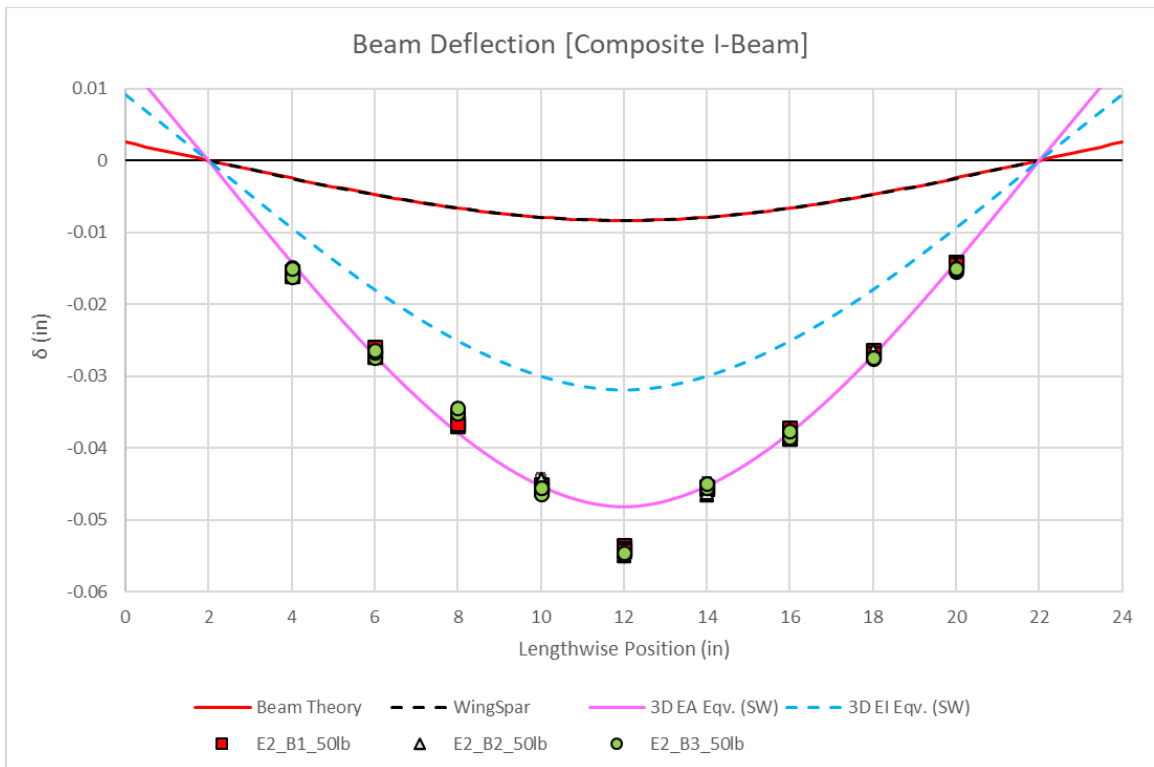
Figure 120: *EA and EI-Method Solid Model Deflection Solutions*

job at modeling the beam stiffness and the resulting beam deflections compared to the theory models and the fully orthotropic FEA models from the previous section. As expected, based on the preliminary calculations conducted in the previous sub-section, the EA-Method produced a deflection prediction that is nearly 100% coincident with the empirically measured spanwise deflections in the I-beams. Likewise, as was also expected, the EI-Method produced a beam model that was not as flexible and, therefore, this model did not achieve the proper deflection magnitudes. Using these methods, what the successful modeling of the I-beam deflections infers is that the orthotropic nature of the materials used causes the beams to be more flexible than would otherwise be expected. This could also be an additional contribution as to why the fully orthotropic models failed to adequately predict these deflections. It is possible that the FEA solving routine for material orthotropy attempts to account for the added material flexibility due to orthotropic properties in such a way that the resulting model becomes overly flexible.

Considering the resulting prediction of the bending strains on the composite I-beams, the EA and EI-Method solid models performed similarly to the Beam Theory and WingSpar models, as Figure 121 indicates. Additionally, this figure better indicates the empirical data variance along the span of the beam as well as the computed measurement uncertainties for each datapoint, which are larger than was found to be the case for the metal beams in Chapter IV. Further discussion into this increase in uncertainty as well as the wider spread in measurement data will be addressed in the next section. Comparing the theory models and the FEA models to the empirical data, both solution approaches result in bending strain magnitudes that are at least bracketed by empirical testing results. Furthermore, the slope of linear stress increase between all models closely follows trends observable in the empirical data. This is most evident in the empirical data gathered at the lengthwise positions of 15 and 19 inches along the I-beams. Additionally, for three out of the four spanwise locations sampled on the physical beams, measurement uncertainties cause nearly all datapoints at these locations to have a likelihood of actually falling on top of any of the bending strain curves produced from the models.
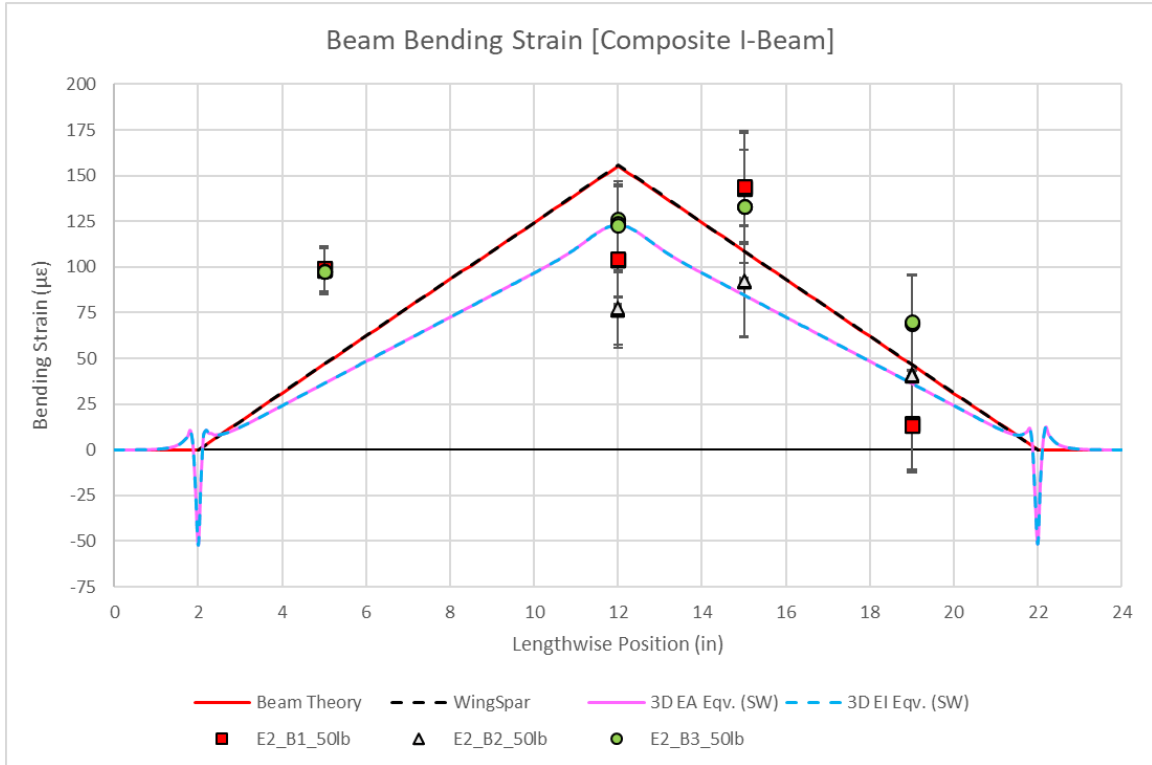
Figure 121: *EA and EI-Method Solid Model Bending Strain Results*

As far as the discrepancy between the theory models and FEA solutions, the explanation is rather straightforward. As covered previously, both the Beam Theory and WingSpar program utilize the area transformation approach for modeling these composite I-beams. A key requirement of this approach is to modify the width of the less stiff material such that the transformed dimensions for this material component represents an equivalent area composition of the stiffer material. In this way, this approach preserves the overall composite beam's bending stiffness (EI) by modifying the original geometry for analysis. This modified geometry subsequently lowers the resulting cross-sectional inertia of the beam, and this inertia is utilized for computing bending stresses and strains through the thickness of the cross-section. For instance, the average actual inertia computed for the physical composite I-beams is 0.065 in^4. From area transformation, the modified geometry inertia is found to be lower at 0.051 in^4. Resulting spanwise bending moments in the I-beams are not dependent on material or cross-sectional properties (see Equation 43); therefore, this parameter is unchanged between all of the

models. Similarly, none of the approaches modify the height of the cross-section, so the resulting 'y' reference distance from the section y-centroid remains unchanged across the models as well. Along with the moment of inertia, these two parameters are necessary to compute the bending stresses in a beam in bending (see Equation 47). The only difference is in the moment of inertia utilized by each of the models.

Because the stress/strain of interest is on the outer surface of the carbon spar caps, the theory models must utilize the transformed inertia of 0.051 in[4] for stress calculations [31]. Meanwhile, the EA and EI-methods do not modify the original geometry, so the inertia utilized for their stress calculations is the original inertia of 0.065 in[4]. Because bending stress and strain is proportional to the inverse of the moment of inertia of the cross-section, a lower inertia will equate to a higher stress. This is exactly the outcome observable in Figure 121. To further prove this, the maximum stress at the beam midspan from the EA and EI-Methods is 2,409 psi. Multiplying this stress by the cross-sectional inertia of 0.065 in[4] results in a value of ~156.59 lb-in[2]. This value is representative of the maximum bending moment multiplied by the distance between the outer face of a spar cap from the y-centroid, which is constant across all of the models presented here. Taking this value and then dividing it by the transformed area inertia of 0.051 in[4] results in a maximum bending stress of ~3,070 psi, which is ~29 psi higher than the maximum stress computed using the Beam Theory and WingSpar models. Therefore, were the theory models to utilize the true cross-sectional inertia, their resulting bending stress and strain solutions would be almost identical to those found using the EA and EI-Method approaches.

For shear strain, similar to the discussion from the orthotropic models, not much useful information about any of these FEA models can be obtained through comparison with the experimentally measured data. As was mentioned earlier in this chapter, this is likely due to an unavoidable error from the instrumentation utilized; however, further discussion of this issue will occur in the following section. Despite this, a consolation is that both the Beam Theory model and the EA/EI FEA models now predict the same shear strain trends and magnitudes while also

adhering to expected through-the-thickness shear trends for an I-beam. As has been the case for all shear strain plots shown in this document, the shear data from the FEA models was only sampled along the shear web whereas the Beam Theory model calculated the shear stresses and strains in the spar caps as well.
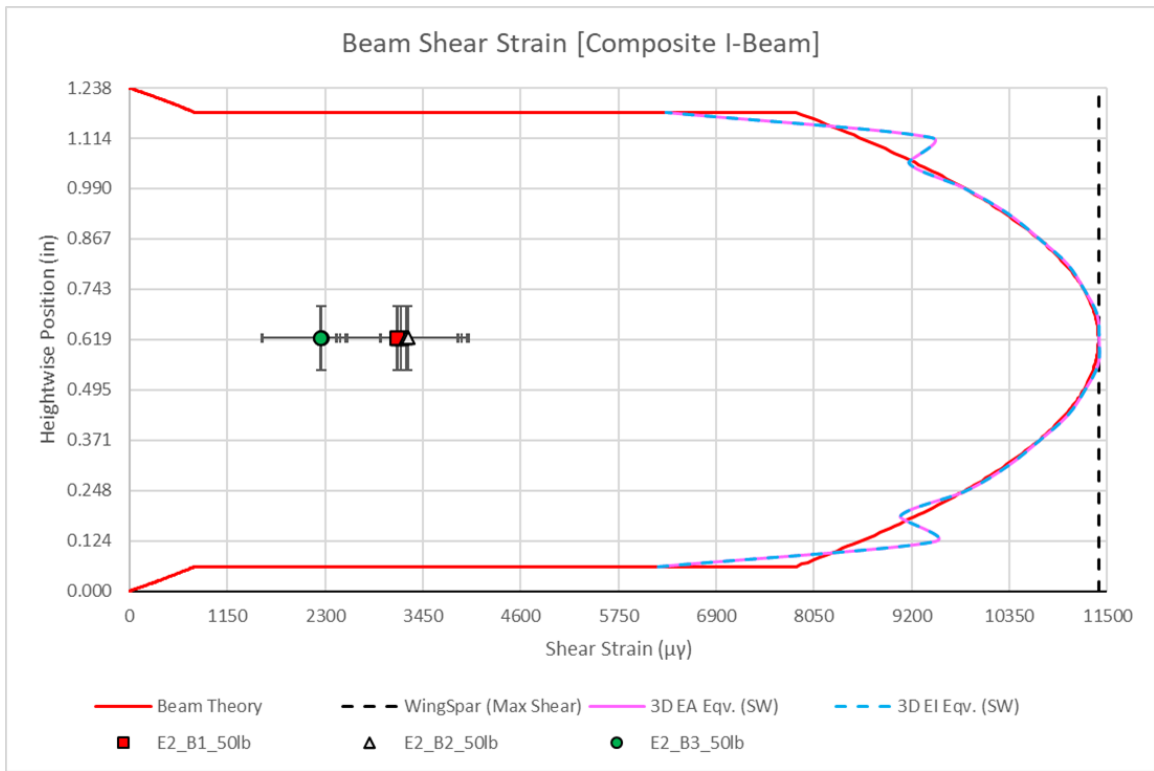
Figure 122: *EA and EI-Method Solid Model Shear Strain Results*

E. SolidWorks FEM Results and Comparison

When compared to the empirical data, the overall performance of each of the shell and solid models discussed in this chapter is best summarized in Table 16. Both theory models are also included in this table, where the root mean squared error between each model and experimentally acquired data, including bounds of measurement uncertainty, have been normalized such that each model's error can be directly compared with one another. In this way, the model(s) with the best match can be determined and, likewise, the model(s) with the worst performance can be

Table 16: *Normalized Errors for Various Models of the Composite I-Beams*

Composite I-Beam Normalized RMSE Values									
		Theory Models		Orthotropic Models		EA-Method Models		EI-Method Models	
Category	Uncertainty Bounds	Beam Theory	WingSpar	2D FEM	3D FEM	2D FEM	3D FEM	2D FEM	3D FEM
Deflection	Actual	88.96%	88.92%	84.98%	76.91%	8.91%	7.07%	40.54%	38.18%
	Max	89.08%	89.04%	88.75%	80.50%	10.12%	7.75%	41.64%	39.32%
	Min	88.85%	88.81%	81.38%	73.49%	8.01%	6.99%	39.41%	37.00%
Bending Strain	Actual	46.43%	46.50%	174.01%	213.66%	51.04%	49.48%	51.04%	49.48%
	Max	71.55%	71.77%	245.04%	298.11%	55.50%	56.67%	55.50%	56.67%
	Min	41.86%	41.82%	133.67%	164.66%	47.32%	46.41%	47.32%	46.41%
Maximum Shear Strain	Actual	294.38%	294.38%	247.16%	247.16%	290.49%	294.60%	290.49%	294.60%
	Max	422.47%	422.47%	359.88%	359.88%	417.32%	422.76%	417.32%	422.76%
	Min	216.75%	216.75%	178.84%	178.84%	213.63%	216.93%	213.63%	216.93%

identified. In this table, the top performing models of these I-beams are identified by columns highlighted in green. For prediction of beam deflection under a bending load, there is no question that the equivalent Elastic Modulus as determined via the solid model EA-Method produced the best solution at a maximum NRMSE of 7.75%. The EI-Method's solid model solution produced a slightly stiffer beam model, but it still managed to perform second best in this category. The Beam Theory and WingSpar Mathcad models, on the other hand, were the worst solution performances for beam deflection prediction at an NRMSE of ~89%. This was largely due to their assumption that the only Moduli of importance for both materials were the Moduli along the length of the beams. Despite this, the fully orthotropic models were not much better.

For prediction of bending strain, all of the models except for the fully orthotropic Finite Element Models had similar performances, with an NRMSE spread of ~4% at most between them. The stress concentrations at the supports as well as the stress spike at the load point are the main contributors to the large error percentages present for the fully orthotropic models. Failure of these models to adhere to the three-point bending V-shaped stress distribution, especially when the empirical data suggested adherence to this shape in its trends, caused errors to increase exponentially. As for the remaining models, general adherence to this V-shaped spanwise trend as

well as predicting bending strains of similar magnitudes along the beam length helped to minimize the buildup of error when compared to actual measurements. Despite this, an error of 50% is not necessarily desirable for accurate prediction of the stresses in these beams. However, a large portion of the error present in these NRMSE totals can be attributed to the large variance in the empirically measured bending strains.

As earlier figures depicted, measurement of bending strain on these composite beams was not uniform, and it was rare for the strains on all three beams to match at each spanwise location sampled. This variability from beam to beam could be caused by a number of contributors such as the orthotropy of the carbon fiber. Recalling Figures 11-12 from the literature review, if the fiber direction of the laminate is not exactly aligned with the spanwise direction of the beam, even by just a few degrees, large changes in the overall global mechanical properties of the laminate will occur [9]. Further, much more importance is placed on proper strain gage alignment for this same reason. If the fibers happen to be properly oriented but the gages are misaligned by a few degrees, the strain that the gages read will not represent the bending strain present in the beams, and their measurements can be noticeably wrong [6] – [9]. Another possible contributor to the wide variability in the measured data is the epoxy texturing observed on the carbon laminates during manufacturing (see Figure 92). Not having a smooth surface under the strain gages can cause errors in measurement due to the ridges in the texturing artificially loading or unloading the strain gage [47]. Additionally, this texture could also have caused the gages not to bond well to the carbon laminate, further adding to the errors in measurement. All identified gage bonding sites along the carbon spar caps were sanded with the intent of removing this epoxy texturing from the site. Based on the data collected, it is possible that some texturing remained despite these efforts.

Even with these large error contributions, a majority of them were quantifiable and were therefore tallied into the overall uncertainty projected for each strain measurement taken. This is then why the overall uncertainties for bending strain measured on these composite I-beams is noticeably higher than what was found on the metal beams in Chapter IV, with some

measurements projected to have a total uncertainty of up to ~31%. This is much higher than the 4-5% uncertainty calculated for most bending strains measured on the metal beams. Reviewing the data as presented in Figure 121, it can be seen that this large uncertainty in the measurements causes many of the data points from all three test beams to overlap with one another. Moreover, it also causes most of the data points to intersect some portion of the theory models, FEA models, or both. The fact that this large uncertainty causes most of the data to fall onto each other as well as onto at least one of the prediction models further increases the likelihood that these models still accurately predict the bending stresses in these composite I-beams. Under a more controlled manufacturing and gage application environment than was available, it is conceivable that the resulting NRMSE range for these models could be lower than what is presented here (perhaps even to an acceptable level).

For shear strain, it is evident by the unacceptably large NRMSE percentages in Table 16 that, justifiably, none of the models came even remotely close to predicting the shear strains actually measured on the balsa shear webs. As such, none of the models are highlighted green to identify the best fit model. All models predicted maximum shear stresses between 160–190 psi while the empirically measured shear strains translate to stresses approximately between 45-65 psi. As has been alluded to numerous times throughout this chapter, one of the more prominent culprits for this vast difference is instrumentation error. Upon completing testing and initial comparison of acquired data to the Beam Theory models, it was quickly identified that something about the empirical data was incorrect. Further research indicated that on low modulus materials, such as wood, the strain gage itself is stiff enough to locally distort the strain measurements around the bond site and thus contribute to significant measurement errors [56]. There are specialized low modulus strain gages available that are supposed to mitigate this local stiffening [56], but they were not pursued for a few reasons.

First among these reasons is that these gages typically are longer than the bondable space available on the composite I-beam shear webs. The one gage of this type found that would fit on

the shear webs was out of stock with no indication of a resupply date at the time of this research endeavor. This lack of availability is the second reason. Lastly, this was not pursued because, in addition to the strain gages distorting the strain, it is very likely that the bonding adhesive is also contributing to the localized stiffening of the wood. The goal of gage application is to apply enough adhesive such that the gage is sufficiently bonded to the surface while maintaining as thin a film of adhesive as possible. Due to the porous nature of the balsa wood, it is probable that more bonding adhesive was absorbed than removed during the application process, thus causing the application site to become more rigid than would actually be the case. Therefore, it is unlikely that application of these specialized gages would actually result in much better strain results, much less bridge the large strain gap present between the empirical and model values.

Another possible contributor to this large variation is simply the mechanical properties of the balsa wood itself. Past and current research into balsa wood has yielded similar variability in testing results between balsa samples [13], [57]. As was discussed in the literature review, it is quite difficult to reliably predict the properties of balsa wood due to the organic nature of its material orthotropy [13] – [16]. Even though the shear webs were found to have a consistent density of ~11.29 lb/ft^3, it is possible that the individual balsa strips that composed each 8-inch section were not of the same density. Further still, as is evident from Figure 93, each balsa strip in the shear webs is from different balsa sources, which can also contribute to wider variability in the mechanical properties of the resulting shear web [14] – [16]. This is reinforced by the empirical shear data acquired as composite I-beams #1 and #2 had their shear strain gages placed on the same balsa strip. As a result, both of these beams can be observed in Figure 122 to have similar shear strain magnitudes regardless of instrumentation errors. During manufacturing, the third I-beam's three shear web pieces were not assembled in the same order as the first two beams, resulting in its shear strain gage being bonded to a different balsa strip at the 18-inch spanwise location from the beam's left end. As a result, the third beam's measured shear strains were noticeably lower than the first two beam's measurements.

There is one possible benefit to this vast difference in shear strain values between experimentation and the analytical models, however. In the event that the empirical data is indeed correct, all of the analytical models have a sizeable safety factor built into them. Considering that shear failure in the balsa shear webs is a primary mode of failure for these composite beams, this comfortable safety factor would be preferable. Based on the findings from testing of the metal beams in Chapter IV, where SolidWorks was found to consistently predict shear stress to within an error of ~13%, it is expected that the true shear strain measured in the shear webs is closer to a magnitude of ~9,870μγ. This corresponds to a shear stress of ~166 psi. Regardless, future investigation into the properties and behavior of balsa wood under bending loads is required to confidently assess the validity of both the shear data and the subsequent claims about it presented here.

CHAPTER VI

SUMMARY AND FUTURE WORK

A. Research Summary and Concluding Remarks

Recalling the short list proposed at the end of Chapter IV regarding expectations of

SolidWorks FEA's ability to model these orthotropic composite I-beams, which were formulated

based on the results of the baseline metal beam testing, the accuracy of these claims can now be

assessed. Considering first the fully orthotropic FEA models generated for this research, only the

last two list items hypothesized were proven true. The addition of material orthotropy into the

FEA models indeed resulted in the FEA solutions further straying from the solutions generated

from the Beam Theory models. Additionally, this material orthotropy further caused the errors

between the FEA solutions and the data obtained experimentally to increase beyond expected

errors as found in Chapter IV. Granted, as has been discussed, the large difference between the

orthotropic FEA solutions and the Beam Theory solutions, in the case of deflection, were due to

theory assumptions that resulted in a much more rigid beam than was empirically found to be the

case. Likewise, a sizeable portion of the calculated errors for these models is due more to the

increased variance and uncertainties in data acquired through experimentation than can be

attributed to the actual FEA solutions. Even so, SolidWorks' inability to correctly model the

stiffness of the I-beam and the increased intensity of the lengthwise bending stress concentrations

in the model would still have resulted in unfavorable agreement with experimentation had the

empirical data spread been tighter.

As for the idealized FEA models produced using the EA and EI-Methods, all but one of the hypothesized solving expectations listed in Chapter IV were in some way proven correct. In the case of the EI-Method models, the trend of deflection and bending stress underprediction when compared to experimentation indeed persisted. Despite this, it was still proven that both the 2D shell model and the 3D solid model were capable of generating solutions within an acceptable error range of the experimentally measured results for deflection and bending strains. For the EA-Method, both the deflection and bending strains determined from the FEA models were again underpredictions. However, the deflection solution was considerably closer to empirical values at an error percentage of ~8%, which is in much closer agreement than was thought possible following the baseline metal beam testing. Once more, this idealizing method again proved that either a 2D shell model or a 3D solid model can generate consistent results for this type of beam geometry, though the solid models for both methods were slightly better in their solution performances. For both methods, there was a noticeable increase in error, especially for bending and shear strains. Once more, however, a majority of this added error is more a result of the increased data variance and measurement uncertainties from experimentation than it is due to the FEA models themselves. Similarly, in the case of beam deflection, both models displayed improved solving performance compared to the models produced using Beam Theory. This can again be attributed to incorrect theory assumptions that resulted in a much more rigid beam.

Considering the results of this research endeavor as presented in this document, a final verdict can be established regarding the efficacy of utilizing SolidWorks Finite Element Analysis to model and analyze these composite I-beam wing spars. This research has shown that it is possible to model these composite I-beams within the SolidWorks FEA package. Despite this, the desired fully orthotropic models have been shown not to be solved properly, resulting in large errors that eliminated it as a preferred modeling approach. In fact, it was also shown that this apparent solving deficiency extends to the overall Finite Element Method, rather than being solely

localized to the solving routine as implemented within SolidWorks itself. As for the more idealized EA and EI-Method FEA models, much better agreement with experimentation was observed, especially in the area of beam deflection. While error percentages for bending strains and shear strains were unfavorably large with these methods (as they also were for the orthotropic models), it was found that both of these idealized FEA models produced solutions that were consistent with the bending strain and shear strain solutions developed from theory. Furthermore, due to the overlapping uncertainty bands of the empirical bending strain data with these solutions, there is a much higher probability that either the theory models or these idealized FEA models are indeed predicting the bending stresses experienced by the physical I-beams. Due to the aforementioned errors associated with measurement of the shear strains experimentally, neither the FEA nor theory model's shear solutions could be adequately assessed. Despite this, it has been shown that these idealized FEA models will produce the same shear solution as the theory models do. Therefore, both models will have practically the same percent error with the shear measured in the physical I-beams regardless of how correct this measurement is.

Ultimately, this research has found that it is both possible and practical to model these composite I-beam wing spars using SolidWorks Finite Element Analysis. Specifically, it would be recommended that the EA-Equivalent Method coupled with the conversion of the orthotropic Moduli of the I-beam materials to their GMI equivalents be utilized for these models. This is so because this modeling approach produced the best fit solution for beam deflection out of all of the FEA and theory models considered in this research. As for the question of replacing the current Wing Spar Mathcad Analysis tool in favor of this FEA modeling technique, the added benefits from the FEA have not been found to be significant enough to warrant such a decision. As mentioned, the only benefit of the EA-Method FEA models is that they correctly account for the stiffness of these wing spars. In terms of shear and bending stress prediction, both analytical approaches yield similar results. Furthermore, the Wing Spar analysis tool can be converted from the Area Transformation Method to this EA-Method, which will effectively nullify the only

benefit of modeling these I-beams in FEA. This would be the case as this conversion would result in the theory beam stiffness (and resulting deflections) becoming equivalent with the EA-Method FEA models. Therefore, modeling of these composite I-beam wing spars utilizing Finite Element Analysis can exist as a companion analytical tool to the Wing Spar program, with either approach being used interchangeably.

B. Recommendations for the Existing Wing Spar Analysis Tool

In light of the findings of this research, it is recommended that the existing Wing Spar Mathcad analysis tool utilized by the DML undergo necessary modifications. Namely, the foundational Beam Theory analysis approach should be converted from relying on the Area Transformation Method to utilizing the EA-Equivalent Method (coupled with the calculation of the carbon fiber and balsa wood GMI equivalent moduli). This conversion will correct an obvious deficiency in the current iteration of the analysis tool by properly accounting for the stiffness of these composite I-beams. As has been shown in this research, this new approach will result in minimal changes in solution performance for both bending and shear stress compared to solutions obtained with the current iteration of the Wing Spar tool (which is reliant on the Area Transformation Method). The main requirements for this conversion are to calculate the EA-Equivalent Elastic Modulus ($E_{eqv.}$) for the composite cross-section (see Section D of the Appendix for an example). From here, adjust the Beam Theory deflection equation such that it is proportional to the inverse of ($E_{eqv.} * I_{zz}$), where I_{zz} is the true cross-sectional inertia and not the transformed inertia as calculated from area transformation.

C. Goals Achieved

The overarching goal of this research effort was to characterize the modeling and solving capabilities of the SolidWorks FEA package such that its feasibility as a new wing spar structural design tool could be determined. A series of research objectives were provided as a road map for achieving this goal. As such, this research endeavor can only be considered a success if all of

these objectives are attained satisfactorily. This list of objectives from the introduction is again provided below:

1) Conduct an extensive review of existing literature pertaining to the following:
    a. Fundamentals of Finite Element Analysis
    b. Orthotropic Mechanical Properties of Carbon Fiber and Balsa Wood
    c. Pre-existing work regarding modeling of orthotropic/composite components
    d. Practical methods of acquiring experimental data for comparison and validation

2) Develop proper experimental testing capabilities so that important parameters, such as beam deflection, bending stress, and shear stress, can be obtained from the physical beams.

3) Simulate a simplistic bending load, such as a point load, on a beam (or beams) of simpler construction and material composition in order to establish a baseline for the capabilities of the SolidWorks FEA package.
    a. Compare these FEA results to experimentation as well as to models developed from theory.
    b. Utilize this baseline test case to establish proper procedure for the application of boundary conditions, loading conditions, model meshing, and other modeling constraints and parameters as needed.

4) Manufacture wing spars for experimental testing, ensuring that the materials and construction techniques utilized for these spars on the UAVs are replicated as accurately as possible.

5) Explore methods of modeling the orthotropic and composite nature of these I-beam spars to determine the best FEA modeling approach.

6) For the models developed as a result of Objective 5, simulate a simplistic load, such as a point load, and compare the results with experimentation as well as with the existing spar analysis tool.

7) Based on the findings in Objective 6, determine the overall feasibility of utilizing the SolidWorks FEA package to model the behavior of these composite I-beams effectively and reliably under load.

Objective 1 was addressed through the completion of background research and documentation of all sub-objectives in the literature review (Chapter II). This extensive literature review proved to be incredibly beneficial as it provided a solid foundational understanding of the problem undertaken for this research. Objectives 2 and 3 were achieved primarily in Chapters III and IV. The content of these chapters, especially as it relates to development of the experimental testing capabilities required for this research, were developed in tandem with the development of the SolidWorks FEA modeling procedures established through baseline testing (as covered in Chapter IV). Completion of these objectives was crucial to the remainder of this research effort, and great care was taken to ensure that they were thoroughly and correctly completed. As a result, Objectives 4 – 6 were achieved in Chapter V. Great care was again taken to ensure that these three objectives were thoroughly and correctly completed. Objectives 4 and 5 especially required significant attention to detail, which the contents of Chapter V convey. Finally, ultimate determination of SolidWorks' FEA modeling and analysis capabilities were properly assessed, and appropriate conclusions were drawn as a result. This was accomplished in both Chapter V and this current chapter. This constitutes completion of Objective 7 and, therefore, satisfactory completion of the main goal for this research effort.

D. Recommendations for Future Work

While this research did conclude that analyzing these composite I-beam wing spars in SolidWorks FEA would ultimately produce solutions comparable to the existing beam theory analysis tool available to the lab, there are a few topics for further research that can be pursued as a result of the findings of this thesis. These are listed below.

1) Verify that the EA-Method (as detailed in Chapter V) works for composite I-beams of different cross-sectional dimensions, balsa wood densities, and unidirectional carbon fiber laminate thicknesses/sizes. Because this method was applied to only one I-beam geometry and one set of possible material mechanical properties, it is advisable to further confirm that this idealizing method for these orthotropic composite beams does, in fact, work as stated in this document. There currently exists the possibility that it is mere coincidence that this method worked as well as it did for the testing and modeling conducted for this research.

2) Consider reproducing this research effort in other FEA programs, such as Ansys and Abaqus, so as to verify that fully orthotropic models of these I-beams result in solutions consistent with those shown in Chapter V. While evidence was shown or cited in this document to support this shared solving deficiency, a more extensive study of each program's capabilities as it relates to fully orthotropic composite modeling would provide a more definitive conclusion. This is especially true for Abaqus, which was not accessible for this research endeavor. Certain sources found and covered in Chapters II and V indicate support that Abaqus should be capable of correctly analyzing such a complex model due to FEA modeling capabilities that were not available in SolidWorks.

3) Further research should be focused on determining a better method for obtaining experimental shear strain measurements from the balsa shear webs on these composite I-beams. As was evident in Chapter V, utilization of strain gages was found not to be the best method for obtaining this particular parameter. Either stiffness of the strain gage, localized stiffening of the balsa due to the gage bonding adhesive, or simply the unpredictability of the mechanical properties of balsa wood are likely to blame. Determination of a better experimental measuring method would then allow for further validation of both the EA-Method FEA models and the Wing Spar Beam Theory model presented in Chapter V.

REFERENCES

[1]   T. Chandrupatla and A. Belegundu, *Introduction to Finite Elements in Engineering*, 4th ed. Cambridge University Press, 2022, pp. 1; 188-210; 273-297; 312-322.

[2]   T. Y. Yang, *Finite Element Structural Analysis*. Englewood Cliffs, NJ: Prentice-Hall, 1986, pp. 262-286; 288-307.

[3]   L. Skotny, Ph.D., "Why is a Triangular Element Stiffer?," *enterfea.com*. Feb. 21, 2019. [Online]. Available: Why is a Triangular Element Stiffer? - Enterfea. [Accessed Feb. 11, 2022].

[4]   "2D Triangular Elements," *unm.edu*. [Online]. Available: 2D Triangular Elements.doc (unm.edu). [Accessed Jan. 15, 2022].

[5]   "FEA Mesh Elements & Nodes Guide | Intro to FEA," *asrengineering.com*. [Online]. Available: FEA Mesh Elements & Nodes Guide | Intro to FEA (asrengineering.com). [Accessed Sept. 20, 2022].

[6]   "Fibre Composites - Mechanics of a Lamina," *empa.ch*. [Online]. Available: 02-UDlaminaMicro_2021.pdf (empa.ch). [Accessed July 9, 2022].

[7]   "Fibre Composites - Laminate Theory," *empa.ch*. [Online]. Available: 03_Laminate_Theory_s_2021.pdf (empa.ch). [Accessed Sept. 21, 2022].

[8]   T. H. G. Megson, *Aircraft Structures for Engineering Students*, 5th ed. Oxford, UK: Butterworth-Heinemann, 2016, pp. 699-714.

[9]   M. W. Hyer, *Stress Analysis of Fiber-Reinforced Composite Materials*. PA: DEStech Publications, Inc., 2009, pp. 57-64, 165-175, 180-218, 310-363

[10]   ACP Composites, "Mechanical Properties of Carbon Fiber Composite Materials, Fiber / Epoxy resin (120°C Cure)," *acpsales.com*. [Online]. Available: ACP-PDS (acpsales.com). [Accessed July 16, 2022].

[11]   CST: The Composites Store, "Unidirectional Carbon Fiber Fabric," *cstsales.com*. [Online]. Available: Unidirectional Carbon Fiber Fabric - CST The Composites Store, Inc. (cstsales.com). [Accessed July 16, 2022].

[12]   Christian-Albrechts-Universität zu Kiel, "Composite Materials," *tf.uni-kiel.de*. [Online]. Available: Composite Materials (uni-kiel.de). [Accessed Sept. 14, 2022].

[13] Z. Watkins, "Modeling and Failure Analysis of Composite I-Beams for UAV Wing Spar Design," M.S. Thesis, Oklahoma State University, Stillwater, OK, 2021.

[14] A. Da Silva and S. Kyriakides, "Compressive Response and Failure of Balsa Wood," *International Journal of Solids and Structures*, vol. 44, pp. 8685-8717, 2007. Available: doi:10.1016/j.ijsolstr.2007.07.003 | Elsevier Enhanced Reader.

[15] D. Green, "Wood: Strength and Stiffness," *Encyclopedia of Materials: Science and Technology*, Elsevier, 2001, pp. 9732-9736. Available: PII: B0080431526017666 | Elsevier Enhanced Reader.

[16] G. Gedeon, "Wood as an Engineering Material: Mechanical Properties of Wood," *Encyclopedia of Materials: Science and Technology*, Elsevier, 2001, pp. 9732-9736. Available: Wood as An Engineering Material Mechanical Properties of Wood R2.pdf (cedengineering.com).

[17] G. Gedeon, "Lightweight Timber I-beams Reinforced by Composite Materials," *Composite Structures*, vol. 233, Elsevier, 2020, pp. 1-13. Available: Lightweight timber I-beams reinforced by composite materials | Elsevier Enhanced Reader.

[18] P. Szeptyński, "Closed-form Analytical Solution to the Problem of Bending of a Multilayer Composite Beam – Derivation and Verification," *Composite Structures*, vol. 291, Elsevier, 2021, pp. 1-15. Available: Closed-form analytical solution to the problem of bending of a multilayer composite beam – Derivation and verification | Elsevier Enhanced Reader.

[19] National Instruments, "Measuring Strain with Strain Gages: How They Work and Types," *ni.com/en-us*. [Online]. Available: Measuring Strain with Strain Gages: How They Work & Types - NI. [Accessed April 12, 2022].

[20] Micro-Measurements, "Stress Analysis Strain Gages (Gauges)," *micro-measurements.com*. [Online]. Available: MicroMeasurements / Stress Analysis (micro-measurements.com). [Accessed Oct. 25, 2022].

[21] Micro-Measurements, *The Three-Wire Quarter-Bridge Circuit*, Tech Tip TT-612. Available: The Three-Wire Quarter-Bridge Circuit - Tech Tip (vishaypg.com).

[22] Omega Engineering, *Practical Strain Gage Measurements*, Appl. Note 290-1. Available: Layout 1 (omega.co.uk).

[23] Omega Engineering, *Strain Gauge Installation: How to Position Strain Gauges to Monitor Bending, Axial, Shear, and Torsional Loads*, Tech. Ref. Available: How to position strain gauges - A guide to installation (omega.co.uk).

[24] Vishay Precision Group, *Plane-Shear Measurement with Strain Gages*, Tech Note TN-512-1. Available: tn5121tn.pdf (vishaypg.com).

[25] *Vernier Structures and Materials Tester*, Vernier Science and Education, 2015. Available: Microsoft Word - VSMT (vernier.com).

[26] McMaster-Carr, "Water-Resistant Electronic Depth Micrometer," *mcmaster.com*. [Online]. Available: https://www.mcmaster.com/6747A6/. [Accessed Nov. 11, 2022].

[27] National Instruments, "cDAQ-9185 Specifications," *ni.com/en-us*. [Online]. Available: cDAQ-9185 Specifications - NI. [Accessed Nov. 12, 2022].

[28] National Instruments, "Operating Instructions and Specifications: NI-9237," *cae-systems.It*. [Online]. Available: NI 9237 Operating Instructions and Specifications (cae-systems.lt). [Accessed Nov. 12, 2022].

[29] Measurements Lab. "Measurements 1 – ½ Bridge Strain Gauge LabVIEW Tutorial," *YouTube*, Sept. 11, 2015. [Video File]. Available: Measurements I - 1/2 Bridge Strain Gauge LabView Tutorial - YouTube. [Accessed Apr. 12, 2022].

[30] R. Budynas and J. Nisbett, *Shigley's Mechanical Engineering Design*, 11th ed. McGraw-Hill Education, 2020, pp. 98-101; 111-122; 176-179; 182-188; 956-974; 1029-1036.

[31] R. C. Hibbeler, *Mechanics of Materials*, 8th ed. Hoboken, NJ: Prentice-Hall, 2011, pp. 312-317.

[32] McMaster-Carr, "Multi-purpose 6061 Aluminum – ¾" x ¾"," *mcmaster.com*. [Online]. Available: https://www.mcmaster.com/9008K12-9008K124/. [Accessed April 22, 2022].

[33] ASM - Matweb, "Aluminum 6061-T6; 6061-T651," *asm.matweb.com*. [Online]. Available: ASM Material Data Sheet (matweb.com). [Accessed April 22, 2022].

[34] McMaster-Carr, "Architectural 6063 Aluminum H-Bar – 0.055" Wall Thickness," *mcmaster.com*. [Online]. Available: https://www.mcmaster.com/4558T53/. [Accessed April 22, 2022].

[35] ASM - Matweb, "Aluminum 6063-T5," *asm.matweb.com*. [Online]. Available: https://asm.matweb.com/search/SpecificMaterial.asp?bassnum=MA6063T5. [Accessed April 22, 2022].

[36] Micro-Measurements, "240 UZA," *micro-measurements.com*. [Online]. Available: pca | Micro-Measurements. [Accessed Nov. 25, 2022].

[37] National Instruments, "Connecting Strain Gauges and Shunt Resistors to the NI-9237," *ni.com/en-us*. [Online]. Available: Connecting Strain Gauges and Shunt Resistors to the NI-9237 - NI. [Accessed Sept. 15, 2022].

[38] Vishay Precision Group, *Strain Gage Rosettes: Selection, Application, and Data Reduction*, Tech Note TN-515. Available: TN-515.pdf (intertechnology.com).

[39] Vishay Precision Group, *Errors Due to Misalignment of Strain Gages*, Tech Note TN-511. Available: TN-511.pdf (intertechnology.com).

[40] Micro-Measurements- VPG. "Strain Gage Installation Tutorial – Advanced Sensors Technology New CEA's," *YouTube*, Feb. 18, 2019. [Video File]. Available: STRAIN GAGE INSTALLATION TUTORIAL - YouTube. [Accessed Sept. 15, 2022].

[41] GoEngineer. "SolidWorks Simulation – Shell Elements for Frames Tutorial," *YouTube*, June 24, 2011. [Video File]. Available: SOLIDWORKS Simulation - Shell Elements for Frames Tutorial - YouTube. [Accessed Aug. 10, 2022].

[42] N. Pusateri. "SolidWorks Simulation: Thick versus Thin Shell Elements," *cati.com*, May 10, 2020. [Online]. Available: SOLIDWORKS Simulation: Thick versus Thin Shell Elements. - Computer Aided Technology (cati.com). [Accessed Jan. 12, 2023].

[43] Hawk Ridge Systems Engineering Team. "Adaptive Meshing in SolidWorks Simulation," *hawkridgesys.com*, Aug. 2, 2013. [Online]. Available: Adaptive Meshing in SOLIDWORKS Simulation (hawkridgesys.com). [Accessed Jan. 14, 2023].

[44] S. Patel. "Avoiding Singularities in SolidWorks Simulation," *goengineer.com*, Nov. 17, 2017. [Online]. Available: Avoiding Singularities in SOLIDWORKS Simulation | GoEngineer [Accessed Jan. 10, 2023].

[45] A. O. Cifuentes and A. Kalbag. "A Performance Study of Tetrahedral and Hexahedral Elements in 3-D Finite Element Structural Analysis," *Finite Elements in Analysis and Design*, vol. 12, no. 3-4, December 1992. [Online Serial]. Available: PII: 0168-874X(92)90040-J (sciencedirectassets.com) [Accessed Jan. 19, 2023].

[46] D. Peterson. "RE: Website Question Regarding VPG" Personal email. (December 5, 2022).

[47] Micro-Measurements- VPG. "Strain Gage Install on Composite Materials," *YouTube*, Aug. 28, 2017. [Video File]. Available: Tutorial: Strain Gage Install on Composite Materials - YouTube. [Accessed Dec. 5, 2022].

[48] Micro-Measurements- VPG. "Four Steps to the Perfect Baseball Swing? (Part 1 – Bonding)," *YouTube*, May 14, 2021. [Video File]. Available: Four Steps to the Perfect Baseball Swing? (Part 1 - Bonding) - YouTube. [Accessed Dec. 5, 2022].

[49] Dassault Systemes, "SolidWorks 2021 Online Help Guide," *Dassault Systemes*. [Online]. Available: Simulation - 2021 - SOLIDWORKS Help. [Accessed: 3/2022 - 4/2023]

[50] AchilleasMil, "Three Point Bending," *forum.ansys.com* [Online]. Available: Three point Bending (ansys.com). [Accessed: Feb. 25, 2023]

[51] K. Pelinski and J. Smardzewski, "Bending Behavior of Lightweight Wood-Based Sandwich Beams with Auxetic Cellular Core," *Polymers*, vol. 12, no. 8, July, 2020. [Online Serial]. Available: Polymers | Free Full-Text | Bending Behavior of Lightweight Wood-Based Sandwich Beams with Auxetic Cellular Core (mdpi.com). [Accessed: Mar. 10, 2023]

[52] A. Aspila, M. Heinisuo, K. Mela, M. Malaska, and S. Pajunen, "Elastic Design of Steel-Timber Composite Beams," *Wood and Material Science & Engineering*, vol. 17, no. 4, pp. 243-252, 2022. Available: Elastic design of steel-timber composite beams (tandfonline.com).

[53] C. Kassapoglou, *Design and Analysis of Composite Structures with Applications to Aerospace Structures*, 1st ed. West Sussex, UK: Wiley, 2010, pp. 182-188. Available: DESIGN AND ANALYSIS OF COMPOSITE STRUCTURES.

[54] Y. Li and J. Barbic, "Stable Anisotropic Materials," *Symposium on Computer Animation*, pp. 41-46, 2014. Available: TVCG-Barbic-2448105-NIH.pdf (ieee.org).

[55] M. Paschero and M. Heyer, "Axial Buckling of an Orthotropic Circular Cylinder: Application to Orthogrid Concept," *International Journal of Solids and Structures*, vol. 46, pp. 2151-2171, 2009. Available: Axial buckling of an orthotropic circular cylinder: Application to orthogrid concept | Elsevier Enhanced Reader.

[56] Althen Sensors, "LFLA Series Strain Gauges for Wood or Gypsum Use," *althensensors.com* [Online]. Available: LFLA Series Strain Gauges for Wood or Gypsum Use | Althen Sensors. [Accessed: Mar. 2, 2023]

[57] T. Matlock, "Experimental Investigation into Microstructures of Aircraft Grade Balsa Shear Webs," M.S. Thesis, Oklahoma State University, Stillwater, OK, 2023.

APPENDICES

APPENDIX A: Strain Gage Wiring Diagrams
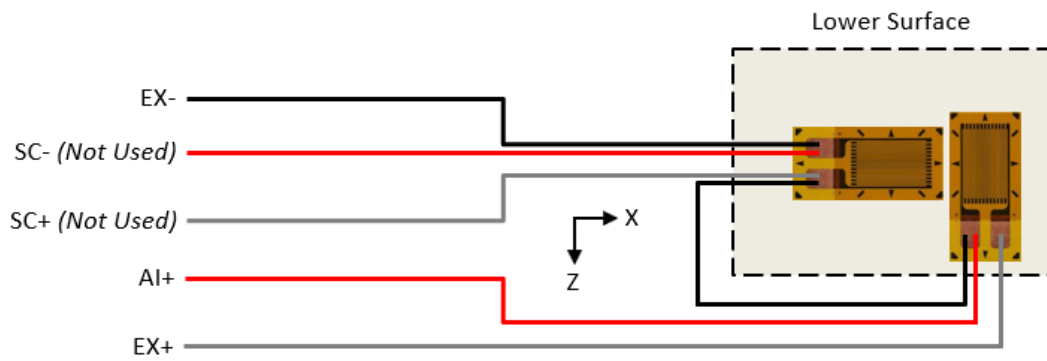
Figure 123: *Bending Strain Half-Bridge Type I Wiring Diagram*
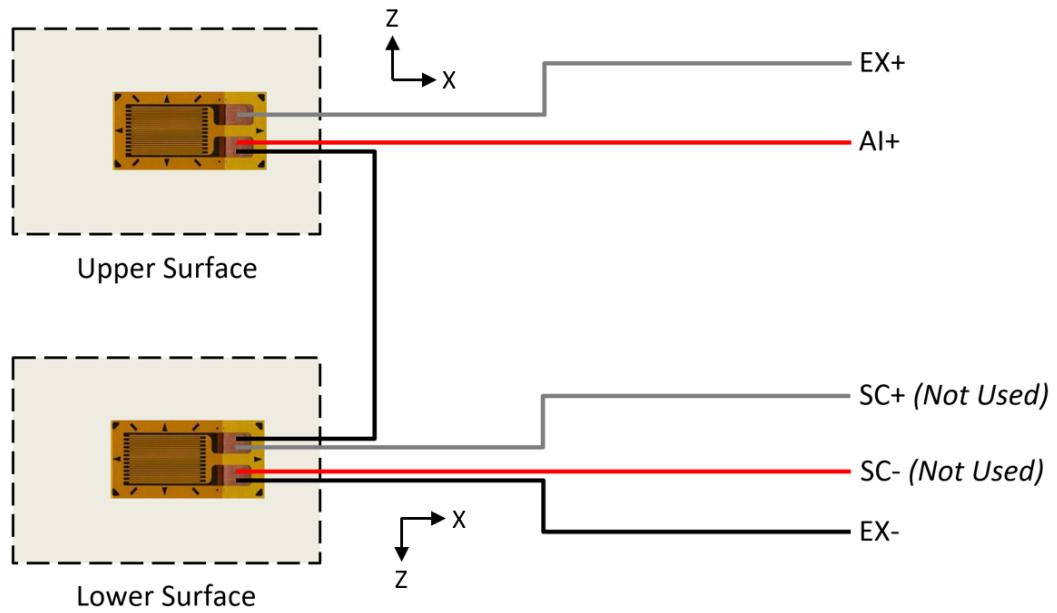
Figure 124: *Bending Strain Half-Bridge Type II Wiring Diagram*

Figure 125: *Shear Strain Half-Bridge Type II Wiring Diagram*

APPENDIX B: Square Cross-Section Metal Beam FEM and Experimental Data Tables
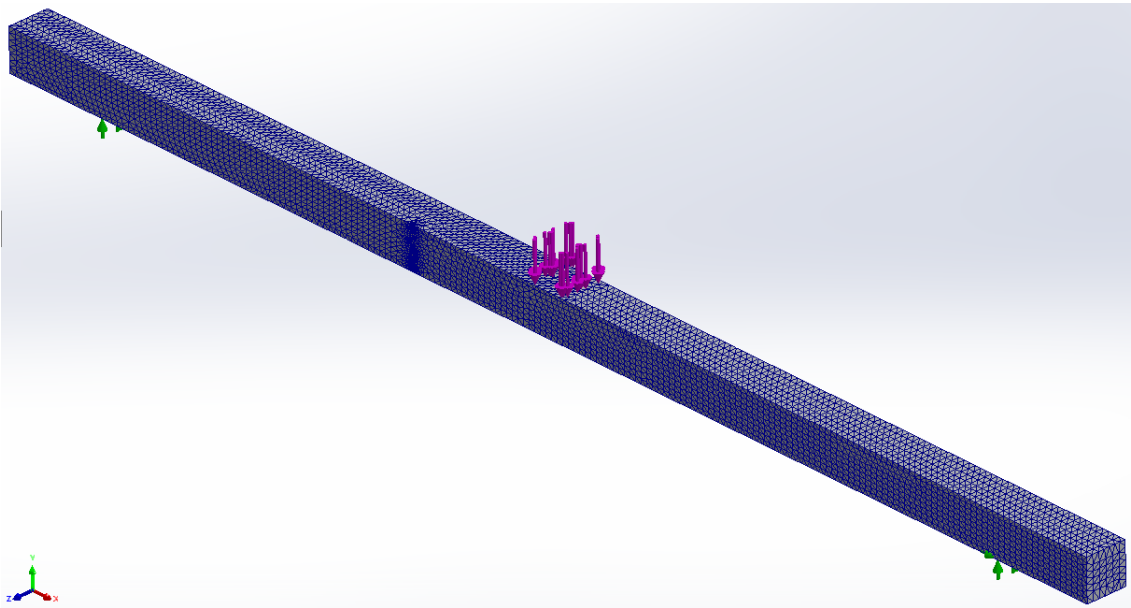
Figure 126: *Square Beam Complete 3D FEM*
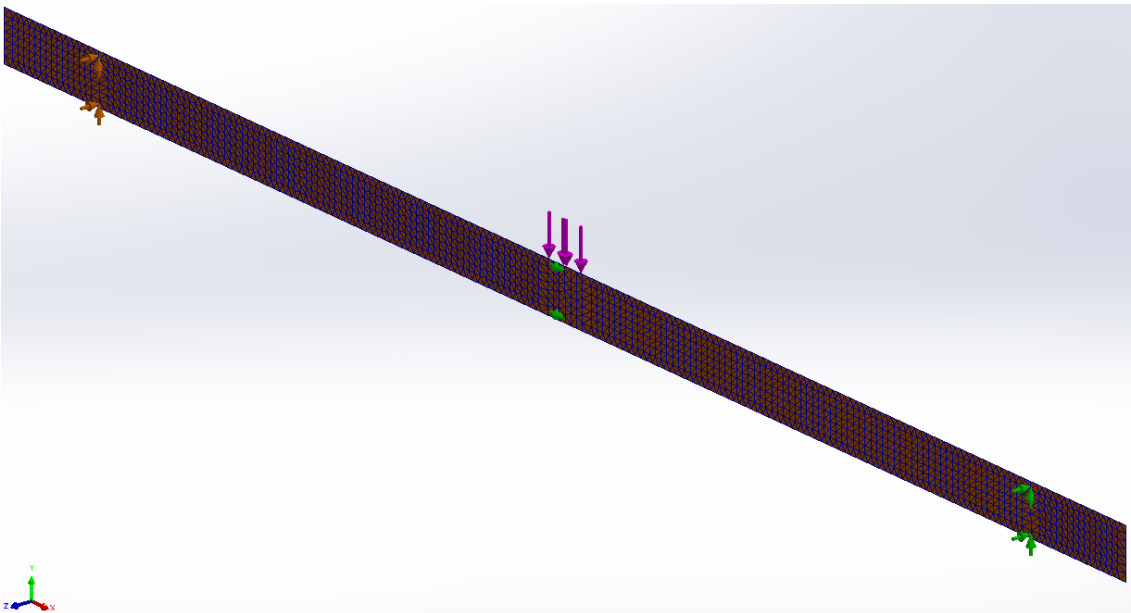
Figure 127: *Square Beam Complete 2D FEM*

Table 17: *Experiment #1 Square Beam Measurements and Uncertainties*

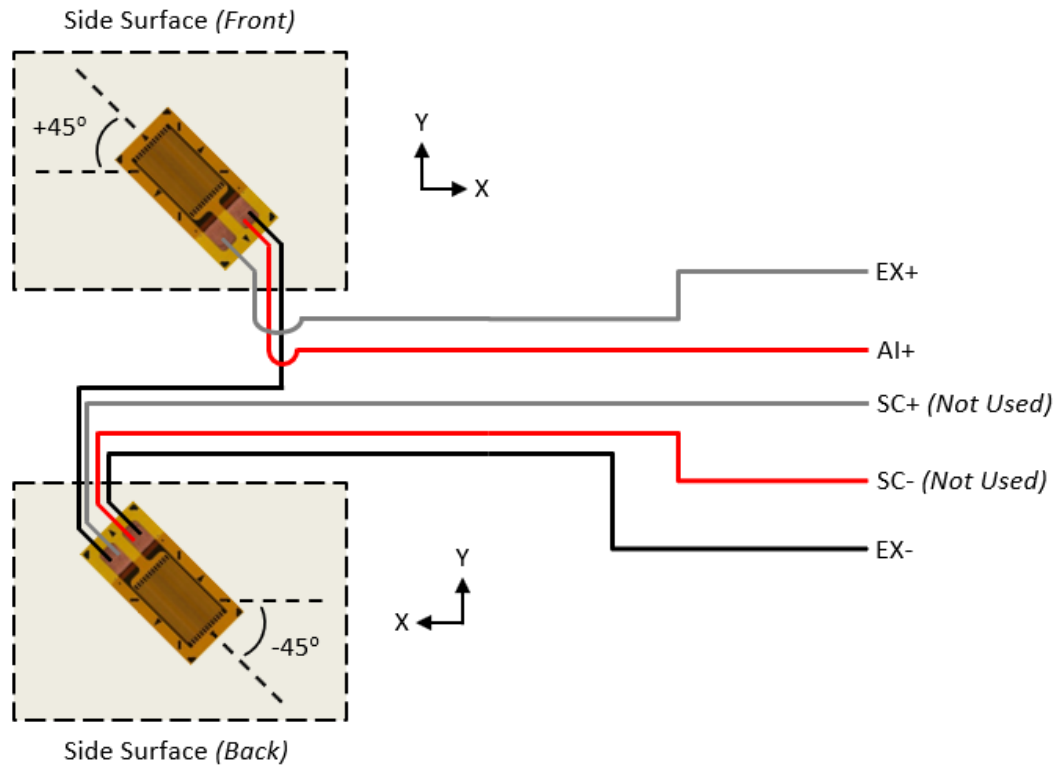| Deflection X-Position (inches)	Bending Trial #1			Bending Trial #2			Bending Trial #3		
	Deflection (inches)	±	Uncertainty	Deflection (inches)	±	Uncertainty	Deflection (inches)	±	Uncertainty
4	0.02580	±	5.64%	0.02600	±	5.60%	0.02630	±	5.53%
6	0.04515	±	3.28%	0.04460	±	3.32%	0.04435	±	3.34%
8	0.05995	±	2.44%	0.06015	±	2.43%	0.06045	±	2.42%
10	0.07155	±	2.00%	0.07090	±	2.02%	0.07215	±	1.98%
12.03125	0.07480	±	1.91%	0.07395	±	1.94%	0.07370	±	1.94%
14	0.07195	±	2.06%	0.07205	±	2.06%	0.07170	±	2.07%
16	0.06070	±	2.49%	0.06075	±	2.49%	0.06065	±	2.49%
18	0.04485	±	3.31%	0.04460	±	3.32%	0.04440	±	3.34%
20	0.02545	±	5.55%	0.02500	±	5.65%	0.02535	±	5.58%

Deflection Measurements [Square Beam]

Gage X-Position (inches)	Bending Trial #1			Bending Trial #2			Bending Trial #3		
	Strain (με)	±	Uncertainty	Strain (με)	±	Uncertainty	Strain (με)	±	Uncertainty
5	266.00	±	5.78%	265.00	±	5.79%	267.00	±	5.75%
12.03125	853.37	±	2.65%	852.00	±	2.65%	855.00	±	2.65%
15	617.00	±	3.14%	616.00	±	3.14%	618.06	±	3.13%
19	270.00	±	5.76%	269.00	±	6.07%	271.00	±	5.75%

Bending Strain Measurements [Square Beam]

Gage Y-Position (inches)	Bending Trial #1			Bending Trial #2			Bending Trial #3		
	Strain (μγ)	±	Uncertainty	Strain (μγ)	±	Uncertainty	Strain (μγ)	±	Uncertainty
0.4075	61.02	±	7.31%	60.99	±	7.40%	60.72	±	7.39%

Shear Strain Measurements [Square Beam]

Table 18: *Square Beam Positional Uncertainties*

X and Y Positional Uncertianties			
Deflection X-Position	±	0.104	inches
Gage X-Position	±	0.078	inches
Gage Y-Position	±	0.078	inches

APPENDIX C: I-Beam Cross-Section Metal Beam FEM and Experimental Data Tables
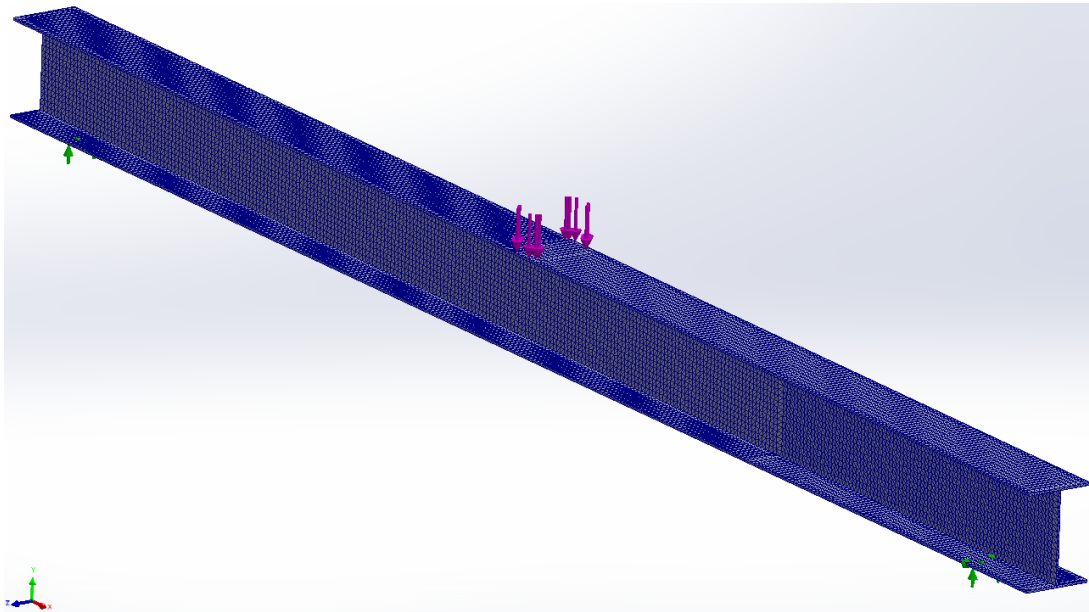
Figure 128: *I-Beam Complete 3D FEM*
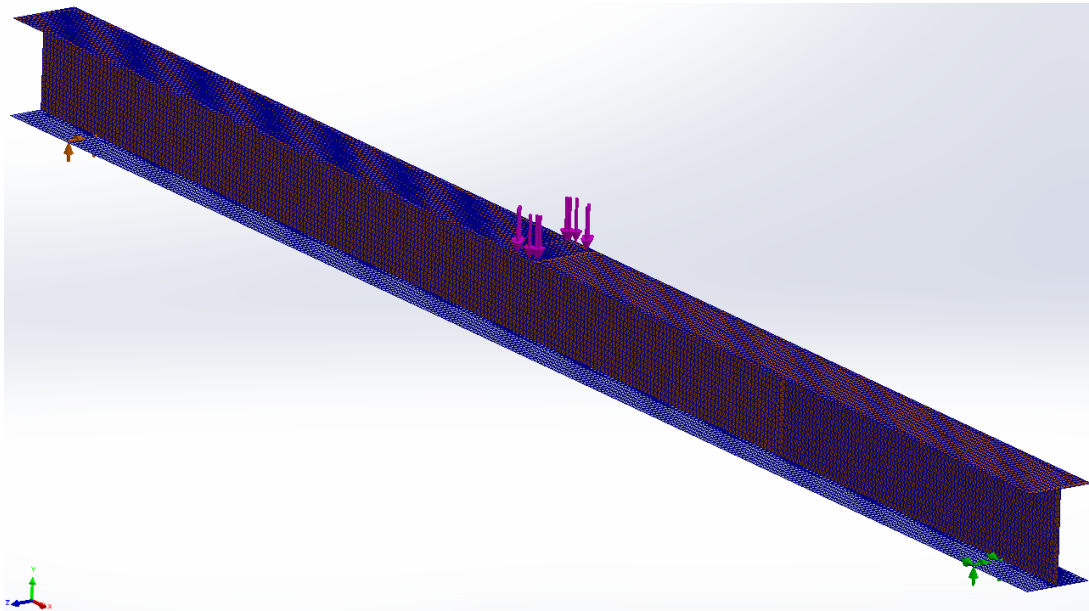
Figure 129: *I-Beam Complete 2D FEM*

Table 19: *Experiment #1 I-Beam Measurements and Uncertainties*

Deflection	Bending Trial #1			Bending Trial #2			Bending Trial #3		
Deflection Measurements [I-Beam]									
X-Position (inches)	**Deflection (inches)**	**±**	**Uncertainty**	**Deflection (inches)**	**±**	**Uncertainty**	**Deflection (inches)**	**±**	**Uncertainty**
6	0.02740	±	2.74%	0.02725	±	2.75%	0.02805	±	2.67%
8	0.03755	±	2.03%	0.03745	±	2.04%	0.03690	±	2.07%
10	0.04575	±	1.69%	0.04580	±	1.68%	0.04560	±	1.69%
12	0.05260	±	1.47%	0.05280	±	1.46%	0.05250	±	1.47%
14	0.05775	±	1.34%	0.05750	±	1.34%	0.05820	±	1.33%
16	0.06150	±	1.26%	0.06160	±	1.25%	0.06115	±	1.26%
17.9375	0.06445	±	1.21%	0.06405	±	1.22%	0.06435	±	1.21%
20	0.06165	±	1.28%	0.06090	±	1.30%	0.06170	±	1.28%
22	0.05785	±	1.38%	0.05750	±	1.39%	0.05740	±	1.39%
24	0.05210	±	1.53%	0.05210	±	1.53%	0.05145	±	1.55%
26	0.04515	±	1.73%	0.04465	±	1.75%	0.04530	±	1.73%
28	0.03635	±	2.09%	0.03650	±	2.08%	0.03645	±	2.08%
30	0.02745	±	2.67%	0.02725	±	2.69%	0.02780	±	2.63%

Gage	Bending Trial #1			Bending Trial #2			Bending Trial #3		
Bending Strain Measurements [I-Beam]									
X-Position (inches)	**Strain (µε)**	**±**	**Uncertainty**	**Strain (µε)**	**±**	**Uncertainty**	**Strain (µε)**	**±**	**Uncertainty**
7	212.00	±	4.05%	213.00	±	4.03%	213.00	±	4.04%
17.9375	674.36	±	2.13%	675.00	±	2.13%	677.00	±	2.13%
23	461.00	±	2.51%	461.18	±	2.51%	463.00	±	2.50%
29	207.00	±	4.17%	207.12	±	4.17%	208.00	±	4.15%

Gage	Bending Trial #1			Bending Trial #2			Bending Trial #3		
Shear Strain Measurements [I-Beam]									
Y-Position (inches)	**Strain (µγ)**	**±**	**Uncertainty**	**Strain (µγ)**	**±**	**Uncertainty**	**Strain (µγ)**	**±**	**Uncertainty**
1.06	195.04	±	4.83%	195.16	±	4.91%	195.60	±	4.81%

Table 20: *I-Beam Positional Uncertainties*

X and Y Positional Uncertianties			
Deflection X-Position	±	0.104	inches
Gage X-Position	±	0.078	inches
Gage Y-Position	±	0.078	inches

Equivalent E Calculation Using the EA-Equivalent Method:

Carbon Fiber Mechanical Properties:

$$\rho_c := 1.6 \frac{gm}{cm^3} = 99.885 \cdot \frac{lb}{ft^3}$$

$$E_1 := 135 GPa = 1.958 \times 10^4 \cdot ksi$$

$$E_2 := 10 GPa = 1.45 \times 10^3 \cdot ksi$$

Balsa Wood Mechanical Properties:

$$\rho_b := 11.287 \frac{lb}{ft^3}$$

$$E_L := 725013.19 psi$$

$$E_T := 9707.55 psi$$

$$E_R := 33197.31 psi$$

Section #3 Calculations:

$$E_3 := \sqrt[2]{E_1 \cdot E_2} = 5.329 \times 10^3 \cdot ksi$$

$$h_3 := 0.06in \qquad w_3 := 1.217in \qquad y_3 := \frac{h_3}{2} = 0.03 \cdot in$$

$$A_3 := h_3 \cdot w_3 = 0.073 \cdot in^2$$

$$\boxed{EA_3 := E_3 \cdot A_3 = 389.126 \cdot kip}$$

Section #2 Calculations:

$$E_2 := \sqrt[3]{E_L \cdot E_T \cdot E_R} = 61.591 \cdot ksi$$

$$h_2 := 1.118in \qquad w_2 := 0.125in \qquad y_2 := h_3 + \frac{h_2}{2} = 0.619 \cdot in$$

$$A_2 := h_2 \cdot w_2 = 0.14 \cdot in^2$$

$$\boxed{EA_2 := E_2 \cdot A_2 = 8.607 \cdot kip}$$

Section #1 Calculations:

$$E_1 := \sqrt[2]{E_1 \cdot E_2} = 5.329 \times 10^3 \cdot ksi$$

$$h_1 := 0.06in \qquad w_1 := 1.217in \qquad y_1 := h_3 + h_2 + \frac{h_1}{2} = 1.208 \cdot in$$

$$A_1 := h_1 \cdot w_1 = 0.073 \cdot in^2$$

$$\boxed{EA_1 := E_1 \cdot A_1 = 389.126 \cdot kip}$$

Overall Section Calculations:

$$A_{total} := A_1 + A_2 + A_3 = 0.286 \cdot in^2$$

$$EA_{eqv.} := EA_1 + EA_2 + EA_3 = 786.858 \cdot kip$$

$$E_{eqv.} := \frac{EA_{eqv.}}{A_{total}} = 2.753 \times 10^3 \cdot ksi$$

$$\rho_{eqv.} := \frac{\rho_c \cdot A_1 + \rho_b \cdot A_2 + \rho_c \cdot A_3}{A_{total}} = 56.561 \cdot \frac{lb}{ft^3}$$

APPENDIX E: EI-Equivalent Elastic Modulus Calculations

Equivalent E Calculation Using the EI-Equivalent Method:

Carbon Fiber Mechanical Properties:

$$\rho_c := 1.6 \frac{gm}{cm^3} = 99.885 \cdot \frac{lb}{ft^3}$$

$$E_1 := 135 GPa = 1.958 \times 10^4 \cdot ksi$$

$$E_2 := 10 GPa = 1.45 \times 10^3 \cdot ksi$$

Balsa Wood Mechanical Properties:

$$\rho_b := 11.287 \frac{lb}{ft^3}$$

$$E_L := 725013.19 psi$$

$$E_T := 9707.55 psi$$

$$E_R := 33197.31 psi$$

Section #3 Calculations:

$$E_3 := \sqrt[2]{E_1 \cdot E_2} = 5.329 \times 10^3 \cdot ksi$$

$h_3 := 0.06in$ $\qquad$ $w_3 := 1.217in$ $\qquad$ $y_3 := \dfrac{h_3}{2} = 0.03 \cdot in$

$$A_3 := h_3 \cdot w_3 = 0.073 \cdot in^2$$

$$I_{3x} := \frac{w_3 \cdot (h_3)^3}{12} = 2.191 \times 10^{-5} \cdot in^4$$

Section #2 Calculations:

$$E_2 := \sqrt[3]{E_L \cdot E_T \cdot E_R} = 61.591 \cdot ksi$$

$h_2 := 1.118in$ $\qquad$ $w_2 := 0.125in$ $\qquad$ $y_2 := h_3 + \dfrac{h_2}{2} = 0.619 \cdot in$

$$A_2 := h_2 \cdot w_2 = 0.14 \cdot in^2$$

$$I_{2x} := \frac{w_2 \cdot (h_2)^3}{12} = 0.015 \cdot in^4$$

Section #1 Calculations:

$$E_1 := \sqrt[2]{E_1 \cdot E_2} = 5.329 \times 10^3 \cdot ksi$$

$h_1 := 0.06in$ $\qquad$ $w_1 := 1.217in$ $\qquad$ $y_1 := h_3 + h_2 + \dfrac{h_1}{2} = 1.208 \cdot in$

$$A_1 := h_1 \cdot w_1 = 0.073 \cdot in^2$$

$$I_{1x} := \frac{w_1 \cdot (h_1)^3}{12} = 2.191 \times 10^{-5} \cdot in^4$$

Overall Section Calculations:

$$A_{total} := A_1 + A_2 + A_3 = 0.286 \cdot in^2$$

$$ybar := \frac{y_1 \cdot A_1 + y_2 \cdot A_2 + y_3 \cdot A_3}{A_{total}} = 0.619 \cdot in$$

$$I_{1p} := A_1 \cdot (y_1 - ybar)^2 = 0.025 \cdot in^4$$

$$I_{2p} := A_2 \cdot (y_2 - ybar)^2 = 0 \cdot in^4$$

$$I_{3p} := A_3 \cdot (y_3 - ybar)^2 = 0.025 \cdot in^4$$

$$I_{total} := (I_{1x} + I_{1p}) + (I_{2x} + I_{2p}) + (I_{3x} + I_{3p}) = 0.065 \cdot in^4$$

$$EI_{eqv.} := E_1 \cdot (I_{1x} + I_{1p}) + E_2 \cdot (I_{2x} + I_{2p}) + E_3 \cdot (I_{3x} + I_{3p}) = 271.122 \cdot kip \cdot in^2$$

$$E_{eqv.} := \frac{EI_{eqv.}}{I_{total}} = 4.154 \times 10^3 \cdot ksi$$

$$\rho_{eqv.} := \frac{\rho_c \cdot A_1 + \rho_b \cdot A_2 + \rho_c \cdot A_3}{A_{total}} = 56.561 \cdot \frac{lb}{ft^3}$$

APPENDIX F: Composite I-Beam Experimental Data Tables

Table 21: *Experiment #2 Measurements and Uncertainties [I-Beam #1]*

Composite I-Beam Deflection Measurements [Beam #1]									
Deflection X-Position (inches)	Bending Trial #1			Bending Trial #2			Bending Trial #3		
	Deflection (inches)	±	Uncertainty	Deflection (inches)	±	Uncertainty	Deflection (inches)	±	Uncertainty
4	0.01580	±	4.51%	0.01550	±	4.59%	0.01600	±	4.45%
6	0.02670	±	2.81%	0.02725	±	2.75%	0.02600	±	2.89%
8	0.03700	±	2.06%	0.03650	±	2.09%	0.03670	±	2.07%
10	0.04565	±	1.63%	0.04505	±	1.66%	0.04525	±	1.65%
12	0.05360	±	1.36%	0.05405	±	1.35%	0.05430	±	1.34%
14	0.04575	±	1.65%	0.04550	±	1.66%	0.04545	±	1.66%
16	0.03870	±	1.99%	0.03720	±	2.07%	0.03820	±	2.01%
18	0.02650	±	2.83%	0.02635	±	2.85%	0.02690	±	2.79%
20	0.01420	±	4.97%	0.01415	±	4.99%	0.01445	±	4.89%

Composite I-Beam Bending Strain Measurements [Beam #1]									
Gage X-Position (inches)	Bending Trial #1			Bending Trial #2			Bending Trial #3		
	Strain (με)	±	Uncertainty	Strain (με)	±	Uncertainty	Strain (με)	±	Uncertainty
5	98.54	±	12.58%	99.09	±	12.52%	99.20	±	12.51%
12	103.72	±	19.86%	103.72	±	19.87%	104.47	±	19.74%
15	143.00	±	21.20%	143.76	±	21.09%	144.04	±	21.06%
19	14.56	±	175.32%	13.74	±	185.88%	13.22	±	193.14%

Composite I-Beam Shear Strain Measurements [Beam #1]									
Gage Y-Position (inches)	Bending Trial #1			Bending Trial #2			Bending Trial #3		
	Strain (μγ)	±	Uncertainty	Strain (μγ)	±	Uncertainty	Strain (μγ)	±	Uncertainty
0.619	3197.28	±	22.39%	3153.51	±	22.74%	3146.16	±	22.71%

Table 22: *Experiment #2 Measurements and Uncertainties [I-Beam #2]*

Composite I-Beam Deflection Measurements [Beam #2]									
Deflection X-Position (inches)	Bending Trial #1			Bending Trial #2			Bending Trial #3		
	Deflection (inches)	±	Uncertainty	Deflection (inches)	±	Uncertainty	Deflection (inches)	±	Uncertainty
4	0.01570	±	4.52%	0.01550	±	4.58%	0.01525	±	4.66%
6	0.02700	±	2.77%	0.02705	±	2.77%	0.02695	±	2.78%
8	0.03505	±	2.17%	0.03510	±	2.17%	0.03485	±	2.18%
10	0.04430	±	1.68%	0.04510	±	1.65%	0.04435	±	1.68%
12	0.05490	±	1.33%	0.05500	±	1.32%	0.05475	±	1.33%
14	0.04660	±	1.62%	0.04620	±	1.63%	0.04515	±	1.67%
16	0.03740	±	2.05%	0.03825	±	2.01%	0.03730	±	2.06%
18	0.02685	±	2.79%	0.02720	±	2.75%	0.02645	±	2.83%
20	0.01455	±	4.84%	0.01470	±	4.79%	0.01460	±	4.83%

Composite I-Beam Bending Strain Measurements [Beam #2]									
Gage X-Position (inches)	Bending Trial #1			Bending Trial #2			Bending Trial #3		
	Strain (με)	±	Uncertainty	Strain (με)	±	Uncertainty	Strain (με)	±	Uncertainty
5	97.99	±	12.82%	97.68	±	12.89%	98.11	±	12.72%
12	76.63	±	26.90%	76.25	±	27.07%	77.78	±	26.42%
15	91.89	±	33.12%	91.94	±	33.12%	92.27	±	32.89%
19	41.52	±	62.07%	40.50	±	63.68%	40.75	±	63.03%

Composite I-Beam Shear Strain Measurements [Beam #2]									
Gage Y-Position (inches)	Bending Trial #1			Bending Trial #2			Bending Trial #3		
	Strain (μγ)	±	Uncertainty	Strain (μγ)	±	Uncertainty	Strain (μγ)	±	Uncertainty
0.622	3251.61	±	22.00%	3258.07	±	22.03%	3275.00	±	21.84%

Table 23: *Experiment #2 Measurements and Uncertainties [I-Beam #3]*

Composite I-Beam Deflection Measurements [Beam #3]									
Deflection X-Position (inches)	Bending Trial #1			Bending Trial #2			Bending Trial #3		
	Deflection (inches)	±	Uncertainty	Deflection (inches)	±	Uncertainty	Deflection (inches)	±	Uncertainty
4	0.01495	±	4.79%	0.01620	±	4.42%	0.01505	±	4.76%
6	0.02745	±	2.75%	0.02665	±	2.83%	0.02645	±	2.85%
8	0.03485	±	2.19%	0.03515	±	2.18%	0.03445	±	2.22%
10	0.04640	±	1.61%	0.04555	±	1.64%	0.04550	±	1.64%
12	0.05475	±	1.34%	0.05490	±	1.33%	0.05465	±	1.34%
14	0.04555	±	1.66%	0.04560	±	1.66%	0.04490	±	1.69%
16	0.03795	±	2.04%	0.03860	±	2.00%	0.03760	±	2.05%
18	0.02740	±	2.75%	0.02765	±	2.73%	0.02750	±	2.74%
20	0.01545	±	4.60%	0.01530	±	4.64%	0.01505	±	4.72%

Composite I-Beam Bending Strain Measurements [Beam #3]									
Gage X-Position (inches)	Bending Trial #1			Bending Trial #2			Bending Trial #3		
	Strain ($\mu\varepsilon$)	±	Uncertainty	Strain ($\mu\varepsilon$)	±	Uncertainty	Strain ($\mu\varepsilon$)	±	Uncertainty
5	97.52	±	12.91%	97.40	±	12.92%	97.65	±	12.90%
12	126.16	±	16.64%	124.00	±	16.93%	122.84	±	17.09%
15	133.21	±	23.17%	133.00	±	23.20%	133.35	±	23.14%
19	69.05	±	37.89%	69.45	±	37.67%	69.92	±	37.43%

Composite I-Beam Shear Strain Measurements [Beam #3]									
Gage Y-Position (inches)	Bending Trial #1			Bending Trial #2			Bending Trial #3		
	Strain ($\mu\gamma$)	±	Uncertainty	Strain ($\mu\gamma$)	±	Uncertainty	Strain ($\mu\gamma$)	±	Uncertainty
0.618	2250.16	±	30.95%	2260.10	±	30.89%	2248.42	±	30.95%

Table 24: *Composite I-Beam Positional Uncertainties*

X and Y Positional Uncertianties			
Deflection X-Position	±	0.104	inches
Gage X-Position	±	0.078	inches
Gage Y-Position	±	0.078	inches

VITA

Michael David Sallaz

Candidate for the Degree of

Master of Science

Thesis: THE EFFICACY OF UTILIZING SOLIDWORKS FINITE ELEMENT ANALYSIS FOR DESIGN OF COMPOSITE I-BEAM WING SPARS IN UAVS

Major Field: Mechanical and Aerospace Engineering

Biographical:

Education:

Completed the requirements for the Master of Science in Mechanical and Aerospace Engineering at Oklahoma State University, Stillwater, Oklahoma in May, 2023.

Completed the requirements for the Bachelor of Science in Aerospace Engineering at Oklahoma State University, Stillwater, Oklahoma in 2021.

Completed the requirements for the Bachelor of Science in Mechanical Engineering at Oklahoma State University, Stillwater, Oklahoma in 2021.

Experience:

Oklahoma State University (*under Dr. Arena*)
   Graduate Research Assistant   [12/2021 – 05/2023]
     – Composite UAS replication, design, fabrication, and testing

Lockheed Martin Aeronautics (*various departments*)
   IFG Stress Analysis Intern   [05/2022 – 08/2022]
   Landing and Arresting Gear Systems Intern   [05/2021 – 07/2021]
   Composites Lab Intern   [05/2020 – 08/2020]
   F-16 Sustainment Intern   [05/2019 – 08/2019]
     – Worked multiple projects for IFG, JSF, and the SNC Dream Chaser